Smart nano-inks for inkjet printing of functional oxide based thin films

Gadea, Christophe

Publication date:
2018

Document Version
Publisher's PDF, also known as Version of record

Technical University of Denmark

DTU Energy

Ceramic and Engineering Science (CES) group

Smart nano-inks for inkjet printing of functional oxide based thin films

Author:

Christophe Gadea

Supervisors

Prof. Vincenzo Esposito

Dr. Jean-Claude Grivel

Dr. Séverine Ramousse

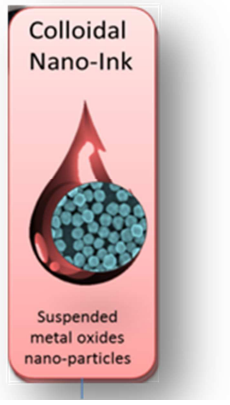

Submitted in candidacy for the degree of Doctor of Philosophy

Preface

This thesis is submitted in candidacy for the *Philosophæ Doctor* (PhD) degree in Material Science from the Technical University of Denmark (DTU). The work was carried out at DTU Energy at Roskilde, Denmark, between December 14th 2014 and December 14th 2017. The project was supervised by Professor Vincenzo Esposito, Dr. Séverine Ramousse and Dr. Jean-Claude Grivel. The project was funded internally by DTU Energy. During the three years, three weeks of the work, divided in three visits, was carried out at the *Ecole Polytechnique Fédérale de Lausanne* (EPFL), at the research group *Laboratoire d'Electrochimie Physique et Analytique* lead by Professor Hubert Girault and under the supervision of Dr. Andreas Lesch. This work included one of the main authoring paper included in this thesis (paper II), and was partially financed by the Fuel Cells and Hydrogen 2 Joint Undertaking under grant agreement No 700266 and the Swiss National Science Foundation (SNSF) grant no. 154297.

Acknowledgments

Firstly, I would like to express my sincere gratitude to my supervisor professor *Vincenzo Esposito* for guiding me through this three year journey and providing me continuous support, both professionally and privately. Your guidance, patience, motivation and immense knowledge helped me in time of research and especially when writing of this thesis and related articles. Thank you for being my mentor and my friend.

I would also like to give a special acknowledgement to my ex-supervisor *Séverine Ramousse*. It is because you gave me a chance to prove myself as master student in 2007 that I have been able to work and study here at DTU Energy. In 2014 you believed in me again when you accepted me as PhD student, and I will never thank you enough for all of that.

Thank you *Jean-Claude Grivel* for accepting to take the vacant supervisor position during the project. You gave me solid advices and knowledge, especially in the laboratory that allowed me to complete this thesis in a proper manner.

Thank you *Debora Marani* for your help along the way, your teaching and for the time you dedicated to my project. You are missed here at DTU Energy and I hope that our paths cross again in the future.

Thank you *Mads Gudik-Sørensen* for your precious help along the years, both professionally and personally, I am grateful for everything you did. I hope we will work together again so we can look funny with our height difference. I also hope we can see France beat Denmark in the World Cup together.

I would like also to thank *Søren Højgaard Jensen* for asking me to start with him the first activities in inkjet printing back in 2014. The amazing work done led to this first PhD position in that domain in our department, and open the path to more development in the future. I also would like to thank the rest of the inkjet printing group that contributed to this work: *Johan Hjelm*, *Qiang Hu* and *Karsten Agersted.*

A big thank you to the whole Ceramic Engineering and Science (CES) group, including those who left in my three year period. I have known most of you for 10 years, and you have always been here for me when I needed. A special thanks to my fellow PhD student *Massimo Rosa*, who is still

struggling with inkjet printing as I am writing these words, to *Nuntanid Phatharapeetranun* from Silpakorn University and to *Giovanni Perin* from Padova University: You did an amazing job during your external stay here, which was a corner stone of some of the work presented here, and I thank you deeply for your contribution. Lastly, I would like to thank Master students *Quentin Hanniet* and *Gaëtan Guellec* for their contribution to this thesis during their 3 month traineeships. Thanks a lot *Connie Westergaard* for helping me with all the administrative paperwork along the three years.

I would like to thank Professor *Hubert Girault* and his team of *Laboratoire d'Electrochimie Physique et Analytique* (LEPA) at the *Ecole Polytechnique Fédérale de Lausanne* (EPFL) for their welcome and productive work during my stays. I would like to particularly thank Dr. *Andreas Lesch* and PhD student *Victor Costa Bassetto* for their help and dedication during my visits, and I hope to work again with both of you in the future.

As promised to my DTU friends, I would like to thank the WhatsApp group named "The Risø Empire". Thank you all for your very interesting and deep discussions about everything, I am going to miss receiving 47 messages per minutes to discuss which pizza should be ordered. A special thanks to *Stéven Pirou*, *Megha Rao*, *Fabrizio Gualandris* and *Kosova Kreka* for the discussions at lunch time that I will miss. I would also like to thank my music band "*Conduction band*" for the fun and the concerts.

A special thanks to all my friends here in Denmark, and also all around the world for their support during this journey, and especially *Caroline Durif, Joris & Joëlle Auert* and *Benoit & Deborah Charlas* for their friendship and support along the years, and my conference buddy *Matteo Pernechele* (I hope to meet you again someday, somewhere in the world).

I would like to warmly thank my mother *Bernadette* and my father *Jean-Claude* for their love and the support since I started studying, despite the long distance that separates us. I also would like to thank my sister *Charlotte* and my niece *Ainoa* for being there, as well as my grandmother *Carmen* and everyone in my family. I am also thankful to my family in-law for their help and support, and particularly *Colette* for helping out at home when I was on business trips.

Finally, I would like to address my eternal thanks to my wife *Clémence* for her daily love and support along this journey that could not been achieved without her, and to our wonderful daughters *Justine* and *Maëlle* for their daily laugh and joy. Je vous aime.

In loving memory of my grandfather Jean (1924-2008)

Abstract

The development of thin oxide based films for energy production and storage has been in the center of attention for the past decades. Performances of film based devices, such as solar cells, solid oxide fuel cells (SOFC), or sensors is strongly linked to the thickness of the active layers, with thinner layers often providing enhanced performances. The success in the development and usability of such energy production devices is linked to the deposition technique chosen for the layer fabrication. The technique should be reproducible, industrially scalable and low cost to be viable as well as commercially attractive. Among thin film fabrication processes, inkjet printing is a high potential candidate.

Inkjet printing is a deposition method based on the jetting of very small droplets (approx. 10^{-12} l) onto substrates. It is a mask-less, non-contact additive patterning technique that allows the deposition of complex patterns with high positional accuracy of the droplets (typically in the micron-range spacing) with high speed and low cost. Due to these features, this processing method shows a strong potential as a thin film fabrication method. For the past decades inkjet printing of functional materials has been developed and studied as an alternative to spin coating, lithography, etching or physical vapor deposition technique such as pulse laser deposition (PLD) for the fabrication of metal oxide based thin films. One critical aspect in inkjet printing is the ink design and its long term stability. Instability can lead to undesirable nozzle clogging and unresolved printing that lower the global performance of the device.

This thesis presents the development and characterization of three inks designs which differs by the oxide source: a suspension of colloidal particles, a solution metallic precursor-based particle free ink, and a combination of both solution and suspension, here called hybrid ink. The major goal of this work was to evaluate the printability and the stability potentials of different ink designs for inkjet printing, and the pros/cons of each of them. The ink printability and stability is particularly evaluated through rheology, chemical characterization and droplet jetting observation. Films made of some relevant functional ceramics such as zirconium-, cerium-and titanium-oxide based materials are successfully fabricated with printers using different droplet ejection principles to demonstrate the versatility of the inks. Microstructure and performance of the films after heat treatment is characterized and show enhanced performance compared to films processed with different methods.

Resume

Udvikling af metaloxid-baseret tynd-film materialer til energiproduktion og -lagring har stor bevågenhed i de sidste årtier. Virkningsgraden af film-baserede enheder, såsom solcelle, brændselsceller (SOFC), eller sensorer, er stærkt forbundet til det aktive lags tykkelse, hvor tyndere lag ofte giver forbedrede virkningsgrader. Resultatet og anvendeligheden af sådant energi produktions udstyr er influeret af den valgte deponerings-teknik. Teknikken skal være reproducerbar, skalerbar til stor-format og billig for at være industrielt attraktiv. Blandt tynd-film fabrikations metoder er inkjet printing en kandidat med højt potentiale.

Inkjet printing er en aflejrings teknik baseret på skud af meget små dråber blæk (ca. 10^{-12} l) mod et substrat. Den er en maskeløs og kontaktløs mønsterdannelses teknik som muliggør aflejringen af komplekse mønstre med høj nøjagtighed af dråberne (typisk i mikrometer størrelse/afstand) med høj hastighed og lav omkostninger. På grund af dette kan tekniken have stærkt potentiale som tyndtlags fabrikationsmetode. I løbet af de sidste årtier er inkjet prining af funktionalle materialer blevet udviklet og studeret som alternativ metode til spin coating, litografi, ætsning eller damp aflejring (f.eks. Pulse Laser Deposition) til fabrikation af metal-oxid baseret tyndfilm. Et kritisk aspekt af inkjet printing er blæk design og blækkets stabilitet over tid. Ustabilitet kan medføre uønsket tilstopning af printerhovedet og defekter i det printede lag, som vil reducere den samlede virkningsgrad.

Denne afhandling præsenterer udviklingen og karakteriseringen af tre blæk design med forskellig metal-oxid kilde: en suspension af kolloide partikler, en partikel fri opløsning baseret på organometallisk reaktant, og en kombination af suspension og opløsning, benævnt hybrid blæk. Hovedmålet med denne afhandling er at evaluere blæk ”printability” og stabilitet af forskellig blæk design til ”inkjet printing” samt deres fordeler/ulemper. Blæk ”printability” og stabilitet bliver evalueret, især gennem reologi, kemisk karakterisering og observation af dråbedannelse. Film baseret på relevante funktionelle keramiske materialer, såsom zirconium-, cerium- og titaniumoxid baserede materialer, er med succes fabrikeret på printere som har forskellige dråbe-udskydnings principper, for at vise blæk alsidighed. Film mikrostruktur og virkningsgrad efter varmebehandling er karakteriseret og viser forbedret virkningsgrad sammenlignet med film fabrikeret med andre metoder.

Contents

Chapter 1 : Thesis introduction

1.1 **Inkjet printing of thin film functional materials: Status, progress and challenges**

Energy production and storage is one of the major challenges in modern society. Research and development of highly-performing, reliable and inexpensive systems has been the focus of research institutes and companies throughout the world in the past half-century. Oxide-based materials are used in the majority of these technologies, from Solar Cells (SC) to Solid Oxide Fuel Cells (SOFCs). One aspect shared by these technologies is their design, which often consists of multilayer systems, either composed of stacked layers, complex patterns or both.

In the past decades, energy converters and harvesters designs evolved towards miniaturization of the devices. Focus on device size reduction is set for several reasons. First, it leads to smaller and lighter devices, which is desirable in mobile applications such as in the automotive industry (SOFC, piezoelectric materials, batteries), laptops and mobile phones (batteries, circuits), or flexible electronics. Moreover the reduction of certain components of the device can improve the global performances. For example, SOFC performances and operating temperatures are strongly linked to the electrolyte thickness [1]. However the fabrication of thin films can become a technical challenge.

Several processes have been considered and studied for the fabrication and miniaturization of oxide based thin films. While traditional processes such as tape casting, screen printing or spray are inexpensive and easy to scale up, the deposition of films thinner than 10 µm is technically challenging. On the other hand, more advanced techniques such as sputtering, pulse laser deposition (PLD), or atomic layer deposition (ALD) yield thicknesses in the nanometric range. They are yet very costly and difficult to scale up for industrial production. A process that interestingly combines economical and technical advantages of both traditional and advanced techniques is spin coating. However, complex geometrical shapes cannot be fabricated using this technique [2]; moreover a considerable quantity of product is wasted during the process, which is non-desired when working for example with expensive raw materials. Devices miniaturization requires the use of new shaping techniques that need to be economically viable so the industry will invest in them in the long term.

Inkjet printing is an alternative that meets the required criteria. This technique is based on the ejection and precise deposition of nano- to picoliter-sized droplets onto a substrate without contact. Both thin (<1 µm) layers and complex shapes can be deposited using this technique with high precision, hence without material waste. The process uses a wide range of solution-phase materials, such as solid material [3–5] (nano particles, colloids, nanowire, etc.) or metal-organic precursors for the sol-gel process in a specific solvent, generally water based [6–8]. Finally, inkjet printing has a high output and can be easily scaled up to large-area applications on different type of substrates (ceramic, polymer, metal). Inkjet shows however some drawbacks compared to other thin films deposition technologies such as a limited microstructural control or the lack of epitaxial growth as in pulse laser deposition.

In the recent years, inkjet printing has been successfully used for the development of layered based energy devices and showed higher performances compared to classical processes. High performance of dye sensitized solar cells using an inkjet-printed ionic liquid electrolyte was demonstrated by showing a 6% enhancement of overall energy conversion compared to reference cells [9]. Complex patterning of ferroelectric materials such as lead zirconate titanate (PZT) and barium titanate ($BaTiO_3$) were successfully deposited by inkjet printing [2,10–12]. Barium strontium titanate (BST) was also deposited by inkjet printing using sol-gel precursors, and the study demonstrated that this method uses 40 times less precursors than standard spin coating technique [13]. The fabrication of SnO_2 and ZnO based gas sensing thin films by inkjet printing [7,14] showed that this technique is a suitable and low-cost method to prepare such thin films. Electrolyte for SOFC was deposited by inkjet printing using colloidal suspensions and performance improvements were recorded compared to standard tape cast electrolyte [15]. Finally titania (TiO_2) photocatalytic layers were produced by inkjet printing of precursor solutions, and proved to be an efficient method for the development of such layers [16]. It is interesting to point out that a large variety of materials could be processed by inkjet printing by using either colloids or precursors. The resulting layers or patterns contributed to the improvement of several key technologies for energy production and storage.

Inkjet printing is flexible, low cost and easily up scalable to the industrial level by for example increasing the number of nozzles. Inkjet printing can be distinguished in three different technologies: continuous, thermal and piezoelectric. These technologies and their principles will be

detailed in Chapter 2. Out of the three, piezoelectric inkjet is the most attractive for the high tech industry due to high precision and versatility in terms of ink composition and printing distance. In the past decades, several industrial fields have chosen inkjet printing for their products, divided in two categories: Macro- and micro-printing. Macro-printing consists of jetting droplets with volume between than 35 pl and 200 pl. Application includes wide-format printing, addressing and bar coding. It also covers new applications such as product decoration (tiles, wood panels, leather), protective layers (scratch resistant coating on eye lenses or mobiles) and conductive/non-conductive patterns. Micro-printing consists of jetting of droplet with a volume smaller than 35 pl and is used in the fabrication of flexible electronic circuits, DNA arrays and biologically sensitive sensors and papers. A survey conducted by Ceramic World Review [17] at seven manufacturers of digital printing machines for ceramics revealed that 1044 machines had been installed worldwide between 2010 and 2011. Around 400 more were expected to be installed in the first semester of 2012, showing a growing interest of the industry for this technology. Continuous inkjet printing is also used in the industry, especially in labelling. However it is less and less desired due to a high quantity of wasted material.

Inkjet printing technology is theoretically a simple process but in practice it suffers of several critical aspects, one of the most critical being the ink design. In most cases inks consist of particles suspended in a medium. This method allows reaching high solid loading to yield dense layer, or to introduce pore formers. A different approach is to use stabilized particle-free metal-organic precursors in water; the precursor is stabilized in water using a nucleophilic ligand, and once deposited, precursors polymerizes to form the particles. These two methods have both advantages and disadvantages. In this work, these designs and original ones inspired from them will be studied for specific materials.

1.2 **Goals and objectives**

Previous research on inkjet printing applied to energy conversion devices demonstrated its high potential as thin film deposition technique. While these studies focused mostly on the final application, very few discussed about the choice of oxide source (colloids, nanoparticles, organometallic precursors) or the inks printability and long-term stability (viscosity, particle size, surface tension, etc.). Inks properties of poorly optimized inks change with time: particle agglomeration can lead to nozzle clogging, instability of precursors to viscosity increase, affecting

the printability. These factors negatively alter the ink usability over time, making the process non reproducible and unattractive.

The principal objective of this work is to study the printability and stability of different inks design for inkjet printing, both in terms of oxide source, materials and applications. Three ink designs were considered: **colloidal based ink**, *i.e.* containing particles between 1nm and 1µm of diameter; metal-organic **reactive inks** using controlled sol-gel reactions; a "**hybrid" ink** combining colloidal particles suspended in a reactive ink. The chosen materials were zirconia and titania based, for their wide range of applications, e.g. in SOFC and photocatalysis/piezoelectricity. Moreover, several compounds and composites studied in the energy production and storage derivate from these two oxides, such as barium titanate $BaTiO_3$, strontium titanate $SrTiO_3$ or lead zirconate titanate $Pb[Zr_xTi_{1-x}]O_3$ ($0 \leq x \leq 1$), also called PZT. These compounds can easily be developed by doping zirconium and/or titanium inks.

Focus was set on inks preparation and characterization, especially their printability *i.e.* the ink ability to form reproducible droplets. A second aspect studied is the long-term stability of these inks in terms of printability and jettabilitty, especially in the case of reactive based inks. Finally the microstructure of the printed layers after heat treatment on various substrates was characterized, and film properties (conductivity, dielectric constant) were measured. To achieve these objectives, I defined the following list of milestones at the beginning of the project:

1. Describe the type of inks (colloidal, sol-gel, hybrid) and the solvent system, and printing systems that will allow the deposition of thin films
2. Define the studied materials and their final application, along with their oxide sources for the different type of inks
3. Establish ink preparation protocols that produced reproducible inks
4. Identify suitable methodology and tools to characterize inks printability and their long term stability
5. Characterize quantitatively and qualitatively the deposited layers in terms of microstructure, phase composition and final dimensions (shrinkage)
6. Use and test the performances of the fabricated layers in their relevant technologies.

This dissertation reports the work done on this project over a period of three years. Several peer-reviewed papers on the topic were published during this period and were used as a support in this thesis. Paper III received the award of "Excellent paper award" at the 230th International Academic Conference on Engineering, Technology and Innovations (IACETI) in Bangkok, Thailand (2017). In addition other unpublished results are reported. During this period, several visits of the *Laboratoire d'Electrochimie Physique et Analytique* (LEPA), a group of the Ecole Polytechnique Fédérale de Lausanne (EPFL) in Sion, Switzerland were organized. A paper was published in collaboration with EPFL (paper II). Finally, results obtained during the three years were presented in several international conferences:

- Oral presentation at the Pacific Rim Conference on Ceramic and Glass Technology (PacRim 12) in Waikoloa Village, HI, USA (May 2017)
  "Inexpensive thermal inkjet printing of sol-gel based YSZ layer on dense and porous substrates"
- Oral presentation at the International Conference and Exposition on Advanced Ceramics and Composites (ICCAC'16) in Daytona, FL, USA
  "Fabrication of titania nano layer by inexpensive inkjet printing via sol-gel route" and "Fabrication of thin yttria-stabilized-zirconia dense electrolyte layers by inkjet printing for high performing solid oxide fuel cells
- Oral presentation at Conference on Ceramic Materials and Components for Energy and Environmental Applications (CMCEE'11) in Vancouver, Canada
  "Fabrication of thin yttria-stabilized-zirconia dense electrolyte layers by inkjet printing for high performing solid oxide fuel cells"

1.3 **Layout of the thesis**

The thesis is structured as follows: the thesis opens by giving the reader some basic knowledge about inkjet printing technology (Chapter 2), followed by the ink designs, including the studied materials (Chapter 3). The characterization tools used to help understand observed phenomenon are presented (Chapter 4) as introductive background to the results (Chapters 5-7). Particularly, the results part starts with a presentation of the work done on **colloidal ink** design, where advantages and disadvantages are listed (Chapter 5). The author would like to stress that chapter 5 reports work performed before the PhD project started. As such, it serves only as an historical basis for chapters 6 and 7 and should *not* be considered for examination. The obtained results lead to designing a

second type of ink, **reactive ink** (Chapter 6). Finally, a third design combining the first two, called **hybrid ink** (Chapter 7), closes the result and discussion part of the thesis before the conclusion and remarks section (Chapter 8). Publications are inserted as appendices at the end of the thesis for more information about the results. Each chapter is described below:

- Chapter 2 introduces inkjet printing technology, the working principles and presents the systems used in this thesis. The concept of ink printability is defined and the considered ink types are presented.
- Chapter 3 focuses on the materials studied and the concept behind each ink designs. The various studied phases are described along with some basic properties which are relevant for this work. The chemical principle of each ink is detailed, along with the raw materials and the substrates used.
- Chapter 4 gives a description and working principle of the characterization methods used in this thesis, both on the inks and the final layers. Equipment and measurement parameters are detailed.
- Chapter 5 presents the work performed on colloidal inks and specifically on yttria-stabilized-zirconia (YSZ) electrolyte for SOFCs. The ink composition and preparation is described, along with the layer microstructural and electrochemical characterization. The advantages and challenges of such type of ink for inkjet printing are discussed.
- Chapter 6 introduces the concept of reactive inks, *i.e.* sol-gel based ink using titania- and zirconia- based materials. Inks compositions and preparation are detailed and a particular attention is given to long-term stability of the inks in term of printability. Resulting layers are characterized and their performances are evaluated. The advantages and disadvantages of this type of ink are discussed.
- Chapter 7 deals with hybrid ink *i.e.* suspension of colloidal particles in a reactive ink using titania- and zirconia based materials. Inks compositions and preparation procedure are detailed. Preparation methods of the inks and ink printability are analyzed, and performances of resulting layers in relevant technologies are described.
- Chapter 8 presents the conclusions of this thesis and open discussions for further work to be performed in this field.

The following appendices are placed at the end of the thesis for further reading:

- Paper I: C. Gadea, D. Marani, V. Esposito, "Nucleophilic stabilization of water-based reactive ink for titania-based thin film inkjet printing", J. Phys. Chem. Solids. 101 (2017) 10–17.
- Paper II: C. Gadea, Q. Hanniet, A. Lesch, D. Marani, S.H. Jensen, V. Esposito, "Aqueous metal-organic solutions for YSZ thin film inkjet deposition", J. Mater. Chem. C. 5 (2017).
- Paper III: N. Phatharapeetranun, C. Gadea, B. Ksapabutr and V. Esposito, "Assembly three dimensional bismuth titanate (3D-bit) by extrusion-based fuse deposition modeling technique", as proceeding paper for "the 230th International Academic Conference on Engineering, Technology and Innovations (IACETI), Bangkok, Thailand" 2017
- Paper IV: C. Gadea, N. Phatharapeetranun , B. Ksapabutr, J.-C. Grivel , V. Esposito, "Stoichiometric control in $Bi_4Ti_3O_{12}$ synthesis by novel hybrid solid state reaction", submitted in "*Materials Letters*" (moderate revision)
- Addition to Chapter 5: V. Esposito, C. Gadea, J. Hjelm, D. Marani, Q. Hu, K. Agersted, S. Ramousse, S.H. Jensen, Fabrication of thin yttria-stabilized-zirconia dense electrolyte layers by inkjet printing for high performing solid oxide fuel cells, J. Power Sources. 273 (2015) 89–95.

Bibliography

[1] S. De Souza, S.J. Visco, L.C. De Jonghe, Thin-film solid oxide fuel cell with high performance at low- temperature, Solid State Ionics. 98 (1997) 57–61.

[2] J. Vukmirovic, D. Tripkovic, B. Bajac, S. Kojic, G. Stojanovic, V. Srdic, Comparison of barium titanate thin films prepared by inkjet printing and spin coating, Process. Appl. Ceram. 9 (2015) 151–156. doi:10.2298/PAC1503151V.

[3] L. Klintberg, G. Thornell, S. Johansson, Drop-by-drop deposition of ceramic slurry for fabrication of PZT microstructurers, 3892 (1999) 158–165.

[4] M. Arin, P. Lommens, D. Vandeput, J. Van Acker, I. Van Driessche, Durability and efficiency of ink-jet printed TiO2 coatings: Influence of processing temperature, Thin Solid Films. 556 (2014) 160–167. doi:10.1016/j.tsf.2014.01.054.

[5] H. Sirringhaus, High-Resolution Inkjet Printing of All-Polymer Transistor Circuits, Science (80-.). 290 (2000) 2123–2126. doi:10.1126/science.290.5499.2123.

[6] X. Ding, Y. Li, D. Wang, Q. Yin, Preparation of (Ba x Sr 1 (x) TiO 3 sols used for ceramic film jet-printing, 99 (2003) 502–505.

[7] W. Shen, Properties of SnO2 based gas-sensing thin films prepared by ink-jet printing, Sensors Actuators B Chem. 166–167 (2012) 110–116. doi:10.1016/j.snb.2012.01.019.

[8] T. Vidmar, M. Topič, P. Dzik, U. Opara Krašovec, Inkjet printing of sol–gel derived tungsten oxide inks, Sol. Energy Mater. Sol. Cells. 125 (2014) 87–95. doi:10.1016/j.solmat.2014.02.023.

[9] S.G. Hashmi, M. Ozkan, J. Halme, K.D. Misic, S.M. Zakeeruddin, J. Paltakari, M. Grätzel, P.D. Lund, High performance dye-sensitized solar cells with inkjet printed ionic liquid electrolyte, Nano Energy. 17 (2015) 206–215. doi:10.1016/j.nanoen.2015.08.019.

[10] T. Wang, B. Derby, Ink-Jet Printing and Sintering of PZT, J. Am. Ceram. Soc. 88 (2005) 2053–2058. doi:10.1111/j.1551-2916.2005.00406.x.

[11] T. Wang, D. Hall, B. Derby, Ink-jet printing of wax-based PZT suspensions, Key Eng. Mater. 264 (2004) 697–700. doi:10.4028/www.scientific.net/KEM.264-268.697.

[12] A. Komatsu, T. Hoshina, S. Kunej, H. Takeda, T. Tsurumi, Fabrication of BaTiO3 Films on Si Substrate by Inkjet Printing, Electroceramics Japan Xiv. 485 (2011) 187–190. doi:DOI 10.4028/www.scientific.net/KEM.485.187.

[13] D. Sette, V. Kovacova, E. Defay, Printed Barium Strontium Titanate capacitors on silicon, Thin Solid Films. 589 (2015) 111–114. doi:10.1016/j.tsf.2015.04.087.

[14] W. Shen, Y. Zhao, C. Zhang, The preparation of ZnO based gas-sensing thin films by ink-jet printing method, Thin Solid Films. 483 (2005) 382–387. doi:10.1016/j.tsf.2005.01.015.

[15] V. Esposito, C. Gadea, J. Hjelm, D. Marani, Q. Hu, K. Agersted, S. Ramousse, S.H. Jensen, Fabrication of thin yttria-stabilized-zirconia dense electrolyte layers by inkjet printing for high performing solid oxide fuel cells, J. Power Sources. 273 (2015) 89–95. doi:10.1016/j.jpowsour.2014.09.085.

[16] M. Arin, P. Lommens, S.C. Hopkins, G. Pollefeyt, J. Van Der Eycken, S. Ricart, X. Granados, Deposition of photocatalytically active TiO 2 films by inkjet printing of TiO 2 nanoparticle suspensions obtained from microwave-assisted hydrothermal synthesis, 165603 (n.d.). doi:10.1088/0957-4484/23/16/165603.

[17] B.P. Crasta, Boom in digital technology, Ceram. World Rev. 97 (2012).

Chapter 2 : Inkjet printing technology

This chapter deals with inkjet printing technology from a technological point of view. The main working principles of inkjet printers are described, together with their respective advantages and inconvenients. The droplet ejection principle and printability are defined together with a description of the ink-substrate interaction upon printing. Finally the printers used in the thesis are presented along with the choice of printing parameters.

As a general definition, inkjet printing is the generic name for non-contact dot matrix deposition technique based on droplet ejection. Figure 2.1 shows a detailed division of the various forms of inkjet processes.

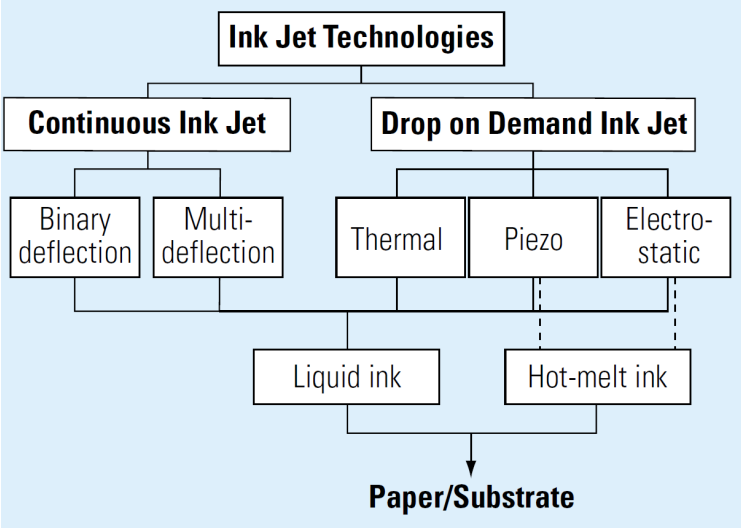

Figure 2.1:Overview of inkjet technologies (borrowed from [1]**).**

In this technique, small quantities of ink are drawn from a reservoir and jetted through micron-sized nozzles as ultrafine droplets, typically in the order of picoliters. Droplets are deposited with high precision onto a substrate situated a few millimeters from the nozzles in a specific position to create a pattern or an image [2]. This technique is simple, cheap and allows using a large variety of inks and substrates not only for documents and photos printing (in households and offices) but also for the development of advanced technologies.

2.1 **Overview of inkjet printing technologies and their principles**

As seen above on Figure 2.1, several technologies were developed and regrouped as inkjet printing. Industrial inkjet printers are broadly divided in two main categories, continuous (CIJ) and Drop-on-Demand (DoD) printers with sub categories within each branch. The main difference between the main categories is the droplet production: while CIJ produces droplets as a continuous stream, DoD printers jet droplets when required. As previously described in Chapter 1, CIJ is mainly used in the labeling industry and very rarely in R&D due to the waste of ink. On the other hand DoD printers are very attractive for the industry owing to their high resolution (720x720 dpi for piezoelectric, 360x360 dpi for thermal) and printing speed. Several industrial players are using such printing for traditional ceramics (tiles decorations) and more advanced ceramic based products (sensors, oxide based thin films). In this work, I have focused my attention on DoD printers as their utilization in the industrial world is constantly growing. This chapter describes the working principles of the main printing technologies and lists their advantages/disadvantages.

2.1.1 Continuous inkjet printing (CIJ)

This technology is mainly used in the labeling and packaging industry and is the most mature technology due to its simple design. In CIJ printers a continuous stream of electrically charged droplets is generated from a biased nozzle without interruption. Figure 2.2 shows the schematic of a CIJ printer.

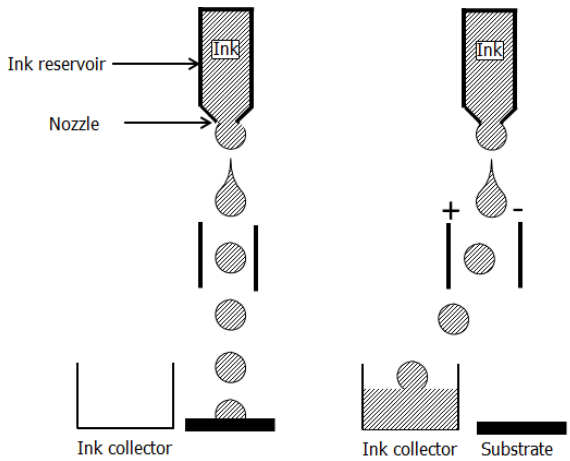

Figure 2.2: Continuous inkjet printing principle.

These droplets are generated either by using a piezoelectric crystal [3] or by Plateau-Rayleigh instability [4], or both. At any moment the stream can be suspended by deflecting the droplets into a collector using an external electric field. For applications such as labeling or graphics, the unused ink is recycled. For applications in material science the collected droplets are too exposed to environment and the risk of ink contamination is high. This leads to a large amount of ink wasted, in addition to the requirement of using electrically charged particles. These limitations made CIJ incompatible with research and development, opening the path to DoD printers, for which such limitations are irrelevant.

2.1.2 Drop-on-Demand (DoD) inkjet printing

Unlike CIJ DoD printers generate droplets when required and are therefore more economical than CIJ printers. Droplet formation is performed by the propagation of a pressure pulse in the ink contained in the reservoir or cartridge. When the pulse exceeds a threshold at the nozzle a droplet is jetted. Below that threshold or in absence of pulse the ink stays on the nozzle plate by surface tension. Droplet size and velocity can be controlled by adjusting the pressure pulse. This pulse can be generated by two different methods: either by using a thermal element or a piezoelectric crystal.

2.1.2.1 Thermal inkjet printing (TIJ)

Figure 2.3 shows the working principle of a thermal inkjet printer.

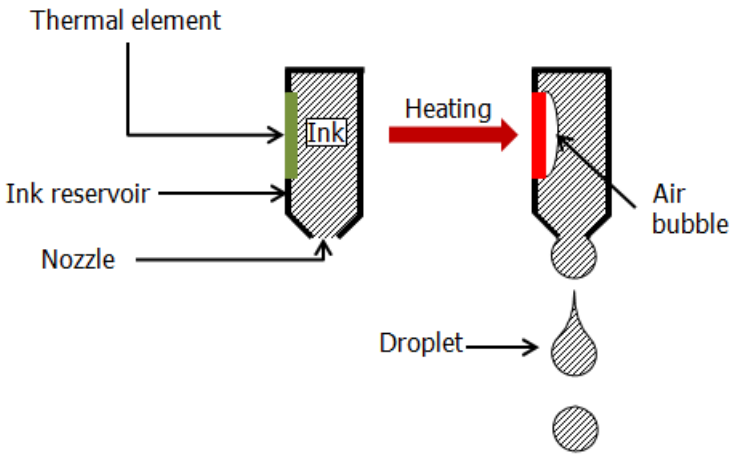

Figure 2.3: Thermal inkjet printing principle.

In TIJ printers a small amount of ink in a closed reservoir is heated in a few µs thanks to a thin resistor. The reservoir is connected to a series of nozzles. The nozzle size is typically of 20µm. As

the ink is warmed up (350-400 °C), the ink vaporizes and forms a bubble inside the reservoir. By overpressure (>1MPa), the bubble pushes the ink out of the reservoir through the nozzle as a small droplet. The resistor cools down rapidly and is ready to jet another series of droplets. Drop frequencies are typically in the 5-8 kHz and, depending on the droplet volume, powerful systems can reach resolution up to 600 x 600 dpi (23pl). Historically this system has been developed in 1965 by Sperry Rand Company [5], who did not use it further. In 1979, Hewlett Packard (HP) and Canon both developed this system. Both companies introduced their respective printers to both households and offices in the 1980's. An advantage of this technique is the relative cheapness of its components (transistor and reservoir) easily fabricated with low cost components. Therefore TIJ are implanted in the market as common household printers as the printer itself and the printheads, sold as cartridges, are inexpensive. A disadvantage of this technique is the incompatibility of certain component with such system, especially some polymers and biomolecules that could be degraded during the warm up of the ink.

2.1.2.2 Piezoelectric inkjet printing (PIJ)

Figure 2.4 shows the working principle of a piezoelectric inkjet printer.

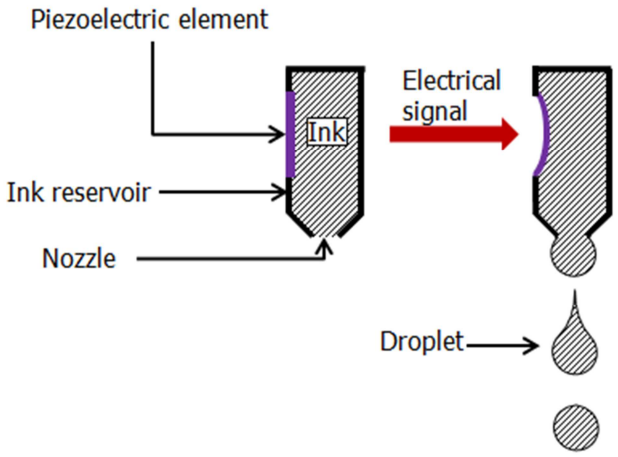

Figure 2.4: Piezoelectric inkjet printing principle.

Droplet formation in piezoelectric printers is induced using a piezoelectric crystal, usually lead zirconate titanate (PZT) which is a material that deforms upon the application of an electric potential. When an electric signal is send to the piezoelectric crystal situated in the ink reservoir, it deforms and squeezes the ink out of the reservoir through the nozzle, jetting droplets. The size,

volume and velocity of the droplet can be adjusted by tuning the electrical signal sent to the piezoelectric material. Figure 2.5 shows a typical signal used in piezoelectric systems.

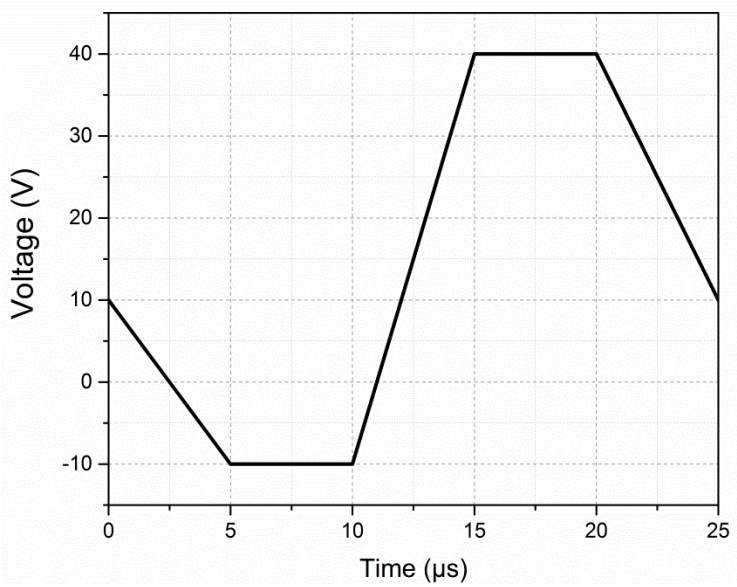

Figure 2.5: Typical waveform used in piezoelectric inkjet printing.

The signal can be decomposed in 2 steps: first voltage is lowered from a baseline value to a negative voltage. This negative voltage leads to piezoelectric material to retract, opening and filling the nozzle with ink. The voltage is then increased to a value higher than the baseline and the piezoelectric material squeezes the ink out of the nozzle. Typical resolution with piezoelectric printers is 720x720 dpi, which is higher than for thermal inkjet printers.

2.1.2.3 Comparison between thermal and piezoelectric inkjet printing

Since the utilization of DoD printers, PIJ has had the preference of the industry for its features compared to TIJ. The main advantages of this technique are the broader range of ink composition and materials that can be chosen due to the absence of heating step, the finer control over the volume/size of the droplet and better resolution. Moreover, PIJ units have other interesting features compared to TIJ, such as nozzle temperature control for viscous inks, substrate heaters, high frequency vibration in the reservoir to avoid ink drying, leading to nozzle clogging. Most of the systems also contain a camera to observe droplets jetting thus making waveform optimization easier (Figure 2.6).

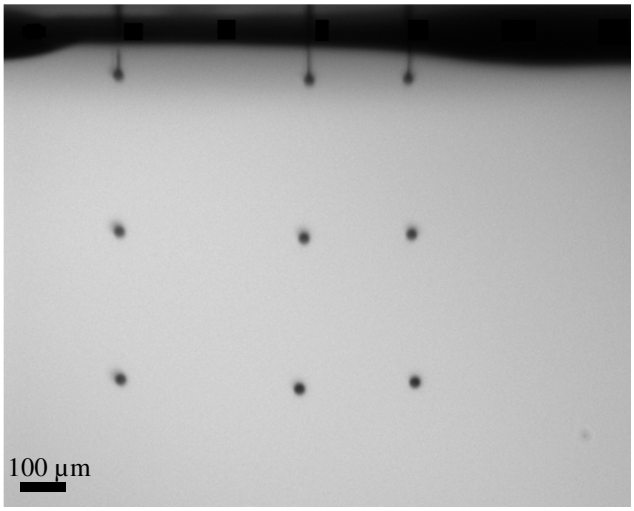

Figure 2.6: Observation of droplet jetting from nozzle plate

Moreover a second camera is usually included for quality control observation of printed surface in between prints, or for measurements. While these features could be implemented into a TIJ printer, no commercial TIJ printing unit has them. It is believed that the reason is purely economical, as these printers are mainly used for households and companies to print on paper. However A drawback of PIJ is that the manufacture of piezoelectric crystals is considerably more expensive than TIJ components.

Despite that PIJ seems to be the ideal method to study ink development and formulation for thin film deposition, both DoD techniques were explored in this thesis. As will be discussed in Chapter 3, the developed inks are water based and their components are not sensitive to local warming. Hence it was the perfect opportunity to explore both system with the same ink and demonstrate that these inks can be used with both systems. To do so, a customized thermal inkjet printing unit was used along with two piezoelectric inkjet printers: one located in our laboratory at DTU Energy, the second one at the Ecole Polytechnique Fédérale de Lausanne (EPFL) in Sion, Switzerland. While the printer systems utilize different principles to eject droplets, the droplet formation phenomenon is purely physical and needs to be understood before developing inks for inkjet printing.

2.2 **Fluid dynamics in DoD inkjet printer**

2.2.1 Droplet formation and printability number

Droplet formation in general is a complex process that is still under investigation [6]. However the behavior of such droplets in inkjet printing can be described and modelled via fluid dynamics equations. The first studies on the topic were conducted by Fromm [7] and he identified the Ohnesorge number (*Oh*) as the most relevant number to describe droplet formation. Fromm defined and used the parameter $Z=1/Oh$ .This dimensionless number is described as a combination of the Reynolds number (*Re*) and the Weber number (*We*):

$$Re = \frac{v.\rho.a}{\eta} \qquad \textbf{Equation 2.1}$$

$$We = \frac{v^2.\rho.a}{\sigma} \qquad \textbf{Equation 2.2}$$

$$Oh = \frac{\sqrt{We}}{Re} \qquad \textbf{Equation 2.3}$$

$$Z = \frac{1}{Oh} = \frac{\sqrt{\sigma.\rho.a}}{\eta} \qquad \textbf{Equation 2.4}$$

where ρ is the dynamic viscosity, σ the surface tension, ρ the density, v the velocity and a a characteristic length, typically taken as the nozzle diameter [8]. Figure 2.7 shows droplets being jetted from a piezoelectric DoD printer at different distances from the nozzle plate.

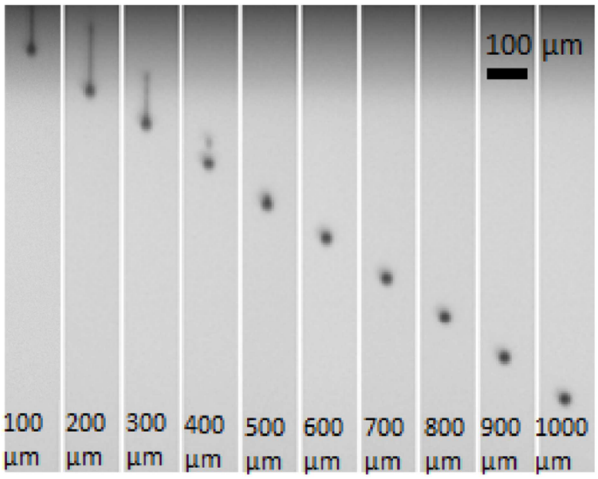

Figure 2.7: Droplet at different nozzle distances on an X-serie Ceraprinter.

These droplets exhibits a head followed by an elongated tail, typically observed in DoD printing [8]. A thin liquid column is formed after ejection and forms a droplet (head) followed by a filament (tail) of several hundred micrometers. The shape of the tail is highly affected by ink viscosity and neither by the type of waveform nor the nozzle geometry while the head of the drop is highly affected by the driving amplitude. This means that long tails will be formed when the drop speed exceeds the speed of the tail. This is especially the case with inks of high viscosity. When the head of the drop has a higher speed than the tail, a long tail is formed which breaks up non-reproducibly into satellite droplets. In most cases these droplets catch up and merge with the head before impact with the substrate. But if satellites are still present at the impact phase then the quality of the deposition will be negatively affected by their presence on the precision, resolution and accuracy. In order to limit this effect a gap is set between the nozzle plate and the substrate, typically around 2-3 mm. This distance is rather large compared to the droplet diameters (typically 20-30 µm) so the satellite droplets have enough time to merge with the head. However a too large gap also affects the accuracy of the print as drag of air currents can deviate the droplet trajectory. This effect is minimized by optimizing the distance and observing the jetted droplets prior to printing hence determining the minimal distance for the satellite droplets to merge.

2.2.2 Ideal range of printability

Fromm determined that stable droplet generation is obtained for $Z > 2$. This result was later refined by Reis & Derby [9] by using numerical simulations of droplet formation. They concluded that stable drop formation occurs in the range $10 > Z > 1$. Jang *et al.* defined an interval between 4 and 14 using experimental observations on jetting of solvent mixtures [10]. At low Z (high viscosity) viscous dissipation prevents droplet formation while at high Z (low viscosity) a large number of smaller droplets, called satellite droplets, surround the primary droplet, possibly due to a too low viscosity. The influence of the fluid/air surface tension at the nozzle is also a limiting factor for droplet generation and a sufficient energy to overcome this barrier for ejection is necessary. Duineveld et al. [11] computed that the energy barrier can be overcome when the droplet velocity is greater than

$$v_{min} = \sqrt{\frac{4.\sigma}{\rho.a}} \qquad \textbf{Equation 2.5}$$

By incorporating the definition of the Weber number (Equation 2.2), Equation 2.5 becomes

$$We = v_{min}\sqrt{\frac{\rho . a}{\sigma}} > 4 \qquad \textbf{Equation 2.6}$$

Lastly the impact of the ejected drop on a substrate has to be taken into account to avoid droplet splashing upon contact. A well-established experimental threshold for the onset of splashing was first proposed by Stow & Hadfield [12] as

$$We^{1/4}Re^{1/4} > f(R) \qquad \textbf{Equation 2.7}$$

where f(R) is a function of surface roughness only. Further studies [8] showed that for flat and smooth surfaces.

$$f(R) \approx 50 \qquad \textbf{Equation 2.8}$$

By combining both previously defined printability limits and Equation 2.5 - 2.8, a $Re\ vs\ We$ graphic can be plotted, as shown on Figure 2.8.

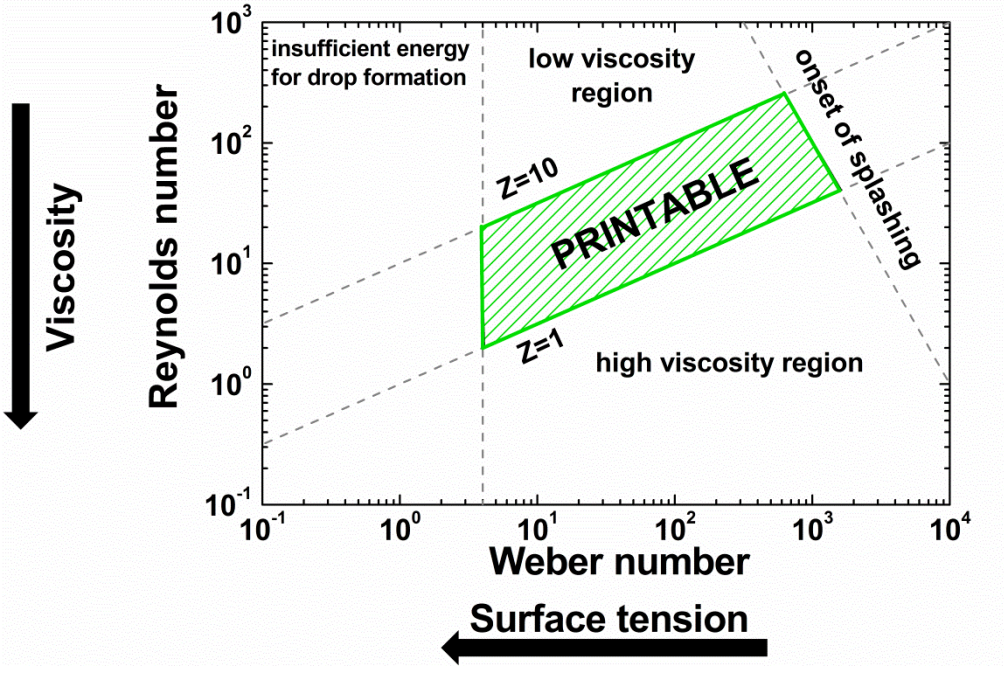

Figure 2.8: Reynolds number vs Weber number plot illustrating printable and non-printable regions.

A map can then be defined and be used to determine the valid fluid properties that can used with DoD printing systems. The defined printability range has been validated through studies based on particle loaded inks and it proves to be a valuable guide for ink optimization [13].

2.2.3 Droplet/substrate interaction

The wetting behavior of a jetted droplet upon contact with a substrate can be described via Young's equation (Equation 2.9). This equation describes a relationship between surface energy of the liquid composing the droplet ($\gamma_{liquid-vapor}$) and that of the substrate ($\gamma_{solid-vapor}$) and is written

$$\gamma_{solid-liquid} + \gamma_{liquid-vapor} \cdot \theta_c = \gamma_{solid-vapour} \qquad \textbf{Equation 2.9}$$

Where θ_c represents the contact angle between the fluid and the substrate. As an example, a measurement of the contact angle of water droplet on indium tin oxide (ITO) is shown on Figure 2.9.

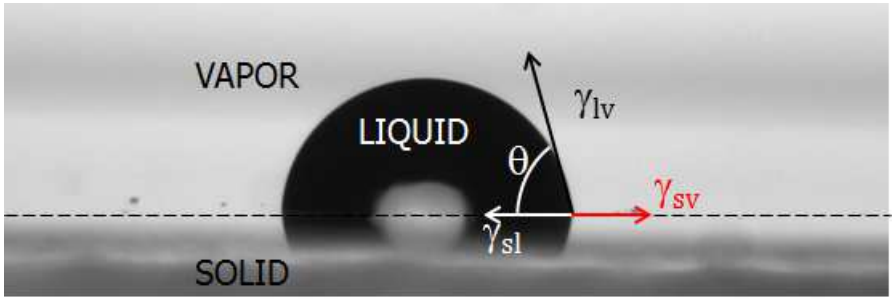

Figure 2.9: Contact angle of a water droplet on an indium tin oxide substrate observed with a drop shape analyzer (EPFL LEPA, Sion, Switzerland).

Due to their high flight velocity, deposited droplets deform upon contact and start to evaporate after relaxation. The composition of the ink, especially the solvent system (substrate wettability, boiling point and evaporation rate) and the printing parameters will play a critical role to yield a proper deposition.

After hitting the substrate the droplet shape is deformed and its diameter increases up to several times its original diameter [14]. At this instant the droplet's shape consists of thick edges and a thin center, as shown in 2) on Figure 2.10 (a).

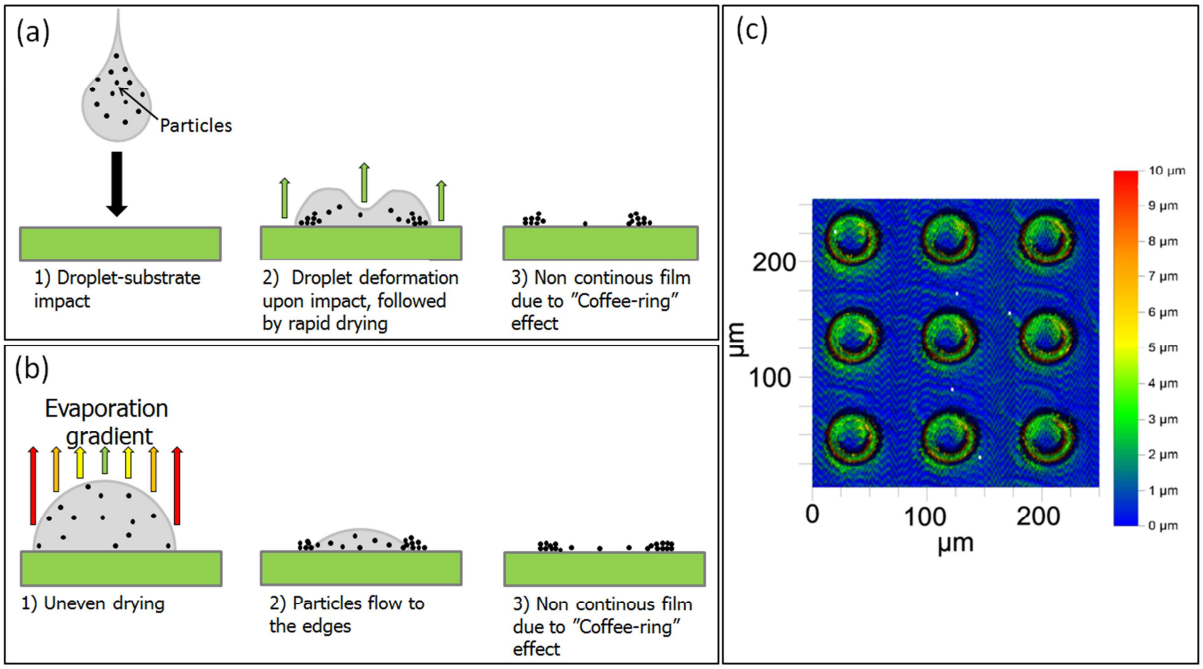

Figure 2.10: "Coffee-ring" effect in case of (a) rapid drying after impact onto substrate and (b) uneven drying between the droplet edges and center; (c) "Coffee-ring" observed on YSZ droplets (profilometry measurement, credits: Massimo Rosa).

If the solvent evaporation rate is too fast, the droplet will dry keeping a "doughnut-like" shape [15]. The thin center will dry faster than thick edges which results in a migration of particles from the center of the droplet to the edges (Figure 2.10 (a)). This affects particularly inks having low boiling point and high volatility. This phenomenon is better known as the "coffee-ring effect" [16,17]. This effect can happen following different mechanisms, specifically in the case of faster solvent evaporation at the edge than in the center of the droplet (Figure 2.10 (b)). As the droplet is thinner on the edge than in the center, the evaporation rate increases and the solvent will migrate from the center to the edge by capillary flow [18], dragging the particles from the center to the edge of the droplet. This migration of solvent, called Marangoni flow, causes the formation of a ring shaped droplet where active particles are only located on the ring's edge and not in the center, as observed on 3D imaging of an YSZ ink shown on Figure 2.10 (c). This effect can be avoided by evening the evaporation rate on the entire droplet. This can be done for example by mixing several solvents having different boiling points such as water and alcohols.

Substrate wettability and hence film quality are strongly influenced both by the ink surface tension and the substrate surface free energy. A poor wettability (high contact angle) leads to non-continuous low quality film due to non-merging of adjacent droplets and cracks due to drying of

thick droplets. The value of the contact angle, formed by the three interfacial energies in Young's equation, gives qualitative indication about the wetting quality. Figure 2.11 shows examples of the contact angle of water droplets on various substrates.

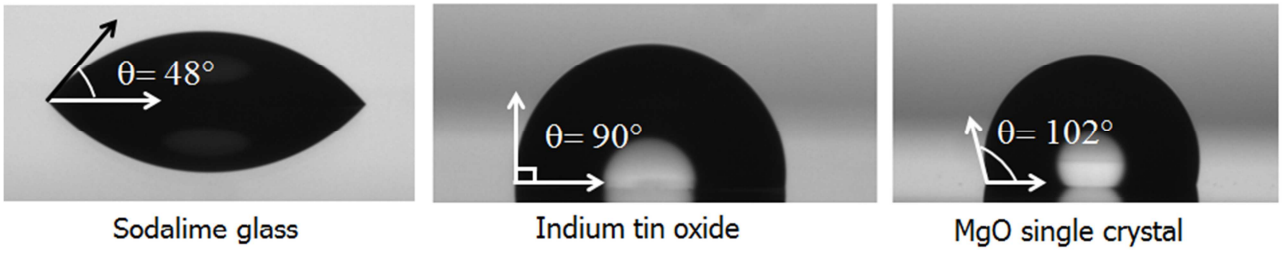

Figure 2.11: Contact angle of water droplets on various substrates

Contact angles values close to zero indicate full wetting and values below 90° a partial wetting while values above 90° indicate a partial non wetting. Some cases of complete non wetting (θ_c = 180°) exists but are really rare (liquids on mercury for example). The contact angle value and its influence on wettability give indication about the quantitative relation between the liquid surface tension and the substrate surface free energy. A contact angle greater than 90° translates to $\gamma_{liquid-vapour}$ greater than $\gamma_{solid-vapour}$ i.e. a poor substrate wetting. This is the case for few liquids such as mercury (485 mN.m^{-1}) and water (72 mN.m^{-1}) which can only wet a few metals and solids, respectively. Substrate wettability is generally optimized following two strategies. The first method consists in adding a surfactant to the water based mixture. Surfactants are amphiphilic compounds; their chemical structure consists of a hydrophobic polar tail and a hydrophilic head (Figure 2.12 (a)).

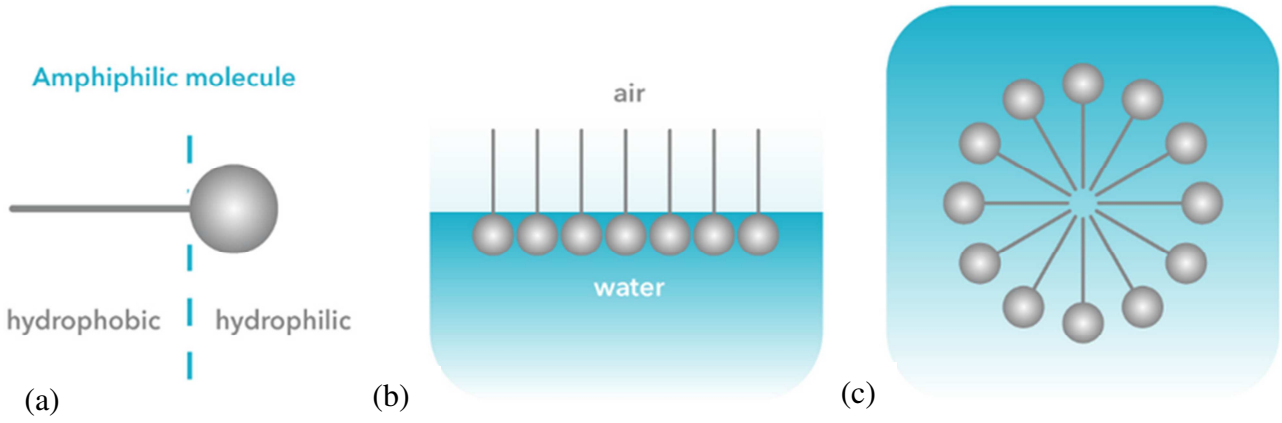

Figure 2.12: Graphical representation of (a) an amphiphilic molecule with a hydrophilic tail and hydrophobic head, (b) surface tension mechanism principle and (c) a spherical micelle. (Borrowed from

The hydrophobic tail is typically a hydrocarbon chain of various lengths, a fluorocarbon, or a dimethylsilohexane chain. The hydrophilic head is an anionic-cationic-ionic- or polar group. Surfactants decrease surface and interfacial tensions and work of adhesion by absorbing on liquid-air and oil-air interfaces. Upon addition of a surfactant in water, the hydrophilic head enters in the liquid while the hydrophobic tail sticks out in between water molecules, breaking the intermolecular forces between them hence and reducing the surface tension (Figure 2.12 (b)). This decrease is observed until a certain critical concentration, called critical micelle concentration (CMC). Above this concentration the liquid surface is saturated in surfactant, and the excess in solution reduces its energy by creating a spherical liquid-like nanometric aggregate, called micelle. The micelle consists of the hydrophobic tails pointing to the center of the micelle and the hydrophilic head pointing at the micelle surface (Figure 2.12 (c)). The micelle formation phenomenon is a disadvantage in using this method for surface tension lowering. Such agglomerate can affect the solution/suspension properties such as rheological behavior, reactivity and stability. Moreover surfactants have to be burnt off during heat treatment and hence contribute to reducing the total concentration of the suspension/solution. The second strategy to reduce surface tension (and thus the contact angle) is to add low surface tension solvents such as alcohols to the mixture. Water molecules then interact (less strongly) with alcohol molecules and the resulting surface tension is lowered. The effect increases with the alcohol chain length; however alcohols having more than 4 carbons (butanol) are not fully miscible in water, and methanol boiling point is very low, therefore ethanol and propanol are usually chosen as surfactants. The water-to-alcohol ratio has to be carefully optimized. While a too low alcohol addition will not sufficiently reduce the surface tension to yield a proper wetting, an excess of alcohol will dramatically affect the drying behavior of the droplet and lead to either clogging at the nozzle plate or to coffee ring effect described earlier.

The substrate surface free energy can also be controlled. Flat and low roughness oxide based substrates have high surface energies and yield high quality films; but the cleanliness of substrates is a crucial parameter to consider. As dust or dirt in general is composed of hydrocarbons, they lower the surface free energy of a substrate thus increasing the contact angle.

2.3 **Printers description**

2.3.1 Thermal inkjet printer

The thermal inkjet printing unit used in this work is a widely commercially available thermal printer (HP Deskjet 1010). The main function of this printer is to print black and colored text or pictures in households or offices, and it possesses the simplest design available on the market. This printer has been chosen for its simplicity, cheapness but mostly for the design of the printheads. On this model the nozzles are mounted on a separate cartridge (HP 301) and the ink is only stored inside the cartridge and never goes through the printer into tubes or channels. This design limits the risk of pollution when printing inks with different compositions, as a single cartridge can be allocated to a specific ink composition and cleaned in between prints. The printer possesses two slots for cartridges and uses the CMYK color system: one for black ink (HP 301 black) and one for colored inks (Cyan, Magenta, Yellow, HP 301 tricolor). Each cartridge provides a 600 x 300 dpi resolution and contains 336 nozzles each having a diameter of 20µm.

Prior to printing, the brand new cartridge is emptied by printing out the black ink onto sheets of paper. Once emptied the cartridge is opened, cleaned, and wiped using millipore water and refilled with clean water. That water is then printed out on some paper to remove the remaining original black ink. At that point, the cartridge is ready to be used for printing ceramic based inks.

The HP Deskjet 1010 was originally designed to print on flexible A4 sized sheets of paper. However substrates used to deposit thin films are smaller and not as flexible as paper (glass, metal plates, single crystals). Hence the design of the printing unit had to be remodeled in order to print onto such substrates. Figure 2.13 shows the HP Deskjet printer 1010 after modification. After modifications flat substrate holders, such as alumina plates (16x16x0.1 cm, see Figure 2.13) could be used to support the substrate during printing.

Figure 2.13: Modified HP Deskjet 1010 printing unit.

2.3.2 Piezoelectric based printers

Two piezoelectric printers were used in this thesis: The first one was a Pixdro LP50 located in our laboratory at DTU (Figure 2.14 (a)) and the second a X-serie CeraPrinter (Ceradrop) is owned by the *Laboratoire d'Electrochimie Physique et Analytique* (LEPA), a group of the Ecole Polytechnique Fédérale de Lausanne (EPFL) in Sion, Switzerland. Unlike the thermal inkjet printer described earlier, Pixdro LP50 is a 3D printer *i.e.* the printheads can move both horizontally (327 x 227 mm) and vertically (maximum 25 mm) allowing the deposition of layered structures onto any type of substrates with an accuracy lower than 20 µm. Compatible materials include solvent based (including nanoparticles) aqueous and UV curable inks. Two independent printhead slots are available, making it possible to deposit two different inks during the same process. The printer was acquired with industrial printheads called Spectra SL128. However these printheads are quite expensive and there was a high risk of clogging due to the experimental nature of the inks. Therefore the printheads slots were modified to install disposable printheads. In this project disposable DMP cartridges DMC-11610 (Fujifilm Dimatix) were used with a custom-made jetting waveform (Figure 2.14 (b))

(a) (b)

Figure 2.14: (a) PixDro LP50 printing unit and (b) disposable Dimatix DMP cartridges DMC-11610.

The cartridge has a volume of 1.5 ml and can be filled and refilled with all type of inks. Each cartridge contains 16 individually addressable nozzles (nozzle diameter = 21.5 µm, nozzle spacing = 250µm) and can jet droplets of 10 pl. According to the manufacturer ideal viscosity and surface tension are 10 mPa.s and 30 $mN.m^{-1}$, respectively. Droplets shape, diameter and velocity can be controlled by adjusting the waveform applied to the piezoelectric crystal. The printing patterns consisted in image files which had to be edited externally, and only their size and resolution can be modified inside the built-in software. Two cameras are installed in the printer: a fiducial camera allows for setting the print coordinates and observation of the printed patterns for quality control, while a second one gives a live view of the droplets during jetting. This second camera is a powerful tool to characterize the droplets prior to printing and to determine if nozzles are clogged. Waveforms can then be optimized while monitoring drop jetting. Several other interesting features are implemented in the printer's design such as temperature control of the substrate holder and of the nozzles (only for industrial printheads) and a suction system to prevent ink dripping when printing is idle. The printer also features an automatic maintenance system with three main parts: unclogging of the nozzles by suction, printhead purging by applying a large overpressure up to 250 mbar to the prinhead, and nozzle plate wiping on soft paper. Figure 2.15 shows a schematic of the printer [19].

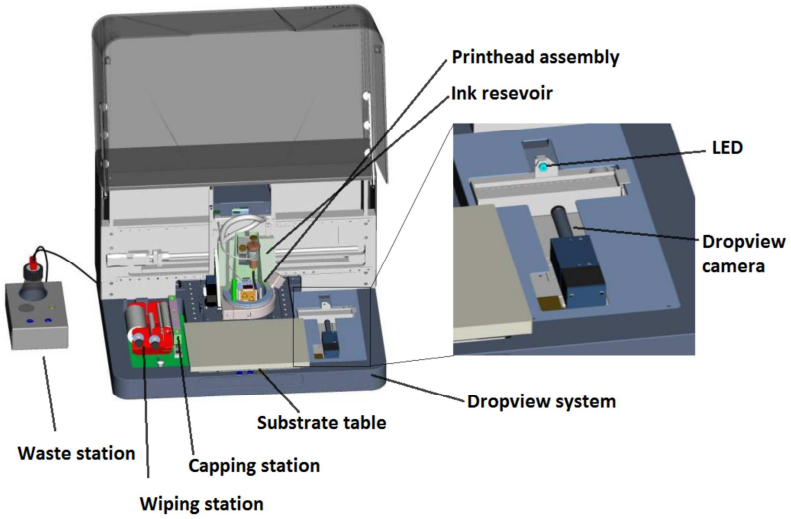

Figure 2.15: Schematic view of the PixDro LP 50 printer (borrowed from [19])

The second piezoelectric printer, X-serie CeraPrinter (Ceradrop), was used during visits at LEPA during the three years period. Figure 2.16 shows a picture of the X-serie printer.

Figure 2.16: X-serie Ceraprint printing unit

These printers function with the same working principle than the Pixdro LP 50 printer and disposable DMP cartridges DMC-11610 could be used. The X-Serie Ceraprinter offers more features than the Pixdro LP 50. The printer can use three independent printheads (against two for the pixdro), has a high printing resolution (<5 µm x 5 µm) and stage accuracy both in x /y (+/- 1.5 µm) and z (+/- 2 µm). The maximum printing size is 305 x 305 mm, with a velocity up to 500

$mm.s^{-1}$. Moreover extra features are available such as photonic curing, and more advanced software to edit printing designs, which allows the user to choose the droplet spacing and the number of droplets. Table 2.1 makes a comparison over the main features of both printers:

Table 2.1: Comparison of the main features between Pixdro LP 50 and X-serie Ceraprint.

	Pixdro LP 50	X-Serie Ceraprint
Number of printheads	2	3
Printing directions	x,y,z	x,y,z
Accuracy	< 20µm	X,Y: < +/- 1.5 µm Z: +/- 2µm
Stage repeatability	< 5µm	X,Y: < +/- 1.5 µm Z: +/- 2µm
Print resolution	20 µm x 20µm	< 5µm x 5 µm
Dropview camera	Yes	Yes
Fiducial camera	Yes	Yes
Printing pattern edition	Limited to resolution and final size	Advanced (droplet spacing, droplet numbers, print shape)
Maximum substrate size	327 mm x 227 mm	305 mm x 305 mm
Maximum substrate thickness	25 mm	10 mm
Maximum printing velocity	500 $mm.s^{-1}$	500 $mm.s^{-1}$
Printhead heating	Up to 50°C	Up to 60°C
Weight	90 kg	1500 kg
Automated cleaning procedure	Yes	Yes

Table 2.1 shows that the X-serie offers many more advantages in terms of printing quality than the Pixdro LP 50. Another point of comparison is the quality of the camera for droplet observation. Figure 2.17 shows a droplet jetted by the Pixdro LP 50 (a) and the X-serie Ceraprint (b).

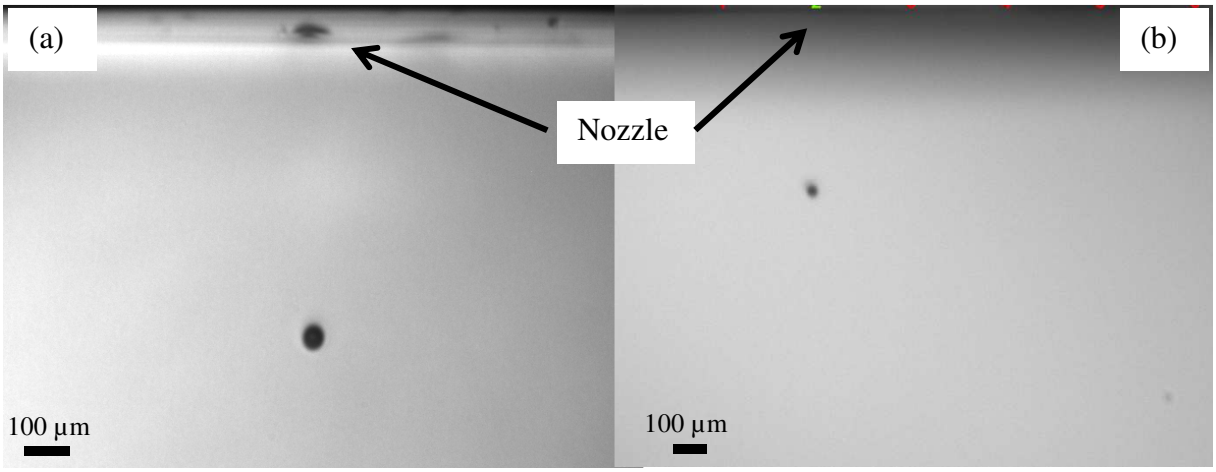

Figure 2.17: Jetted droplet observed with dropview camera on (a) the Pixdro LP 50 and (b) the X-serie Ceraprint (b).

Figure 2.17 shows that Pixdro LP 50 display a better image quality for dropview analysis making the droplet features (volume, diameter, velocity) calculation more accurate. The fluidity of the droplet observation in real time is however faster on the X-serie. Both printing units have advantages and disadvantages and their use depend on the final goal. The Pixdro is a small tabletop machine mainly conceived for R&D development, while the X-Serie can, in addition to utilization in R&D, be implemented in an industrial process.

Bibliography

[1] Helmut Kipphan, Handbook of Print Media, 2001.

[2] H.P. Le, Progress and Trends in Ink-jet Printing Technology, J. Imaging Sci. Technol. 42 (1998) 49–62.

[3] M.D. Croucher, M.L. Hair, Design Criteria and Future Directions in Inkjet Ink Technology, Ind. Eng. Chem. Res. 28 (1989) 1712–1718. doi:10.1021/ie00095a023.

[4] D.T. Papageorgiou, On the breakup of viscous liquid threads, Phys. Fluids. 7 (1995) 1529–1544. doi:10.1063/1.868540.

[5] M. Naiman, Sudden steam printer, 3,179,042, 1965. http://aip.scitation.org/doi/10.1063/1.868540.

[6] G.D. Martin, S.D. Hoath, I.M. Hutchings, Inkjet printing - the physics of manipulating liquid jets and drops, J. Phys. Conf. Ser. 105 (2008) 12001. doi:10.1088/1742-6596/105/1/012001.

[7] J.. Fromm, Numerical-calculation of the fluid-dynamics of drop-on-demand jets, IBM J.Res.dev. 28 (1984) 322–333.

[8] B. Derby, Inkjet printing of functional and structural materials: fluid property requirements, feature stability, and resolution, Annu. Rev. Mater. Res. 40 (2010) 395–414. doi:10.1146/annurev-matsci-070909-104502.

[9] N. Reis, B. Derby, Ink jet deposition of ceramic suspensions: modelling and experiments of droplet formation, in: MRS Symp. Proceeding, 2000: pp. 65–70.

[10] D. Jang, D. Kim, J. Moon, Influence of fluid physical properties on ink-jet printability., Langmuir. 25 (2009) 2629–35. doi:10.1021/la900059m.

[11] P.C. Duineveld, M.M. de Kok, M. Buechel, A. Sempel, K.A.H. Mutsaers, P. van de Weijer, I.G.J. Camps, T. van de Biggelaar, J.-E.J.M. Rubingh, E.I. Haskal, Ink-jet printing of polymer light-emitting devices, Proc. Conf. Org. Light. Mater. Devices V. (2002) 59–67. doi:10.1117/12.457460.

[12] C.D. Stow, M.G. Hadfield, An Experimental Investigation of Fluid Flow Resulting from the Impact of a Water Drop with an Unyielding Dry Surface, Proc. R. Soc. A Math. Phys. Eng. Sci. 373 (1981) 419–441. doi:10.1098/rspa.1981.0002.

[13] B. Derby, N. Reis, Inkjet Printing of Highly Loaded Particulate Suspensions, MRS Bull. (2003) 815–818.

[14] E. Tekin, P.J. Smith, U.S. Schubert, Inkjet printing as a deposition and patterning tool for polymers and inorganic particles, Soft Matter. 4 (2008) 703. doi:10.1039/b711984d.

[15] D. Soltman, V. Subramanian, Inkjet-printed line morphologies and temperature control of the coffee ring effect, Langmuir. 24 (2008) 2224–2231. doi:10.1021/la7026847.

[16] J. Fukai, Y. Shiiba, T. Yamamoto, O. Miyatake, D. Poulikakos, C.M. Megaridis, Z. Zhao, Wetting effects on the spreading of a liquid droplet colliding with a flat surface: Experiment and modeling, Phys. Fluids. 7 (1995) 236–247. doi:10.1063/1.868622.

[17] R. Dou, T. Wang, Y. Guo, B. Derby, Ink-jet printing of zirconia: coffee staining and line stability, J. Am. Ceram. Soc. 94 (2011) 3787–3792. doi:10.1111/j.1551-2916.2011.04697.x.

[18] R. V. Craster, O.K. Matar, K. Sefiane, Pinning, retraction and terracing of evaporating droplets containing nanoparticles, Langmuir. 25 (2009) 3601–3609. doi:10.1021/la8037704.

[19] Pixdro, PixDro LP 50 Documentation, (2010).

Chapter 3 : Materials and chemical processing

This section focuses on the materials studied and the concept behind each ink designs. The various studied phases are described along with some basic properties which are relevant for this work. The chemical principle of each ink is detailed, along with the raw materials and the substrates used.

3.1 **Studied phases**

In this work, focus was set on the development of titania (TiO_2) - and zirconia (ZrO_2)-based thin films by inkjet printing. These two materials have been extensively studied as thin films for application in diverse key technologies (e.g. solar cells and solid oxide cells) and were the ideal material to demonstrate the potential of thin films designed by inkjet printing.

3.1.1 Titanium-based compounds

Titanium dioxide TiO_2, or Titania, is found in nature as minerals rutile, anatase and brookite, as well as two high pressure forms: a monoclinic baddeleyite-like form and an orthorhombic α-PbO_2-like form. Anatase and rutile are the most abundant polymorphs, and are widely used in industry. Figure 3.1 shows the structure of the two compounds.

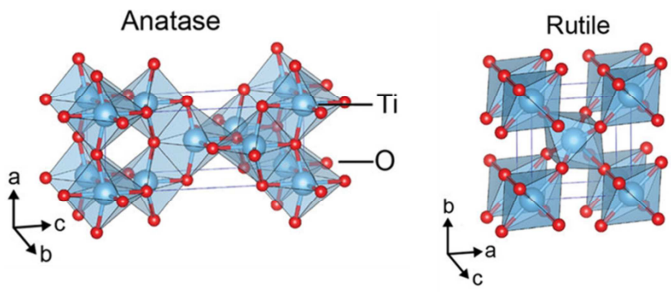

Figure 3.1: Structure of anatase and rutile (borrowed from [1]**).**

Anatase is metastable and transforms to rutile at high temperatures [2]. This phase transformation occurs because rutile is thermodynamically more stable than anatase [3]. The phase transition normally occurs between 600 and 800 °C but the exact temperature depends strongly on the system (presence of impurities, particle size, etc.). Particularly, titania-based thin films have been in the center of interest in the past decades for their interesting application as photocatalytic layer [4] (self-cleaning glass, solar energy harvester), in precision optics [5], high-temperature gas sensing devices [6] and thin film capacitors [7].

Titania can be easily doped to form phases with enhanced or even new properties. These phases include materials such as barium titanate $BaTiO_3$, lead zirconate titanate $Pb[Zr_xTi_{1-x}]O_3$ ($0 \leq x \leq 1$) both used for their ferroelectricity, strontium titanate $SrTiO_3$, or bismuth based compounds such as $Bi_{0.5}Na_{0.5}TiO_3$ (BNT) and $Bi_4Ti_3O_{12}$ (BiT). The latter is a particularly interesting material as piezoelectric material. Discovered by Aurivillus in 1949 [8], BiT has been studied for its excellent properties such as ferroelectricity, high dielectric constant, and high breakdown stress [9,10]. Because of its high Curie temperature (675°C) and electro-optical properties [11], BiT is a potential candidate for high temperature piezoelectric applications, optical displays, and memory storage. It belongs to the group of ferroelectric materials with a perovskite structure and is a bismuth-based layered ferroelectric oxide [12]. The structure of these phases named "Aurivillius phases" can be described by the general formula $(Bi_2O_2)^{2+}$ $(M_{n-1}R_nO_{3n+1})^{2-}$ ($1 < n < 6$). The structure consists of n pseudo perovskite $(M_{n-1}R_nO_{3n+1})^{2-}$ units sandwiched in between two $(Bi_2O_2)^{2+}$ layers. M is a rather large mono-, di- or trivalent cation (e.g. Na^+, Pb^{2+}, Bi^{3+}) and R a smaller cation in size and either a tri-, tetra-, penta-or hexavalent cation (e.g. Fe^{3+}, Ti^{4+}, Ta^{5+}, W^{6+}) [13]. BiT is obtained with n = 3, M = Bi^{3+} and R= Ti^{4+}. Figure 3.2 shows the structure of BiT.

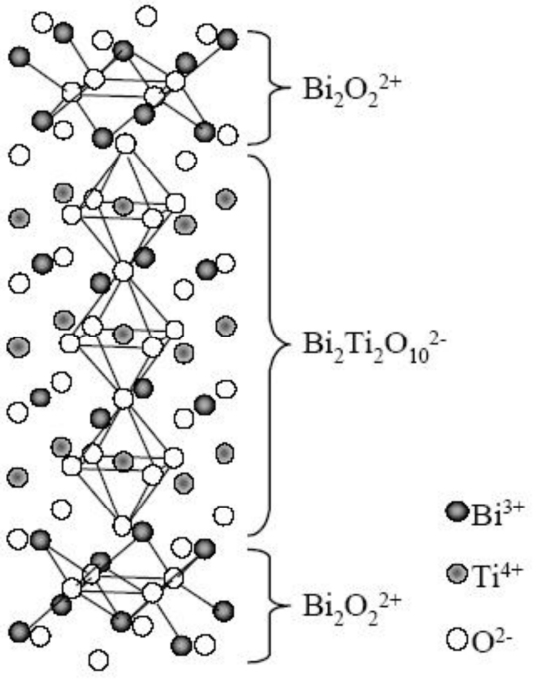

Figure 3.2: Structure of $Bi_4Ti_3O_{12}$ (BiT) (Borrowed from [14]**).**

$Bi_4Ti_3O_{12}$ is monoclinic at room temperature, and very–high–resolution powder diffraction data suggest that powder samples of $Bi_4Ti_3O_{12}$ are actually orthorhombic at room temperature [15].

3.1.2 Zirconia-based compounds

Zirconium dioxide ZrO_2, or Zirconia, is a well know material for its high temperature stability and corrosion resistance [16]. It is also broadly studied as structural and functional material characterized by good ionic conductivity, large band gap and wide spectral transparency range in both visible and near-infrared bands [17]. As a thin film zirconia has been the focus of many studies for its application in oxygen sensors [18] and thermal barrier coating [19]. Zirconia naturally occurs as mineral baddeleyite, with a monoclinic crystalline structure. This monoclinic phase is stable at temperatures below 1170°C. At higher temperature two more phases will form: tetragonal (1370-2320°C) and cubic (T > 2320°C) zirconia. Figure 3.3 shows the crystal structure of the different zirconia phases and their transition temperature.

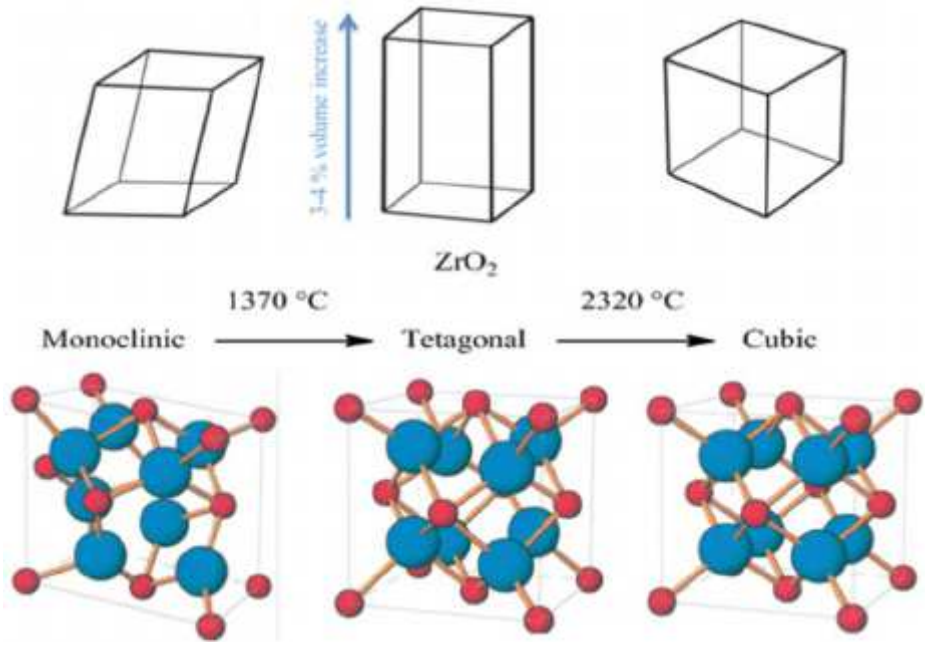

Figure 3.3: Structure of zirconia at different temperature (borrowed from [20]**).**

Phase transformation from monoclinic to tetragonal is accompanied by an important volume change (≈ 3-4 vol %), leading to instability and cracks, complicating the manufacture of sintered zirconia in that temperature range. The suppression of such phase transformation is done by stabilizing Zirconia via the substitution of Zr^{4+} atoms (0.82 Å) in the crystal lattice by slightly larger atoms. An example of such dopant is yttrium ions Y^{3+} (0.96 Å) [21], which stabilize the structure at temperature higher than the monoclinic/tetragonal transition temperature. Figure 3.4 shows the structure of YSZ.

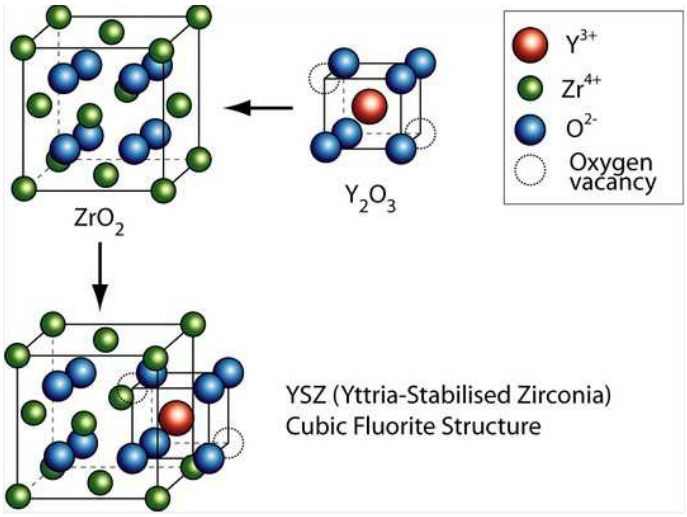

Figure 3.4: Doping of zirconia by yttria and YSZ structure (borrowed from [20]**).**

This substitution has another effect on the properties of zirconia. Indeed the substitution of valence (IV) by valence (III) ions leads to the creation of oxygen vacancies $V_O^{\cdot\cdot}$, which in this case can be noted in Kröger-Vink notation:

$$Y_2O_3 \xrightarrow{ZrO_2} 2Y'_{Zr} + 3O_O^x + V_O^{\cdot\cdot}$$

These created oxygen vacancies make yttria-doped-zirconia (YSZ) a good oxygen conductor. As such YSZ is nowadays the reference material as electrolyte for solid oxide fuel cells [22]. Zirconia is also used to enhance the dielectric behavior of many oxides such as barium ($BaZrO_3$), strontium ($SrZrO_3$) and lead ($PbZrO_3$).

3.1.3 Gadolinium doped ceria

Cerium oxide CeO_2, or ceria, is a widely studied material as fuel cell electrode, for hydrogen production by water splitting and is also one of the most important catalysts. Ceria has a fluorite structure, showed on Figure 3.5.

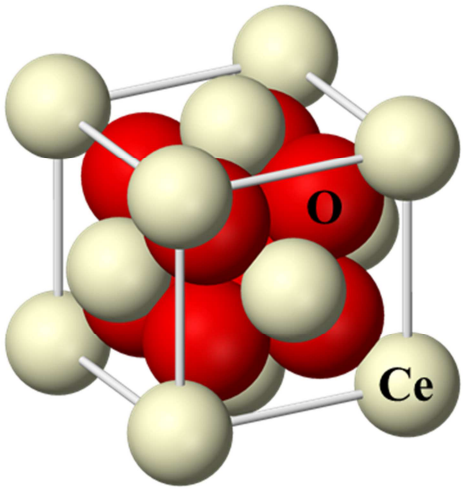

Figure 3.5: Structure of ceria (borrowed from ([23])).

Ceria releases oxygen at high temperature and a non-stoichiometric, anion deficient form is formed. This material has the formula $CeO_{(2-x)}$, where $0 < x < 0.28$ [24]. The value of x depends both on the oxygen partial pressure and the temperature.

Similarly to zirconia, ceria can be doped with trivalent ions, such as gadolinium ion, to substitute Ce^{4+} with Gd^{3+}. Due to the Gd ions lower valence compared with Ce, the doping creates oxygen vacancies in the structure making doped ceria a good oxygen ions conductor [25]. Gadolinium doped ceria (CGO) exhibits a higher ionic conductivity than YSZ at low temperature (< 600°C) and ceria thin films are considered as a solution for intermediate temperature SOFC electrolyte. However ceria based electrolyte can lead to stability issues during operation of SOFCs due to partial reduction of Ce^{4+} in Ce^{3+} in reducing conditions; Mixed ion electrical conduction is developed and can result in an internal short circuit and degrade cell performance [26]. To avoid this, mixed CGO/YSZ structures are studied to increase the ionic conductivity of SOFC electrolyte. However these material react at high temperature to form an insulating phase ($(YSZ)_{1-x}(CGO)_x$, $0 < x < 1$) as solid solution so heat treatment should be optimized below that critical temperature.

3.2 **Ink design and raw materials**

3.2.1 Colloidal ink

3.2.1.1 Ink formulation and processing

The first type of studied ink consisted in a suspension of colloidal oxide particles. Figure 3.6 shows an icon that represents the ink.

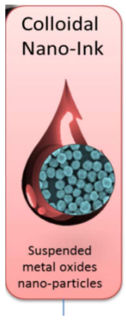

Figure 3.6: Graphical icon of the colloidal ink.

Colloidal inks are widely used in ceramic processing and are formulated as typical ceramic suspensions for other ceramic processes like tape casting, dip coating, or spraying. High solid loading can be used and viscosity adjustments can be easily performed for these processes. However, it becomes more complicated with inkjet printing due to the restrictions in terms of particle size and viscosity values.

A critical aspect in the design of such ink is their stabilization. Stabilization of suspension results from the control over various physical and electrochemical forces. Generally speaking, a suspension consists of two phases: a dispersed phase and a dispersion medium, also called vehicle. The dispersed phase can be solid particles (colloids, nanoparticles), liquid droplets (emulsion) or gas droplets (foam). In the current discussion, we will focus on colloidal particles as the dispersed phase, but the description is also valid for liquid or gaseous dispersed phases. The dispersion medium can be either aqueous or non-aqueous.

An important parameter that influences the stability of a suspension is the particle size distribution (PSD). This parameter is particularly critical in the case of inkjet printing. To avoid clogging of the nozzles, synonym of process failure, PSD of 2% of the nozzle diameter is recommended by most inkjet printer manufacturer, which corresponds to 400 nm for most of the printheads available on

the market (nozzle diameter: 21µm). Moreover the PSD is an indicator of settling properties and rheological behavior. Suspensions are fundamentally unstable and will agglomerate or aggregate through random motion over time. This is due to the tendency of particles to lower their excess surface energy by lowering their surface area. This phenomenon is gradually particularly important the smaller the particle size, and becomes especially relevant for colloidal particles (particle size below 1 µm). Over time, the particle size will always incline to increase unless the particles are kept separated from each other by some "chemical obstacle" and stay stable for a long period of time. We define then the suspension stability by the resistance of the dispersed phase to agglomerate. It is also relevant to precise that the definition of stability depends on the time scale observation of the product. For commercial and industrial applications, the stability is measured in years while an intermediate product in a process line only need to stay stable for a few hours. There are two types of interaction between two particles - attractive and repulsive [27,28]. Depending on the potential energy barrier between them, the particle will agglomerate or not. The potential energy barrier is calculated as the magnitude difference between the repulsive and the attractive forces. When attractive forces are stronger than repulsive ones particles agglomerate while if repulsive forces predominate the particles are suspended (Figure 3.7).

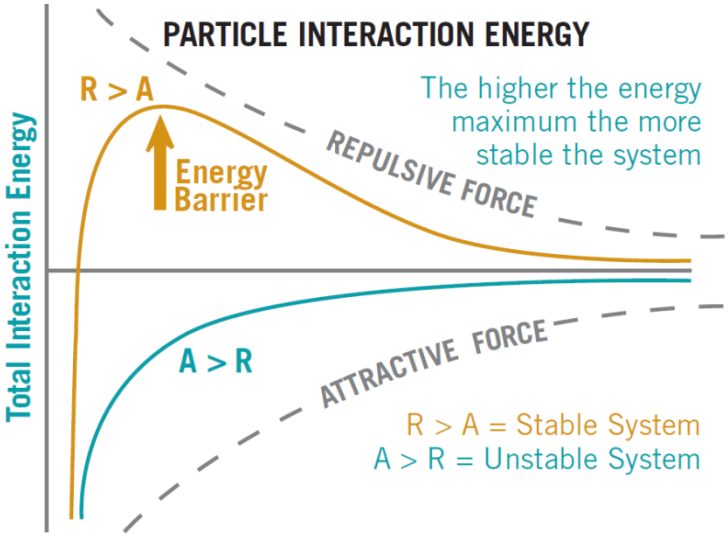

Figure 3.7: Description of particle-particle interaction energy (borrowed from [29]**).**

Figure 3.7 describes the different types of interactions. Attraction forces, called Van der Waals forces are always attracting the particles close to each other even in completely non polar systems and also at large distance of separation. Moreover the magnitude of the attractive forces increases as the polarity of the dispersion medium decreases. Hence stability will be preserved by (1) keeping

the attraction forces as low as possible and (2) counter these attractive forces with sufficient repulsive forces. This objective can be reached by two different methods – electrostatic and steric stabilization. Figure 3.8 shows a graphical sketch of both methods.

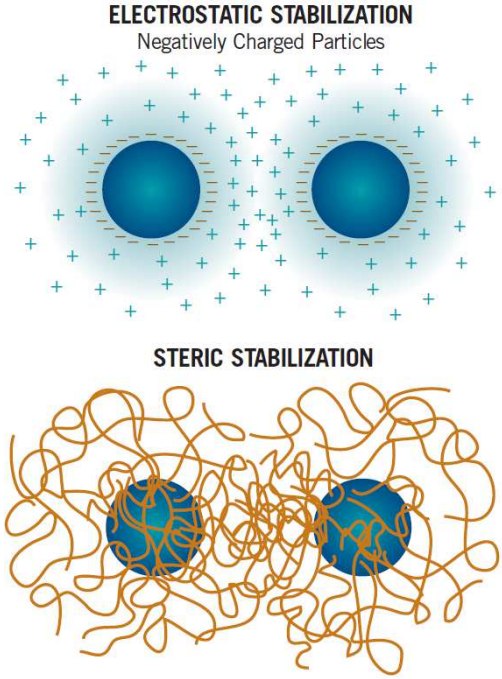

Figure 3.8: Illustration of electrostatic and steric stabilization (borrowed from [29]**).**

- Electrostatic stabilization consists in placing an ionic charge at the particle surface so the particles repulse each other. Maximum stability is reached for large electrostatic force of repulsion, which means that the particle surface charge should be as high as possible. Repulsion forces become weaker as the ionic strength of the medium increases, thus the lowest electrolyte concentration has to be used. Several methods to electrostatically stabilize exist. A common one is through the physical adsorption of ionized surfactants and polyelectrolytes, or the dissociation of ionogenic surface hydroxyl or carboxyl groups. The surface charge of the particle is evaluated by measuring the zeta potential [30].
- Steric stabilization consists in adding long-chained molecules to the surface of the particle that will act as a mechanical barrier, preventing collision between them. The dispersion solvent and the macromolecule should be compatible so the macromolecule will extend at its maximum length, and the surface coverage must be total.

As described in the previous chapter, viscosity is one of the major ink properties that control the printability of the fluid for inkjet, and as such it should be easily tunable. With that in mind, I

decided to use the second stabilization method, i.e. steric. I chose this method because the steric stabilization gives a better control over viscosity, compared to electrostatic stabilization. The dispersant used is polyvinylpyrrolidone (PVP), which is a water-soluble polymer made from the monomer N-vinylpyrrolidone. PVP is often used as a binder in ceramic processing but it is also a very efficient dispersant for oxides. The amount of PVP is important for several critical aspects. Primarily optimal PVP amount is necessary to fully cover the particles surface to optimize the suspension stability by steric effect and avoid particle agglomeration, leading to nozzle clogging. However a too high amount of PVP can significantly increase the suspension viscosity and thus compromise the ink printability.

The solid loading is also an important aspect of colloidal inks. It is clear that the higher solid loading will lead to more efficient printing process. However the viscosity of the suspension changes with increasing the solid loading. For dilute systems, i.e., < 2vol%, Einstein's generalized equation [31] illustrates the viscosity behavior with solid loading (Equation 3.1):

$$\eta = \eta_0.(1 + A.\phi), \qquad \textbf{Equation 3.1}$$

where η is the suspension viscosity, η_0 the viscosity of the dispersion medium (without particles), ϕ the volume fraction of particles in suspension and A is a particle shape-dependent constant. Equation 3.1 shows that in that domain viscosity increases linearly with solid loading. At higher solid content there is an increase of particle-particle interaction that cannot be modeled by Equation 3.2 anymore and empirical relations are used to describe the viscosity behavior. The behavior is generally described using a modified Krieger-Dougherty equation (Equation 3.2) [32]:

$$\eta = \eta_0.\left(1 - \frac{\phi}{\phi_{max}}\right)^{-n} \qquad \textbf{Equation 3.2}$$

where ϕ_{max} is the maximum volume fraction of solids in suspension, and n an empirical constant. The maximum fraction is reached when the suspension behaves like an elastic solid due to the direct contact between the particles (typically 50-60 vol %). Equation 3.2 illustrates the problematic one faces when developing suspensions for inkjet printing. It is desired to increase the solid loading as

much as possible but at the same time viscosity should not exceed a certain value for the droplet to be ejected. For typical DoD inkjet printers, this value is around 20 mPa.s. Figure 3.9 illustrates the problematic using the example of the relative viscosity of a colloidal ink (alumina, borrowed from [33]) versus the apparent particle volume fraction.

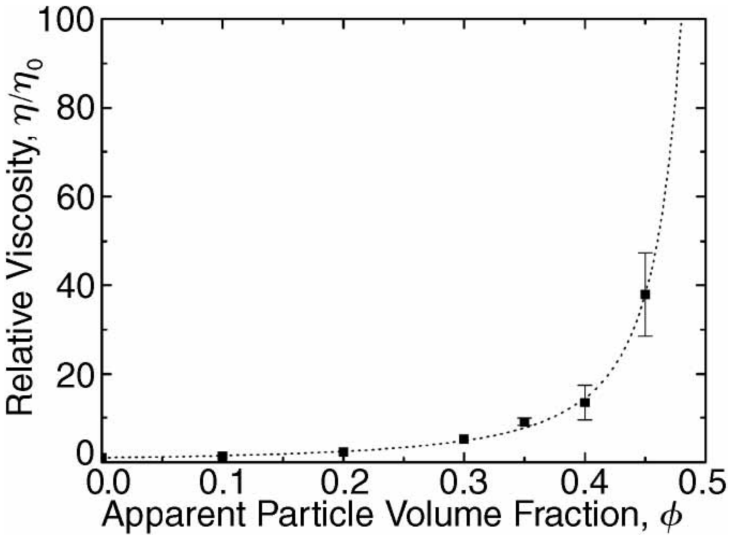

Figure 3.9: Example of the viscosity of a colloidal alumina in paraffin as a function of solids loading (experimental points) fitted with a modified Krieger–Dougherty mode (dotted line) (borrowed from [33]**).**

Figure 3.9 shows the trend in viscosity follows the behavior described in Equation 3.2. The figure shows clearly that developing ink with sufficiently high solid loading and suitable particle is one of the challenges in colloidal inkjet printing.

Finally the interaction between the ink and the substrate is important to obtain continuous layers, as discussed in Chapter 2. An issue with aqueous systems is the high surface tension of water, which leads to high contact angle between the droplet and the substrate. Surface tension is usually decreases via the addition of either a surfactant or a second solvent with a lower surface tension. This matter has been described in section 2.2.3 (p.20). For this work, I have decided to add ethanol to the formulation in addition to particles, water, and dispersant (PVP). In addition to being a suitable surfactant to reduce water high surface tension, ethanol allows a better control of the ink drying rate.

Using suspended colloidal particles has both advantages and disadvantages: On one hand colloidal inks are easy to process, cheap, and their solid loading and thus the final film thickness can be easily controlled. On the other the risk of nozzle clogging is high, the drying behavior of such an

ink critical to avoid "coffee ring effects" leading to non-continuous films, and the consolidation of ceramic-powder based layers occurs at high temperatures (e.g. 1300°C for ca. 100–500 nm YSZ powders),which can be incompatible with other components (substrates for example).

3.2.1.2 Studied materials and substrates for colloidal inks

In this work the colloidal inks of YSZ were developed to fabricate thin electrolyte film for SOFC. Colloids were commercial 8YSZ powder (TOSOH). The substrates consisted in thin green NiO/YSZ functional anode layer deposited onto a thicker NiO/YSZ anode support. The ratio between Ni and YSZ was 40/60 vol.% both for the support layer and the active electrode layer [34] . ZrO_2 stabilized with 8 mol.% Y_2O_3 was used for the anode layer while ZrO_2 stabilized with 3 mol.% Y_2O_3 was used for the support layer. The layer produced by tape-casting and co-laminated as green materials at ca. 150°C [34]. The substrates had a 10-15 µm thick anode of Ni/ YSZ cermet laminated to a ~300 µm thick Ni/YSZ support layer. Figure 3.10 shows a graphical description of the substrate.

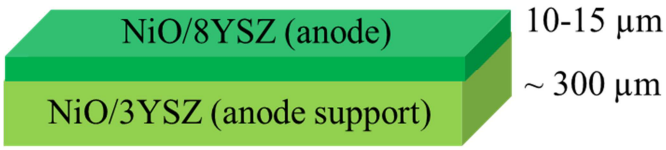

Figure 3.10: Structure of the NiO/anode substrate.

During heat treatment at 1300 °C, the green substrate will undergo a lateral shrinkage of typically 20%. During the shrinkage, the particles in the printed layer will come closer to each other and the sintering of the particle will be favored, leading to better densification. However, as the substrate is still flexible and very porous and be the time of deposition, it absorbs a lot of the solvent upon printing. After a certain number of depositions, the substrate deforms due to the high quantity of water absorbed. This can lead to non-flat layers after sintering and many undesired microstructural effects (cracks, delamination) on the film.

3.2.2 Reactive ink

3.2.2.1 Ink formulation and processing

The second type of studied ink consisted in a solution of precursors. Figure 3.11 shows an icon that represents the ink.

Figure 3.11: Graphical icon of the reactive ink.

Alternative to colloidal suspensions, reactive inks are particle-free, chemically reactive solutions containing dissolved precursors, such as metal alkoxide molecules in alcoholic solution [35,36]. After printing, the precursors are converted into solid particles based on thermal, chemical or photochemical post-processing steps. Reactive inks can be found in various forms [37,38]. The sol–gel process consists of a combination of reactions (hydrolysis and condensation) of the metal alkoxide which leads to the formation of a homogeneous oxo/hydroxopolymeric matrix at room temperature [39].

Hydrolysis

$$M - OR + H_2O \longrightarrow M - OH + R - OH \qquad \textbf{Equation 3.3}$$

Condensation

Dehydration

$$M - OH + HO - M \longrightarrow M - O - M + H_2O \qquad \textbf{Equation 3.4}$$

Dealcoholation

$$M - OR + HO - M \longrightarrow M - O - M + R - OH \qquad \textbf{Equation 3.5}$$

where M is a metallic cation (ex: Si, Ti, Zr, etc) and R an alkyl group. Due to the presence of such a structure, sol gels do not need mass diffusion steps such as sintering at high temperatures to become dense; the precursor only requires a calcination step (400-700°C) to remove by-products and additives and to crystallize the phase from the polymeric form. Finally the final oxide phase can be easily doped *via* the addition of ions from nitrates (yttrium, gadolinium, etc.), widening the list of potential materials that can be synthetized by reactive inks.

However alkoxide precursors are highly reactive towards water, leading to an unavoidable premature gel formation. Therefore, full control of the sol gel precursor reactivity is crucial, especially for inkjet, where inorganic polymerization can lead to irreversible clogging of the nozzle or the reservoir before printing. A fine control over the sol-gel process can be achieved by nucleophilic ligands, also called chelating agents [40]. These stabilize the alkoxides by coordinating the metallic center and forming more stable molecular complexes precursors [40]. Figure 3.12 shows a representation of such chelation.

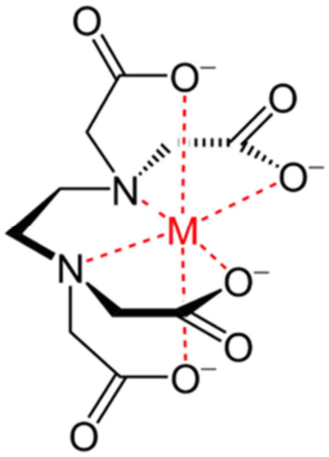

Figure 3.12: Illustration of the chelation of metal alkoxide by MDEA.

The hydrolysis/condensation reactions are thus inhibited and tolerance towards water is then achieved. Among the most used ligands there are carboxylic acids (e.g. acetic acid) [40] and alkanolamines (e.g. triethanolamine and methyldiethanolamine) [41,42].

An important parameter to consider is the pH of the solution, which will be determined in this case by the ligand nature. In the case of material having different possible phases, the pH will play an important role into the formation of a specific phase. An example is the synthesis of titania by sol gel, which can be either as anatase or rutile. Studies showed that low pH environment leads to rutile

formation while high pH leads to anatase formation. This mechanism can be described by the concept of partial charge model [43]. This model shows that titanium cation hydrolysis happens at low pH. In this condition, a stable $[Ti(OH)(OH_2)_5]^{3+}$ will form, but these species cannot condense due to the positive charge of the hydroxo group. When the pH is not low enough, $[Ti(OH)_2(OH_2)_5]^{2+}$ will form by deprotonation. Similarly these species cannot condense. Anatase and rutile are condensed when the solution activity permit a further deprotonation to $[TiO(OH)(OH_2)4]^{+}$, which can withstand de-oxolation of $[TiO(OH)_3(OH2)_3]^{+}$. In the high acidity region (low pH), de-oxolation cannot happen and linear growth happens along the equatorial plane of cations by oxolation, leading to rutile formation. In lower acidity conditions (high pH), de-oxolation happens and the condensation occurs along all directions and leads to the branch-like chain of anatase structure. Figure 3.13 summarizes this mechanism and demonstrates the importance of pH in titania formation

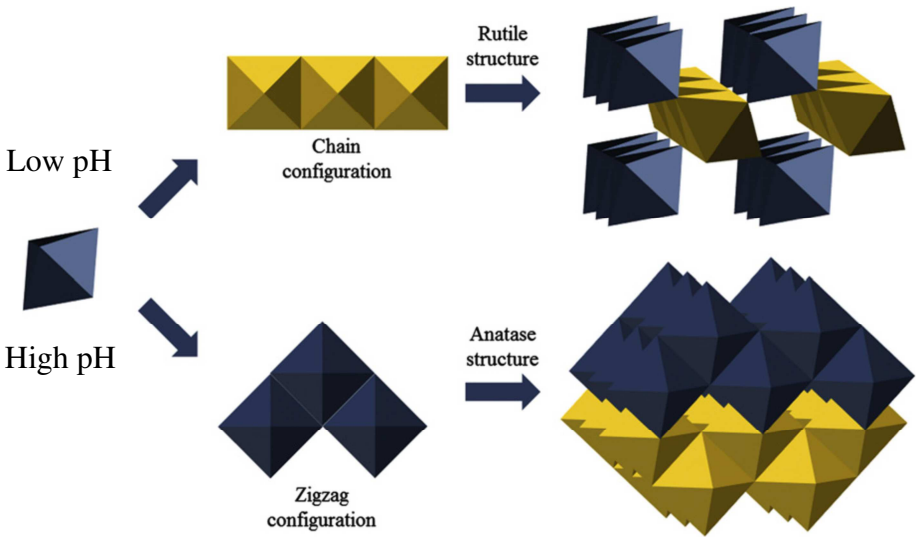

Figure 3.13: TiO_2 rutile and anatase formation from different octahedral configurations (borrowed from [44]**).**

A fine control of the precursors' reactivity towards water is thus critical for the printability. An insufficient amount of chelating agent leads to premature hydrolysis/condensation reactions and particle formation. On the other hand, since chelating agent introduces electrostatic attraction in the solution, an excess of ligands can change the rheological properties, modifying the printability properties of the reactive inks.

In this work the amine N-methyldiethanolamine (MDEA) is chosen as basic nucleophilic ligand. This choice was firstly motivated to promote branch-like anatase polymerization in titania thin film development [45]. Moreover MDEA has a low viscosity at room temperature and is

environmentally friendly. While this strategy has several advantages (particle-free, doping possibility, low processing temperature) reactive inks contain a large amount of water and organics that evaporate at low temperature. The resulting shrinkage of such inks is thus very high, potentially leading to film cracks and defects. Moreover a stable printability over time can be complicated to reach.

3.2.2.2 Materials and substrates

Two materials were considered in the development of reactive inks to demonstrate the versatility of the ink design. The materials, titanium- and zirconium- based, were chosen for their interest in thin film technologies.

- Titania thin films were fabricated using an aqueous titanium isopropoxide based ink stabilized with MDEA. Titania was chosen for its well-known chemistry to understand the mechanism behind precursor chelation. The printing of these films was performed on several flat and dense substrates with different surface free energies. These substrates were chosen to (1) demonstrate the ability to deposit the ink on substrates having various free surface energy, (2) to verify that crack free film can be obtained in quasi ideal surface conditions (flat and dense). Substrates used in this study are soda lime glass (Sigma Aldrich), indium tin oxide (ITO, Sigma Aldrich) and polycrystalline alumina (Keral 96, Kerafol).
- YSZ thin films were deposited using reactive inks on dense and porous substrates. Similarly to the colloidal ink, these films are developed for utilization as electrolyte for SOFC. The aqueous ink was based on zirconium propoxide and yttrium nitrate, and stabilized with MDEA. The ink was first deposited on flat, dense and insulating substrates such as Si(100), quartz (Crystal GmbH) and polycrystalline alumina (Keral96, Kerafol) to (1) demonstrate the ability to deposit in quasi ideal surface conditions (flat and dense) and (2) to measure the electrical conductivity of the films. Insulating and dense substrates are necessary for these measurements to remove any contribution of the substrate to the measurement. Lastly, films were deposited on usual nickel oxide/yttria-stabilized-zirconia (NiO/YSZ) anodes for SOFC made in-house. For the latter, the layers have a similar preparation and composition than the one described in section 3.2.1.2 (p.43). However green tapes could not be used in this case, unlike colloidal inks. As mentioned previously, reactive inks are processed at low temperature (400-700°C). In this range of temperature, NiO/YSZ anodes made by tape

casting are not mechanically stable enough to be manipulated for further observation or testing. Therefore the substrates were sintered at 1300°C prior to deposition. Using sintered substrates bring however a series of disadvantages: the substrate are not as flat as a tape cast green layer, due to previous processing and heat treatment at high temperatures. Moreover, as the substrate is already sintered, it cannot contribute to the densification of the layer thanks to lateral shrinkage (section 3.2.1.2, p.43).

3.2.3 Hybrid ink

3.2.3.1 Ink composition and processing

The third and last ink design consists in a mixture of the 2 first, *i.e.* a suspension of particles into a stabilized reactive ink. Figure 3.14 shows an icon that represents the ink.

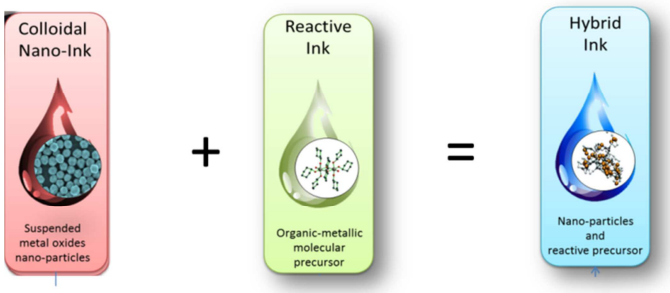

Figure 3.14: Graphical icons for the three inks.

This ink type was designed with the idea of countering the principal disadvantages of the colloidal and reactive inks while keeping advantages of both. Similarly to reactive inks, the calcination of the sol gel part at low temperature will yield a matrix of crystalline nanometric particles, surrounding in that case much bigger particles. The final microstructure after calcination should look like a wall made of bricks (particles) surrounded by mortar (sol-gel). Figure 3.15 illustrates the final microstructure.

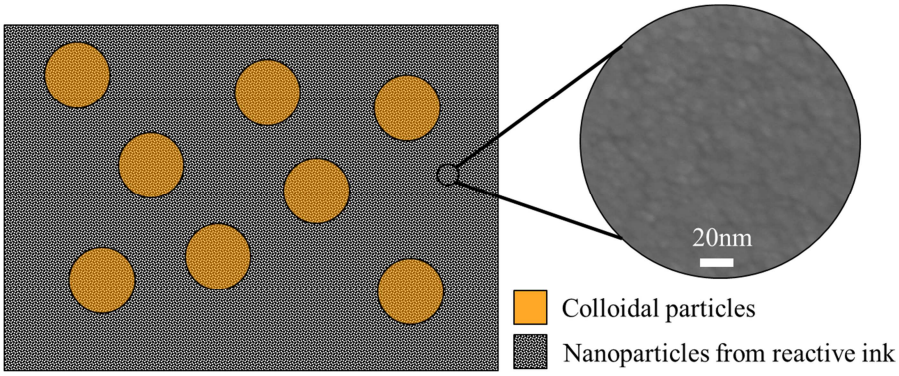

Figure 3.15: Illustration of the hybrid ink morphology after calcination (circular inset: SEM picture of TiO_2 particles made from calcination of reactive ink at 400°C).

As previously explained, reactive inks undergo a high shrinkage during heat treatment due to the high amount of organics. Crystalline particles in hybrid inks are then replacing some volume fraction of the liquid phase by a solid phase, reducing the shrinkage of the film during heat treatment, preventing the formation of defects and cracks.

Several sources of particles can be used such as commercial colloidal particles or synthetized nanoparticles. The environment of these particles in a hybrid ink, compared to a classic colloidal design, is very different, particularly in terms of pH, due to the presence of alkoxides, nitrates and chelating agent. Particles surface and stability will be affected by this change of environment to keep a stable and printable ink. Stabilization of such particles, independently from their source, will be the key in depositing the ink. This conceptual system can also be enlarged to more than a single material system:

- Multi-material systems: different combinations of materials can be arranged in order to elaborate composite films with enhanced properties. One can imagine for instance a combination of various materials as nanoparticles in a matrix of another different material made from sol-gel. These architectures can be used to improve existing properties of the layers, add functionalities to the film or create porosity by suspending pore formers. The case of CGO nanoparticles stabilized in an YSZ reactive ink is treated in this thesis (Chapter 7) to develop a composite electrolyte for SOFC operating at lower temperature.
- *In-situ* solid-state reaction: this ink concept can also be considered to synthetize a solid phase from two starting materials (one as nanoparticles and one as sol-gel) in a solid state reaction at high temperature following the equation:

$$xA\ (s) + \ yB\ (l) \longrightarrow A_xB_y\ (s)$$ **Equation 3.6**

In this study, bismuth titanate $Bi_4Ti_3O_{12}$ was synthetized at 750°C by suspending bismuth oxide nanoparticles into a stabilized Ti-based reactive ink.

To the knowledge of the author, no studies were performed on such systems in literature. An objective of the thesis is to explore the possibilities, advantages and limitations of such systems for the development of thin films for inkjet printing.

3.2.3.2 Materials and substrates

Two materials systems were studied in the development of hybrid inks:

- YSZ-YSZ: this basic system was used as a starting point in the development of hybrid inks. The YSZ particles were the same as those used in the development of colloidal inks, *i.e.* commercial 8YSZ (TOSOH). The aim of this ink was to study the effect of ink preparation on the final ink properties and the influence of solid loading on the shrinkage of the film. The shrinkage was measured using 3D profilometry in which the thickness and lateral dimensions of the films are optically measured at different calcination temperatures. As reference for thickness measurement, it is ideal to use a surface as flat as possible. As such YSZ-YSZ inks were deposited on flat dense glass substrates.
- YSZ-CGO: were deposited using hybrid inks. CGO nanoparticles were synthetized by hydrothermal synthesis, the aqueous ink based on zirconium propoxide and yttrium nitrate, and stabilized with MDEA. Similarly to YSZ reactive inks, the ink was first deposited on flat, dense and insulating substrate such as quartz (Crystal GmbH) and alumina single crystal (sapphire, Crystal GmbH). Films were also deposited onto polished sintered nickel oxide/yttria-stabilized-zirconia (NiO/YSZ) made in-house, already described in section 3.2.1.2 (p.43), to see the effect of particle addition on the film quality when depositing onto porous substrate.
- Bi_2O_3-TiO_2: This system was used as demonstration of the utilization of hybrid inks as an *in-situ* synthesis method. In this commercial bismuth oxide (III) particles (Bi_2O_3, Alfa Aesar) were dispersed in a stable aqueous titanium isopropoxide based ink, described in section 6.1 (p.99). Bismuth titanate $Bi_4Ti_3O_{12}$ was synthesized by calcining the ink. Due to

dispersion issues described in Chapter 7, the ink could not be inkjet printed. However the material was deposited by 3D printing to demonstrate the possibility of adapting the ink to other deposition processes.

Bibliography

[1] J.E.S. Haggerty, L.T. Schelhas, D.A. Kitchaev, J.S. Mangum, L.M. Garten, W. Sun, K.H. Stone, J.D. Perkins, M.F. Toney, G. Ceder, D.S. Ginley, B.P. Gorman, J. Tate, High-fraction brookite films from amorphous precursors, Sci. Rep. 7 (2017) 1–11. doi:10.1038/s41598-017-15364-y.

[2] A.A. Gribb, J.F. Banfield, Particle Size Effects on Transformation Kinetics and Phase Stability in Nanocrystalline TiO_2, Am. Mineral. 82 (1997) 717–728. doi:10.2138/am-1997-7-809.

[3] T. Spring, A. Bj, M. Einarsrud, C. Simon, I. Kumakiri, S. Materials, M. Science, Photocatalytic activity of TiO 2 -based nanoparticles produced by spray pyrolysis, (2009).

[4] M. Arin, P. Lommens, N. Avci, S.C. Hopkins, K. De Buysser, I.M. Arabatzis, I. Fasaki, D. Poelman, I. Van Driessche, Inkjet printing of photocatalytically active TiO2 thin films from water based precursor solutions, J. Eur. Ceram. Soc. 31 (2011) 1067–1074. doi:10.1016/j.jeurceramsoc.2010.12.033.

[5] T. Thoř, J. Václavík, Sol-gel preparation of silica and titania thin films, (2016) 101511A. doi:10.1117/12.2257325.

[6] P.. Gouma, P.. Dutta, M.. Mills, Structural stability of titania thin films, Nanostructured Mater. 11 (1999) 1231–1237. doi:10.1016/S0965-9773(99)00413-4.

[7] B.K. Roy, G. Zhang, R. Magnuson, M. Poliks, J. Cho, Electrodeposition of titania thin films on metallic surface for high-k dielectric applications, J. Am. Ceram. Soc. 93 (2010) 774–781. doi:10.1111/j.1551-2916.2009.03452.x.

[8] B. Aurivillius, Mixed bismuth oxides with layer lattices. II. Structure of Bi4Ti3O12, Ark. Kemi. 1 (1949) 499–512.

[9] J. Dorrian, R. Newnham, M. Kay, Crystal-structure of Bi4Ti3O12, Ferroelectrics. 3 (1971) 17.

[10] H.S. Shulman, M. Testorf, D. Damjanovic, N. Setter, Microstructure, Electrical Conductivity, and Piezoelectric Properties of Bismuth Titanate, J. Am. Ceram. Soc. 79 (1996) 3124–3128. doi:10.1111/j.1151-2916.1996.tb08086.x.

[11] J.S. Patwardhan, M.N. Rahaman, Compositional effects on densification and microstructural evolution of bismuth titanate, J. Mater. Sci. 39 (2004) 133–139. doi:10.1023/B:JMSC.0000007737.19267.60.

[12] B. Aurivillius, Mixed bismuth oxides with layer lattices. I. The structure type of CaNb2Bi2O9 tle, Ark. Kemi. 1 (1949) 463–480.

[13] M. Villegas, C. Moure, J.F. Fernandez, P. Duran, Low-temperature sintering of submicronic randomly oriented Bi4Ti3O12 materials, Ceram. Int. 22 (1996) 15–22. doi:10.1016/0272-8842(95)00047-X.

[14] Z. Lazarevic, B.D. Stojanovic, J. a. Varela, An approach to analyzing synthesis, structure and properties of bismuth titanate ceramics, Sci. Sinter. 37 (2005) 199–216. doi:10.2298/SOS0503199L.

[15] C.H. Hervoches, P. Lightfoot, A Variable-Temperature Powder Neutron Diffraction Study of Ferroelectric Bi 4 Ti 3 O 12, Chem. Mater. 11 (1999) 3359–3364. doi:10.1021/cm991090d.

[16] G. Orange, G. Fantozzi, F. Cambier, C. Leblud, M.R. Anseau, A. Leriche, High temperature mechanical properties of reaction-sintered mullite / zirconia and mullite / alumina / zirconia composites, J. Mater. Sci. 20 (1985) 2533–2540.

[17] L.Q. Zhu, Q. Fang, G. He, M. Liu, L.D. Zhang, Interfacial and optical properties of ZrO2/Si by reactive magnetron sputtering, Mater. Lett. 60 (2006) 888–891. doi:10.1016/j.matlet.2005.10.039.

[18] J.D. Fidelus, W. ?ojkowski, D. Millers, K. Smits, L. Grigorjeva, Advanced nanocrystalline ZrO<inf>2</inf> for optical oxygen sensors, Proc. IEEE Sensors. (2009) 1268–1272. doi:10.1109/ICSENS.2009.5398385.

[19] D.R. Clarke, C.G. Levi, a G. Evans, Enhanced zirconia thermal barrier coating systems, Proc. Inst. Mech. Eng. Part A J. Power Energy. 220 (2006) 85–92. doi:10.1243/095765005X31126.

[20] J.-P. Brog, C.-L. Chanez, A. Crochet, K.M. Fromm, Polymorphism, what it is and how to identify it: a systematic review, RSC Adv. 3 (2013) 16905. doi:10.1039/c3ra41559g.

[21] H. Yanagida, K. Koumoto, M. Miyayama, The Chemistry of Ceramics, John Wiley & Sons, 1996.

[22] M. Han, X. Tang, H. Yin, S. Peng, Fabrication, microstructure and properties of a YSZ electrolyte for SOFCs, J. Power Sources. 165 (2007) 757–763. doi:10.1016/j.jpowsour.2006.11.054.

[23] Ceria structure, (n.d.). https://commons.wikimedia.org/wiki/File:Ceria-unit-cell-3D-ionic.png.

[24] W. Hayes, A.. Stoneham, Defects and defect processes in nonmetallic solids, Courier Dover publications, 2004.

[25] M. Mogensen, N.M. Sammes, G.A. Tompsett, Physical, chemical and electrochemical properties of pure and doped ceria, Solid State Ionics. 129 (2000) 63–94. doi:10.1016/S0167-2738(99)00318-5.

[26] N.P. Brandon, D. Corcoran, D. Cummins, A. Duckett, K. EI-Khoury, D. Haigh, R. Leah, G. Lewis, N. Maynard, T. McColm, R. Trezona, A. Selcuk, M. Schmidt, Development of metal supported solid oxide fuel cells for operation at 500-600 ??c, J. Mater. Eng. Perform. 22 (2013) 2900–2903. doi:10.1007/s11665-013-0716-7.

[27] P. Hiemenz, Principles of colloid and surface chemistry, Marcel Dekker, New York, NY, 1986.

[28] D. Everett, Basic Principles of Colloid Science, RSC Publications, 1988.

[29] M. Mitchnick, Particles Science, Drug Dev. Serv. Tech. Br. 1 (2009) 2.

[30] R. Hunter, Zeta Potential in Colloid Science, Academic Press, New York, NY, 1981.

[31] T. Ring, Fundamentals of Ceramic Powder Processing and Synthesis, Academic Press, London, 1996.

[32] L. Bergström, Rheological Properties of Concentrated, Nonaqueous Silicon Nitride Suspensions, J. Am. Ceram. Soc. 79 (1996) 3033.

[33] B. Derby, N. Reis, Inkjet Printing of Highly Loaded Particulate Suspensions, MRS Bull. (2003) 815–818.

[34] A. Hauch, M. Mogensen, Ni/YSZ electrode degradation studied by impedance spectroscopyEffects of gas cleaning and current density, Solid State Ionics. 181 (2010) 745–753. doi:10.1016/j.ssi.2010.04.001.

[35] B. Yoldas, Design of sol-gel coating media for ink-jet printing, J. Sol-Gel Sci. Technol. 13 (1998) 147–152. doi:10.1023/A:1008640413941.

[36] H.S. Chen, R.V. Kumar, B. a. Glowacki, Chemical solution deposited lanthanum zirconium oxide thin films: Synthesis and chemistry, Mater. Chem. Phys. 122 (2010) 305–310. doi:10.1016/j.matchemphys.2010.02.028.

[37] D.A. Gregory, Y. Zhang, P.J. Smith, X. Zhao, S.J. Ebbens, Reactive inkjet printing of biocompatible enzyme powered silk micro-rockets, Mater. Views. (2016) 4048–4055. doi:10.1002/smll.201600921.

[38] K. Black, J. Singh, D. Mehta, S. Sung, C.J. Sutcliffe, P.R. Chalker, Silver ink formulations for sinter-free printing of conductive films, Nat. Publ. Gr. (2016) 1–7. doi:10.1038/srep20814.

[39] L.L. Hench, J.K. West, The sol-gel process, Chem. Rev. 90 (1990) 33–72. doi:10.1021/cr00099a003.

[40] C. Sanchez, J. Livage, M. Henry, F. Babonneau, Chemical modification of alkoxide precursors, J. Non. Cryst. Solids. 100 (1988) 65–76.

[41] T. Kemmit, N.I. Al-Salim, G.J. Gainsford, CHEMISTRY N -Methyldiethanolamine-Modified Titanium Isopropoxide :, Aus. J. Chem. 55 (2002) 513–517. doi:10.1071/CH02087.

[42] N. Martín-Arbella, I. Bretos, R. Jiménez, M.L. Calzada, R. Sirera, Metal complexes with N-methyldiethanolamine as new photosensitive precursors for the low-temperature preparation of ferroelectric thin films, J. Mater. Chem. 21 (2011) 9051–9059. doi:10.1039/c1jm10846h.

[43] a Zaban, S.T. Aruna, S. Tirosh, B. a Gregg, Y. Mastai, The Effect of the Preparation Condition of TiO2 Colloids on Their Surface Structures, J. Phys. Chem. B. 104 (2000) 4130–4133. doi:10.1021/jp993198m.

[44] M.R. Golobostanfard, H. Abdizadeh, Effects of acid catalyst type on structural, morphological, and optoelectrical properties of spin-coated TiO2 thin film, Phys. B Condens. Matter. 413 (2013) 40–46. doi:10.1016/j.physb.2012.12.040.

[45] S.A. Ibrahim, S. Sreekantan, Effect of pH on TiO_2 Nanoparticles via Sol-Gel Method, Adv. Mater. Res. 173 (2010) 184–189. doi:10.4028/www.scientific.net/AMR.173.184.

Chapter 4 : Characterization tools and experimental

Different methods were applied to characterize the inks before printing (printability, particle size distribution, etc.), during printing (droplet analysis), and at high temperatures (thermal analysis). Crystallographic phase determination at different temperature was also performed on inks to confirm the formation of the desired phases, assess possible phase transformations, or to identify the presence of secondary phases. The printed patterns were also observed before and after printing as well as after heat treatment to estimate the film thickness, shrinkage, and the surface quality. Finally, characterization methodologies, specific to a certain applications, were used to demonstrate the efficiency of the thin films.

In this chapter, the principle of these techniques is described, with their advantages and limitations. Additionally the parameters used experimentally are listed for each technique.

4.1 **Ink characterization**

4.1.1 Printability

Printability Z of an ink for inkjet printing has been previously defined (Equation 2.4) as a relationship between nozzle diameter (a), viscosity (η), surface tension (σ), and density (ρ) :

$$Z = \frac{\sqrt{\sigma . \rho . a}}{\eta} \qquad \textbf{Equation 4.1}$$

Prior to printing, the printability of the inks was assessed through various measuring methods of those parameters.

4.1.1.1 Rheology

Rheology describes the flow and deformation behavior of liquid based media (ink, pastes, slurries, etc.) when external forces are applied. The measured responses can be divided into several categories: viscous, elastic, and viscoelastic. Inks for inkjet inks are quite diluted and thus are characterized by the viscous behavior. Suspensions can exhibit Newtonian or non-Newtonian behaviors. The viscosity of Newtonian fluids is constant and independent of the applied force. On

the other hand, viscosity of non-Newtonian fluids is shear rate-dependent: viscosity can either decrease (shear thinning) or increase (shear thickening) with shear rate. Most non Newtonian fluids exhibit shear thinning behavior, only a few cases of shear thickening have been observed. Figure 4.1 shows examples of the three described behaviors.

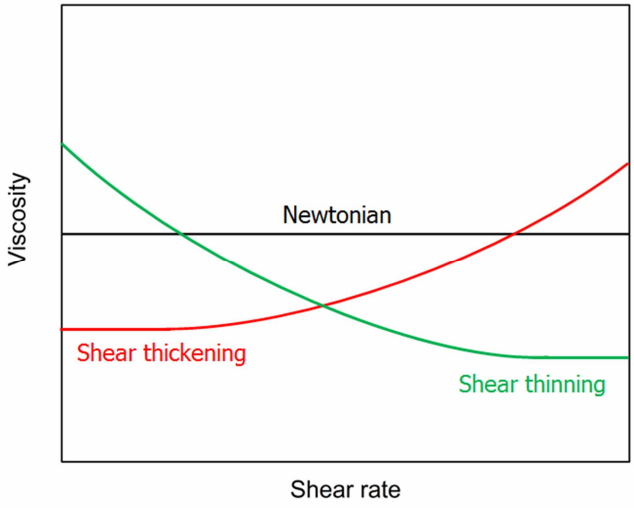

Figure 4.1: Flow behaviors of Newtonian and non-Newtonian fluids.

Viscosities are estimated differently for both types of flows, as shown on Figure 4.2.

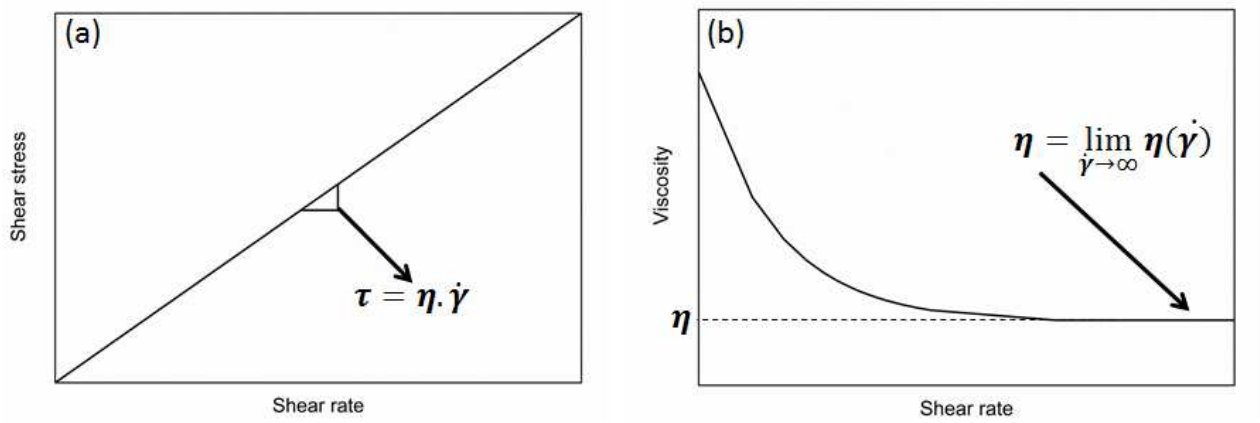

Figure 4.2: Viscosity measurement method for (a) Newtonian and (b) non Newtonian (here shear thinning) fluids.

The viscosity of Newtonian fluids is calculated by measuring the shear stress $\boldsymbol{\tau}$ (Pa) at different shear rates $\dot{\boldsymbol{\gamma}}$ (s^{-1}). Ink viscosity $\boldsymbol{\eta}$ (mPa.s) is described by the generalized Newton's law (Equation 4.2):

$$\boldsymbol{\tau = \eta . \dot{\gamma}} \qquad \textbf{Equation 4.2}$$

Viscosity $\boldsymbol{\eta}$ (mPa.s), defining the material resistance to flow is then calculated by plotting shear stress $\boldsymbol{\tau}$ (Pa) versus shear rates $\boldsymbol{\dot{\gamma}}$ (s^{-1}) and calculating the slope (Figure 4.2 (a)). Viscosity curves of non-Newtonian fluids are obtained following the same measuring protocol than Newtonian fluids. As the ink undergoes high shear rate during printing, it is considered that fluid viscosity corresponds to the one measured at the plateau reached at high shear rates (Figure 4.2 (b)). The characteristic flow behavior (Newtonian/Non-Newtonian) can be quantitatively evaluated via the estimation of the flow index. This parameter is mathematically determined via the analysis of rheological data using the logarithmic form of the power law (Equation 4.3) [1]:

$$\log(\tau) = \log(K) + n.\log(\dot{\gamma}) \qquad \textbf{Equation 4.3}$$

where is n the flow index and K the consistency coefficient. This equation has a linear form in which the flow index n is the slope identifying the character of the fluid: Newtonian when n=1, shear-thinning when n < 1 and shear-thickening when n >1.

Viscosity is the parameter that has the most influence on ink printability. Its value can span over very wide intervals and the term is not under a square root (unlike the three other terms) so its weight on the printability is higher than the other parameters. As viscosity is very sensitive to slurry preparation and external environment (temperature, hydrometry, etc.) it thus should be measured thoroughly after ink preparation and before each printing session to ensure printing reproducibility. In this study, ink viscosity was measured using an Anton Paar Rheometer (MCR 302) at a constant temperature of 21°C in rotational mode. A parallel-plate measuring system was chosen, using a 50mm diameter plate and a gap distance of 0.5mm. A solvent trap was placed over the measurement plate to avoid solvent evaporation. Figure 4.3 shows the equipment used and the PP50 measurement plate.

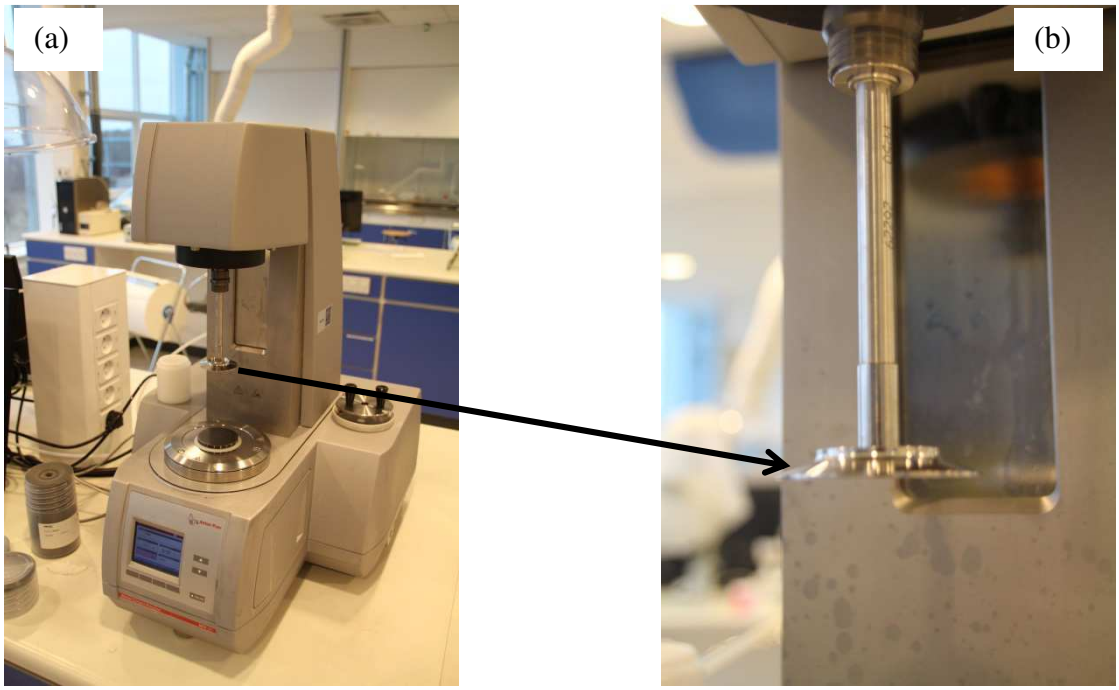

Figure 4.3: Picture of (a) the Anton Paar Rheometer (MCR 302) and (b) the PP50 measurement plate.

Prior to measurement, inks underwent a pre-treatment procedure that removed any effects due to the sampling and loading of the inks. This procedure consisted of three steps: the first one at a shear rate of 1 s^{-1} for 1 min followed by 1 min at rest (shear rate = 0 s^{-1}), and the third one at 1 s^{-1} for 1 min. Flow curve measurements were conducted in the step mode using 60 steps with a waiting time of 10s in the shear rate range 1 s^{-1}-1000 s^{-1}.

4.1.1.2 Surface tension

The last crucial parameter that influences printability is ink surface tension. Not only is this parameter important to control droplet jetting, its value also affects the interaction between the ink and the substrate. When ink surface tension is higher than the substrate surface free energy, jetted droplets do not fully cover the substrate and form a discontinuous film (Figure 2.11). This instrument allows determining the dynamic surface tension by measuring the internal pressure of a gas bubble (here air) which is formed in a liquid using a capillary. The surface tension of the liquid phase is then measured using the Laplace equation (Equation 4.4), which links internal pressure,p, surface tension, σ, and the radius of curvature, r:

$$p = \frac{2.\sigma}{r} \qquad \textbf{Equation 4.4}$$

When the gas bubble is produced at the tip of the capillary its curvature increases, reaching a maximum, and then decreases. The maximum curvature is reached at a maximum pressure p_{max} for which the radius of the curvature is equal to the capillary radius. Surface tension can then be calculated from the pressure maximum p_{max}, capillary radius r.and hydrostatic pressure resulting from the immersion depth and the density of the liquid (Equation 4.5):

$$\sigma = \frac{(p_{max} - p_0).r}{2} \qquad \textbf{Equation 4.5}$$

It is important to precise that the measured surface tension is dependent of the surface age, *i.e.* the time between the beginning of the bubble formation and the occurrence of the pressure maximum. Figure 4.4 summarizes the measurement process by plotting the evolution of pressure versus time.

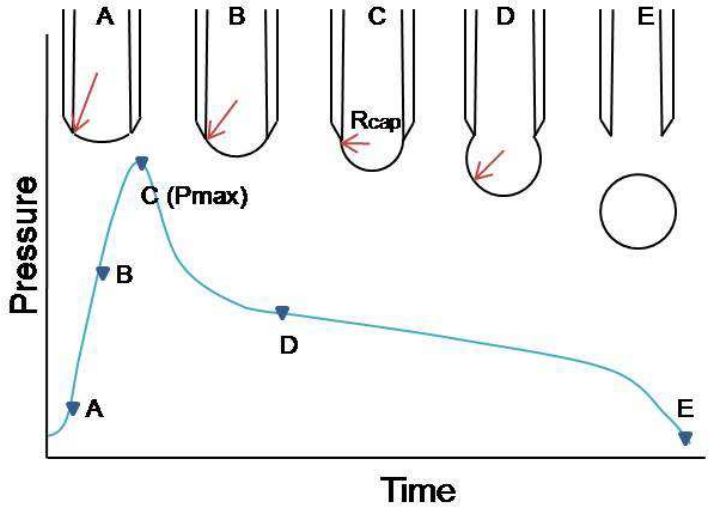

Figure 4.4: Evolution of pressure during measurement time (borrowed from [2]**).**

The dependence of surface tension on surface age can be evaluated by measuring surface tension at various surface ages. At low surface age the bubble reaches its maximal curvature in a short time, so short that the surfactant does not have time to reach the liquid-air interface to decrease the surface tension. This results in a high value of surface tension. As surface age is increased, surfactant will have more time to reach the interface, lowering the surface tension before reaching a plateau corresponding to the considered surface tension for our studies. In this work, dynamic surface tension was measured using a bubble pressure tensiometer (BP 50, Krüss), shown on Figure 4.5.

Figure 4.5: (a) Picture of the BP 50 bubble tensiometer and (b) a close-up picture of the equipment.

4.1.1.3 Density

Density was evaluated by weighing 10 ml of ink. Figure 4.6 shows a picture of the measurement.

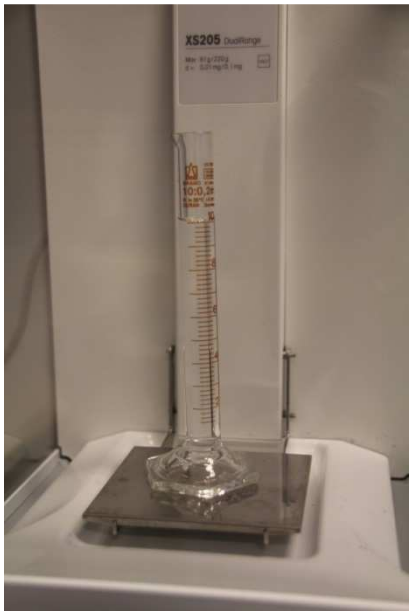

Figure 4.6: Picture of the density measurement.

Although this method is not exactly precise, density does not strongly affect the printability.

4.1.2 Particle size measurement

Traditionally particle size measurement is performed through laser diffraction. In this technology, a laser beam passes through any object ranging from nanometers to millimeters in size. Resulting diffraction patterns are used to evaluate the geometrical dimensions of a particle and give a distribution of particle size. The analysis is based on the Fraunhofer diffraction theory which states that the intensity of light scattered by a particle is directly proportional to the particle size [3]. Figure 4.7 summarizes the working principle of such technology.

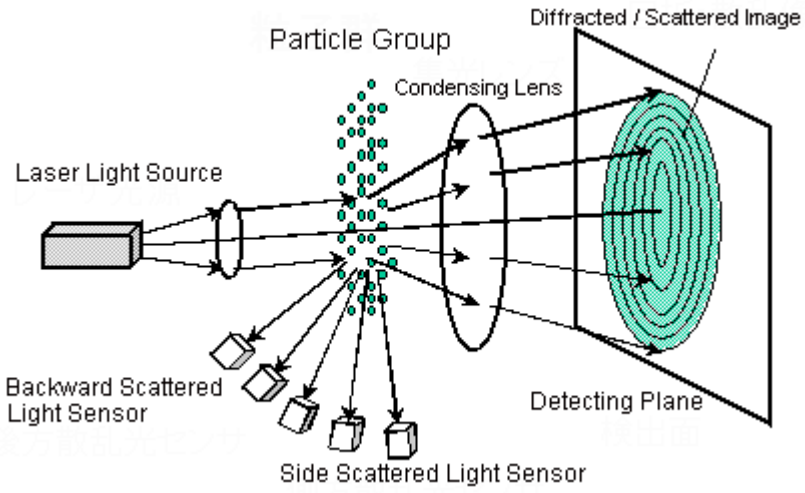

Figure 4.7: Principle of particle size measurement by laser diffraction scattering (borrowed from [4])

This technology has however some critical limitation, especially in terms of low limit size measurement. This technology cannot measure with precision particles below 0.1 µm, making characterization of nanoparticles challenging. Another technology patented by the manufacturer Malvern allows the measurement of particle size down to 0.3 nm using non-invasive backscattering. (NBIS). This technology measures the light scattered by the sample at a backscattering angle of 175º which yields many advantages. The volume of irradiated sample is increased, which improves sensitivity. Moreover, backscattering detection is less sensitive to larger particles, which primarily scatter at forward angles. Figure 4.8 summarizes the working principle of NBIS.

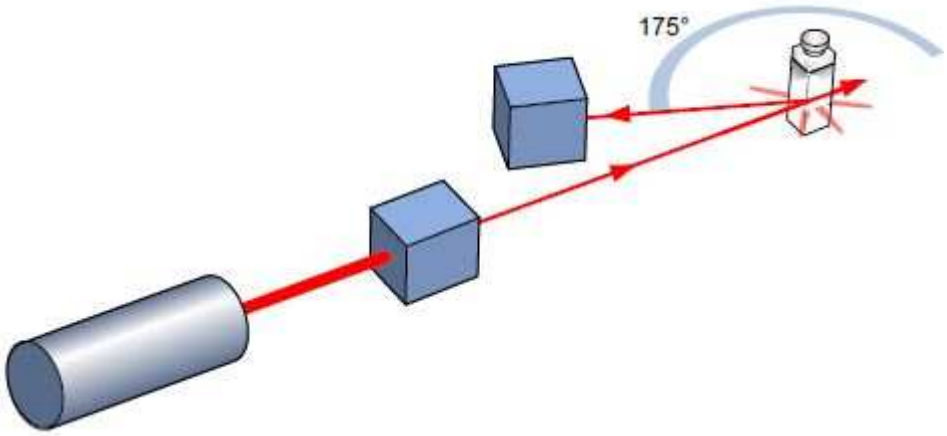

Figure 4.8: Principle of particle size measurement by NBIS (borrowed from [5]).

In this work, particle size was measured using both methods based on laser diffraction. A Beckman Coulter LS 13320 located at DTU Energy was used in this work to measure the particle size measurement of colloidal particles. Measurement of nanoparticles was performed using the NBIS technology using a Zetasizer ZS (Malvern) located in the laboratory of EPFL in Sion.

4.1.3 Fourier Transformed InfraRed spectroscopy (FTIR)

Fourier Transformed InfraRed spectroscopy (FTIR) is s a measuring technique used to obtain the absorption or emission infrared spectrum of a solid, liquid or gas. This technique is particularly widely used in organic chemistry to determine the bonding of chemicals. Figure 4.9 illustrates the working principle of FTIR.

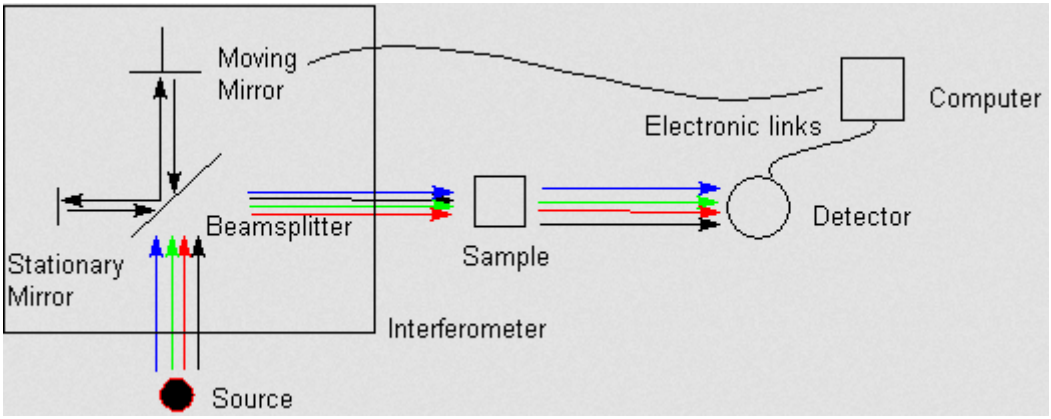

Figure 4.9: Working principle of FTIR (borrowed from [6]).

In this technique a light source (4000 cm^{-1} to 600 cm^{-1}) is sent first through an interferometer and then through the sample. The interferometer is composed of a several pieces of equipment: the light

goes through a beam-splitter that sends the light in two different directions: One goes to a stationary mirror and back to the beam-splitter while the other one goes to a moving mirror. The movement of the mirror makes the total path length of the beam variable compared to the one obtained by the stationary-mirror beam. The two beams recombined at the beam-splitter and the difference in path length creates an interferogram due to constructive and destructive interferences. The recombined beam is then sent through the sample. The sample absorbs the entire wavelength and the detector detects variation of energy versus time simultaneously for all wavelengths. Energy versus time is recorded and converted to an intensity *vs* frequency spectrum using a Fourier transformation:

$$A(r) = \sum X(k) \,.\, exp(-2\pi.\frac{irk}{N}) \qquad \textbf{Equation 4.6}$$

where A(r) and X(k) are the frequency domain and time domain points, respectively, for a spectrum of N points

An example of a spectrum is shown on Figure 4.10.

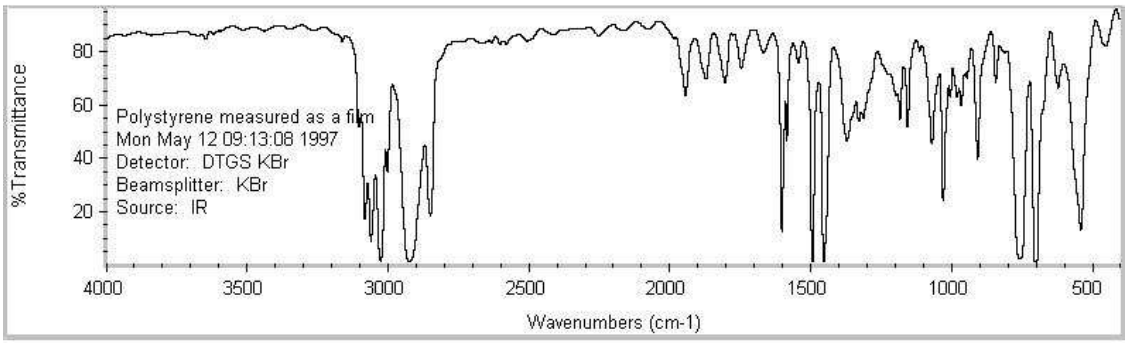

Figure 4.10: Example of typical pattern recorded with an FTIR spectroscope (borrowed from [6]**).**

The peaks observed on Figure 4.10 correspond to bonding vibration during irradiation. Each wavenumber position corresponds to a specific type of bonding (C-H, O-H, etc.). This technique permits to identify chemical bonding in molecules and to identify the chemical structure of a compound. The main advantage of this technique over classical spectroscopy is that the sample gets all the source energy, improving the signal-to-noise ratio. Moreover, this technique is fast and several scans can be run and collected, further improving the signal ratio. However the data treatment, and especially bonding and chemical structure determination, can become a very complicated task even with the help of peak position databases.

In this work, interactions between ligand and alkoxides in reactive inks were studied using FTIR. Measurements were performed on a Bruker Tensor 27 (Bruker, Germany) on liquid and gelified

inks in the 4000-400 cm^{-1} region at room temperature. Figure 4.11 shows a picture of the equipment.

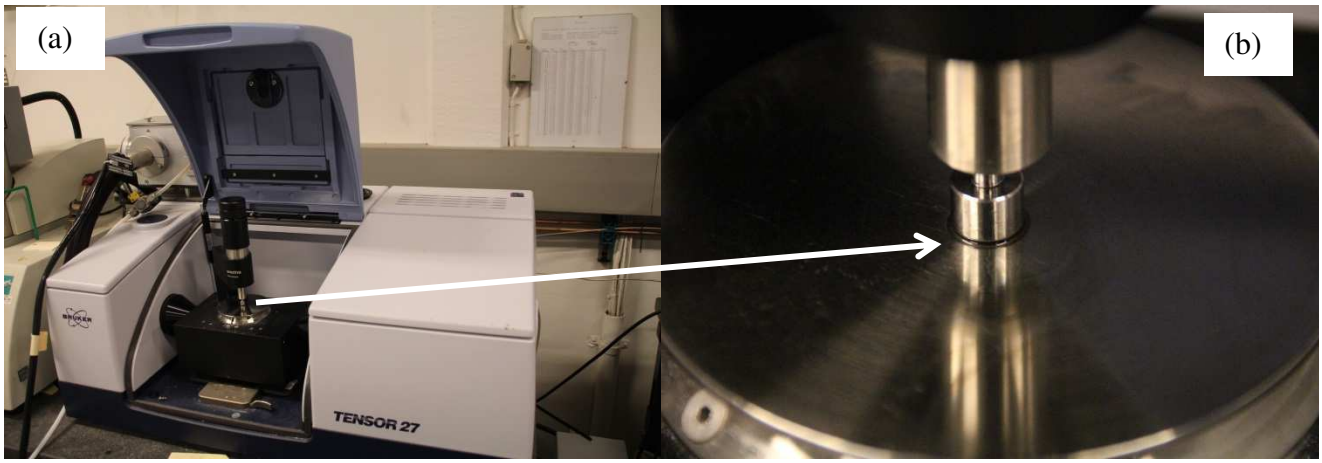

Figure 4.11: (a) Picture of the FTIR measurement equipment and (b) close up picture of the measurement plate.

4.1.4 Droplet analysis

Prior to printing, the ability of the ink to be jet is verified via a so-called drop-view camera. The camera observes the droplets ejection at the nozzle plate to detect the presence of satellite droplets, droplet deviation and clogged/deflective nozzles. In addition to check that the process is functioning before the deposition, this analysis is helpful to understand the ink behavior under jetting using a defined waveform and how to optimize such waveform to obtain reproducible and stable droplets. Droplet diameter, volume and velocity at different distances from the nozzle plate can be precisely measured with this method, as shown on Figure 4.12.

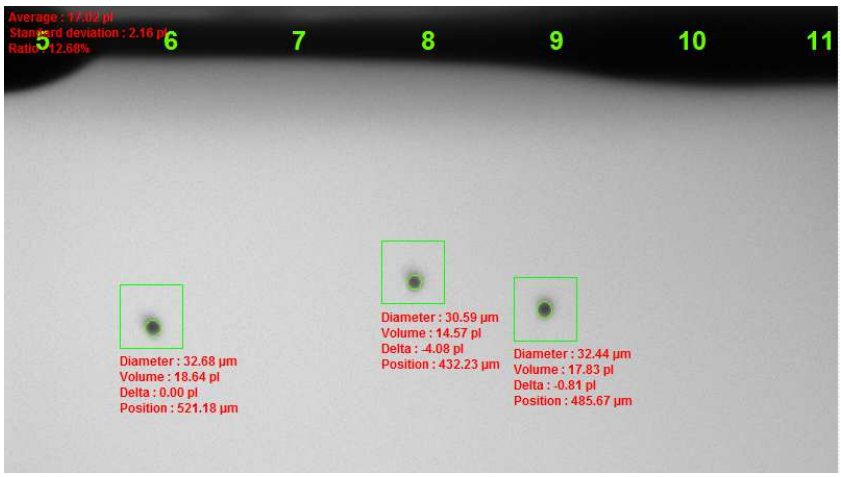

Figure 4.12: Droplet observation and characterization with the drop-view camera (X-serie Ceraprint).

4.1.5 Thermal analysis

After deposition inks will undergo a heat treatment to evaporate solvents, burn-off organics and calcine/sinter particles. It is fundamental to determine a suitable heat treatment cycle that will lead to the right material phase and without compromising the film integrity (cracks, pin holes) and microstructure. Moreover phase transformations can occur during the heat treatment cycle; their identification is crucial to detect the formation of secondary phases that can alter the material properties. Thermal analysis methods are powerful tools to determine at which temperature the inks undergo changes such as evaporation or binder burn off. Two methods were used in this study: Differential Thermal Analysis (DTA) and Thermo-Gravimetric Analysis (TGA). These techniques are usually coupled and complementary.

Differential thermal analysis (or DTA) is a thermoanalytic method in which the material under study and an inert reference undergo similar thermal cycles, any temperature difference between sample and reference is recorded [7]. This differential temperature is then plotted against temperature or time (DTA curve, or thermogram). Changes in the sample visible as peaks, either exothermic or endothermic (depending on the change in the sample), are detected relative to the inert reference and give information on the transformations that have occurred, such as solvent evaporation, crystallization, glass transitions or melting. Thermogravimetric analysis or thermal gravimetric analysis (TGA) is a thermal analysis method which consists in measuring the mass of a sample as the temperature changes over time. This measurement gives information about chemical phenomena, such as thermal decomposition or solid-gas reaction; as well as physical phenomena like absorption and desorption [8]. Both techniques have to be used simultaneously to thoroughly identify each physical and/or chemical phenomenon happening during the heat treatment. In this study, thermal analysis (TG-DTA) were performed on inks and powders using an STA 409 PG (Netzsch) at a constant rate of 10 $K.min^{-1}$ under air between 25 and 700 °C using alumina crucibles. Figure 4.13 shows a picture of the equipment.

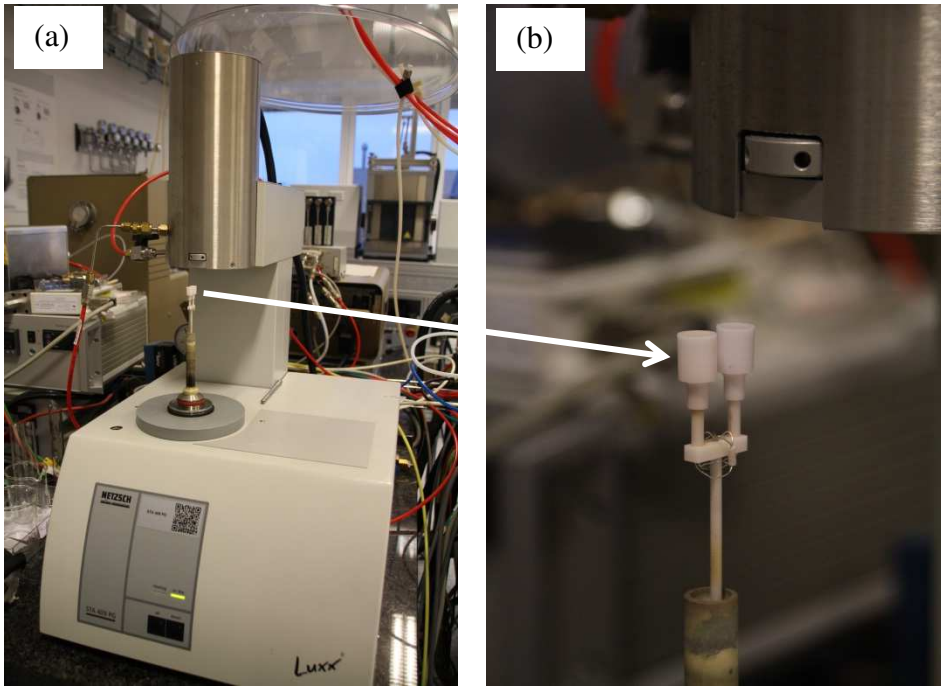

Figure 4.13: (a) Picture of the DTA/TG measurement equipment and (b) close up picture on the alumina crucibles (left: sample, right: reference).

4.2 Characterization of printed layers

4.2.1 Scanning electron microscopy (SEM)

A scanning electron microscope (SEM) is a type of microscope using a focused beam of electrons to produce images of a solid sample. Upon interaction, electrons interact with atoms in the sample, and produce several signals that contain information about the sample's composition microstructure and topography. Moreover as the electron beam is scanned along the surface, its position and the detected signal are combined to create an image of the sample. Resolution around 1 nanometer can be obtained with this technique. SEM offers a wide range of magnifications from about 10 times to more than 500,000 times. This technique is powerful for material observation and is the standard in material science. Figure 4.14 shows the different signals that can be produced and analyzed with a SEM.

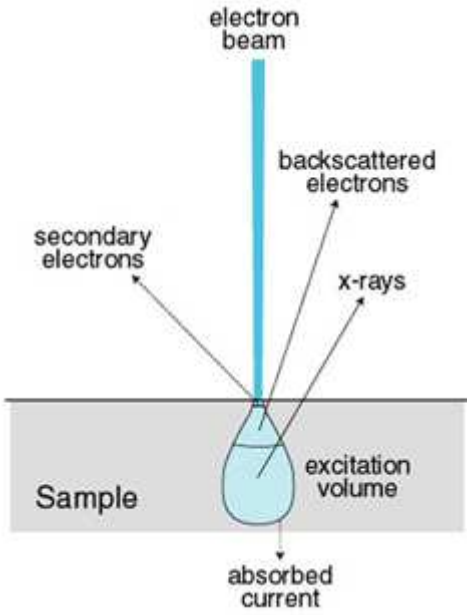

Figure 4.14: Signals generated upon interaction between the electron beam and the sample in an SEM (borrowed from [9]**).**

The usual SEM signal used to observe a sample in an SEM is the "secondary electrons" (SE) emitted by excited atoms. The amount of detected secondary electrons depends greatly on specimen topography. The secondary electrons are collected during scanning using specific detectors, creating an image of the sample topography. Other types of signals are produced, among them reflected or back-scattered electrons (BSE) and characteristic X-rays.

Back-scattered electrons (BSE) are beam electrons reflected from the sample by elastic scattering. Compared to SE, they are produced deeper in the sample and images produced with this type of signal have then a lower resolution than SE. However, BSE images provide information about the nature and distribution of elements in the sample. Characteristic X-rays can also be detected during observation. Upon interaction, the electron beam interacts with the atoms in the sample and removes electrons from the inner shell. This causes an electron from a higher energy level to fill the shell, producing X-rays. These characteristic X-rays are used to identify the elemental composition in the sample.

However, this technique has some limitations: the technique is limited to solid samples that can fit into the chamber, usually around 10 cm (horizontal) and 40 mm (vertical) maximum. Moreover, in the case of insulating samples, an electrically conductive layer (usually carbon or gold nanoparticles) must be applied on the surface to avoid accumulation of electrons on the surface, also called charging. This effect results in an unresolved image, making observation impossible. The

addition of such conductive layer can be problematic for the observation and composition identification of nanoparticles in the samples.

In this work, structure and morphology of the calcined and sintered layers by inkjet printing were examined in a Merlin electron microscope (Zeiss, Germany). Prior to observation carbon nanoparticles were sputtered onto the sample surface to reduce electron charging due to the high dielectric constant of the substrates. Secondary electrons are used to observe the topography of the films and detect any crack or delamination.

4.2.2 X-Ray Diffraction (XRD)

The phase characterization of a synthetized material is a crucial step to validate the process. The phase composition is determined using X-ray diffraction (XRD). XRD is a technique used to determine the chemical structure of a crystal. By definition, a crystal consists of regular arrays of atoms and X-rays are considered as waves of electromagnetic radiation. Figure 4.15 illustrates the interaction between the X-ray beam and the atoms in the crystal

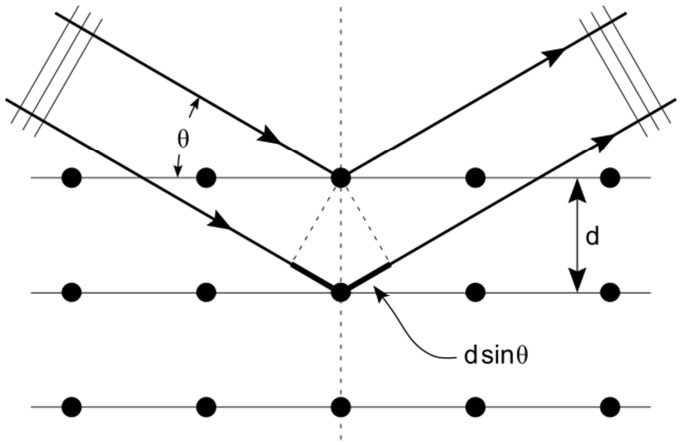

Figure 4.15: Interaction between an atom array in crystals and X-rays (borrowed from[10]**).**

Upon interaction, atoms' electrons scatter X-ray waves, producing secondary spherical waves emanating from the electron, known as elastic scattering. The electron is called the scatterer. A regular array of scatterers produces a regular array of spherical waves. Although these waves produced by the array of electrons cancel one another out in most directions (destructive interference), they will add constructively in a few specific directions established by Bragg's law:

$$2.\sin\theta = n.\lambda$$ **Equation 4.7**

where d is the spacing between diffracting planes, θ the incident angle, n an integer, and λ the wavelength of the beam. These specific directions, named reflections, appear on the diffraction pattern as spots or peaks. The pattern can be seen as a fingerprint for each material, and the material composition is determined by identifying the position of the peaks. XRD permits also to determine the crystallite size of particles using the Scherrer equation [11] (Equation 4.8):

$$\tau = \frac{K.\lambda}{\beta.\cos(\theta)}$$ **Equation 4.8**

where τ is the mean size of the ordered (crystalline) domains which may be smaller or equal to the grain size, K a dimensionless shape factor with a value close to 1 (typical value is about 0.9 and varies with the crystallite shape), λ the X-ray wavelength, β the Full Width at Half Maximum (FWHM), after subtracting the instrumental line broadening, in radians and θ the Bragg angle. The value of the Cu Kα radiation λ used for determination is 0.15406 nm and the K value is equal to 1. XRD has many advantages. It is a powerful and quite fast method to identify unknown materials, and in most cases the determination is unambiguous and relatively straightforward. Moreover a minimal sample preparation is necessary. However, as any technique, XRD has some limitations. For mixed materials, the detection threshold is below 2%, making the detection of minor secondary phases complicated. Usually other measurements are coupled to X-ray for secondary phase detection, such as thermal analysis or SEM.

The evolution of the crystallographic phase for each material was investigated by X-ray diffraction (XRD) using a solid state detector, 0.011 step size, and 0.5 s step time (Bruker D8, Cu Ka radiation). Diffraction patterns of powder resulting from the ink calcination at various temperatures were recorded.

4.2.3 Measurement of print dimensions and shrinkage

Precursor based inks such as reactive inks developed here are mostly composed of solvents. Upon heat treatment, the solvent evaporation will lead to high shrinkage, which is critical for the resulting film. Such size reduction can create cracks and delamination that can compromise the film integrity and properties. The measurement of film volumetric shrinkage here was determined by using 3D

profilometry. A 3D profilometer is a non-contact profiling system where a laser beam sweeps the surface of the sample and records the distance difference between the source and the sample. The sweep can be performed as a line (2D measurement) or a quadrilateral (3D measurement) and profiles/mapping can be obtained. This technology allows measuring the thickness of films and surface characteristics (roughness, waviness etc.) with high resolution (0.01 µm). Figure 4.16 shows example of profiles obtained with a 3D measurement.

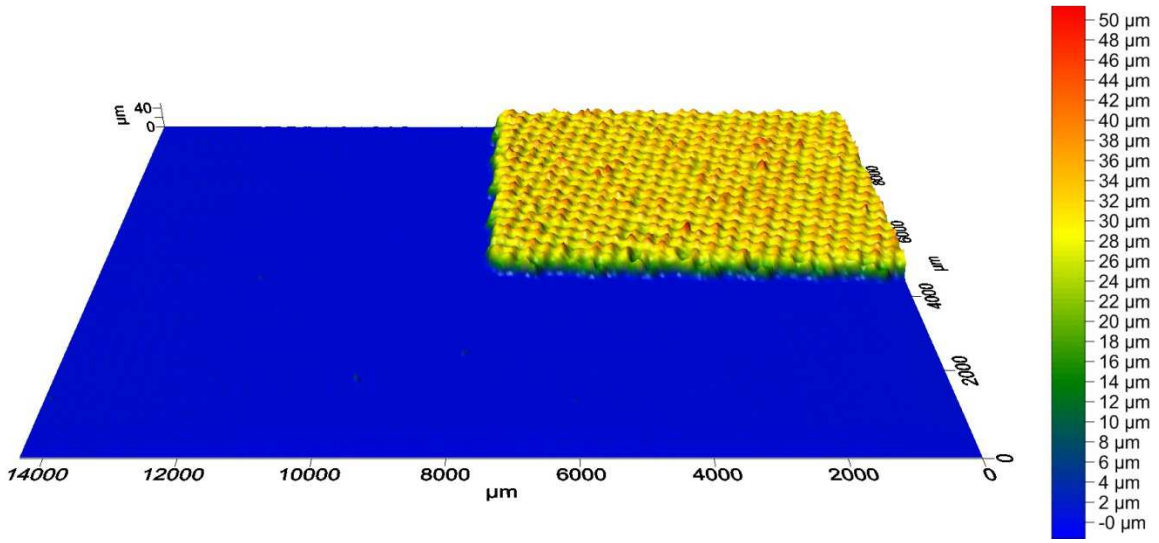

Figure 4.16: 3D profilometry mapping of a layer deposited by screen printed.

This method is fast, non-destructive, and reliable and micro-scale objects as wet, fragile, pliable or highly contoured can be characterized. One limitation of this technique is in the thickness measurement of the film. The film must be deposited on a flat substrate that is used as a reference for thickness evaluation which limits the choice of substrates for measurements. In this work, shrinkage of the films deposited by inkjet has been estimated by measuring the film dimensions (*x*-,*y*- and *z*-axis) by profilometry after heat treatment at different temperatures. Film surface and thickness characterization was carried out by using a high resolution 3D profilometer (Cyberscan, Vantage, using an LT9010 detector, a non-contact laser based method to analyze surfaces), shown of Figure 4.17

Figure 4.17: Picture of the Cyberscan Vantage profilometer.

The measured film dimensions were 5x5 mm^2 and the measurement step size was 50 µm for both *x*- and *y*-axis.

4.3 **Applied characterization**

4.3.1 Electrochemical impedance spectroscopy

Electrochemical impedance spectroscopy (EIS) is a measurement technique for the characterization of electrochemical systems. EIS permits with a single experimental procedure in a broad range of frequencies to isolate the influence of the governing physical and chemical phenomena at a given applied potential. Impedance is, similarly to a resistance, defined as the measure of the ability to of a circuit to resist to an electrical flow. Unlike resistance, it is not limited to an idea transistor. EIS consists in applying an alternative current (AC) at fixed frequency to a material, as bulk or thin film. The response is measured and the resulting impedance is computed at each frequency according to the following relation (Equation 4.9)

$$Z_w = \frac{E_w}{I_w}, \qquad \textbf{Equation 4.9}$$

where E_w is the frequency-dependent potential and I_w the frequency-dependent current. This method, though theoretically complex, is very powerful to characterize materials properties. EIS is able to distinguish several electrochemical reactions that take place at the same time, to give information about the capacitive behavior of the system or test components of an assembled system device using the electrode of the device.

As the measurement is performed using an alternative current, the excitation signal E_t as a function of time is expressed by (Equation 4.10)

$$E_t = E_0.\sin(\omega t) \qquad \textbf{Equation 4.10}$$

where E_t is the potential at time t, E_0 is the amplitude of the signal, and ω is the radial frequency in rad.s^{-1}($\omega = 2.\pi.f$, with f the frequency in Hz). The current signal obtained during the measurement is shifted (φ) and is expressed by (equation)

$$I_t = I_0.\sin(\omega t + \varphi) \qquad \textbf{Equation 4.11}$$

By reporting Equation 4.10 and Equation 4.11 in Equation 4.9, we obtain

$$Z_t = \frac{E_t}{I_t} = \frac{E_0.\sin(\omega t)}{I_0.\sin(\omega t + \varphi)} = Z_0 \frac{\sin(\omega t)}{\sin(\omega t + \varphi)} \qquad \textbf{Equation 4.12}$$

With Euler's equation, we have

$$\exp(j\varphi) = \cos(\varphi) + i.\sin(\varphi) \qquad \textbf{Equation 4.13}$$

Where φ is a real number and i is imaginary unit. By expressing the imdepdance as a complex function we obtain

$$E_t = E_0.exp(j\omega t) \qquad \textbf{Equation 4.14}$$

And

$$I_t = I_0.exp(j\omega t - \varphi) \qquad \textbf{Equation 4.15}$$

The impedance can then be represented as a complex number

$$Z(\omega) = \frac{E}{I} = Z_0.ex\,p(j\omega t) = Z_0(\cos(\varphi) + i.\sin(\varphi)) \qquad \textbf{Equation 4.16}$$

From Equation 4.16, the impedance can be plotted using the imaginary part Z_{im} vs the real part Z_{real} part of the impedance expression. Such diagram is called a Nyquist plot, and is shown on Figure 4.18 (a). Impedance can also be represented as the absolute value of impedance versus frequency. This plot is named Bode plot, and is shown on Figure 4.18 (b) as an example from [12].

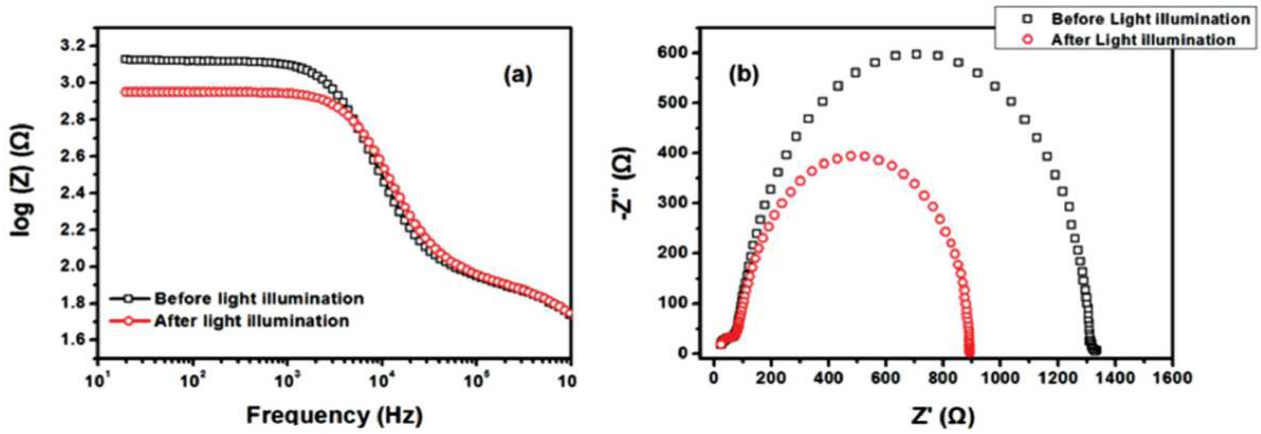

Figure 4.18: Representation of impedance by (a) Bode plot and (b) Nyquist plot (borrowed from [12]**).**

EIS is a powerful tool in to characterize the conductive properties of materials in an easy, nondestructive one time measurement. Application of this technique will be further developed with two examples of measurements that are discussed in this thesis: the measurement of a thin film electrical conductivity and of a dielectric constant.

4.3.1.1 Electrical characterization of thin films (Film conductivity)

The thin film conductivity is usually performed using in a symmetric 2-electrode configuration in which 2 conductive electrodes, usually silver, are painted on the surface of the considered film material. Such a configuration, showed on Figure 4.19 can be used to characterize the in-plane ionic conduction at the thin film samples on dielectric substrates [13,14].

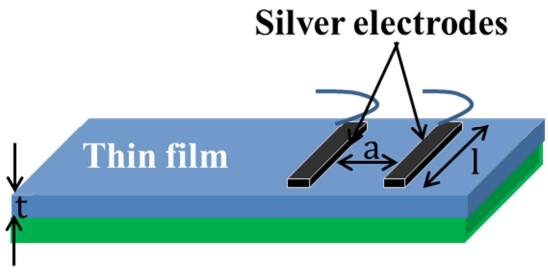

Figure 4.19: Setup of the symmetric 2-electrode configuration with gemometrical factors.

The substrate supporting the film needs to be dielectric to prevent measuring any extra contribution to the resistance of the film. An alternative current is applied and the impedance is measured between the two electrodes at different temperatures. The resulting conductivity σ is then calculated using the geometrical factor of the film (Equation 4.17).

$$\sigma = \frac{l}{R.a.t} \qquad \textbf{Equation 4.17}$$

where l is the length of the electrodes, a is the gap distance between the electrodes, R is the resistance of the film measured by EIS and t is the thickness of the film. R is evaluated by plotting the Nyquist plot obtained by EIS. The response observed in thin films is a semicircle, due to a single contribution. The resistance of the film is the value of Z_{im}at low frequencies. Conductivity at different temperatures is usually represented as a plot named Arrhenius plot which consist of $log_{10}(\sigma)$ versus $^{1000}/_{T}$, T being the temperature in Kelvin. An example of such diagram is showed on Figure 4.20.

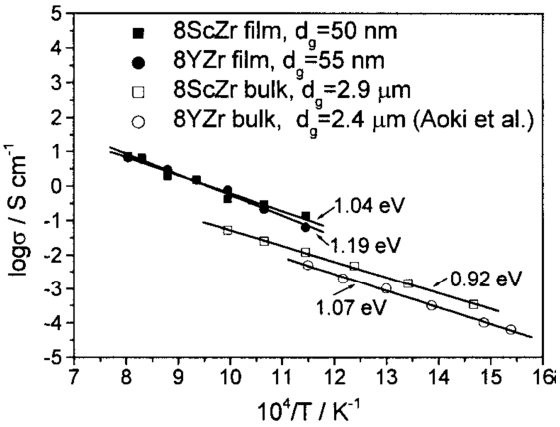

Figure 4.20: Example of Arrhenius plot of log σ vs 1/T for 8ScZr and 8YZr thin films and the corresponding bulk materials (borrowed from [15]**).**

Finally, the activation energy (E_a) is measured by EIS. The activation energy is defined by the minimum quantity of energy which the reacting species must possess in order to undergo a specified reaction. This value is specific to every material. However values can slightly differ for the same material depending on the material (bulk, thin film) and the microstructure. The activation energy is calculated using a different form of the Arrhenius equation described in Equation 4.18

$$k = A.e^{\left(-\frac{E_a}{R.T}\right)} \qquad \textbf{Equation 4.18}$$

Where k is a rate constant (here σ), R the gas constant (8.314 J·mol^{-1}·K^{-1}) and T the temperature (in K). By taking the natural logarithm of Equation 4.18 we obtain Equation 4.19

$$\ln \sigma = \ln(A) - \frac{E_a}{R.T} \qquad \textbf{Equation 4.19}$$

Equation 4.19 is plotted as $\ln(\sigma)$ *vs.* $^{1000}/_{T}$. A linear regression on such plot will give the slope that corresponds to $\frac{E_a}{R.T}$ and thus yields the value of E_a. An example is shown on Figure 4.21.

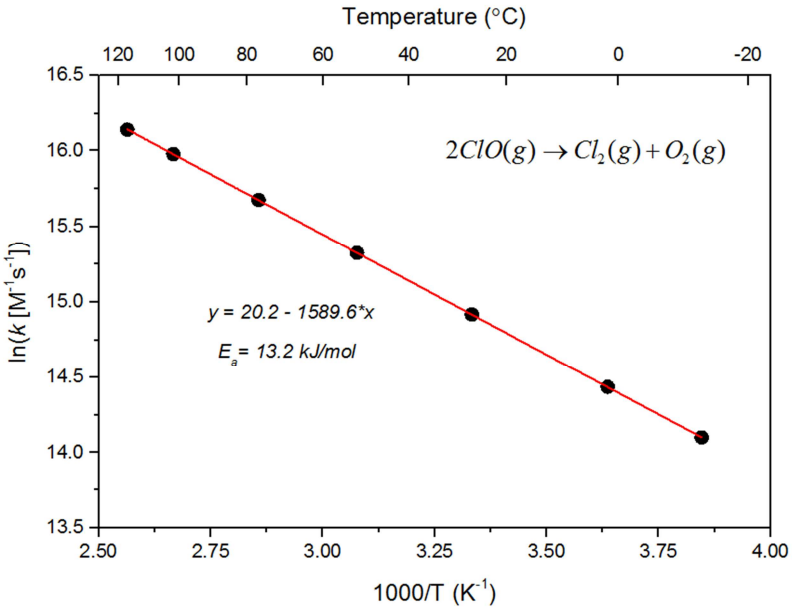

Figure 4.21: Example of activation energy calculation using EIS (borrowed from [16]**).**

Electrochemical impedance spectroscopy (EIS) was performed on thin films deposited by inkjet printing in a symmetric 2-electrode configuration by using a Solartron 1260 frequency response analyzer over the frequency range of 1 Hz–86 kHz. Due to the high impedance of the thin films in the lateral direction, 200mV AC voltages were used for the acquisition. Symmetric silver electrodes were painted on the surface to measure the lateral conductivity of the calcined samples, and gold wires were inserted in the electrodes before drying. Figure 4.22 shows a picture of the sample holder for the measurement along with a picture of the sample after electrode deposition.

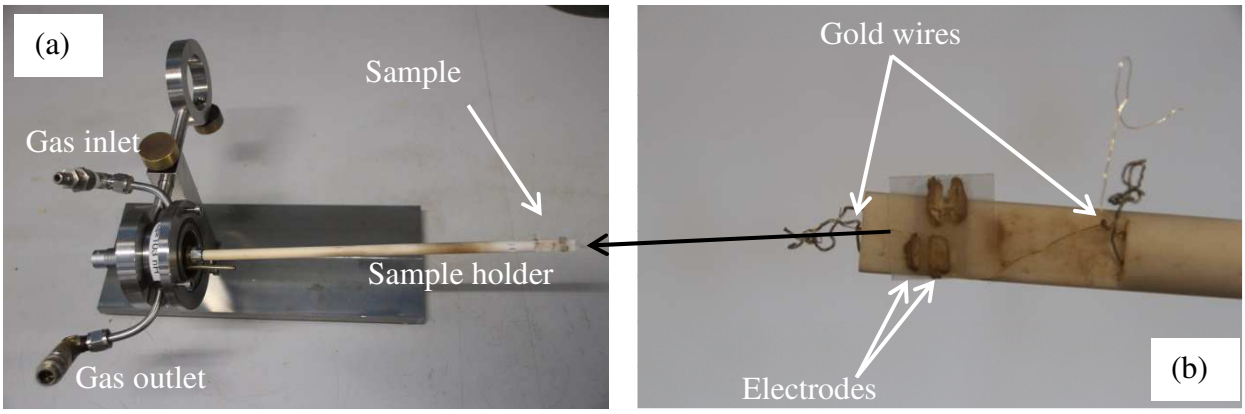

Figure 4.22: (a) Picture of the sample holder for EIS measurement and (b) close up picture of the sample before measurement.

The electrode dimensions were measured to be ca. 1 mm in distance and 2 mm in width. EIS measurements were performed in the temperature range of 525–750 °C in synthetic air flow (10 sccm).

4.3.1.2 Dielectric spectroscopy

Dielectric spectroscopy is determined by impedance spectroscopy measuring the dielectric properties of a material as a function of frequency [17,18]. The principle is based on the interaction between an external field and the electric dipole moment of the sample, often expressed by permittivity.

The capacitance of a material is defined Equation 4.20

$$C_p = -\frac{1}{\pi . f . Z_{im}} \qquad \textbf{Equation 4.20}$$

where f is the frequency (Hz) and Z_{im} the imaginary part of the impedance. The impedance is measured at room temperature at different frequencies. The dielectric constant is then calculated with Equation 4.21.

$$\varepsilon' = \frac{C_p . t}{A . \varepsilon_0} \qquad \textbf{Equation 4.21}$$

Where t is the thickness of the sample (m), A the electrode area (m^2) and ε_0 the vacuum permittivity (ε_0 = 8.85E-12 $F.m^{-1}$).

In this work, the dielectric constant of bismuth titanate was measured with this technique. The dielectric constant of pellets sample was measured with an Impedance/Gain-Phase Analyzer (Solartron 1260A, Solartron Analytical, UK). Pellets were fabricated by pressing powder by uniaxial hydraulic press and sintered. Symmetric silver electrodes were painted on the surface to measure the dielectric constant. All measurements were carried out in air at room temperature, in the frequency range of 100 Hz to 1 MHz and applied biasing voltage of 0.5 V.

4.3.2 Cell test

4.3.2.1 Gas leak testing

The leak testing system used in this study works by sealing a cell of 5.3 x 5.3 cm^2 in area. The half-cells, including the sintered ink-jet printed YSZ electrolyte, were tested before cathode deposition over a manifold connected to a vacuum system. In the test, the space beneath the cell was evacuated and the pump closed off. The flow of gas into the system was measured from the rate of pressure increase, measured by a barometric gauge. The test returns a measured vacuum leak as a pressure drop slope, which was compared with a fully dense reference. Leak measurements were also carried out by monitoring the cell voltage during electrochemical single cell testing as a function of the fuel flow rate, and are described below.

4.3.2.2 Test fixture

The electrochemical tests were carried out using an alumina test fixture with 0.8 mm and 2.1 mm recessions on the anode and cathode side, respectively. The recessions were 40 mm wide and 40 mm long. The cathode side was contacted using a custom alumina flow-field with 19 gas channels (1 mm wide) and 20 contact ribs (1 mm wide, except the outermost ribs which were 1.5 mm wide) clad with gold strip current collectors and fine gold meshes. The anode compartment seal was made using a thin (0.08 or 0.1 mm) Au foil cut into a frame and two alumina frames were placed on top of the cells (on the cathode side) to press the cell down onto the gold seal. The anode contact component was a flat Ni-mesh resting on a Ni flow field of the same design as the cathode alumina flow-field. Figure 4.23 shows an illustration of the gas distribution and sealing.

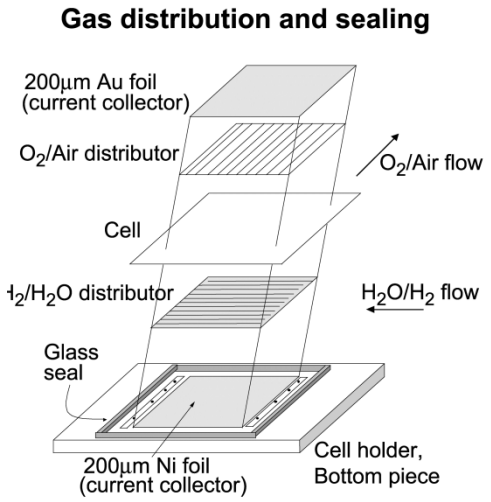

Figure 4.23: Illustration of the gas distribution and sealing (borrowed from [19]**).**

4.3.2.3 Electrochemical measurements

The electrochemical test was performed in a FuelCon test rig. Figure 4.24 shows an illustrated description and a picture of the rig.

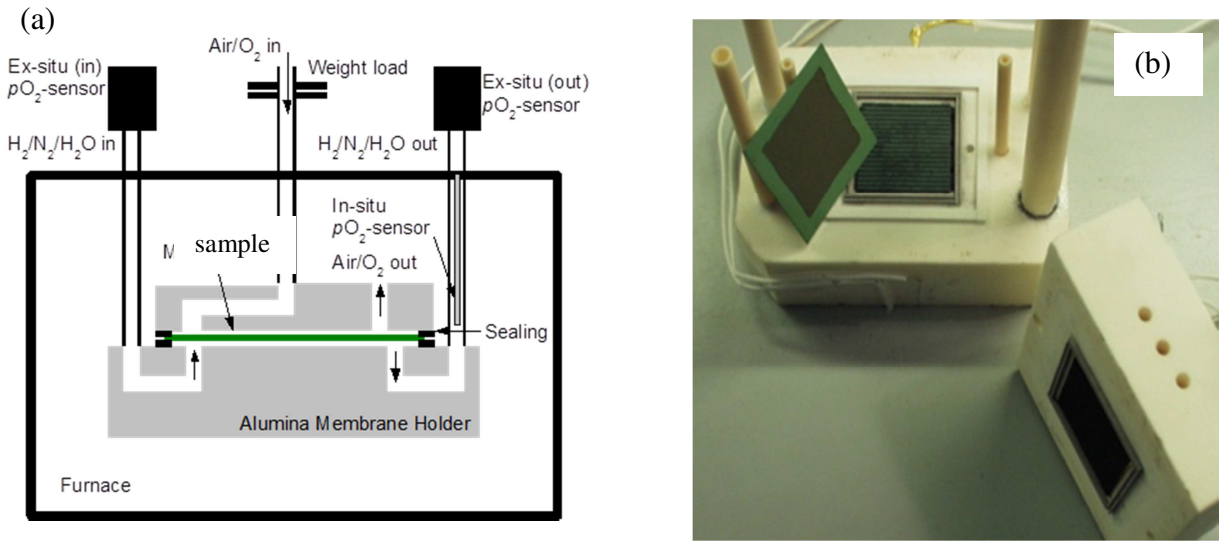

Figure 4.24: (a) Description of the rig and (b) picture of the sample holder with a fuel cell.

The sample is placed in the alumina membrane holder (Figure 4.24 (a) and (b)) sealed and placed into a furnace. Air is sent to the cathode side of the fuel cell and fuel is fed to the anode side. The impedance was recorded using a Solartron 1255B unit with amplitude of 60 mA (rms). The impedance data was collected from 96.9 kHz to 96.8 MHz with 12 points per decade. The cell voltage and voltage across the current shunt resistor (reference channel) were compensated (set to

zero) with custom-built electronic circuitry in order to maintain maximum resolution of the Solartron unit. I-V curve measurements were carried out using current steps with variable step lengths and step duration of 10 s. The leak testing system used in this study works by sealing a cell of 5.3 x 5.3 cm^2 in area. The half-cells, including the sintered ink-jet printed YSZ electrolyte, were tested before cathode deposition over a manifold connected to a vacuum system. In the test, the space beneath the cell was evacuated and the pump closed off. The flow of gas into the system was measured from the rate of pressure increase, measured by a barometric gauge. The test returns a measured vacuum leak as a pressure drop slope, which was compared with a fully dense reference. Leak measurements were also carried out by monitoring the cell voltage during electrochemical single cell testing as a function of the fuel flow rate.

Bibliography

[1] D. Marani, J. Hjelm, M. Wandel, Rheological analysis of stabilized cerium-gadolinium oxide (CGO) dispersions, J. Eur. Ceram. Soc. 34 (2014) 695–702. doi:10.1016/j.jeurceramsoc.2013.09.022.

[2] Maximum bubble pressure method, (n.d.). https://en.wikipedia.org/wiki/Maximum_bubble_pressure_method.

[3] A. Mudroch, Manual of Physico-Chemical Analysis of aquatic sediments, Lewis Publishers, 1997.

[4] No Title, (n.d.). https://www.shimadzu.com/an/powder/support/practice/p01/lesson22.html.

[5] HeNe Laser and APD in the Zetasizer, (n.d.).

[6] FTIR Spectroscopy principle, (n.d.). https://chemistry.oregonstate.edu/courses/ch361-464/ch362/irinstrs.htm.

[7] H.K.D.H. Bhadeshia, Thermal Analysis Techniques, (n.d.). https://www.phase-trans.msm.cam.ac.uk/2002/Thermal1.pdf.

[8] S. Vyazovkin, Thermogravimetric Analysis: A review, Analyst. 88 (2012). doi:10.1002/0471266965.com029.pub2.

[9] Signals in electron microscopy, (n.d.). https://nau.edu/cefns/labs/electron-microprobe/glg-510-class-notes/signals/.

[10] X-ray Crystallography, (n.d.). https://en.wikipedia.org/wiki/X-ray_crystallography.

[11] A. Monshi, Modified Scherrer equation to estimate more accurately nano-crystallite size using XRD, World J. Nano Sci. Eng. 2 (2012) 154–160. doi:10.4236/wjnse.2012.23020.

[12] W. Xu, R. Xia, T. Ye, L. Zhao, Z. Kan, Y. Mei, C. Yan, X.W. Zhang, W.Y. Lai, P.E. Keivanidis, W. Huang, Understanding the light soaking effects in inverted organic solar cells functionalized with conjugated macroelectrolyte electron-collecting interlayers, Adv. Sci. 3 (2015). doi:10.1002/advs.201500245.

[13] K. Mohan Kant, V. Esposito, N. Pryds, Strain induced ionic conductivity enhancement in epitaxial Ce0.9Gd0.1O2−δ thin films, Appl. Phys. Lett. 100 (2012) 16–20. doi:10.1063/1.3676659.

[14] S. Sanna, V. Esposito, J.W. Andreasen, J. Hjelm, W. Zhang, T. Kasama, S.B. Simonsen, M. Christensen, S. Linderoth, N. Pryds, Enhancement of the chemical stability in confined δ -Bi 2 O 3, Nat. Mater. 14 (2015) 1–5. doi:10.1038/NMAT4266.

[15] Y.W. Zhang, S. Jin, Y. Yang, G.B. Li, S.J. Tian, J.T. Jia, C.S. Liao, C.H. Yan, Electrical conductivity enhancement in nanocrystalline thin films, Appl. Phys. Lett. 77 (2000) 3409–3411. doi:10.1063/1.1328099.

[16] No Title, (n.d.). http://blog.originlab.com/graphing/display-celsius-as-top-axis-in-arrhenius-plot.

[17] F. Kremer, A. Schonals, W. Luck, Broadband Dielectric Spectroscopy, Springer-Verlag, 2002.

[18] A.. Hippel, Dielectric and waves, John Wiley and Sons Ltd, 1954.

[19] S.H. Jensen, A. Hauch, P.V. Hendriksen, M. Mogensen, Advanced Test Method of Solid Oxide Cells in a Plug-Flow Setup, J. Electrochem. Soc. 156 (2009) B757. doi:10.1149/1.3116247.

Chapter 5 : Preliminary research on colloidal inks

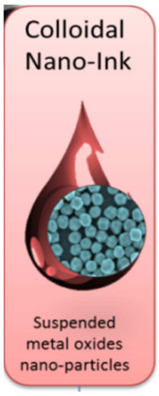

The work described in this chapter was performed before the PhD project started and was used as a background work for the research described in chapter 6 and 7. As mentioned in chapter 1, this work should not be considered for examination. Here, the fabrication and development of these inks for inkjet printing was demonstrated through the fabrication of thin dense electrolyte layers for SOFC based on YSZ. In a first part the Ink printability and stability at different solid loadings were assessed by rheological characterization and particle size measurement. The inks were then deposited on porous NiO/YSZ substrates and the performances of the HP thermal inkjet printer (HP Deskjet 1000) as a printing unit were assessed. Layers microstructure at different temperatures was studied by SEM. Finally electrochemical performances of a fuel cell using such electrolyte are detailed. This chapter contains results and discussions of a paper published in "*Journal of power sources*" before the PhD project started. The article can be found in the appendix section for further reading (p.223).

5.1 **Ink fabrication and characterization**

Colloidal inks present several advantages for the deposition of films. In addition to being easy to process and cheap, the starting material is already crystalline, particles can cover substrate porosity to yield a defect-free film, and the final film thickness can be easily controlled by changing the solid loading. However these inks can be problematic to process with inkjet printing. The first main issue is the particle size distribution. To avoid clogging of the print head nozzle the particle size should preferably be less than 10% of the nozzle diameter, while the optimal value has been estimated to be around 2% [1]. For instance, The cartridges used in the HP-Deskjet 1000 having a nozzle diameter of around 20 μm diameter, the ink particle size has to be less than (20 . 2%) = 400 nm and show stability over time not to clog while printing. Particle stabilization has to be achieved through addition of a dispersant in the suspension. These chemicals are usually the most viscous component of the mixture, and their content will strongly affect printability. Finally, the ink solid loading is a crucial factor to consider. Not only the solid loading influences the printability through rheological behavior, it also affect the continuity of the film after drying and sintering.

5.1.1 Ink fabrication

An ink was prepared using commercial 8YSZ (8mol % Yttria, TOSOH) nanometric powder. The powder was suspended in a mix of 80 wt.% water and 20 wt.% ethanol. The powder was added to the liquid medium at two concentrations: 3.7 vol% (20 wt%, called "concentrated ink") and 0.9 vol% (6 wt%, called "dilute ink") of YSZ. Typical solid loading concentrations in colloidal inks for inkjet applications are below 10 vol.% [2]. The dilution in these inks was kept high with the aim to produce thin layers. Small particles are ideal for such diluted inks and small particles are usually easily dispersed in the liquid media. Polyvinylpyrrolidone (PVP), dissolved in 53% weight ratio in pure ethanol, was used as dispersant and added into the YSZ suspension at ca. 8 mg/m^2 of solid surface area. All constituents were then milled in a rotational mill in a PET flask at 100 rpm using zirconia milling balls for 10 days.

5.1.2 Particle size measurement

After preparation, inks particle size distribution was characterized. Figure 5.1 shows the particle size of both inks after milling for 9, 10 and 100 days.

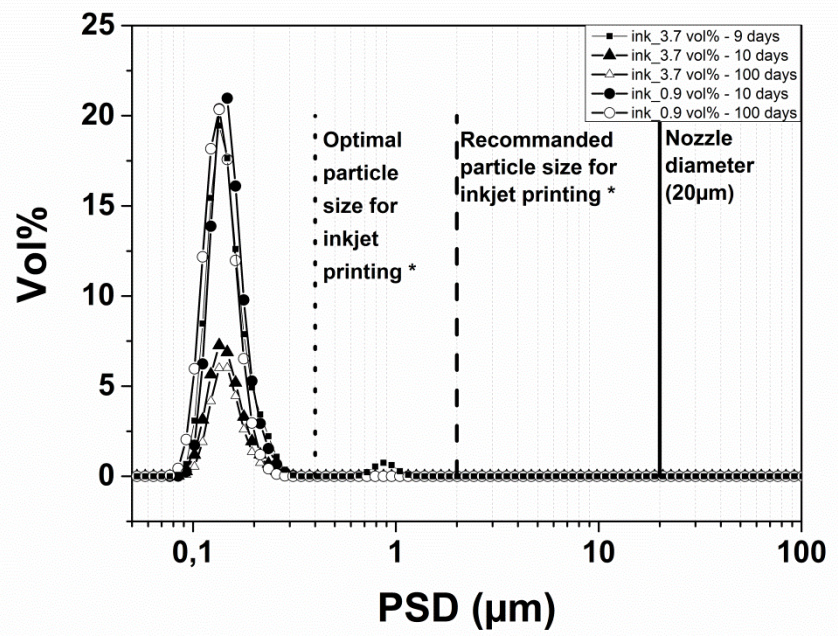

Figure 5.1: Particle size distribution for the YSZ ink at low (3.7 vol. %) and high dilution (0.9 vol.%) after milling for 9 and 10 days, and after 100 days of storage.

Figure 5.1 shows the typical particle size distribution within the range of 0.06 and 0.34 µm with a max at around 100 nm. Such nanometric powders exhibited high stability with no precipitation and

preserving the same distribution even after 100 days of storage. Figure 5.1 show that the measured particle size for both inks is compatible with optimal recommendations for inkjet printing to avoid clogging, estimated to be around 2% of the nozzle diameter. Cartridges for HP-Deskjet 1000 have a nozzle diameter of around 20 µm diameter which for a maximum particle size of 0.34 µm corresponds to (0.34 µm /20 µm) = 1.7 %. However a small peak around 1 µm is visible after 9 days of milling. This peak disappears after an extra 24 hours of milling (10 days) and does not reappear after 100 days. While this peak is still in the optimal printing zone, these particles around 1 µm diameter are a threat to proper printing and can lead to clogging. While the obtained inks have a satisfactory particle size for inkjet printing, these measurements highlight a clear disadvantage of using colloid, *i.e.* a long and intense milling is necessary to obtain suitable particle size distribution for inkjet printing.

5.1.3 Printability

The ink printability was assessed by measuring inks viscosity, surface tension and density. Figure 5.2 shows the flow curves for the two inks with the correspondent viscosity curves (inset).

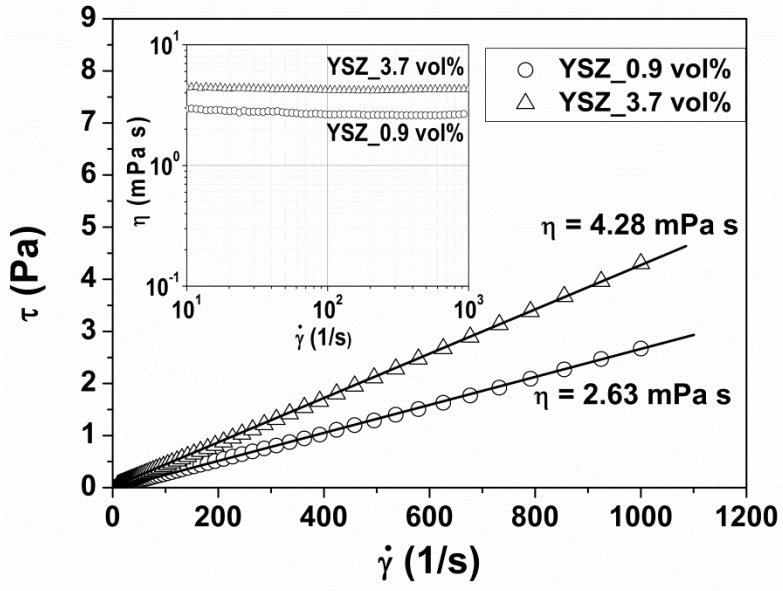

Figure 5.2: Flow curves and viscosity curves (inset) for the two YSZ developed inks.

Both inks exhibit Newtonian behavior with a constant viscosity independent of the shear rate (inset). The viscosity values were calculated from the slope of the flow curves. The values obtained were 4.28 mPa.s for the 3.7 vol% ink and 2.63 mPa s for the 0.9 vol % ink. These values are usually considered suitable for a thermal DoD inkjet system [2]. The surface tension of the ink was

measured using a bubble pressure tensiometer and yielded a value of 36 $mN.m^{-1}$. The inks density was measured and the value was close to 1 for both solid loadings. The properties of the developed inks are summarized in Table 5.1.

Table 5.1: Inks properties.

	Loading	η	σ	ρ	Z
	Vol%	mPa·s	$mN.m^{-1}$	$g.cm^{-3}$	-
20 wt%	3.7	4.28	36.4	1.14	6.73
6 wt%	0.9	2.63	36.2	1.01	10.28

A *Re vs We* graphic (as described in section 2.2.2, p.18) was plotted for both inks. As the velocity of the droplets could not be measured on the HP printer, The *We* and *Re* numbers were calculated within the typical reported range of values for the drop velocity (1-30 $m.s^{-1}$) [3].

Such a diagram is displayed in Figure 5.3 and shows that the *We* and *Re* values calculated for the two developed inks are within the identified printability region defined by Derby ($1<Z<10$) and Jang ($4<Z<14$). The properties of both inks are compatible with inkjet printing requirements and inks are thus ready to be deposited.

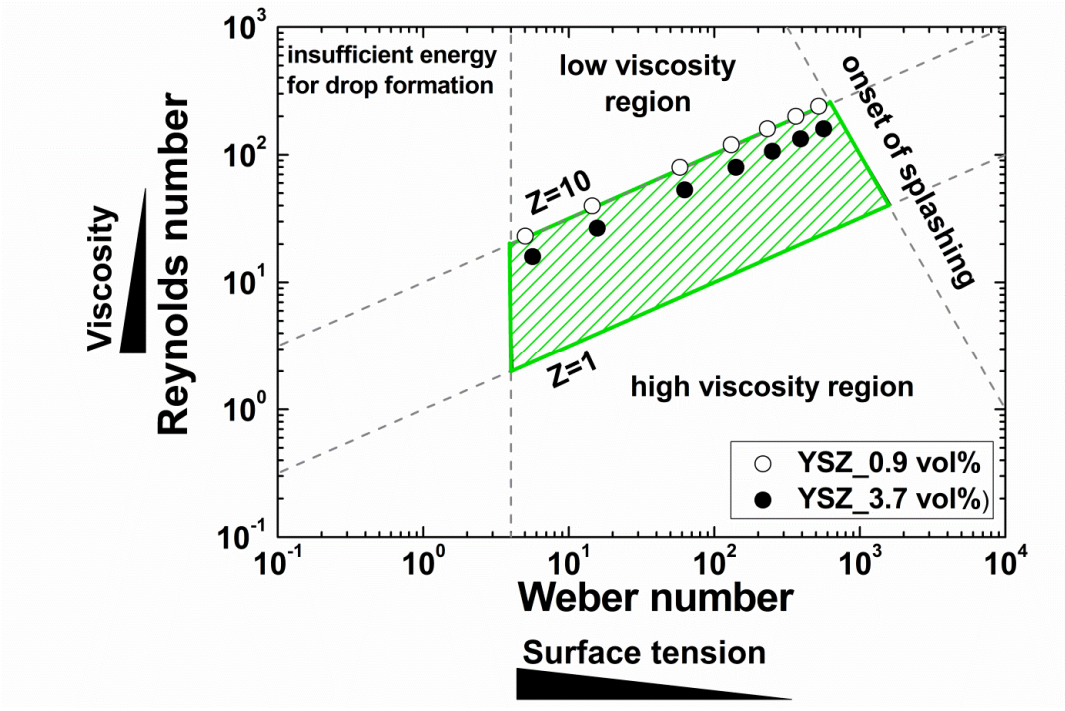

:

Figure 5.3: Weber-Reynolds numbers diagram defining the regime for ink properties which ensure good printing characteristics. This diagram has been proposed by Derby [4]**.**

5.2 **Characterization of inkjet printed layers**

5.2.1 Inkjet printing of the YSZ electrolyte

The ability of the low-cost printing unit to reproducibly deposit droplets was investigated using the optimized inks developed in the previous part. The use of a low-cost inkjet process for the fabrication of a continuous layer can lead to formation of some critical flaws. Particularly, since each single layer is formed drop by drop, any alignment errors and/or lack of deposition (missing drops) during the printing create discontinuity in the layer. For this purpose two printing procedures were used for the printing:

- "Single Droplets" printing (SD), consisting in printing isolated droplets using a square-chess-like pattern, it was aimed to control the quality of the single droplet or presence of flaws in the DoD printing;
- "Continuous Printing" (CP), consisting in printing droplets one after the other sequentially in lines, it was used to print a continuous layer. Additive depositions were carried out on the CP pattern, depositing a layer on top of the other, up to 5 times.

The patterns were created on the software Microsoft Word and are showed on Figure 5.4.

(a) (b)

Figure 5.4: (a) "single droplets" and (b) "continuous printing" patterns used for deposition of colloidal inks.

After deposition the resulting patterns (SD) and layers (CP) were sintered at 1300°C. This temperature is the classical sintering temperature used to obtain dense YSZ layers [5] and was chosen so the printed patterns and layers would become dense. As such the presence of any "defects" such as cracks, pores, pinholes would then be due to the printer and not the film.

Figure 5.5 (a)-Figure 5.5 (d) show the typical flaws observed by SEM after printing and sintering of the diluted and concentrated YSZ inks.

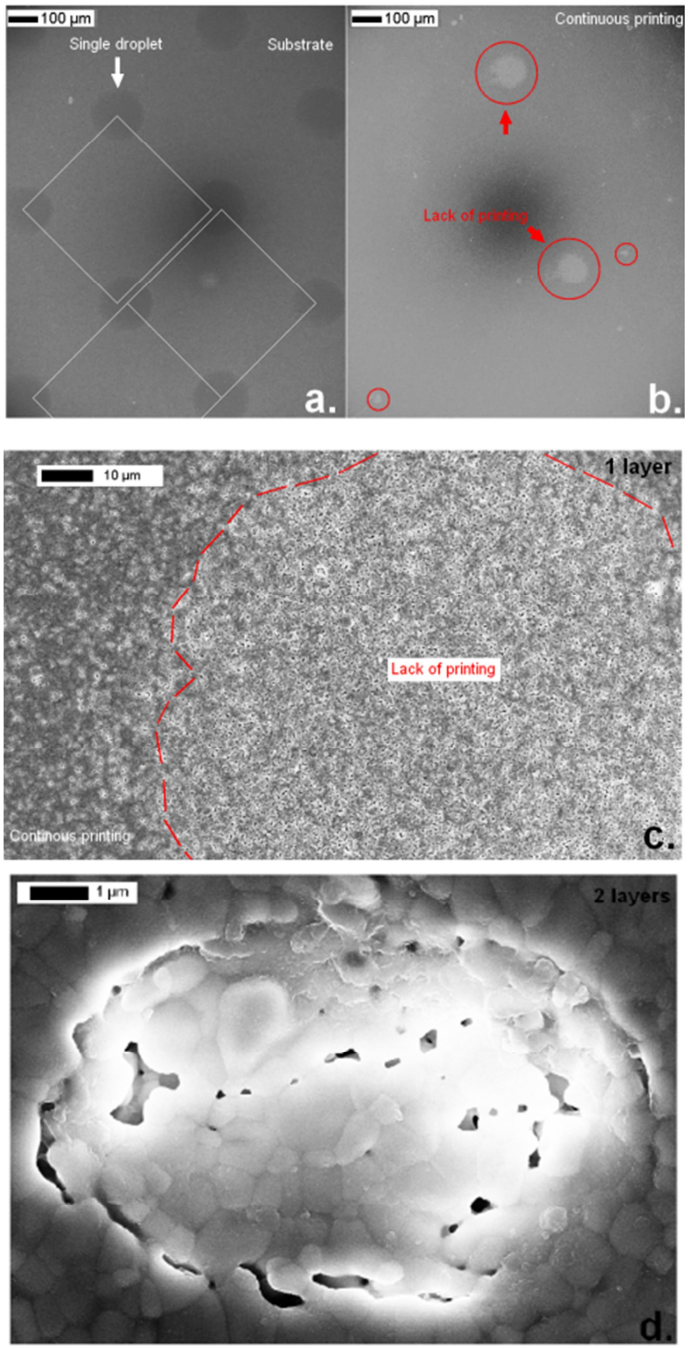

Figure 5.5: SEM observations of the YSZ printings, after sintering at 1300 °C for 5 minutes. (a) 0.9 vol% ink printed as single droplets, (b) continuous print using the 3.7 vol% ink. (c) high magnification of printing flaw shown in (b). (d) typical defect on a two layer deposition.

Figure 5.5 (a) shows the typical alignment of the droplets obtained by inkjet (SD) of the highly diluted ink (0.9 vol% of YSZ loading) after sintering at 1300 °C for 6 hours. The SEM observations on the layers produced using single droplet printing (SD) indicated that, although the droplets were designed in an ordered pattern, a certain misalignment in the range of few micrometers occurred for some of the droplets (see white squares superimposed in Figure 5.5 (a)). This effect is possibly associated with the lack of precision in the mechanical movement system. This misalignment can lead to discontinuous single layer. Figure 5.5 (b) and (c) show the results of continuous printing (CP) of a single layer of the concentrated (3.7 vol% of YSZ loading) ink. The figures show evidence of missing droplets in several areas of various sizes and shapes, probably caused by an imprecise impact of the droplets on the substrate, a defective droplet formation at the nozzle or presence of imperfections at the substrate surface (red circles). The bright area in Figure 5.5 (c) corresponds to the slightly porous surface of the substrate and red lines are superimposed to highlight the edges of the defect. Presence of porosity around the edge could be observed, suggesting an excessive dilution of the ink at the boundary between the drops. Covered areas however showed homogeneity and a high degree of packing of the particles which led to densification of the layer after sintering at 1300 °C. No coffee-stain rings or other particle agglomeration effects were detected in the samples, which confirm the suitable printing characteristics of the developed inks. However, the presence of several defects detected at the CP single layer highlights the need for using a multiple-printing approach to fabricate a gas-tight electrolyte with the present printing technology. To verify this hypothesis, a layer consisting of two printing passes was made with the same ink (3.7 vol%) and sintering condition than layer showed on Figure 5.5(b)-(c). A waiting time of around 15 seconds between each print was necessary to allow the solvent in the ink to evaporate and the print to dry. Figure 5.5 (d) shows a typical SEM of the 2-layer deposition by the 3.7 vol% ink after sintering at 1300 °C for 6 hours. Particularly, the picture shows the filling-in of a small defect in the first layer by the second print-pass. The particles in the flaws exhibited sintering with presence of residual porosity. This effect can possibly be attributed to an excessive dilution on the solid, where the low concentrations of the material can only partially cover the defect. This effect generated porosity and resulted in a discontinuous layer. Increasing the number of print-passes (depositions) should minimize this issue.

5.2.2 Sintering of the layers

As shown in Figure 5.1, the printed layers are made of submicronic particles. Such particles have a high surface area and it results that their sintering temperature can be lower than the one usually used for larger particles, i.e. 1300°C. By lowering the sintering temperature, a larger choice of substrates could be available for the deposition of the electrolyte. The microstructure of the printed layer (CP) of concentrated ink after exposition to various sintering temperature was studied by SEM to determine the sintering temperature for which dense films are obtained. Figure 5.6 (a) - (c) show the particles sintered at 1000 °C, 1150 °C and 1300 °C for 6 minutes.

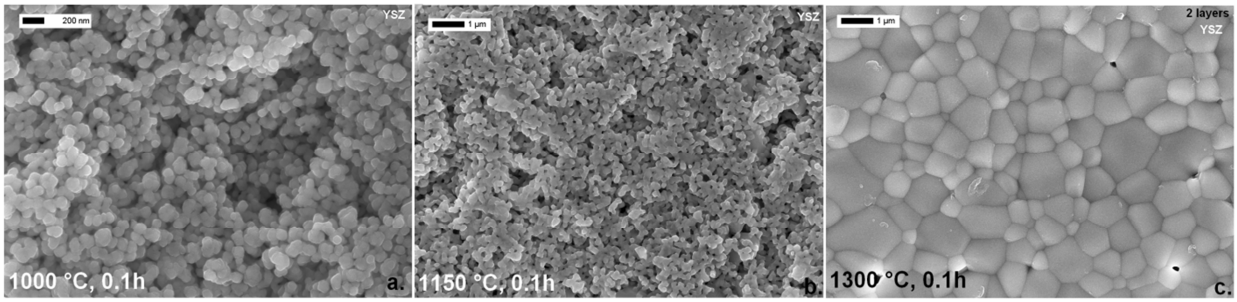

Figure 5.6: SEM observations of the YSZ printings by the 3.7 vol% ink. (a) Continuous printing sintered at 1000 °C for 6 minutes, (b) 1150 °C for 6 minutes, (c) 1300 °C for 6 minutes.

Figure 5.6 (a) shows that, at 1000 °C, the YSZ particles in the deposit are of a round shape and with a homogenous size of ca. 100 nm. The packing is rather high with no agglomeration. Figure 5.6 (b) shows that at 1150 °C the YSZ particle are connected by the typical necking, indicating an incipient sintering at the layer with formation of small and larger porosity (below 1 µm), where the latter probably was due to the voids as shown in Figure 5.6 (a) . The result after sintering at 1300 °C is shown in Figure 5.6 (c). The figure clearly shows that the treatment led to a full densification and grain growth. The original particles grew to the micrometer range and the resulting layer was rather dense with annihilation of all the porosity, including the voids in Figure 5.6 (b).

Figure 5.7 (a) and (b) show the cross-section at the half cells, after sintering at 1300 °C for 6 hours, for 2-layer and 5-layer depositions using the 3.7 vol% ink.

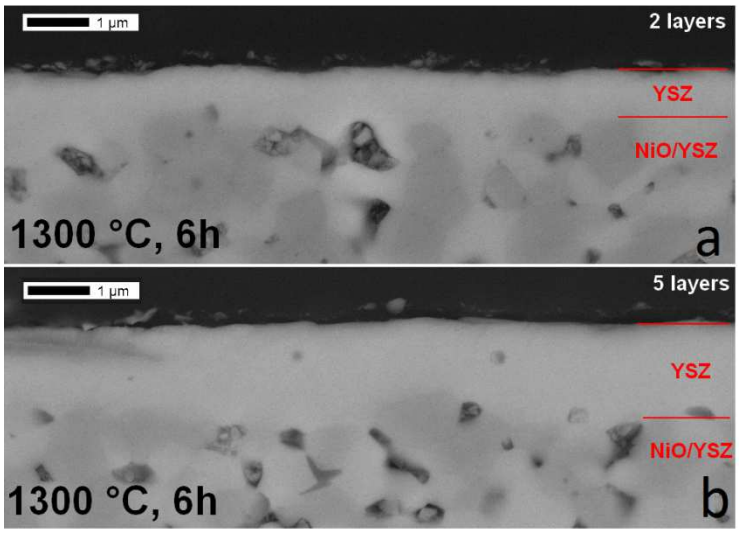

Figure 5.7: SEM observations of the YSZ printings cross section pictures of the half cells made by of (a) 2-layer and (b) 5-layer depositions after sintering at 1300 °C for 6 hours.

Both resulting layers are dense and homogenous and typical thicknesses of *app.* 0.6 µm and 1.2 µm were estimated for the 2-layer and the 5-layer samples, respectively. The relation between the thickness and number of depositions/print-passes was found to be non-linear. This was attributed to heterogeneous roughness of the substrate surface and to the lack of deposition of the continuous printing.

To further characterize the tightness of the printed layers leak tests were carried out with the sintered 5x5 cm^2 half cells. Table 5.2 shows that leak test performed on the 2-layer electrolyte exhibits a measured pressure slope value similar to the reference pressure slope, indicating insufficient electrolyte gas tightness.

Table 5.2: Leak test results and thickness measurements of 2-layer and 5-layer electrolyte half cells.

	Number of printed layers	*Sintering conditions*	*Reference pressure slope*	*Measured pressure slope*	*Electrolyte thickness*
	-	mPa·s	$mN.m^{-1}$	$g.cm^{-3}$	µm
2-layer	2	1300°C /6h	0.460403	0.460339	0.6
5-layer	5	1300°C/6h	0.460403	0.079086	1.2

The pressure slope measured with the 5-layer electrolyte was very low compared to the reference (sheet of steel), indicating a high tightness of the electrolyte.

5.3 **Performance**

Two SOFCs with a 2-layer and a 5-layer electrolyte, respectively, were manufactured with a 4x4 cm^2 active area defined by the cathode. The cathode ink was deposited by screen printing onto the electrolyte. The cathode ink was a mixture of $La_{0.75}Sr_{0.25}MnO_{3-\delta}$ (LSM) and YSZ (LSM/YSZ=50/50 vol. %). The printing speed used was 60 mm/s, the printing gap was 1 mm and the squeegee pressure was 7 bar. The printed cathode layers were then sintered at 1050°C for 2 hours. A LSM cathode contact layer has then be screen printed on top of the cathode layer using the same printing described above and sintered at 1000°C for 5 hours.

The cell produced with the 2-layer electrolyte was not leak tight and open circuit voltages of less than 0.7 V were observed in dilute (9%) hydrogen. Moreover, the electrolyte gas tightness decreased rapidly during the test, most likely due to re-oxidation of the Ni-cermet anode. This is in agreement with the ex-situ leak testing that was carried out and reported in the previous section. The cell with the 5-layer electrolyte was significantly more leak tight. Open circuit cell voltages in the range 1.07 – 1.15 V were observed in dry hydrogen fuel at flow rates in the range 6.7 – 31.7 ml min^{-1} cm^{-2}, as can be seen in Figure 5.8.

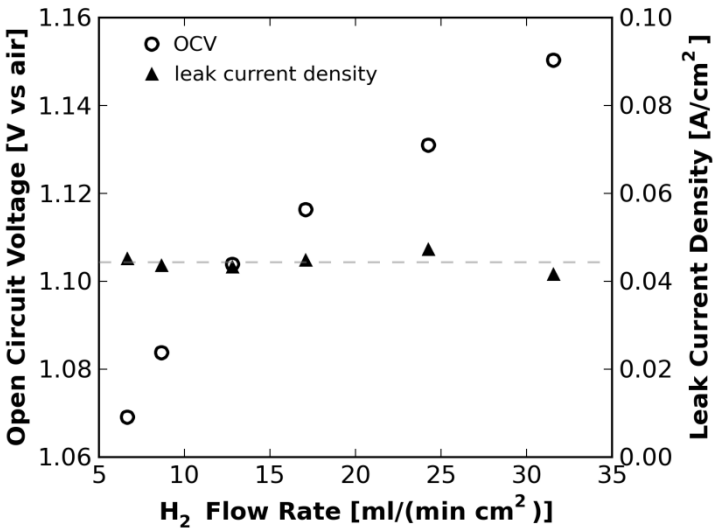

Figure 5.8: Observed open circuit cell voltage (open circles) and calculated total leak current density (according to Rasmussen et al., filled triangles) of 5-layer electrolyte SOFC operates with dry hydrogen supplied as fuel at the indicated flow rates and air as the oxidant. The dotted horizontal line represents the average leak current density (0.044 A.cm^{-2}), calculated using the active area of the cell (= 16 cm^2).

The leak was quantified by calculation of a total leak current, a measure of the total leak, both external (e.g. through seals and anode support) and internal (electrolyte pinholes, cracks), using the relations derived by Rasmussen et al. [6]. No systematic variation of the leak current with the fuel flow was observed, indicating the absence of large cracks or holes in the cell or the sealing gasket used on the anode side. Polarization curves were recorded at operating temperatures in the range from 850 °C down to 650 °C with 50 °C increments. Figure 5.9 shows polarization and power curves for the 5-layer electrolyte SOFC.

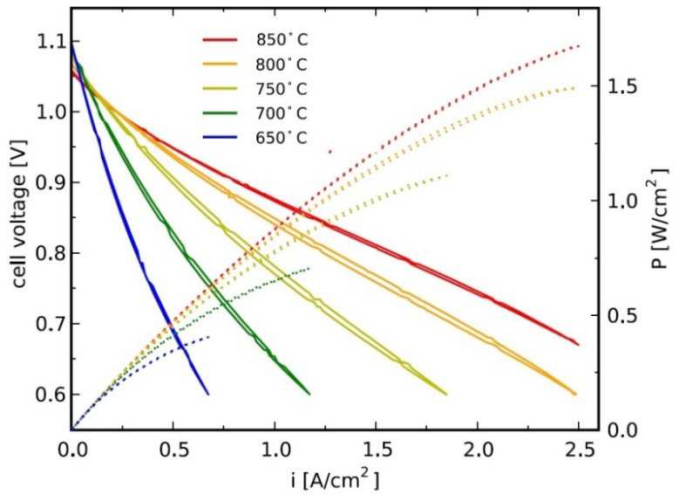

Figure 5.9: Polarization curves recorded for the 5-layer electrolyte SOFC (active area = 16 cm^2) which was tested with a composite LSM-YSZ cathode and a LSM current collection layer. The fuel was 96% H_2 and 4% H_2O supplied at a total flow rate of 26 $ml.min^{-1}.cm^{-2}$. The lower voltage limit was set to 0.6 V and the maximum current limit to 2.5 $A.cm^{-2}$ (40 A).

At 750 °C the area specific secant resistance was 0.26 $\Omega \cdot cm^2$ (0.21 $\Omega \cdot cm^2$ after correction for fuel utilization) and the observed power density at 0.6 V was 1.2 $W \cdot cm^{-2}$ [7].The theoretical area specific resistance contribution from a 1.2 µm thick 8YSZ layer is 0.004 $\Omega \cdot cm^2$ at 750 °C based on bulk conductivity data for 8YSZ [8]. An ohmic resistance of approximately 0.05-0.06 $\Omega \cdot cm^2$ was observed at 750 °C (see Figure 5.10).

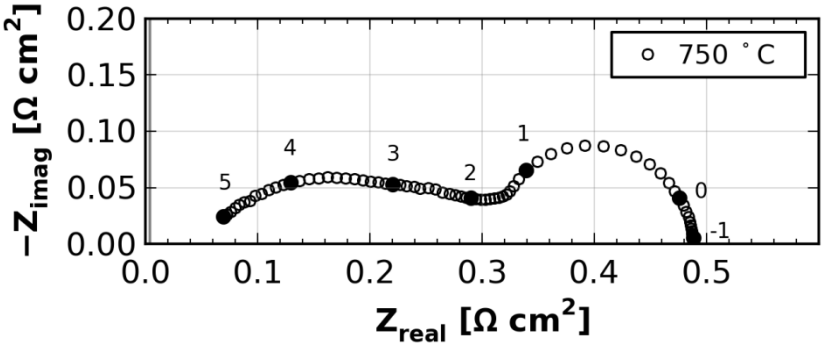

Figure 5.10: Nyquist plot of the electrochemical impedance spectrum recorded with the 5-layer electrolyte SOFC at 750 °C and with 96% H_2 + 4% H_2O as fuel and air as the oxidant. The impedance data was collected with 12 points per decade, indicated in the figure by filled symbols (also marked with the logarithm of the frequency), starting at 96.9 kHz (at low Zreal values). The dashed grey line indicates the theoretical resistance of the 1.2 µm thick 8YSZ electrolyte based on bulk conduction properties. The data in the plot was corrected for lead inductance.

This is more than ten times greater than the theoretical resistance expected from the electrolyte layer in the tested cell, but on the other hand a quite similar offset of 50-60 mΩ·cm^2 is often seen and has previously been reported with a 10 µm thick ink-jet printed YSZ electrolyte [9]. Additionally, the cathode deposition method was reported to affect the series resistance [9]. Explanations to the observed high series resistance could be limited measurement range (the maximum frequency was 96.5 kHz). Other contributions to the observed ohmic resistance could be imperfect contacting of the electrolyte by the cathode layer, current constriction, or secondary phases formed at the interface [10]. Significant current collection losses are deemed unlikely as a sufficiently conducting current collection layer was used.

The ohmic resistance observed in electrochemical impedance spectroscopy can be assigned to the electrolyte, if it is measured to sufficiently high frequency, and assuming that there are no additional contributions to the ohmic resistance from current collection and the porous composite electrodes. Sufficient conductivity in the cathode current collection layer was confirmed by in-plane van der Pauw conductivity measurements [11]. Even though the observed ohmic resistance was much higher than the theoretical value, most of the impedance of this cell is related to the electrodes, and by improving the electrodes and ensuring a better contact to the electrolyte, a significant reduction in both ohmic and polarization resistance can be expected. This highlights the potential performance gain of cells with thin electrolyte, and further supports the feasibility of ink-jet based printing techniques for production of solid oxide cell components.

5.4 **Conclusion**

In this work, we present how a low-cost thermal HP Deskjet 1000 inkjet printer was used to fabricate a 1.2 µm thin, dense and gas tight 16 cm^2 solid oxide fuel cells (SOFC) electrolyte. The electrolyte was printed using a colloidal ink made of highly diluted (<4 vol.%) nanometric yttria stabilized zirconia (YSZ) powders (50 nm in size) in an aqueous medium. The ink was designed to be a highly dispersed, long term stable colloidal suspension, with optimal printability characteristics. Missing droplets and imprecise impact on the anode substrate were observed to produce areas with lack of deposition when printing single layers. Inks with low dilution and nanometric particles improve printability and stability, however printing of multiple layers seems necessary to cover the defects formed during single layer printing. 2 layers were insufficient, but 5 layers resulted in a gas tight electrolyte. Together with an optimized sintering procedure this resulted in good adhesion and densification of the electrolyte. The SOFC exhibited a close-to-theoretical open circuit voltage and a remarkable peak power density above 1.5 W cm^{-2} at 800°C. This work showed the interest of designing colloid inks, but also brought their weaknesses to light, such as a restrictive particle size, long processing time and high sintering temperature to reach full densification. To solve these issues, a different type of ink, based on free-particles solutions were designed and are presented and discussed in the next chapter.

Moreover the results showed that while the customized inkjet printer allows the deposition of thin layers, it suffers from several limitations: droplet deposition misalignment was observed, probably due to its low cost, and multilayer printing was necessary to overcome this misalignment. Another drawback from this printer is the lack of control of droplet ejection and of drop-view camera to detect clogged nozzles. As thermal printers are generally designed for paper printing in households and offices, it is not surprising that these expensive features are not available. However these tools are essential to have more control over the process and optimizing it and are available on piezoelectric based printers. In the rest of the studies, piezoelectric printers will be used to study the ink in more details. The thermal printer will still be used as printing unit to demonstrate the ink versatility in terms of droplet ejection.

Bibliography

[1] I.M. Hutchings, Inkjet technology for digital fabrication, Wiley, 2013.

[2] Helmut Kipphan, Handbook of Print Media, 2001.

[3] A.L. Yarin, Drop Impact Dynamics : Splashing , Annu. Rev. Fluid Mech. 38 (2006) 159–192. doi:10.1146/annurev.fluid.38.050304.092144.

[4] B. Derby, Inkjet printing of functional and structural materials: fluid property requirements, feature stability, and resolution, Annu. Rev. Mater. Res. 40 (2010) 395–414. doi:10.1146/annurev-matsci-070909-104502.

[5] M. Han, X. Tang, W. Shao, The properties of YSZ electrolyte sintering at 1300 °c, J. Wuhan Univ. Technol. Mater. Sci. Ed. 23 (2008) 775–778. doi:10.1007/s11595-007-6775-6.

[6] J.F.B. Rasmussen, P. V. Hendriksen, A. Hagen, Study of Internal and External Leaks in Tests of Anode-Supported SOFCs, Fuel Cells. 8 (2008) 385–393. doi:10.1002/fuce.200800019.

[7] M. Mogensen, P.V. Hendriksen, Testing of Electrodes , Cells and Short Stacks, in: S.. Singhal, K.Kendals (Eds.), High Temp. Solid Oxide Fuel Cells, Elsevier Science, 2003: pp. 261–289.

[8] C.C. Appel, N. Bonanos, A. Horsewell, S. Linderoth, D.- Roskilde, Ageing behaviour of zirconia stabilised by yttria, J. Mater. Sci. 6 (2001) 4493–4501.

[9] M. a Sukeshini, R. Cummins, T.L. Reitz, R.M. Miller, Ink-Jet Printing: A Versatile Method for Multilayer Solid Oxide Fuel Cells Fabrication, J. Am. Ceram. Soc. 92 (2009) 2913–2919. doi:10.1111/j.1551-2916.2009.03349.x.

[10] D.Z. de Florio, R. Muccillo, V. Esposito, E. Di Bartolomeo, E. Traversa, Preparation and Electrochemical Characterization of Perovskite/YSZ Ceramic Films, J. Electrochem. Soc. 152 (2005) A88. doi:10.1149/1.1824043.

[11] M. Van der Pauw, A method of measuring specific resistivity and Hall effect of discs of arbitrary shape, Philips Res. Reports. 13 (1958) 1–9.

Chapter 6 : Reactive inks

In the previous chapter, a 1.2 µm thick YSZ electrolyte layer was deposited by inkjet printing of a colloidal based solution (*i.e.* a stabilized oxide particles suspension in an aqueous medium) on a 9×9 cm^2 porous nickel oxide/yttria-stabilized zirconia (NiO/YSZ) anode [1]. The YSZ printing showed a high potential in terms of both processing flexibility and electrochemical performance of the cell [1]. Despite successful results, limitations in the use of this ink design were put in evidence. Indeed, the minimum layer thickness depends on the particle size in the colloid as the total thickness is the result of the particles' packing and the number of layers needed to achieve a full coverage of the substrate [1]. The limitations in particle size to avoid nozzle clogging (2% of nozzle diameter) can be quite challenging to fulfill. Moreover, stabilizing nanoparticles below 100 nm to achieve thinner films is challenging due to the large amount of stabilizers and additives needed to cover the particles´ high surface area [2]. Finally, the consolidation of ceramic-powder based layers occurs at high temperatures (e.g. 1300 °C for ca. 100-500 nm YSZ powders [3]). This step imposes limitations on the substrates selection to be used, excluding silicon, metals, and nanostructured substrates. Alternatively to colloidal suspensions, particle-free, chemically reactive solutions contain only dissolved precursor salts or molecules, such as metal alkoxide molecules in alcoholic solution [4–6]

This chapter describes the work performed on the development of two metal-organics, or reactive, inks for inkjet printing based on titanium and zirconium precursors, respectively. The chapter is thus divided in 2 sections, with 1 material per section, and contains results and discussions of **paper I** and **II** in addition to unpublished results.

6.1 **Nucleophilic stabilization of water-based reactive ink for titania-based thin film inkjet printing**

Some of the results described in this section were published in the "*Journal of Physics and Chemistry of Solids*" and can be found in the appendix (**paper I**).

An alternative to using colloidal suspensions for inkjet printing deposition is to use reactive inks, starting from chemically reactive solution such as sol gel. This technique is one of the most often

used methods for the synthesis of metal oxide thin films and nano materials at low temperature and it permits obtaining structured nanoparticles at low temperatures [7]. Metal oxides are prepared via sol-gel by a combination of reactions such as hydrolysis of metal alkoxide to form intermediate oxo-polymers. These materials then condensate by either dehydration or de-alcoholation into an oxide network [8]). The metal precursor, or alkoxide, is generally extremely reactive towards water at room temperature, depending on the metal oxide, and will quickly react with water to produce the final oxide. Zirconium, titanium and tungsten based alkoxides are examples of such high reactivity in aqueous media. Dry conditions or specific atmospheres (argon, for instance) are required to manipulate such alkoxides to avoid uncontrolled hydrolysis and condensation. This strong reactivity is an obstacle to the development of sol-gel ink for inkjet printing in a water based system, due to the ink instability which could prematurely react at the nozzle or even in the ink reservoir, leading to severe clogging of the printer.

In this work, a chemical strategy has been elaborated to formulate reactive ink based on alkoxide able to be tolerant to water presence and suitable for a printable ink. The elaborated reactive ink is based on the optimized use of a nucleophilic ligand which promotes a temporary inhibition of the hydrolysis/condensation reaction via an electrostatic shielding of the metal center at the alkoxide molecules. Particularly, the use of nucleophilic-chelating agent promotes the nucleophilic attack from water at the solution level, allowing a safe storage of the reactive ink and during the printing operation. After printing the ligand is quickly disintegrated by the solvent evaporation and by condensation and polymerization the inorganic M-O-network is formed [9]. Few studies described the elaboration and deposition of sol-gel based ink using either commercial or laboratory drop-on-demand (DoD) printers [7,10]. Although these studies show the feasibility of developing suitable sol-gel based inks for inkjet printing, the impact of the chelating agent on the printability and the long term stability of the ink was not studied. In this chapter, the stability of printable reactive inks and the chelation mechanism is studied through the example of titanium based inks, using titanium isopropoxide as alkoxide. Titania was selected for various reasons: it has a high relevance in a variety of strategic technologies, a strong potential as thin film material by inkjet printing (either as colloidal or sol-gel ink) and because the chemistry of titania is well known and extensively studied [11–13], which makes this material a suitable case-study to understand nucleophilic stabilization mechanisms. Finally, titania can be easily doped to form new materials and phases. The importance of the sol-gel pH on the final titania phase and the potential of inkjet printing for deposition of water based sol-gel was demonstrated [7]. Indeed acidic conditions will favor the formation of linear

chain of rutile while a branched-like morphology of anatase will be obtained in basic conditions [9]. Here focus was set on the formation of the anatase phase for its applications such as photocatalytic active layer [7,14] or solar hydrogen production [15]. As such, N-methyldiethanolamine (MDEA) was selected during the early stages of the ink development as a nucleophilic ligand. Apart from its suitable basic pH, MDEA is soluble in water and ethanol, has a rather low viscosity at room temperature and is environmental friendly. The key to printing such type of reactive ink solution is to determine the optimal amount of ligand to stabilize the precursor while keeping the ink printable. To do so, series of inks having different concentrations of ligand have been prepared and the evolution of their viscosity/printability over time were studied.

6.1.1 Ink fabrication and characterization

Titanium (IV) isopropoxide (Ti(OPr)4, hereafter TiTIP) (Sigma- Aldrich) and MDEA were mixed under argon to avoid uncontrolled reactions (i.e. hydrolysis and condensation) between air moisture and the metal precursor. TiTIP and MDEA were mixed and stirred for 5 min. Ethanol-water solution was separately prepared and slowly added to the TiTIP/MDEA blend and mixed for 5 min. Ethanol is added to the suspension to reduce the high surface tension of water (72.8 $mN.m^{-1}$). Decrease in surface tension results in better coverage of substrates, and opens the possibility of using a larger choice of substrates. However, while increasing the volume of ethanol can be beneficial for droplet formation and wettability, the water/ethanol ratio can also have a strong influence on the drying, where too fast drying can lead to clogging at the nozzle. Particularly clogging due to drying for water volume < 40 vol% ink (i.e. inks with more than 60 vol% ethanol) was observed. On the basis of these observations a 40-60 vol% ethanol-water ratio was chosen.

To study the effect of MDEA on the final ink properties, inks at different molar ratio of complexation (i.e. x = [MDEA]/[TiTIP]=2, 4, 6, 8 and 10) have been prepared. The titanium concentration in the ink was kept at c = 0.1 $mg.l^{-1}$. The inks at different x are hereafter indicated as Ink$x$, where x refers to the molar ratio complexation and thus varies from 2 to 10.

The printability of the inks developed in this work was estimated with respect to both printability ranges defined in section 2.2.1 (p.17). Viscosity, surface tension, and density and the corresponding Z number were calculated for all considered complexation ratio.

Figure 6.1 shows the flow curves for the five prepared inks 4 h after the preparation, while the inset plot shows the corresponding viscosity curves.

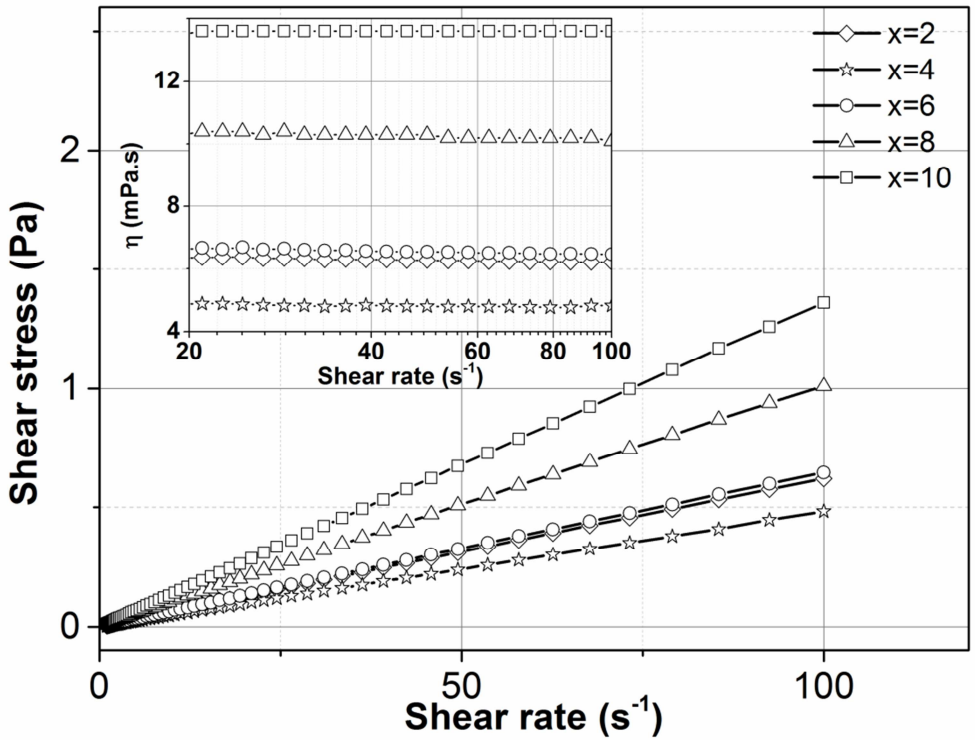

Figure 6.1: Flow curves and viscosity curves (inset) for the five inks developed (4 hours after preparation).

All the prepared inks exhibited a Newtonian behavior with constant viscosity independent on the shear conditions (inset). Accordingly, the viscosity values were simply determined from the slope of the flow curves. The obtained values together with the measured values of the surface tension and the derived Z values for all the inks are reported in Table 6.1.

Table 6.1:Inks printability after 4 hours. 600 hours and 1200 hours of aging (ρ=0.95.cm^{-3}, a=20 µm for all measurements).

	t=4 hours			t=600 hours			t=1200 hours		
	η(mPa.s)	σ(mN.m^{-1})	Z	η(mPa.s)	σ(mN.m^{-1})	Z	η(mPa.s)	σ(mN.m^{-1})	Z
Ink2	6.22	27.01	3.64	36.50	27.43	0.63	66.5	27.3	0.34
Ink4	4.79	27.38	4.76	22.20	26.87	1.02	27.1	26.9	0.83
Ink6	6.47	28.77	3.61	44.91	28.13	0.51	56.4	28.3	0.41
Ink8	10.13	29.79	2.35	126.00	30.09	0.19	262	29.9	0.09
Ink10	14.64	30.48	1.76	145.00	30.94	0.17	421	30.9	0.06

The role of the MDEA is thus to "shield" the alkoxide from water, preventing the premature and uncontrolled ink gelation. As the most viscous component, its amount should be limited to an

optimal value for which the ink viscosity (and printability) is not compromised. A trend as function of the MDEA amount can be identified with the Ink4 possessing the lowest viscosity. The corresponding MDEA amount can be then recognized as the optimal amount that minimizes the interactions between the alkoxide and water, thereby hindering the hydrolysis/condensation process. At lower amount of ligand (e.g. Ink2) a slightly higher viscosity value is obtained likely as a result of an inefficient "shielding" of the alkoxide towards water. Interestingly, when the amount of the ligand exceeds the optimal value (e.g. Ink6, 8, 10), even higher viscosity values are observed and likely associated with polycondensation of the alkoxide-ligand complexes [41]. However, the increments of MDEA content does not impact on the surface tension (see Table 6.1) as the observed values only vary in a range of few $mN.m^{-1}$. For the printability, while all the inks (four hours after the preparation) possess a Z number within the printability domain defined by Derby et al. [16] ($1 < Z < 10$), only ink4 is within the domain defined by Jang et al. ($4 < Z < 14$) [17]. The long-term stability of the prepared inks was then evaluated following the evolution of the rheology behavior over time. Except for the ink4 that maintained its Newtonian behavior on long-term, the other inks exhibited a transition to shear thinning flow, with a deviation from the Newtonian behavior that varies depending on the MDEA content. The shear thinning character of the inks was evaluated via the estimation of the flow index. Figure 6.2 (a) shows the obtained values as function of the ageing time for all the developed inks.

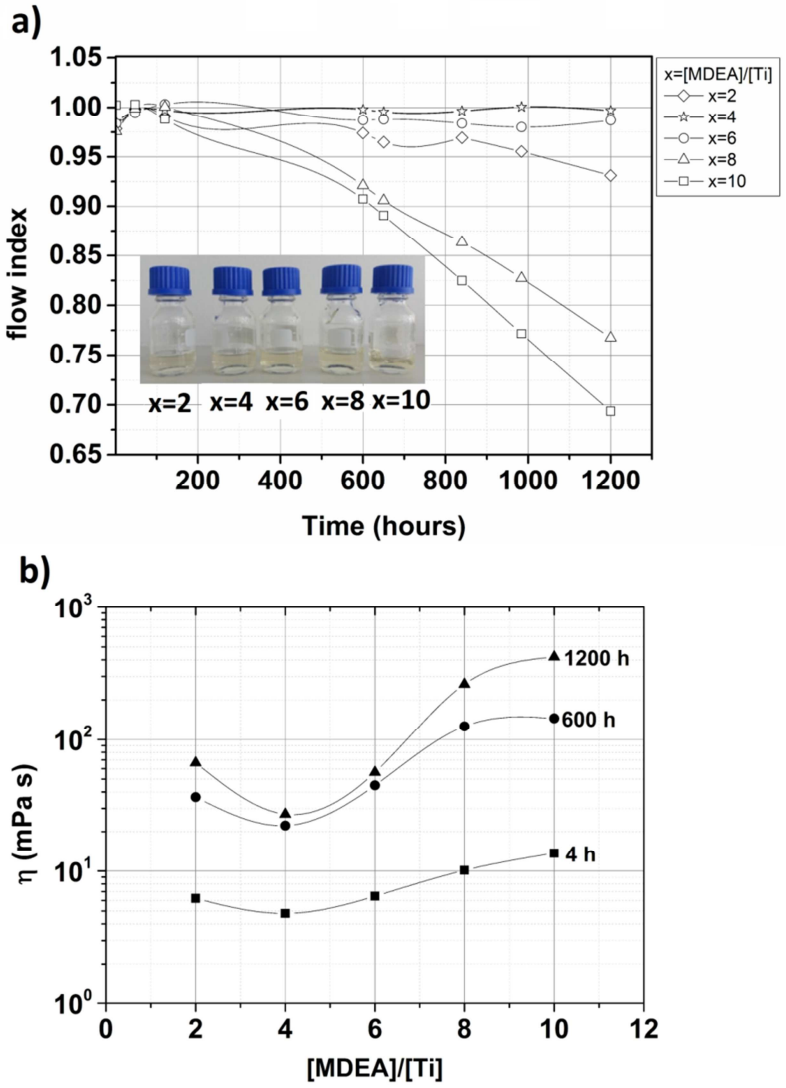

Figure 6.2: Inks flow index measured over resting time (a) (inset: aspect of the inks after 1200 hours of storage) and inks viscosity ($\dot{\gamma}$ = 100s-1) at 3 different resting time versus complexation ratio (b).

A slight and slow decrease of the flow index from the unit to around 0.93 and 0.98 was observed for the Ink2 and Ink6 respectively, whereas a rapid and marked variation down to 0.76 and 0.67 was obtained for the Ink8 and Ink10, respectively. An increment over time of the viscosity was also observed for all the inks as indicated in Figure 6.2 (b), where the viscosity at 100 s^{-1} for each ink is plotted as function of the MDEA concentration for three selected ageing times: 4 h, 600 h, and 1200 h (see also Table 6.1). Ink4 is characterized by a slight variation of the viscosity values (less than 30 mPa.s), whereas larger increments are detected for the other inks. Specifically, after 1200 h the viscosity values of Ink2 and Ink6, with a similar trend, increases of around 50–60 mPa.s, while for Ink8 and Ink10 variation within a range of hundreds of mPa.s is observed. Interestingly, all the inks after 1200 h are still transparent solutions and no sign of TiO_2 precipitation could be detected as

indicated in the inset picture. This experimental finding is consistent with the formation of clear monolithic gels when a ligand is used with an alkoxide (titanium alkoxides) [18]. The rheological analysis clearly indicates a superior stability for the Ink4. The persistence of the Newtonian character over a long period indicates that the interactions among the components are efficiently and fully minimized and minimal alteration of this stable state occurs (e.g. small increasing of the viscosity). For Ink2 and Ink6 only slight differences from Ink4 are observed. By contrast, significant deviations are observed for Ink8 and ink10 [18]. The resulting increment of the viscosity can be explained as an effect of the increased internal interactions among the constituents that also cause the shear thinning flow behavior. Remarkably, no variations in the surface tension over time at fixed amount of MDEA are observed for all the inks (see Table 6.1). This designates the viscosity as the only physical property changing and affecting the printability of the developed inks. After 600 h of ageing, Ink4 is the only ink still within the printability domain defined by Derby, whereas after an ageing of 1200 h none of the inks exhibits a Z number value within such a domain. Interestingly, none of the inks exhibit a printability number within Jang's domain even after 600 h.

To confirm the hypothesis of a polycondensation at the highest content of ligand and clarify the ligand interactions with the central atom (Ti), inks stored during 600 h were characterized by FTIR spectroscopy. Figure 6.3 (a) shows IR spectra for the two starting compounds (TiTIP and MDEA) and for the five developed inks in the entire range of frequencies explored.

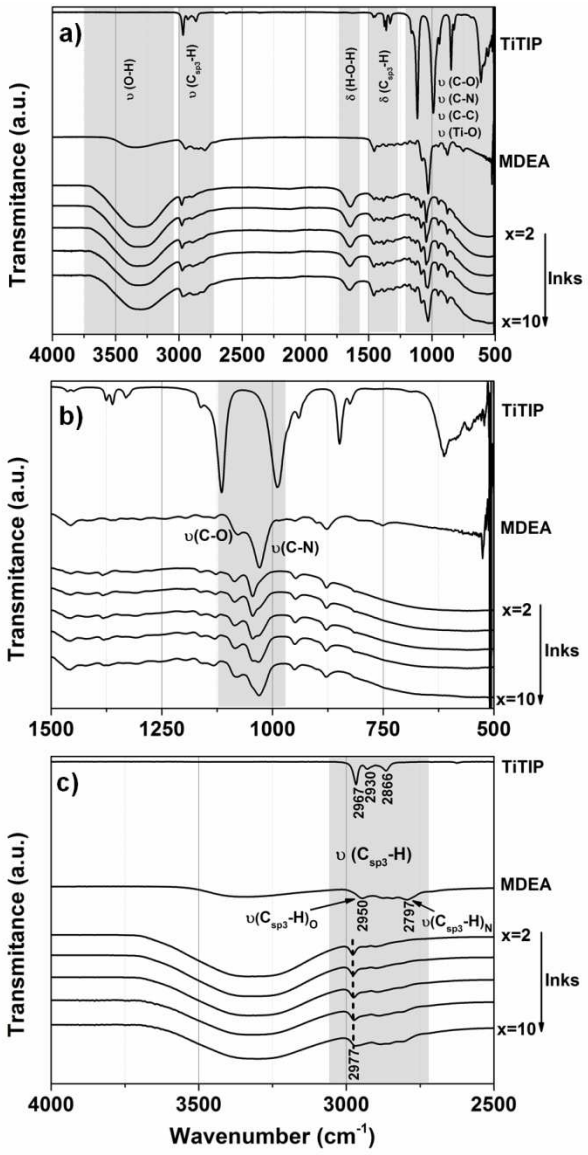

Figure 6.3: FTIR spectra for the inks after 600 h resting (a), and detailed view of the pattern in the ranges 1500–1000 cm^{-1} (b) and 3200–2500 cm^{-1} (c).

For the five inks and for the MDEA, the broad bands attributed to the vibrational stretching of O–H bonds are observed in a wide range of frequency, centered at around 3350 cm^{-1}. These absorptions are significantly intense for the developed inks because of the presence of water, responsible also for the absorption at 1650 cm^{-1}, due to the H-O-H bending. The characteristics bands for the vibrational stretching (in the broad range of 2980–2780 cm^{-1}) and bending (in the broad range of 1450–1325 cm^{-1}) for C_{sp3}–H bonds can be identified for all the materials investigated. Eventually the stretching for the C-O, C-C, and Ti–O bonds are observed in the characteristic range of frequency (1110–600 cm^{-1}). The stabilization of the alkoxide in the aqueous solution is here identified by following the variation of the bands associated with stretching υ(C-O) and υ(C-N).

Figure 6.3 (b) shows the same spectra in a narrower range of frequencies (1500– 500 cm^{-1}). In the spectra of pure MDEA, the two bands are centered at 1076 (υ(C-O)) and 1028 (υ(C-N)) cm^{-1}, respectively. Since titanium is less electronegative than O and N, both the υ(C-O) and υ(C-N) bands are shifted to higher frequency (see positions of the peaks in Table 6.2).

Table 6.2: υ(C-O) and υ(C-N) FTIR peaks position in MDEA and in the developed inks (600 hours of ageing).

	υ(C-O) cm^{-1}	υ(C-N) cm^{-1}	
MDEA	1076	1028	
Ink2	1088	1044	
Ink4	1085	1044	shoulder
Ink6	1085	1044	1029
Ink8	1084	1043	1029
Ink10	1083	shoulder	1030

The largest shift is obtained for the Ink2. As the amount of MDEA increases, the band associated with υ(C-O) is only slightly shifted to lower frequencies without reaching again its original positions. This likely indicates that the alcoholic functions of MDEA, from low to high concentrations, are not free but coordinated with Ti atom of the alkoxide. As further support for this, the stretching of the (C_{sp3}–H) bonds next to the C-O functions coordinated with Ti, are also shifted to higher frequencies (2977 cm^{-1}) with respect to the same bonds in free MDEA (see also Figure 6.3 (c)). By contrast, the band associated with υ(C-N) modes exhibits a splitting into two distinct absorptions. The additional band, located at lower frequency, initially appears as a shoulder, visible starting from Ink4. Its intensity and resolution increase with the content of MDEA until in Ink10 it is the main signals, centered at 1030 cm^{-1}, corresponding to the frequency υ(C-N) in pure MDEA (see Table 6.2). The υ(C-N) band centered at 1044 cm^{-1} in Ink2 is observed to follow an opposite evolution with its intensity and resolution progressively weakening until it appears as a shoulder in Ink10. This likely indicates that, as the amount of MDEA increases, a growing fraction of amine functions are not involved in a coordination of the Titanium atom and thus they are free.

In summary, according to FTIR spectra, different complexes are generated in the water/ethanol solution depending on the MDEA content. Possible coordination complexes are also represented in Figure 6.4.

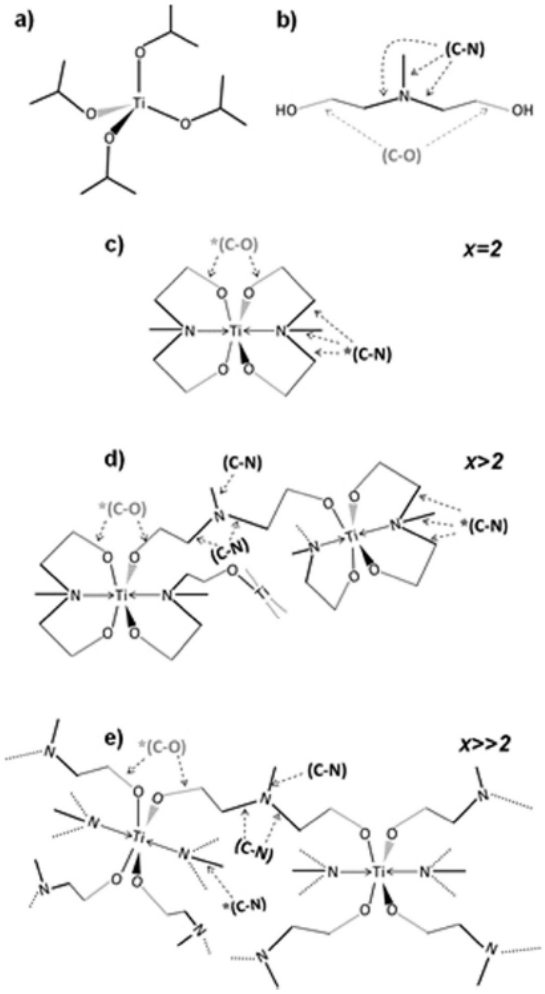

Figure 6.4: Chemical structures of (a) Titanium isopropoxide (TiTIP), (b) MDEA, and (c), (d), (e) possible complexes formed at different [MDEA]/[Ti] molar ratio.

Specifically, when the [MDEA]/[Ti] molar ratio is equal to 2, both the amine and alcoholic functions are involved in the coordination of the Ti central atom. In these conditions, MDEA acts as a tridentate ligand, favoring the coordinative saturation of the Titanium atoms [19] (Figure 6.4 (c)). Despite the high stability of the obtained species, over time the hydrolysis/condensation process is occurring (viscosity increases and the flow index deviates from the unit) as the solvent mostly consists of water. At higher complexation ratio (e.g. 6), an increasing fraction of amine functions are free, likely as consequence of a bridging coordination of MDEA via the alcoholic functions as indicated in Figure 6.4 (d) and (e). Accordingly, the absorption υ(C-N) due to free amine functions is dominant. Extended complexes are thus generated with a consequent increasing of the viscosity.

These experiments showed the importance of controlling the amount of chelating agent to reproducibly produce stable inks. However other ink components can influence the ink stability.

After a deposition of ink4, I cleaned the cartridge for later re-use with ethanol, as it is the solvent usually used for this procedure. Upon cleaning, the ethanol and the rest of the ink left in the container reacted and formed a thick deposit. From this observation came the hypothesis that the water/ethanol ratio has an influence on the ink rheology and possibly on the gelation. Additional rheological measurements were performed on a stable ink (x = 4, c = 0.1 mg.l^{-1}) with different water/ethanol ratio to demonstrate that hypothesis. Inks were stored in sealed glass bottles to avoid solvent evaporation and measurements were performed over 6 days. Figure 6.5 shows the obtained values as function of the ageing time for all the developed inks and some selected ink aspects after 10 days of aging.

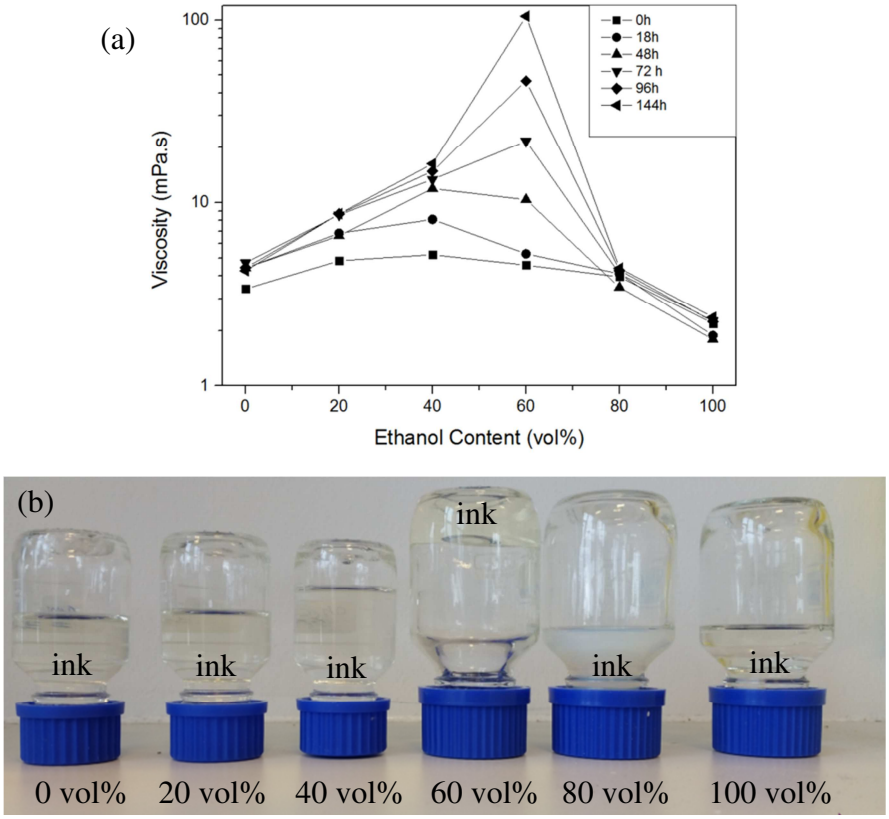

Figure 6.5: (a) inks viscosity (at $\dot{\gamma}$ = 100s^{-1}) at different aging time versus ethanol content and (b) the inks aspect after 10 days aging.

Figure 6.5 (a) shows the viscosity evolution with time over 6 days at different ethanol contents. The viscosity of all formulations increased with time until reaching a quasi-constant value, except for the ink having 60 vol % ethanol. The viscosity of this ink kept increasing in the whole measurement interval. Furthermore, Figure 6.5 (b) shows that after 10 days of aging, the ink gelified, while the other ones stayed in a liquid state. Moreover, the ink with 80 vol % was cloudy after 10 days, synonym of particles formation even though it was still in a liquid state. Interestingly particle

formation did not occur when using 100% of ethanol as solvent, or ethanol volumes lower than 40 vol % in water. However the mechanisms behind this fast gelation were not fully understood, and additional measurements, such as FTIR would be necessary to fully understand the role of water and ethanol in this gelation process. These measurements were outside of the frame defined in the beginning of the thesis and hence not performed here. These observations show that certain water/ethanol ratios are triggering the sol gel process, and demonstrate the importance of a controlled solvent environment when designing reactive inks, at least for titanium isopropoxide. We will see later that it is not necessarily the case with other precursors.

6.1.2 Phase characterization

After deposition and drying, the ink condenses into an amorphous oxide network and a crystalline structure is obtained after heat treatment at a specific temperature, dependent of the material. Optimal calcination temperature needs to be determined. At this optimal temperature, the desired phase should be obtained and there should not be traces left of organics. The calcination temperature is determined using two measurements. First the minimal temperature to remove organics is determined by thermal analysis. In the case of the ink, the important organic part to look at is the burn-off temperature of MDEA. Figure 6.6 shows the thermal analysis performed on the MDEA.

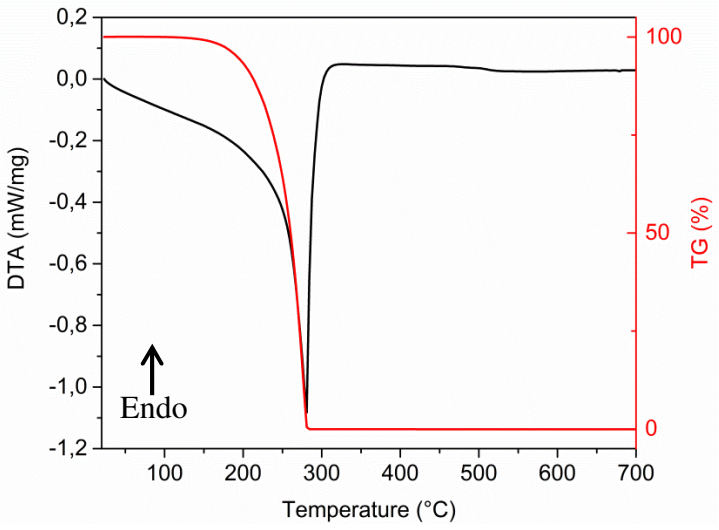

Figure 6.6: Thermal decomposition of MDEA measured by DTA (black) and TGA (red).

Figure 6.6 shows a strong weight loss from 100 to 0 wt % between 200 and 350 °C, coupled with an exothermic peak. This weight loss and exothermal peak correspond to the decomposition of MDEA

and shows that the chelating agent decomposition is completed at 350 °C. This temperature is then the minimum calcination temperature that should be considered for the film processing. Secondly, the minimum temperature at which the film becomes crystalline needs to be determined. X-ray diffraction is a powerful tool to identify the crystallization temperature threshold and the crystallite size. In the case of titania, thermal X-ray can give information not only on the minimum temperature to reach to yield a crystalline phase but also at which temperature the phase transition from anatase to rutile is occurring, usually between 600-700°C. The crystallization behavior for ink4 was explored by in-situ XRD experiments at different calcination temperatures. All characterizations have been performed on both fresh and aged inks. Figure 6.7 shows XRD patterns at increasing temperature on Ink4 sample deposited as drops on the holder sample (Pt wire, used as reference).

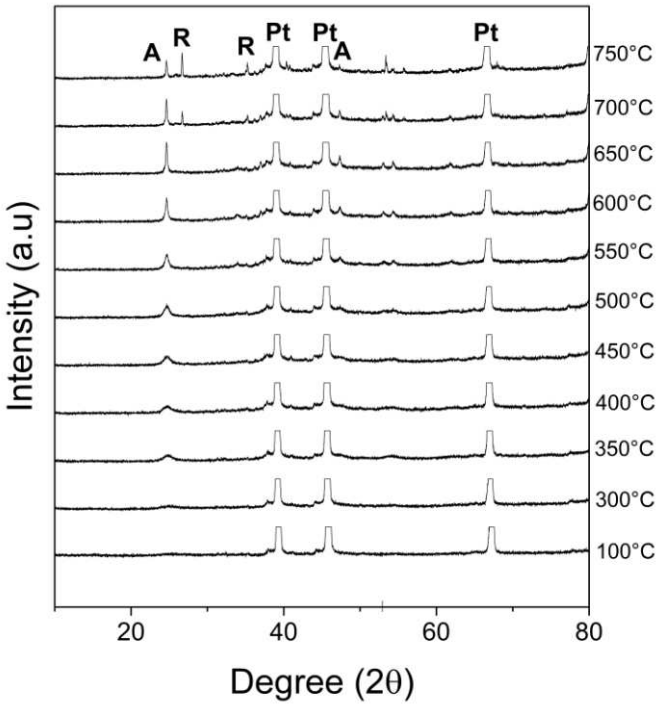

Figure 6.7: XRD patterns of Ink4 (600 hours of resting) at different temperature (A=anatase; R=rutile, Pt= Platinum).

In all the patterns the signals deriving from Pt are identified. The anatase crystallographic phase is already detectable at a temperature as low as 350 °C. At higher temperatures, the peaks associated with the anatase phase become sharper and more intense indicating an increase in the crystallite size. As expected, at 700 °C transformation from anatase to rutile phase occurs.

Based on these results, a crystallization temperature of 400 °C was then selected for the printings and crystallite size for the material treated at that temperature was estimated via the Scherrer equation (Equation 4.8) to be around 7 nm.

6.1.3 Printing and microstructure characterization

An optimal ink for inkjet printing has been designed through rheology analysis and optimal calcination temperature was determined. Before depositing the ink its printing ability is checked via observation of jetted droplet from the nozzle plate. Drop view cameras are generally mounted on piezoelectric printers to perform such droplet analysis. This observation permits to determine the droplet shape, volume, velocity and to detect the presence of tails or satellite droplets. Finally this observation permits to determine what the minimum gap between the nozzle plate and the substrate is to deposit reproducible droplets. Such type of observation is usually not possible on thermal printers as they are primarily used as household printing units. Figure 6.8 (a) shows the typical shape of the Ink4 ejected droplet, as observed using the fiducial camera mounted on the Pixdro printer. Remarkably the droplet exhibits a sphere-like shape with diameter of ca. 35 μm. The snapshot is taken at ca. 530 μm from the nozzle where the droplet does not exhibit any presence of satellite droplets. This result is consistent with the ability to print as indicated by the printability domain $1 < Z < 10$, which for Ink4, is $Z = 1.02$.

From that point the ink was ready to be deposited. To demonstrate the ink substrate versatility, optimized Ink4 was printed on three substrates with different surface energies, i.e., ITO (36 mJ m^{-2}), polycrystalline alumina (65 mJ m^{-2}) and soda lime glass (70 mJ m^{-2}). Figure 6.8 (b)-(e) shows a selection of features at the printing.

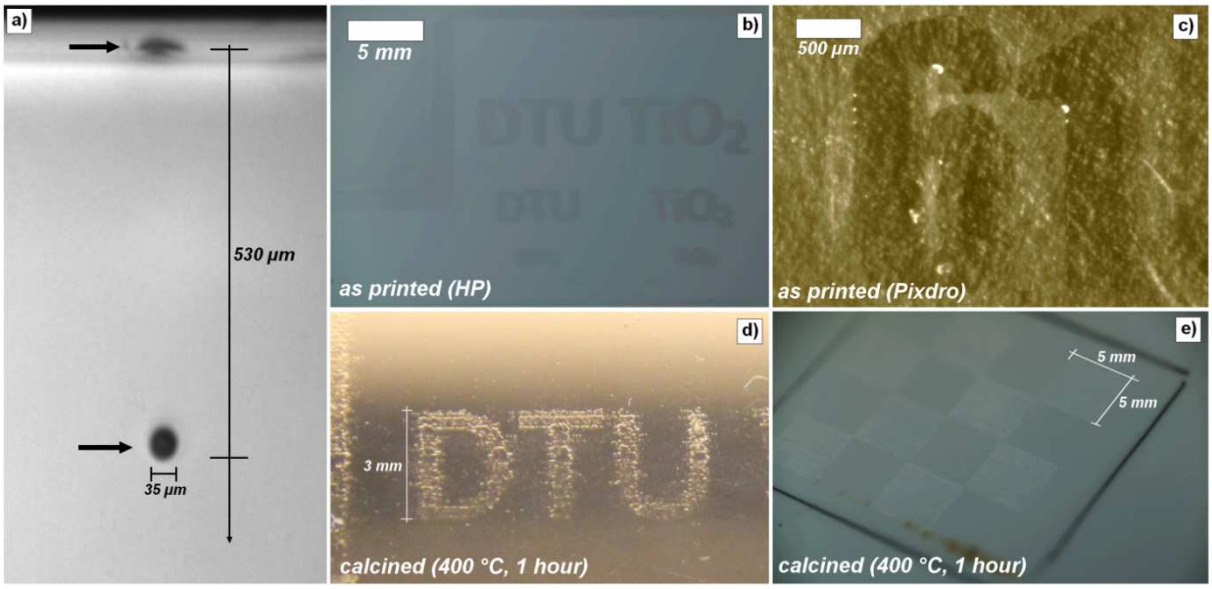

Figure 6.8: (a) Droplet ejected from Pixdro nozzle, (b) as deposited "DTU" and "TiO_2" letters onto alumina (HP) , (c) as deposited number "61" onto ITO (Pixdro), (d) letters printed (HP) onto alumina and calcined at 400°C, (e) chessboard pattern printed (HP) onto ITO and calcined at 700°C.

Figure 6.8 (b) and (c) show complex as deposited printings and defined shapes, such as letters and numbers on different substrates: Figure 6.8 (b) shows the printed "DTU" letters (Danmarks Tekniske Universitet) and "TiO_2" with different size on alumina substrate. This is done by using an inexpensive HP printer which indeed has a limited resolution and quality of the printing, as observed in Chapter 5. However, while letters and numbers appear rather clear in millimeter scale (first raw at the top) the precision is lost at the micron scale (last raw at the bottom). Angles and lines in the print resulted rather homogeneous and continuous in large size printings. On the other hand, Figure 6.8 (c) shows a rather small printing, i.e. the number "61", on ITO using the Pixdro printer. The higher quality of this printing with respect of the HP lays on the size of the characters with typical size between 100 and 400 µm as well as on complexity of the shape, e.g. sharp corners and smooth bending in the numbers. Similar results were observed on the soda-lime glass substrates, indicating a good coverage of the ink on substrates with surface tension in the range 36–70 mJ m^{-2}. Ink4 was thus successfully deposited using both printing techniques (thermal and piezoelectric) despite the different requirements for the techniques. Figure 6.8 (d) and (e) show the effect of calcination at 400 °C for 1 h after printing. In Figure 6.8 (d), the "DTU" letters deposited are still perfectly visible and recognizable. However the prints definition is not as sharp as in the as printed material (compare Figure 6.8 (b) and (d)). Possibly, this is due to shrinkage of the ink as

well as to possible wetting issues developed during the calcination. Similar features were also measured on a chessboard pattern in Figure 6.8 (e). In this case, the printing was stable and exhibited continuous squares connected at each corner. The continuity at the printing, e.g. at the letters (d) and the squares corners (e), indicates that a relatively low shrinkage in the plane directions occurred after calcination. This is a remarkable result for the reactive ink, especially considering that large mass loss (□80%), measured by TG. Considering the TiO_2 theoretical density (4.23 g ml^{-1}) and the other organic components of the solutions, such a loss corresponds to a large change of volume in the printing after calcination. Such a large shrinkage is indeed critical and these results confirm the importance of controlling the printability parameters. For the microstructural features of the printing, Figure 6.9 shows SEM images after calcination.

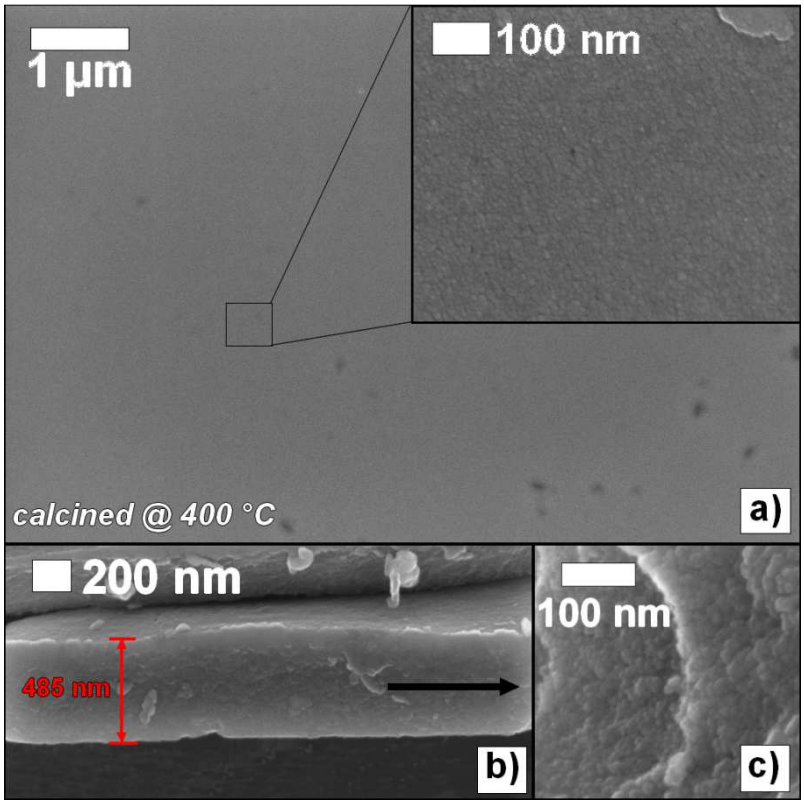

Figure 6.9: SEM images of the printed layer surface at low (a) and high ((a) inset) magnification, followed by the layer cross section (b) together with a broken piece of thin film (c).

Particularly, Figure 6.9 (a) shows the top view of an Ink4 layer deposited on ITO coated glass by inkjet printing and calcined at 400 °C for 1 h. The resulting films is continuous and homogeneous on the substrate and microstructural features could be observed only at nanoscale at high magnification (inset Figure 6.9 (a)), showing a dense polycrystalline deposition. Average particle size is estimated by picture analysis at 11 nm ± 1 nm (based on 30 measurements from 2 different locations along the sample). Figure 6.9 (b) and (c) show the printed layer at a cold fracture: in Figure 6.9 (a), a typical thickness of a single deposition by the HP was estimated to be around 480 nm, while, in Figure 6.9 (c), high resolution at the cross section reveals a dense and polycrystalline morphology of the film. This is kept throughout the deposition without any detectable flaws.

6.1.4 Results summary of titanium based reactive inks

In conclusion, this study demonstrated the efficiency of MDEA as nucleophilic ligand to design alkoxide based solutions. A stable aqueous sol-gel based ink for inkjet printing using MDEA to delay hydrolysis and condensation reactions was successfully designed by rheology. Printability and stability were optimized by varying the amount of MDEA and measuring ink viscosity over time. The use of MDEA to achieve the proper printability is a balance between an effective coordination of the metal center in the metal alkoxide, at low concentration, $x < 2$, and an early organic-inorganic polymerization of TiTIP and MDEA at high concentrations, $x \gg 2$. An optimized ink at $x=4$ was thus proven by printing small complex shapes (e.g. letters) and thin dense layers of ca 500 nm in thickness, on various substrates with surface tension in the 36–70 mJ m^{-2} range. The ink is purified from the organics at ca. 400 °C while phase transitions from amorphous titania to anatase, and from anatase to rutile, occur at 400 °C and at 700 °C, respectively.

It was demonstrated that MDEA can bind and stabilize an alkoxide such as titanium isopropoxide in a highly reactive water environment. The amount of MDEA is a corner stone in reactive ink formulation, along with solvent composition. This study served as a benchmark to understand such stabilization mechanisms and permitted to elaborate preparation procedures, measurement protocol and methodology to efficiently design reactive inks. From this study, the focus went back to the development of YSZ thin film for SOFC electrolyte such as the one discussed in the previous chapter about colloidal inks.

6.2 **Aqueous metal–organic solutions for YSZ thin film inkjet deposition**

Some of the results described in this section were published in the "*Journal of Material Chemistry C*" and can be found in the appendix (**paper II**).

In the previous chapter, colloidal based YSZ inks were designed and deposited by inkjet printing, and demonstrated a promising potential as electrolyte for SOFC. However they also showed some limitations, especially in terms of ink preparation, particle size, and sintering temperature. Previously, TiO_2 films were inkjet printed by designing aqueous particle-free solutions in which a nucleophilic ligand (MDEA) stabilizes metallic precursors. This system showed promising results in the design of particle free suspension. In this study, the same ink design was applied to yttria-stabilized zirconia as an alternative to colloidal based inks (see Chapter 5) for fabrication of an SOFC electrolyte. While several studies describing the deposition of sol-gel based YSZ electrolytes for SOFC are reported in the literature using other processing methodologies such as spin coating [20,21] or dip coating [22], no research on inkjet printing of YSZ sol-gel based ink with nanometric features has been reported this project started. The use of reactive inks for SOFC electrolytes was solely done by Wang *et al.* [3] for the deposition of Gadolinium-doped Ceria (CGO) thick layers (10 µm and thicker) on porous NiO/YSZ and YSZ/CGO substrates and no analysis of inks rheology and stability of YSZ reactive inks are available in the literature. In this work, this gap is filled for an environmental-friendly water-based reactive YSZ ink, demonstrating its long term stability, suitable printability and versatility in depositing on several substrates by using both thermal and piezoelectric DoD inkjet printers [23] by following preparation protocols and measurement described in the titania study.

6.2.1 Ink fabrication and characterization

The YSZ ink formulae were elaborated to produce 8 mol% YSZ (i.e. $0.08Y_2O_3$-$0.92ZrO_2$) starting from zirconium (IV) propoxide ($Zr(OPr)_4$, 70 wt.% in propanol, Sigma Aldrich) as zirconium precursor and yttrium (III) nitrate hexahydrate ($Y(NO_3)_3$,$6H_2O$, 99.8% trace metals basis, Sigma Aldrich) as dopant. MDEA was used as the nucleophilic agent. Ink preparation was carried out under argon atmosphere to avoid any undesired reactions between zirconium alkoxide and ambient water. MDEA and $Zr(OPr)_4$ were mixed to chelate alkoxide molecules, followed by the addition of ethanol. In a separate reactor, yttrium nitrate salt was dissolved in water and kept under stirring until complete salt dissolution. The aqueous yttrium salt solution was then slowly and dropwise added to

the solution containing the chelated propoxide and mixed for 5 min. To screen the ink properties and identify an optimized formulation for printing, several parameters were varied: the water/ethanol volume ratio from 100/0 to 0/100, molar ratio r = [MDEA]/ [$Zr(OPr)_4$] and the concentration c of zirconium from 0.1 to 0.2 g.ml^{-1}. The hydrolysis ratio h = [H_2O]/ [$Zr(OPr)_4$] was kept constant for all inks (h = 8). Herein, inks are labeled as **Ink *r-c-X***, where r refers to the molar ratio of complexation, c to the zirconium concentration, and X to the water volume percentage. It is important to precise that, unlike titania based inks, the water /ethanol ratio was not fixed, as zirconium isopropoxide is diluted into propanol, which acts as a surfactant the same way ethanol does.

To identify the optimal MDEA content required for stability, the physical properties that define the printability number were investigated for a series of ink samples having different molar complexation ratios r = [MDEA]/[Zr(OPr)4] from 9 to 15. Preliminary tests with $r < 9$ (results not shown) exhibited extremely quick gelation of the inks, and were not investigated further. Too high concentration of MDEA, e.g. $r > 15$, was not considered to avoid excessive shrinkage of the final printed pattern and polymerization of the ligand [24]. Moreover, inks having only water as the solvent system were investigated in a first instance, i.e. ink ***r-0.1-100***, to understand the water–precursor interaction, avoiding any possible effects of the co-solvents on the ink stability as observed in the case of titania (Figure 6.5). Figure 6.10 shows the flow curves of four such water-based inks, 1 h after their preparation.

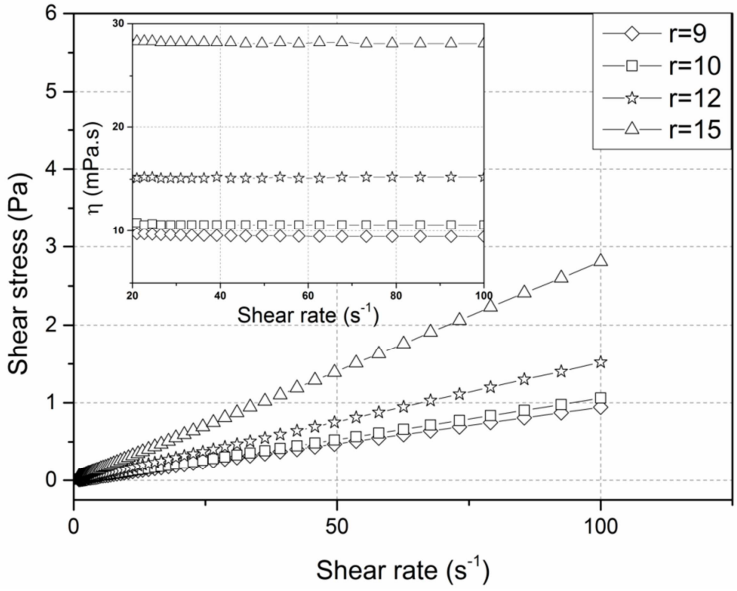

Figure 6.10: Flow curve and viscosity curves (inset) of the four developed inks measured 1 h after preparation.

The corresponding viscosity curves are presented in the inset. All prepared inks showed a Newtonian behavior, *i.e.* a constant viscosity value for the considered shear rate range [24]. Table 6.3 lists the viscosity values calculated from the slope of the flow curves in Figure 6.10, along with the measured surface tensions and printability.

Table 6.3: table viscosity and printability values (η in mPa.s and σ in mN.m^{-1}).

	t=1h			*t*=48h			*t*=192h			*t*=360h		
	η	*σ*	*Z*	*η*	*σ*	*Z*	*η*	*σ*	*Z*	*η*	*σ*	*Z*
Ink 9-0.1-100	9.4	33.4	2.83	11.5	33.6	2.32	37	33.5	0.72	148	33.3	0.18
Ink 10-0.1-100	10.6	33.1	2.50	13.1	32.9	2.02	18.3	33.4	1.45	25.9	33.2	1.02
Ink 12-0.1-100	15.2	31.4	1.70	16.7	31.1	1.54	16.7	31.7	1.55	18	31.2	1.43
Ink 15-0.1-100	28.1	31.3	0.92	29	31.5	0.89	26.5	31.2	0.97	28.9	31.6	0.90

This analysis clearly indicates that viscosity values increased with the amount of MDEA in the ink as a possible effect of polycondensation of the alkoxide-ligand complexes [18,24]. However, increasing the amount of MDEA did not affect the surface tension of the inks, which fluctuated by a few mN.m^{-1}. The calculated printability numbers of inks aged for 1h from Table 6.3 indicate that all inks except *ink* ***15-0.1-100*** exhibited a printability number within the $1 < Z < 10$ range [16].

The long-term stability of the inks at different concentrations was evaluated following the evolution of printability over time. Figure 6.11 shows stability tests carried out with the ink samples and reported as printability as a function of *r* at different ageing times, from 1 to 360 h.

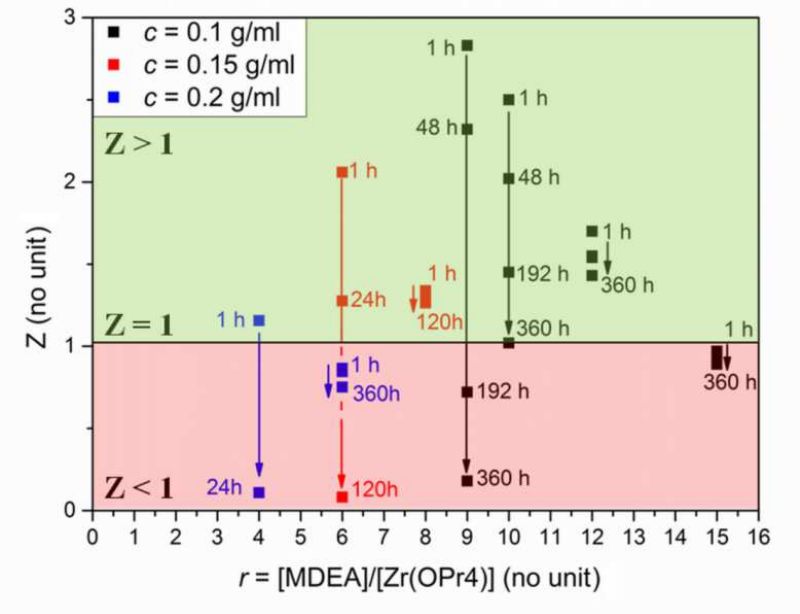

Figure 6.11: Inks printability at different concentrations and aging time *versus* complexation ratio.

A green area in the plot represents the printable zone, which corresponds in this study to the viscosity range of inks having a printability number equal or lower than 1, while a red area represents the viscosity range where inks are theoretically not printable ($Z < 1$). In this long-term stability study, the decrease in Z value is strongly linked to a viscosity increase caused by a less effective hydrolysis/polymerization inhibition over time. The frontier viscosity value between the 2 zones ($Z = 1$) is based on typically observed values for surface tension (31 $mN.m^{-1}$) and density (1 $g.cm^{-3}$) for this type of inks (see also Table 6.3). As the hydrolysis ratio h was kept constant for all the inks, different complexation ratio intervals were studied for each concentration. For the inks with $c = 0.2$ $g.ml^{-1}$ (blue dots in Figure 6.11), ***ink 4-0.2-100*** was in the printability range for ca. 1 h, before going out of it with a too low Z after 24 h of aging. Despite being all the time outside of the printability range, the ***ink 6-0.2-100*** gave a very stable Z value. For inks with $c = 0.15$ $g.ml^{-1}$ (red dots in Figure 6.11), ***ink 6-0.15-100*** was printable for approximately 24 h before its printability number dropped below 1. On the other hand, ***Ink 8-0.15-100*** exhibited a stable printability number > 1 over 120 h. For $c = 0.1$ $g.ml^{-1}$ (black dot in Figure 6.11), data showed that inks made with low MDEA content ($r = 9$ and 10) exhibited a rapid decrease of printability number after a few days of aging. Finally, at higher MDEA content ($r = 12$ and 15), ink viscosities showed a remarkable long-term stability but only ***ink 12-0.1-100*** remains printable after 360 h.

In the previous section, the same study was performed on titanium isopropoxide and showed that stability was reached at a complexation ratio of 4. In the case of zirconium, the necessary amount of MDEA to stabilize the alkoxide is three times higher at the same propoxide concentration than for titanium. This method allows quantifying the reactivity of alkoxides towards water, with zirconium being more reactive than titanium.

In summary, these observations indicate clearly that long term-stability was more difficult to achieve at high concentrations of zirconium in the solution. The reason is as the complexation ratio is reduced due to concentration increase, the alkoxide is less and less “protected” towards water, leading to YSZ polymerization which increases viscosity over time [24]. However, improved stability might be reached by increasing the complexation ratio r, and decreasing the hydrolysis ratio h. At low concentration ($c = 0.1$ $g.ml^{-1}$), the same effect is observed for low complexation ratios ($r = 9$ and 10), which resulted in unstable inks. On the other hand, high MDEA content in ***ink 15-0.1-100*** had the undesirable effect to decrease the printability. As also observed and demonstrated for Ti-based inks, the increase of viscosity for high MDEA concentrations can be the

consequence of alkoxide-ligand complex polycondensation [18,24]. As a result of this detailed analysis, we defined a proper long-term stabilization for the complexation ratio with an optimal *r* of 12. As a consequence ***ink 12-0.1-100*** achieved a suitable chelation effect on the alkoxide and preserved the printability in the long term.

It is worth noticing from Table 6.3 that ink surface tension σ was very slightly affected by MDEA content over time, making viscosity the main physical property controlling the printability. Another important feature of such inks is that the printability can be further refined and improved by diluting the solvent with a less viscous compound. We proposed ethanol, which not only reduces viscosity but also can improve the ink drying rate and reduce the surface tension. Such a use of alcohols in general is crucial in surface chemistry, especially when depositing water based inks. For example, the inks developed in this study contain propanol from the alkoxide, which reduces the high surface tension of water (72.8 $mN.m^{-1}$ at 20 °C) to much lower values (ca.31 $mN.m^{-1}$, see Table 6.3). Such decrease improves the substrate wettability to maximize the substrate coverage, leading to homogenously printed continuous thin films [25]. The key point in tailoring the solvent composition is then not only in the ink jetting process, but also in depositing the ink on substrates with different surface free energies and in improving the drying rate.

As result of such an analysis, a series of optimized inks with r = 12 and c = 0.1 $g.ml^{-1}$, with different water/ethanol ratios (from X = 0 to 100) were synthesized to evaluate the most promising ink for inkjet printing. The measured physical properties of the inks at different aging times are reported in Table 6.4.

Table 6.4: viscosity/printability of ethanol diluted inks for ink 12-01-*X* ((η *in mPa.s,* σ *in* $mN.m^{-1}$, *and* ρ *in* $g.cm^{-3}$).

	t=1h				*t*=360h			
X (vol%)	η	σ	ρ	*Z*	η	σ	ρ	*Z*
100/0	15.2	31.4	1.06	1.70	18	31.7	1.06	1.43
80/20	15.1	30.3	1.03	1.65	17	30.1	1.03	1.47
60/40	14.9	29.5	1.01	1.64	16.7	29.1	1.01	1.46
40/60	12.8	27.3	0.99	1.82	14.8	27.8	0.99	1.57
20/80	12.5	26.1	0.96	1.79	11.3	26.4	0.96	1.98
0/100	7	24.5	0.94	3.07	8.01	24.8	0.94	2.68

Such values indicate that all the inks were within the defined printable range in the considered aging time frame. As expected, both viscosity and surface tension were significantly decreased as the

ethanol content increases, rising up the inks printability after 360 h of aging from 1.4 for $X = 100$ to 2.7 for $X = 0$. Moreover, the surface tension of the ink spans from 31 to 24 $mN.m^{-1}$, when X is reduced. As mentioned in the previous chapter, a too high amount of ethanol can lead to uncontrolled drying and ultimately to nozzle clogging. Finally, it is worth to notice that, unlike the case of titanium based reactive ink (Figure 6.5), no uncontrolled gelation and particle formation and thus change in viscosity were observed when for different water/ethanol ratio. This observation demonstrates that the gelation triggering observed on Figure 6.5 is case specific and not a general tendency for reactive inks, as the only changed parameter between both cases in the precursor source.

Based on these observations we conclude that from the presented matrix of inks, the ink with formula ***ink 12-0.1-60*** is the most suitable ink for printing.

6.2.2 Ink jettability

The jettability of ***ink 12-0.1-60*** was studied first by using the piezoelectric printer. Figure 6.12 (a) shows a droplet of fresh ***ink 12-0.1-60*** after ejection at a firing frequency of 1 kHz at different distances from the nozzle, observed with the camera mounted on the printer.

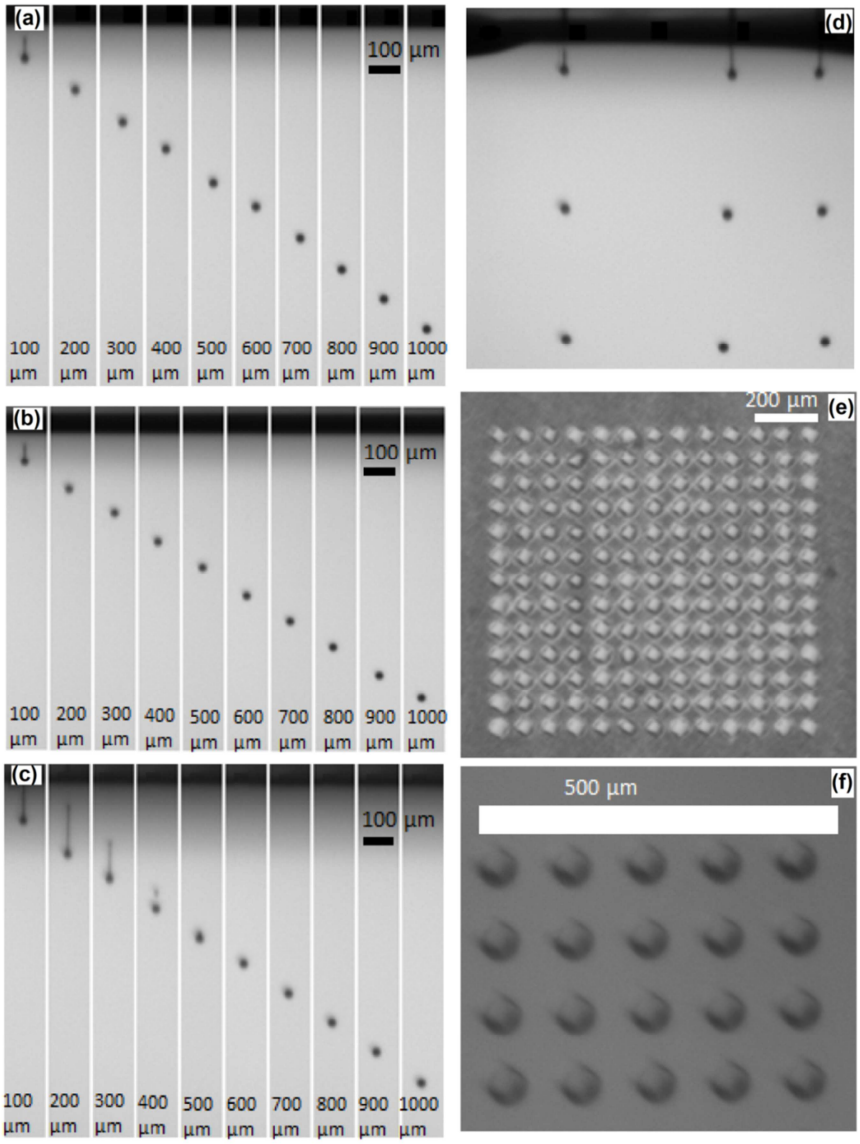

Figure 6.12: Droplet at different nozzle distances (frequency=1 kHz) of ink 12-0.1-60 as prepared (a), aged for 48h (b), and aged for 1200h (c), followed by droplets of fresh ink 12-0.1-60 (frequency = 10 kHz) (d) and optical pictures of an array of fresh ink 12-0.1-60 printed on NiO/YSZ (e) and alumina (f).

At a distance of 100 µm, a filament with a round head is formed, due to the ejection process and the surface tension difference between the ink and the nozzle plate. The droplet was not completely spherical at this stage. However, in the range 200-1000 µm, the ejected droplet exhibited a remarkable stable spherical shape in the considered nozzle-droplet distance range. Moreover, no satellite droplets could be observed in the whole distance range, indicating high quality printability. Such a result is in accordance with the ability to print when the printability (here, Z = 1.7) is in the range $1 < Z < 10$. Figure 6.12 (b) shows the result of the same analysis carried out with ***ink 12-0.1-60*** aged for 48 h on the shelf (Z = 1.5) with similar results than for the fresh ink, verifying the

reliability of the 48 h-term stability and printability at the jetting. With the conditions of jetting used in the experiment, the fully formed droplets showed a stable diameter in the range of 30-32 µm up to 48 h. Finally, Figure 6.12 (c) shows the jettability of ***ink 12-0.1-60*** aged for 1200 h (50 days). This latter ink required a minor adjustment of the waveform, where just the nozzle filling voltage was slightly modified from -10 to -7 V while keeping the general waveform shape and the firing voltage the same. A long tail, which was not observed for fresher inks, could be noticed above the droplet in the distance range 100-300 µm, followed by a breaking of the tail at 400 µm, resulting in a main droplet and satellite droplets. However, satellites merged at 500 µm to form again a spherical and stable droplet in the range 500-1000 µm. Such a change of the jetting was attributed to a slight viscosity increase in the long term (18.1 mPa.s, Z = 1.3 at 1200 h). Despite the presence of a long tail and satellite droplet in the first hundreds of micrometer from the nozzle, this observation demonstrates the outstanding stability of the ink after a long term aging of 50 days. Yet, the jetted droplet diameter was comparable to the one measured for the fresh inks and similar droplet shape stability was also observed in the 48 h aged ink at increased firing frequency, from 1 kHz to 10 kHz (Figure 6.12 (d)).

A series of droplets was deposited on two different substrates with different microstructures, *i.e.* dense alumina and porous NiO/YSZ anode, using a lateral droplet spacing (*i.e.*, distance between the center of two adjacent droplets) of 100 µm. Figure 6.12 (e)-(f) shows the resulting patterns after deposition. For both substrates, the deposited droplets appear as circular dots and exhibited a reproducible diameter of ca. 52±2 µm. This further illustrates the versatility to deposit this ink on very different surfaces at the micrometric scale.

6.2.3 Phase and microstructure characterization

The deposition of reactive ink based on sol-gel leads to the formation of an amorphous polymeric matrix. This material results from the hydrolysis and condensation reactions of the zirconium alkoxide, the yttrium based dopant, as well as solvents and agents such as MDEA. Therefore, a calcination step is necessary to remove the organics and crystallize the deposited layer. Previous thermal analysis (TG/DTA) performed on the sol-gel system using MDEA showed that the mass loss relative to solvent evaporation and chelating agent were completed at 350 °C (Figure 6.6). Based on those results, the crystallization behavior of ***ink 12-0.1-60*** was studied using thermal XRD at temperatures above 350°C. Figure 6.13 shows the XRD patterns performed on powder synthesized by calcining the ink at 400°C and 500°C for 1h.

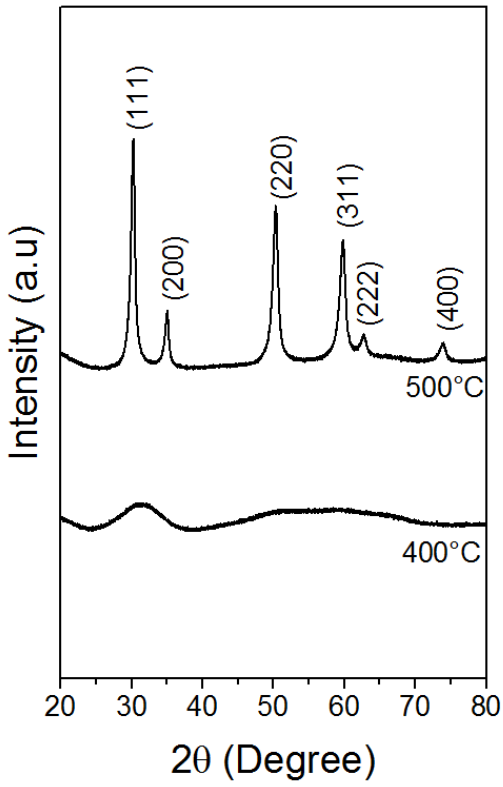

Figure 6.13: XRD pattern of fresh ink 12-0.1-60 at different temperatures.

The diffraction patterns show that no clear crystalline formation could be observed for the powder calcined at 400°C, while a well-defined pattern was observed at 500°C. The pattern observed at 500°C indicates that the formed material is indeed 8YSZ [26], with a crystallite size evaluated at 15 nm *via* the Scherrer equation. In the light of such results, the calcination temperature of 500°C was chosen for the firing of the printing.

Figure 6.14 shows the microstructures of the film deposited with the thermal HP printer after calcination at 500°C.

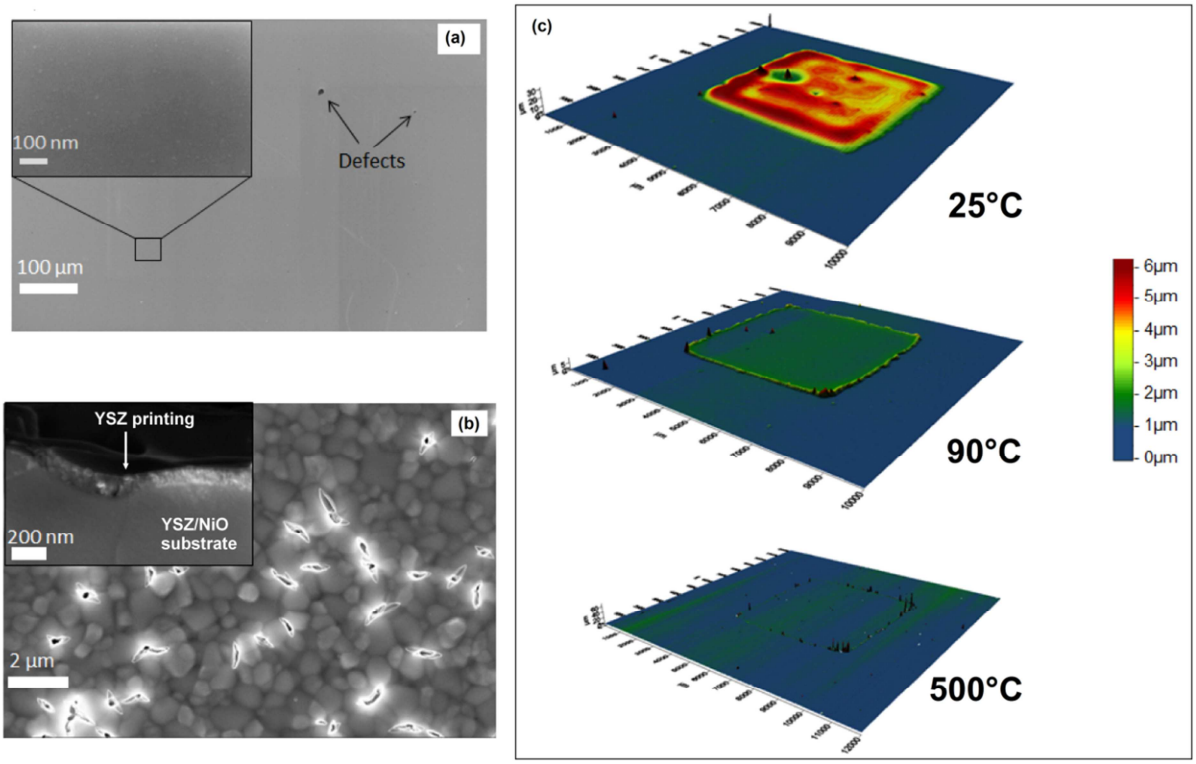

Figure 6.14: SEM images of the printed fresh ink 12-0.1-60 on glass calcined at 500°C for 1h at low (a) and high (inset) magnification, printed and calcined on NiO/YSZ (b) (inset: cross section view), and 3D reconstruction of profilometry data at different temperatures (c).

Particularly, Figure 6.14 (a) shows the surface of calcined ***ink 12-0.1-60*** on dense glass substrate at low magnification after calcination. The resulting film is homogeneous and continuous, with a few defects probably due to the inaccuracy of the used HP printer [1]. Microstructural features could only be observed at very high magnification (inset Figure 6.14 (a)) and exhibits a very dense microstructure with very small grains of ca. 15 nm. The crystallite size estimation by SEM pictures was consistent with the crystallite size obtained from XRD measurements. The film thickness was estimated by SEM of sample cross sections while the evolution of the thickness with the calcination was measured by using 3D profilometry. The printing thickness was found slightly dependent on the substrate porosity with average values below 150 nm for one-layer printing. Figure 6.14 (b) shows the typical microstructure of the printed electrolyte layer on a porous NiO/YSZ SOFC anode. Some notable differences with the deposition on glass (Figure 6.14 (a)) are readily noticed. Due to the porosity of the NiO/YSZ surface, the resulting film after calcination shows a relatively high

number of cracks, all located above pores. The presence of such cracks can possibly be attributed to the following two effects:

- First, the combination of large pores and very low film thickness, (measured on a cross section (inset Figure 6.14 (b)) at around 100 nm) might induce film cracks due to capillary forces.
- Secondly, the film shrinkage during calcination could also induce these cracks. Sol gel based solutions contain a high amount of solvent and volatile elements and it results in very high volume shrinkage during heat treatment [27]. Note however, that the cracks were not observed with the flat, pore-free soda-lime glass substrate (Figure 6.14 (a)).

The shrinkage of this ink has been estimated using 3D profilometry on a 5×5 mm^2 print of fresh ***ink 12-0.1-60*** by measuring the print dimensions (length *x*, width *y*, and thickness *z*) at different stages of heat treatment. 3D images were then reconstructed and are shown on Figure 6.14 (c). No shrinkage was measured in the lateral (i.e. *x*- and *y*-) directions, even after calcination at 500°C. However, a remarkable shrinkage of 90 vol % volume reduction after calcination was measured in the vertical (*z*-) direction. Such a high shrinkage, along with capillary pressure effect, will strongly participate to the collapsing of the film through the pores of the substrate. Optimization of the substrate surface prior to printing and modification of the printing process (multilayer deposition, intermediate drying step for example) could help to enhance the quality of thin film electrolytes.

Several different strategies were elaborated to avoid crack formation on porous substrates. The first one consisted in printing multiple layers on top of each other. This method was applied to colloid inks to tight the electrolyte, and it was showed that increasing the number of layers had a beneficial effect (section 5.2.1, p.89). Several printing iterations of ***ink 12-0.1-60*** from 1 to 3 layers were deposited onto porous sintered NiO/YSZ, and each layer was dried for 15 min at 120°C to allow gel formation before the next printing. Resulting layers were then calcined at 500°C for 1h. Figure 6.15 shows the surface of the different samples after calcination.

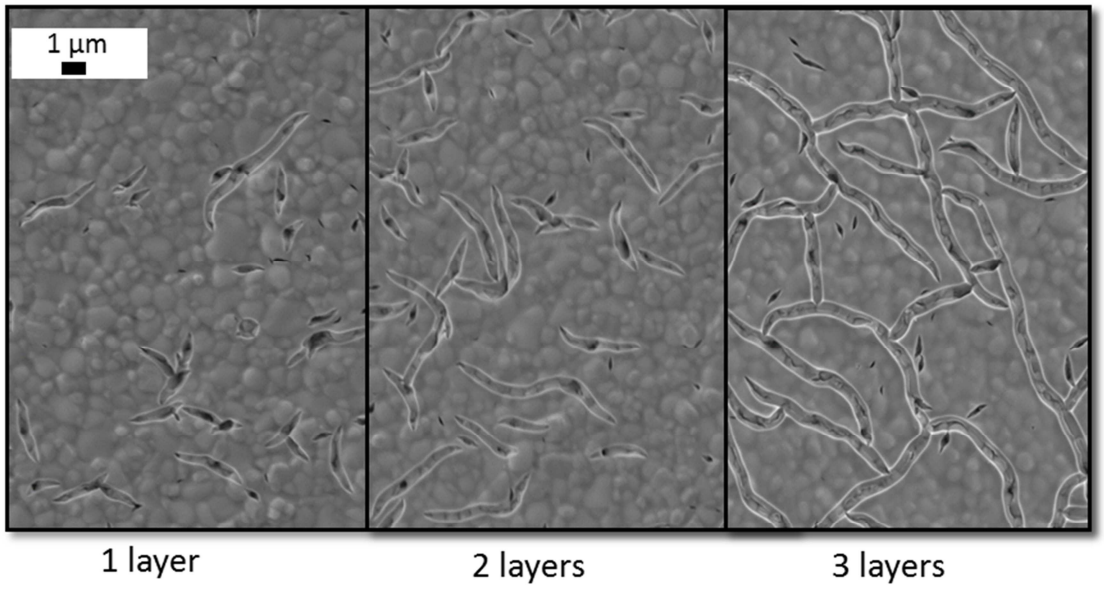

Figure 6.15: YSZ film surface after calcination at 500°C for 1h of (a) 1 layer, (b) 2 layers, and (c) 3 layers.

Figure 6.15 shows that cracks increase both in number and size as the number of layer increases, unlike colloid inks where a higher amount of layers had a positive effect on the film surface and tightness. From this observation it is believed that cracks are formed during drying of the first layer, and they are bigger than the pores of the substrate, according to Figure 6.15 (1 layer); When the second layer is deposited on the cracked gelled film, the cracks act as pores and create larger cracks instead of filling them with materials. This is confirmed with the 3 layer picture in Figure 6.15, where the density and size of cracks is larger than on the 2 layer picture. It is interesting to point out that compared to colloidal inks printed with the same printer (Section 5.2.1, p.89), for which the printer was determining the print quality, the reactive ink seems to be more sensitive to the substrate surface. However, the colloidal ink and the reactive one were not deposited on the same type of substrate (green for colloids and sintered for reactive ink). It would be interesting in future work to deposit colloidal ink on sintered substrates to determine whether its final microstructure depends on the type of substrate.

A second strategy was elaborated to avoid crack formation due to capillary pressure by depositing an intermediate dense film onto the porous anode prior to reactive ink printing. The film is made of a polymer that can be easily burnt off at temperatures lower than the ink calcination temperature (*i.e.* 500 °C in the case of YSZ). The purpose of this dense film is to clog the pores and level the substrate waviness (due to substrate fabrication by tape casting) so the ink is deposited onto a flat surface. Once the reactive ink has dried the temporary film is removed during thermal treatment.

Polyvinylpyrrolidone (PVP) has been selected as a potential candidate, and inkjet as deposition method. The ink was prepared by dissolving PVP (Sigma-Aldrich, MW=10000 $g.mol^{-1}$) in ethanol in different concentrations. As previously performed the printability of the ink was assessed by measuring inks properties.

Table 6.5 lists the measured properties for the elaborated PVP inks.

Table 6.5: viscosity and printability values of PVP inks.

		η	σ	ρ	Z
	PVP wt%	mPa·s	$mN.m^{-1}$	$g.cm^{-3}$	-
Ink_PVP_5	**5**	1,68	21.6	0.78	10.93
Ink_PVP_10	**10**	2,62	21.4	0.8	7.06
Ink_PVP_15	**15**	3,87	21.2	0.822	4.82

Table 6.5 shows that inks with 10 and 15 wt% have a suitable printability number for inkjet printing; ink_PVP_5 has a printability number slightly above the range defined by Derby but was still considered printable. Inks were deposited onto a porous NiO/YSZ substrate and dried at 110°C for 1 hour to allow polymerization and stiffening of the film.

Figure 6.16 shows the microstructure of the YSZ films deposited onto PVP films at different concentrations after calcination at 500°C.

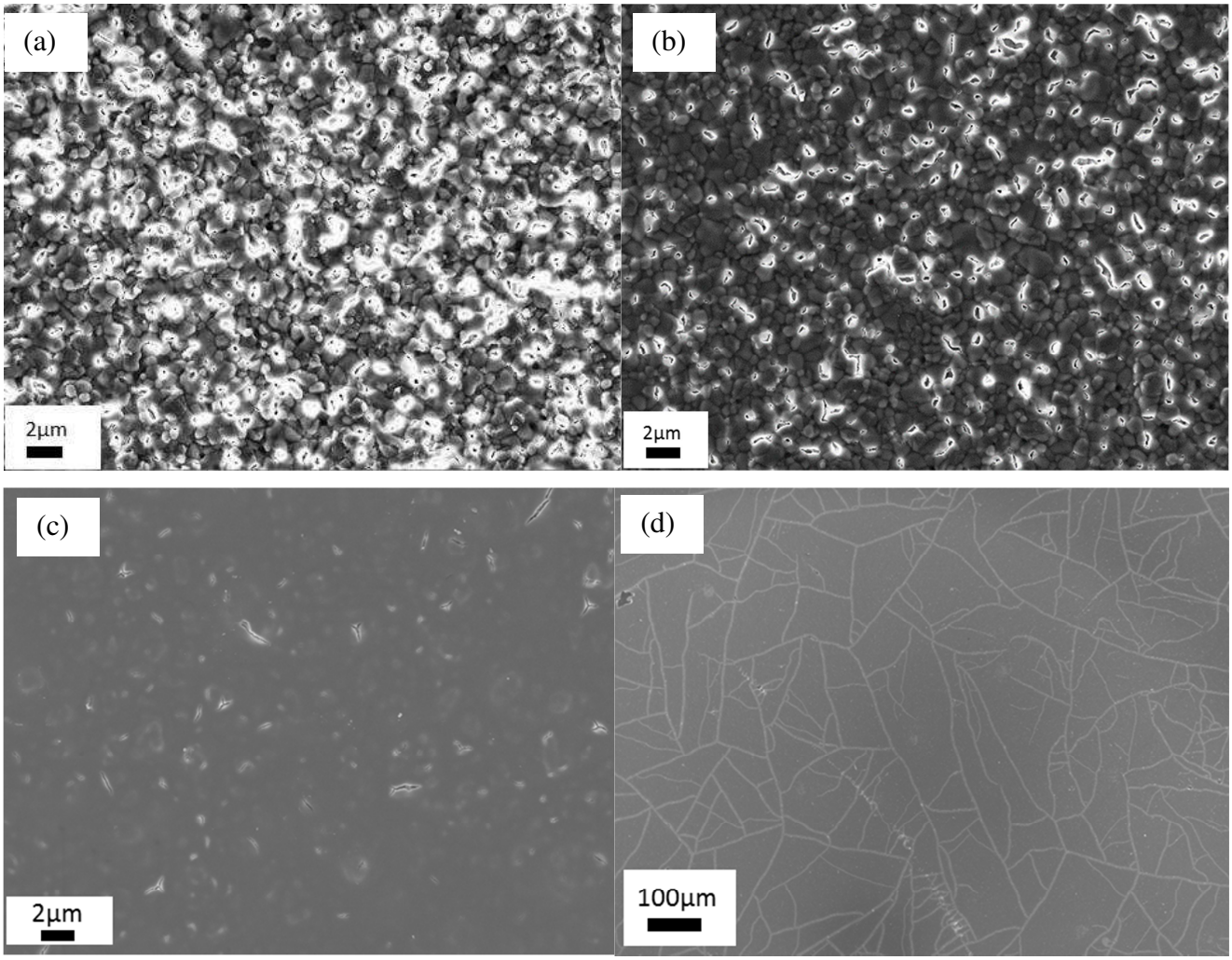

Figure 6.16: High magnification images of YSZ film surface after calcination at 500°C when using a PVP sacrificial film with a weight percent equal to (a) 5%, (b) 10%, (c) 15% and (d) high magnification of the film when using ink_PVP_15.

Particularly Figure 6.16 (a)-(c) show the surface of the YSZ film after using ink_PVP_5 ink_PVP_10, and ink_PVP_15, respectively, as sacrificial film. Numerous cracks similar to the ones observed on Figure 6.14 (b) are visible on the surface in all cases, showing the inefficiency of the sacrificial film. However figures show that the increase of PVP concentration in the film reduces significantly the amount of cracks, especially in the case of ink_PVP_15 where cracks appear to be open porosity. However a lower magnification of the same microstructure, showed on Figure 6.16 (d) shows larger cracks all over the surface. It is believed that these cracks originated from the PVP burning off and that an optimization of the thermal treatment, not performed here, could improve the results.

The last strategy to solve the cracking issue is to add particles to the reactive ink (hybrid inks). The aim of these particles is to work as a "patch" for the cracks by filling them up, reducing crack formation. Moreover the shrinkage of such ink will be reduced due to the particle loading. This ink design will be discussed in the next chapter.

6.2.4 Electrical characterization

For the electrical characterization, optimized ink 12-0.1-60 was printed onto quartz and alumina substrates using the thermal inkjet printer. The ionic conductivity of the calcined thin film was measured by electrochemical impedance spectroscopy (EIS) in air between 500-750 °C. The measurements were taken in the lateral configuration, i.e. in-plane electrodes deposited on the film surface (see drawings Figure 6.17 (a)). This is an optimal electrode/electrolyte configuration for nanometric thin films due both to the maximization of electrolyte impedance with respect of the geometrical features (thickness is below 150 nm) and to the minimization of the electrodes contribution to the total impedance [28,29]. Figure 6.17 shows typical Nyquist and Bode plots of the film on quartz taken at 750 °C in air (Figure 6.17 (a)) and the Arrhenius plot of the films on quartz and alumina calculated from the EIS data at different temperatures (Figure 6.17 (b)). Recorded Nyquist plots on quartz exhibited a single semi-arc due to a dominant grain boundary contribution, i.e. a single R//C Voight element. This is modeled by a typical RQ circuit (solid line in Figure 6.17 (a)) while the inset Figure 6.17 (a) shows a Bode plot of the same data. The RQ circuit resistance was 9.00 MΩ and the summit frequency 972 Hz. The *n*-value for the constant phase element Q was 0.892. The calcined films on quartz resulted crack-free and homogeneous. The results are consistent with the average grains size of 15 nm measured by XRD and SEM. This electrical behavior is typical of nanocrystalline thin films [28,29] and the electrolyte ohmic resistance ($R_{eletrolyte}$ in Figure 6.17 (a)) is calculated at the relaxation of the equivalent RQ circuit. Total conductivity and activation energy (E_a) were then calculated from the measured real impedance components (R_{el}) at different temperatures and normalized for the electrolyte/thin film geometry (Figure 6.17 (b)).

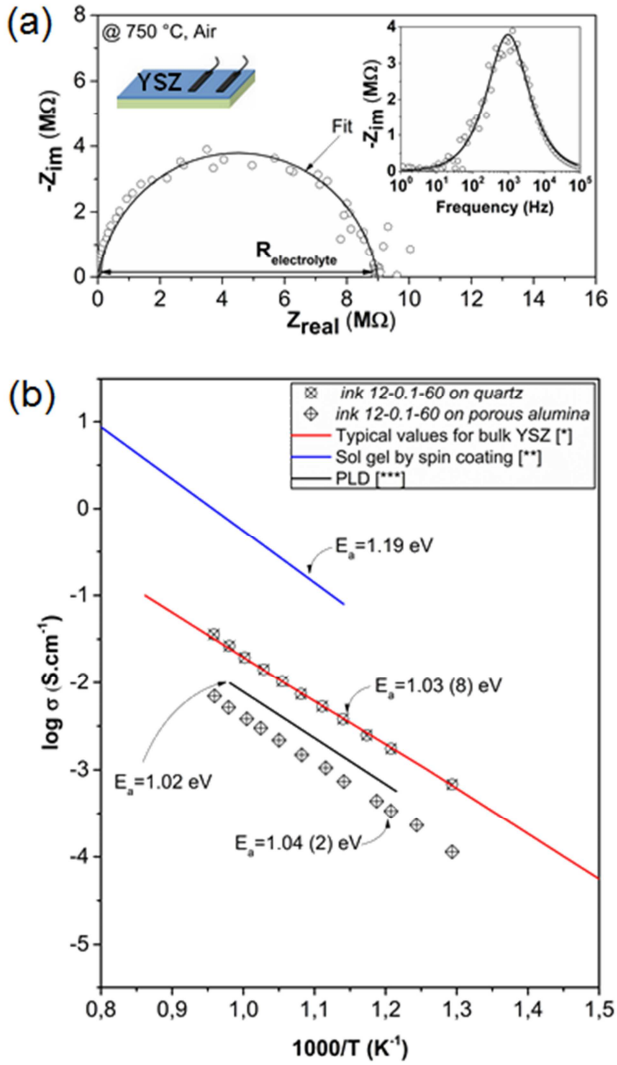

Figure 6.17: (a) Typical Nyquist and Bode plots of the film on quartz taken at 750 °C in air and (b) Arrhenius plot of the films on quartz and alumina calculated from the EIS data at different temperatures along with typical conductivity values reported for YSZ thin film (red line, *=[30]), and values reported for 8YSZ thin film deposited by sol gel spin coating (blue line, **=[31]) and PLD (black line, *=[32]).**

For comparison typical YSZ thin film conductivity measured by EIS [30] is shown in Figure 6.17 (b) (red line) as well as Arrhenius plots from previous studies of 8YSZ thin films deposited by sol-gel (spin coating) (blue line) [31], and PLD (black line) [32]. The calculated conductivity and activation energy (1.03 ±0.08 eV) of our inkjet printed thin film, are consistent with typical values reported for 8YSZ thin films. The conductivity at 750°C ($3.1.10^{-2}$ S.cm^{-1}) is as expected for bulk YSZ [30] and the inkjet printed thin film shows performances comparable with other films deposited by PLD [32]. Figure 6.17 (b) also shows results collected on the alumina substrate. In that case the film was partially cracked, due to the roughness and asperities of the alumina substrates.

Despite the lower conductance, the inkjet layer showed comparable conductivity with PLD films, indicating an overall reliability of the deposited layers by inkjet on rough substrates.

6.2.5 Results summary of zirconium based reactive inks

Stable aqueous-based metal-organic solutions for inkjet printing were designed and demonstrated for printing of 8YSZ thin films and micrometric patterns. Ink printability and long term stability was optimized by the adjustment of the nucleophilic agent, metal oxide concentration and solvent composition. An optimized ink with c = 0.1 g.ml^{-1}, [MDEA]/ [Zr(OPr)4] = 12 and water/ethanol = 60/40 vol% shows remarkable long term stability of 360 h, with a printability Z number around 1, and an exceptional jettability after 1200 h of storage. Several factors were identified as source of instability of the reactive ink, such as the MDEA amount and the propoxide concentration.

Nanocrystalline 8YSZ thin films of 100-150 nm were obtained after calcination at 500 °C on different substrates including Si, quartz, polycrystalline Al_2O_3 and tape cast NiO/YSZ SOFC anode substrate. The measured ionic conductivity agrees well with previously reported 8YSZ thin-film conductivity data. However, formation of cracks in the printed films mainly depends on the quality of the substrate and porous substrates lead to cracked films.

6.3 **General conclusion**

In conclusion, stable aqueous metal organic based inks for inkjet printing were successfully designed by rheology, and yielded crystalline phases, as single (titania) and doped (YSZ) materials. These inks were stabilized using a nucleophilic ligand to delay hydrolysis and condensation reactions, and optimal ligand amounts were determined for both cases to obtain a printable and stable ink. Bonding mechanisms were analyzed and described in a first study about titania based ink. The knowledge acquired in this study could be transferred to the development of zirconia-based inks. Crack-free films were obtained on dense and flat substrates for both inks. However crack formation could be observed when printing on porous substrates, due to either high shrinkage or capillary pressure effect. Several strategies were considered to solve this issue, i.e. multilayer deposition of reactive ink and using a polymeric sacrificial layer, but none of them solved the issue. A third option is to add stabilized particles to the reactive ink to reduce both shrinkage and block substrate porosity, like colloidal inks do. Such hybrid inks will be discussed in the next chapter.

Bibliography

[1] V. Esposito, C. Gadea, J. Hjelm, D. Marani, Q. Hu, K. Agersted, S. Ramousse, S.H. Jensen, Fabrication of thin yttria-stabilized-zirconia dense electrolyte layers by inkjet printing for high performing solid oxide fuel cells, J. Power Sources. 273 (2015) 89–95. doi:10.1016/j.jpowsour.2014.09.085.

[2] A.D. Pomogailo, V.N. Kestelman, Metallopolymer Nanocomposites, 2005.

[3] C. Wang, R.I. Tomov, R. Vasant Kumar, B.A. Glowacki, Inkjet printing of gadolinium-doped ceria electrolyte on NiO-YSZ substrates for solid oxide fuel cell applications, J. Mater. Sci. 46 (2011) 6889–6896. doi:10.1007/s10853-011-5653-y.

[4] B. Yoldas, Design of sol-gel coating media for ink-jet printing, J. Sol-Gel Sci. Technol. 13 (1998) 147–152. doi:10.1023/A:1008640413941.

[5] H.S. Chen, R.V. Kumar, B.A. Glowacki, Study on chemical-solution-deposited lanthanum zirconium oxide film based on the Taguchi method, J. Sol-Gel Sci. Technol. 51 (2009) 102–111. doi:10.1007/s10971-009-1936-z.

[6] M. Chouiki, R. Schoeftner, Inkjet printing of inorganic sol–gel ink and control of the geometrical characteristics, J. Sol-Gel Sci. Technol. 58 (2010) 91–95. doi:10.1007/s10971-010-2360-0.

[7] M. Arin, P. Lommens, N. Avci, S.C. Hopkins, K. De Buysser, I.M. Arabatzis, I. Fasaki, D. Poelman, I. Van Driessche, Inkjet printing of photocatalytically active TiO2 thin films from water based precursor solutions, J. Eur. Ceram. Soc. 31 (2011) 1067–1074. doi:10.1016/j.jeurceramsoc.2010.12.033.

[8] L.L. Hench, J.K. West, The sol-gel process, Chem. Rev. 90 (1990) 33–72. doi:10.1021/cr00099a003.

[9] S.A. Ibrahim, S. Sreekantan, Effect of pH on TiO_2 Nanoparticles via Sol-Gel Method, Adv. Mater. Res. 173 (2010) 184–189. doi:10.4028/www.scientific.net/AMR.173.184.

[10] M. Arin, P. Lommens, D. Vandeput, J. Van Acker, I. Van Driessche, Durability and efficiency of ink-jet printed TiO2 coatings: Influence of processing temperature, Thin Solid Films. 556 (2014) 160–167. doi:10.1016/j.tsf.2014.01.054.

[11] T. Thoř, J. Václavík, Sol-gel preparation of silica and titania thin films, (2016) 101511A. doi:10.1117/12.2257325.

[12] P. Dzik, Photocatalytic and Self-cleaning Properties of Titania Coatings Prepared by Inkjet Direct Patterning of a Reverse Micelles Sol-gel Composition, J. Adv. Oxid. Technol. 15 (2012) 89–97.

[13] K. Kadota, H. Tamura, Y. Shirakawa, Y. Tozuka, A. Shimosaka, J. Hidaka, Interfacial sol–gel processing for preparation of porous titania particles using a piezoelectric inkjet nozzle, Chem. Eng. Res. Des. 92 (2014) 2461–2469. doi:10.1016/j.cherd.2014.03.004.

[14] A.B. Haugen, I. Kumakiri, C. Simon, M.A. Einarsrud, TiO2, TiO2/Ag and TiO2/Au photocatalysts prepared by spray pyrolysis, J. Eur. Ceram. Soc. 31 (2011) 291–298. doi:10.1016/j.jeurceramsoc.2010.10.006.

[15] U. Tipparach, P. Limsuwan, Properties and Photocatalysis of Nanostructured Titania Prepared by Sol-Gel Method for Solar Hydrogen Production, Adv. Mater. Res. 93–94 (2010) 263–267. doi:10.4028/www.scientific.net/AMR.93-94.263.

[16] B. Derby, Inkjet printing of functional and structural materials: fluid property requirements, feature stability, and resolution, Annu. Rev. Mater. Res. 40 (2010) 395–414. doi:10.1146/annurev-matsci-070909-104502.

[17] D. Jang, D. Kim, J. Moon, Influence of fluid physical properties on ink-jet printability., Langmuir. 25 (2009) 2629–35. doi:10.1021/la900059m.

[18] S. Doeuff, M. Henry, C. Sanchez, J. Livage, Hydrolysis of titanium alkoxides: Modification of the molecular precursor by acetic acid, J. Non. Cryst. Solids. 89 (1987) 206–216. doi:10.1016/S0022-3093(87)80333-2.

[19] N. Martín-Arbella, I. Bretos, R. Jiménez, M.L. Calzada, R. Sirera, Metal complexes with N-methyldiethanolamine as new photosensitive precursors for the low-temperature preparation of ferroelectric thin films, J. Mater. Chem. 21 (2011) 9051–9059. doi:10.1039/c1jm10846h.

[20] L. Rose, O. Kesler, Z. Tang, A. Burgess, Application of sol gel spin coated yttria-stabilized zirconia layers for the improvement of solid oxide fuel cell electrolytes produced by atmospheric plasma spraying, 167 (2007) 340–348. doi:10.1016/j.jpowsour.2007.01.081.

[21] S. Kim, S. Pil, S. Woo, Fabrication and characterization of a YSZ / YDC composite electrolyte by a sol – gel coating method, 110 (2002) 222–228.

[22] M. Gaudon, C. Laberty-robert, F. Ansart, P. Stevens, Thick YSZ films prepared via a modified sol – gel route : Thickness control (8 – 80 □ m), 26 (2006) 3153–3160. doi:10.1016/j.jeurceramsoc.2005.09.026.

[23] A. Lesch, F. Cortés-Salazar, V.C. Bassetto, V. Amstutz, H.H. Girault, Inkjet printing meets electrochemical energy conversion, Chim. Int. J. Chem. 69 (2015) 284–289. doi:10.2533/chimia.2015.284.

[24] C. Gadea, D. Marani, V. Esposito, Nucleophilic stabilization of water-based reactive ink for titania-based thin film inkjet printing, J. Phys. Chem. Solids. 101 (2017) 10–17. doi:10.1016/j.jpcs.2016.10.004.

[25] Y. Yuan, T.R. Lee, Contact angle and wetting properties, in: Springer Ser. Surf. Sci., Springer Berlin Heidelberg, Berlin, Germany, 2013: p. 3. doi:10.1007/978-3-642-34243-1.

[26] D.S Patil, K. Prabhakaran,C. Durgaprasad, N.M. Gokhale, A.B. Samui, S.C. Sharma, Synthesis of nanocrystalline 8 mol % yttria stabilized zirconia by the oleate complex route, Ceramics. 35 (2009) 515–519. doi:10.1016/j.ceramint.2008.01.023.

[27] C.B. Carter, M.G. Norton, Ceramic Materials: Science and Engineering, 2007.

[28] K. Mohan Kant, V. Esposito, N. Pryds, Strain induced ionic conductivity enhancement in epitaxial Ce0.9Gd0.1O2−δ thin films, Appl. Phys. Lett. 100 (2012) 16–20. doi:10.1063/1.3676659.

[29] S. Sanna, V. Esposito, J.W. Andreasen, J. Hjelm, W. Zhang, T. Kasama, S.B. Simonsen, M. Christensen, S. Linderoth, N. Pryds, Enhancement of the chemical stability in confined δ -Bi 2 O 3, Nat. Mater. 14 (2015) 1–5. doi:10.1038/NMAT4266.

[30] J. Jiang, J.L. Hertz, On the variability of reported ionic conductivity in nanoscale YSZ thin films, J. Electroceramics. 32 (2014) 37–46. doi:10.1007/s10832-013-9857-1.

[31] Y.W. Zhang, S. Jin, Y. Yang, G.B. Li, S.J. Tian, J.T. Jia, C.S. Liao, C.H. Yan, Electrical conductivity enhancement in nanocrystalline thin films, Appl. Phys. Lett. 77 (2000) 3409–3411. doi:10.1063/1.1328099.

[32] X. Guo, E. Vasco, S. Mi, K. Szot, E. Wachsman, R. Waser, Ionic conduction in zirconia films of nanometer thickness, 53 (2005) 5161–5166. doi:10.1016/j.actamat.2005.07.033.

Chapter 7 : Hybrid inks

In the previous chapters, two ink designs for inkjet printing were proposed to deposit oxide thin films. In chapter 5, we discussed colloidal based inks, in which stabilized particles in aqueous suspension are deposited onto a substrate and calcined at high temperature. These inks showed great potential to deposit thin dense layers onto porous substrates; however they showed some limitations such as a low particle size, achieved by long and intense milling and a high temperature heat treatment (1300 °C) to reach full density. As an alternative, metallic precursor based inks, called reactive inks were developed to solve issues observed with colloidal inks. Thin and dense films (100-400nm) were fabricated onto dense substrates after calcination at 400-500°C, depending on the deposited material. However crack formation was observed when the ink is deposited onto porous and irregular substrates, originating from high ink shrinkage during heat treatment and substrate surface (roughness and pores). To solve this issue, a third ink design, based on both colloidal and reactive ink is here proposed. This ink, called hybrid ink, consists in a stabilized suspension of crystalline colloidal particles into a reactive ink. After deposition and heat treatment, the microstructure of resulting layer is expected to be crystalline particles embedded into a nanoparticles network, formed by sol-gel. The starting colloidal particles have a double role in this design: first they will help reducing the high shrinkage by "replacing" a part of the solvent, and second they will fill up the substrate pores thus limiting crack formation. As the colloids are already crystalline at room temperature, a low temperature heat treatment will be sufficient to reach full density, similarly to reactive inks. Two types of particles were mixed with the YSZ reactive ink, and they differed by their composition (YSZ and CGO) and their size (colloidal YSZ and nanoparticles of CGO).

The hybrid ink concept was pushed a little further and used as a material synthesis method using *in-situ* solid state reaction. The concept was demonstrated here using the titania reactive ink developed in Chapter 6 and bismuth oxide as colloidal particles to produce bismuth titanate. This section contains results and discussions of **paper III and paper IV** published as proceeding paper for "the 230th International Academic Conference on Engineering, Technology and Innovations (IACETI), Bangkok, Thailand" 2017, and in "*Materials Letters"*, respectively.

7.1 **YSZ/YSZ hybrid inks**

The first hybrid ink design consisted of an YSZ/YSZ system developed based on the results obtained with YSZ colloidal inks (Chapter 5) and YSZ reactive inks (Chapter 6).

7.1.1 Ink preparation

The first step into the ink development was to elaborate the ink preparation protocol that will yield suitable ink properties for inkjet printing such as particle size and printability. The ink was prepared following a similar protocol than the one used for colloidal inks. First the dispersing agent polyvinylpyrrolidone (PVP) was dissolved into the stabilized reactive ink (***ink 12_0.1_60***). Commercially available 8YSZ (8mol % Yttria, TOSOH) was then added to the suspension to obtain a 1 vol% solid loading. All the constituents were then milled in a rotational mill in a PET flask at 100 rpm using zirconia milling balls for several days. The final ink is named H1. The protocol is summarized on Figure 7.1.

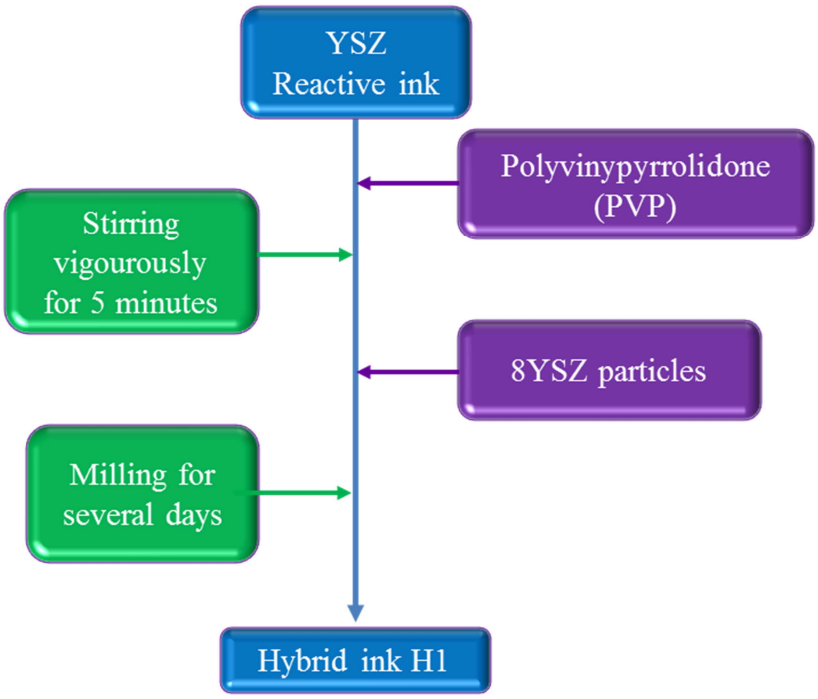

Figure 7.1: Preparation protocol for hybrid ink H1.

The particle size distribution was measured regularly after a few days of milling. As a reminder, colloidal inks prepared in chapter 5 achieved a suitable particle size distribution (2% of nozzle diameter, i.e. 400nm in this case) after 10 days of milling. Figure 7.2 shows the normalized particle distribution of ink H1 after 3 and 10 days of milling.

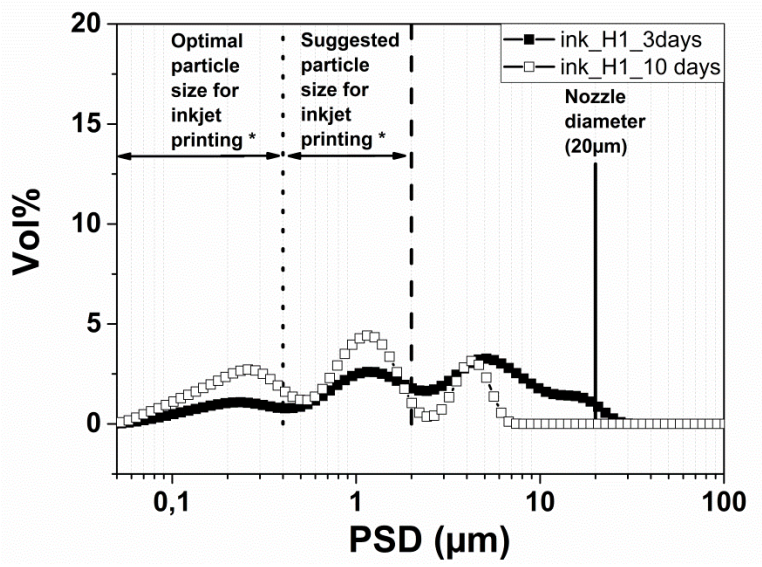

Figure 7.2: Particle size distribution of hybrid ink H1 after 3 and 10 days.

Figure 7.2 shows that the particle size after 3 days consists of a large distribution between 0.04 and 30 µm with a main peak at 7 µm. This particle size does not meet the requirements of the suitable size domain for inkjet. Further milling resulted in a narrower distribution range between 0.04 and 7µm, with three peaks at 0.2, 1.5 and 6 µm, and the ink is still out of the required range. This particle size evolution with milling is very different from the one observed for aqueous colloidal ink, for which a single peak around 0.1 µm was observed after 10 days of milling. A possible explanation for this behavior is the difference of pH between the reactive ink and water. Agglomeration of particles is highly dependent on the surface charge on the particles and this charge can be tuned by changing the solvent pH. Figure 7.3 shows a zeta potential measurement vs pH for nanosized YSZ particles in suspension of water/ethanol from literature [1].

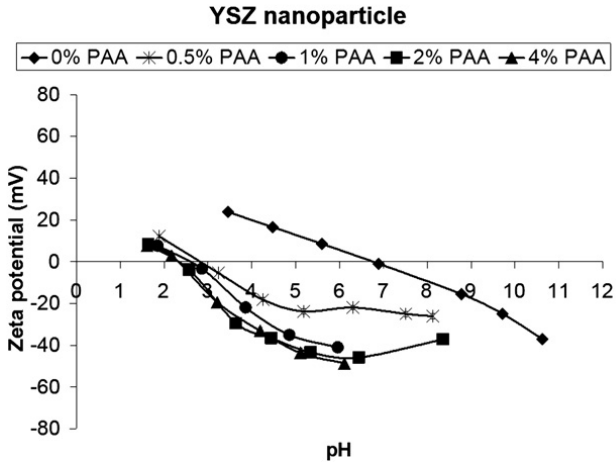

Figure 7.3: Zeta potential measurement of YSZ nanoparticles from literature [1]

Figure 7.3 shows that YSZ nanoparticles without surfactant have an isolectric point of 7. The pH of the reactive ink used to suspend the particles is around 8 and the zeta potential at that pH is around -10 mV. A suspension is considered stabilized with a zeta potential greater than ±25 mV and at the isoelectric charges cancel each other, resulting in agglomeration.When a dispersant is added (here polyacrylic acid), the zeta potential curve and the isoelectric point are shifted to a lower pH value. This results in a higher zeta potential absolute value at higher pH. The high and spread particle size distribution of ink H1 is explained by the basic pH of the reactive ink that creates instability and agglomeration in the suspension. Even if the dispersing agent PVP was added to the reactive ink prior to powder addition, the particle surface is not bonded to the dispersant when entering the reactive ink. To improve the dispersion of the particles, they need to be stabilized before being added to the reactive ink, shifting then the isoelectric point, increasing the zeta potential value at basic pH and thus stabilizing the particles. As such a new preparation method was designed to validate this theory and obtain a suitable particle size distribution. In this method, I used a similar aqueous colloidal ink described in Chapter 5 as source of particles, but without ethanol (unlike the ink described in Chapter 5). YSZ particles are stabilized by PVP in water and have a suitable particle size distribution for inkjet printing after 10 days of milling in this ink design. Moreover this suspension contains water, which is also required in the preparation of the reactive ink. As such the new hybrid ink, called hybrid H2, can be formulated by chelating zirconium propoxide and MDEA, adding yttrium nitrate dissolved in ethanol under argon atmosphere, followed by the addition of the colloidal ink as source of water and YSZ particles. Figure 7.4 describes the preparation protocol of hybrid ink H2. The solid loading is similar to that of for hybrid ink H1.

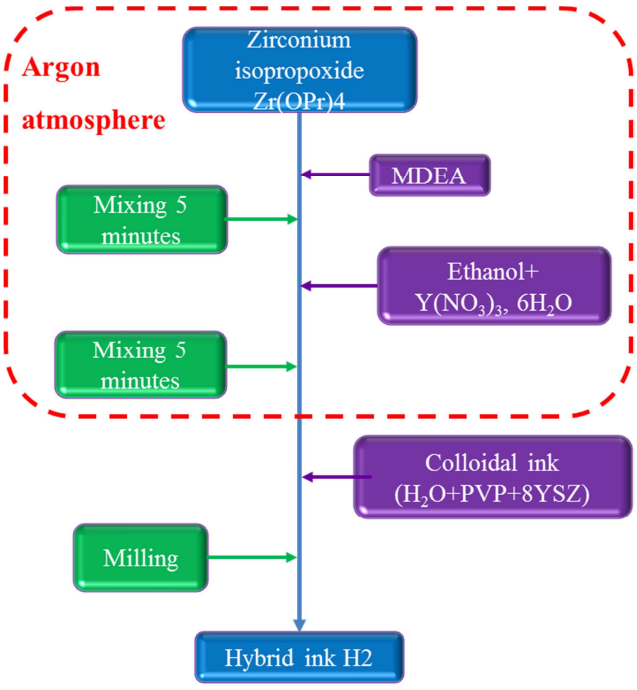

Figure 7.4: Preparation protocol for hybrid ink H2.

The particle size distribution of ink H2 was measured regularly after a few days of milling and is reported on Figure 7.5.

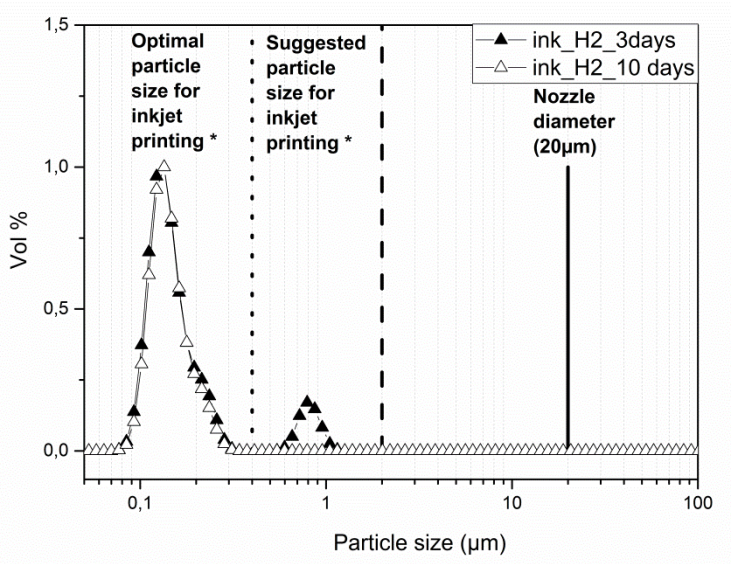

Figure 7.5: Particle size distribution of hybrid ink H1 after 10 days of milling.

Figure 7.5 shows that the particle size distribution after 3 days of milling consists of 2 size populations, with one between 0.09 and 0.34 µm and the second one between 0.6 and 1.2 µm. After further milling for a total of 10 days, the second size population disappears and the distribution

consists of a single peak in the "optimal size for inkjet printing" zone. Particularly this particle size is very similar to the one observed for colloidal inks (Figure 5.1). This measurement shows the efficiency of this preparation method compared to the previous one for which no suitable particle size was obtained for the same milling time.

One of the objectives in designing hybrid inks is to reduce shrinkage and observe if such reduction can lead to crack free films. To test this hypothesis, four hybrid inks with different solid loadings from 0.5 to 4 vol% were produced following the protocol H2. After verifying that these inks are all printable, the inks are printed and their dimensions are characterized by 3D profilometry after deposition and calcination. Figure 7.6 shows the normalized particle size distribution of the four inks after milling for 10 days.

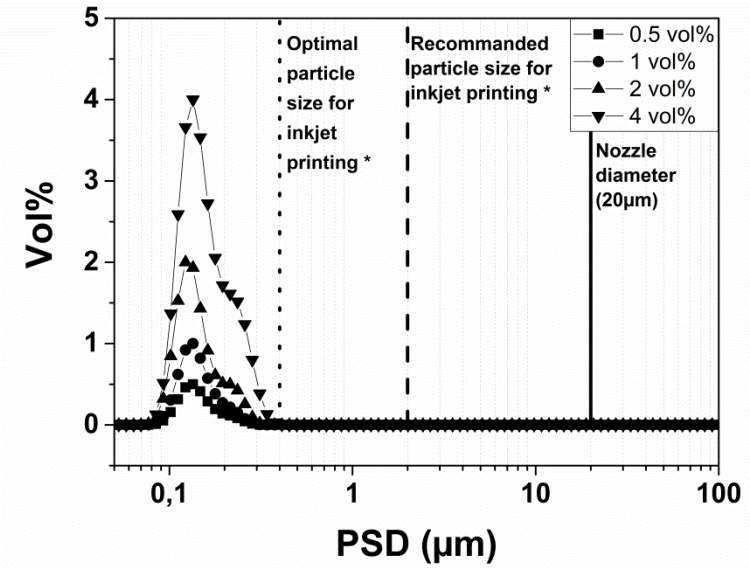

Figure 7.6: Particle size distribution (PSD) of hybrid inks with different solid loading after 10 days of milling.

Figure 7.6 shows that the four particle size measurements after 10 days consist of a single size distribution peak in the optimal range for inkjet printing. It is interesting to notice that a shoulder is visible on the right side of the distribution (higher sizes) and the shoulder becomes more prominent with increasing solid loading. A too high solid loading could then lead to 2 populations of particles, and possibly outside the frame of inkjet printing.

The printability of those inks was evaluated by measuring the diverse properties that define it, *i.e.* viscosity, surface tension, and density. Figure 7.7 shows the viscosity of the four inks after 10 days of milling along with the viscosity of the reactive ink (no particles) after 10 days aging.

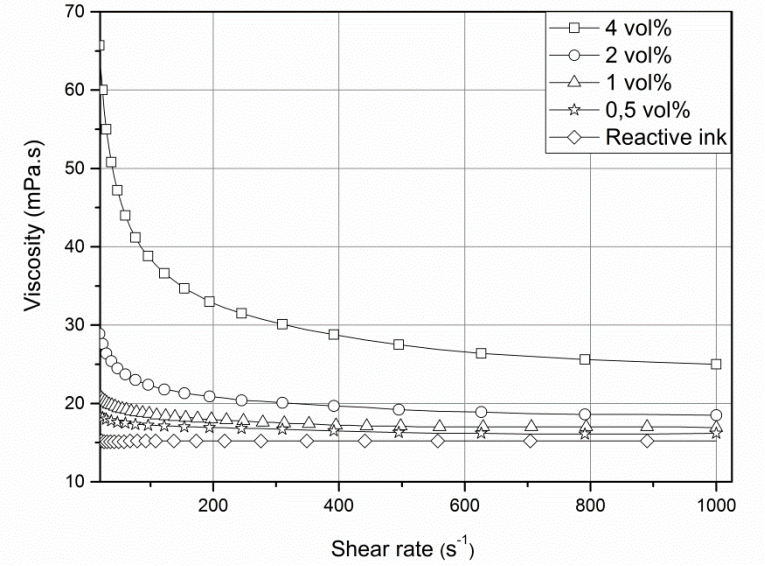

Figure 7.7: Viscosity curves of the four YSZ/YSZ hybrid inks and the reactive ink12_0.1_60 after 10 days.

Figure 7.7 shows that the four hybrid inks have a shear thinning behavior (Non-Newtonian), i.e. their viscosity decrease with increasing shear rate unlike the reactive ink which has a Newtonian behavior (viscosity independent of shear rate). At low shear rate particles in hybrid inks are close to each other and thus create some resistance to the flow materialized by a high viscosity. As the shear rate increases, the particles are realigned in the same direction than the flow, resulting in a decrease of viscosity until a plateau. Particularly, the higher the solid loading, the more pronounced the shear thinning behavior as particles are closer to each other. During printing, a shear rate is applied to the liquid to pass through the nozzles so it is assumed that the value at high shear rate is the most representative for the calculation of the printability. Surface tension and density depend mostly on the solvent system and the proportion of each solvent. As the solvent nature and proportions used are similar to the one used for the reactive ink (water/ethanol=60/40 vol %), similar values were measured. All measurements and resulting printability values are reported in Table 7.1.

Table 7.1: Table viscosity and resulting printability values of hybrid inks.

	Solid loading	η ($\dot{\gamma}$=100 s^{-1})	σ	ρ	Z
	wt%	mPa·s	$mN.m^{-1}$	$g.cm^{-3}$	-
Ink_H2-0.5	0.5	16.2	29.6	1.01	1,51
Ink_H2-1	1	16.9	29.4	1.01	1,44
Ink_H2-2	2	18.5	29.2	1.01	1,31
Ink H2-4	4	25	29.3	1.01	0,97

Table 7.1 shows that inks with solid loading from 0.5 to 2 are in the printable zone (Z > 1). Printability of ink H2-4 is slightly below the threshold value of one. However, the value is so close to the border value that this ink was still included in the study to characterize the influence of solid loading on shrinkage.

7.1.2 Shrinkage and microstructure

The four inks were deposited using the thermal inkjet printing unit (HP printer) onto glass substrates. This type of substrate was chosen for its flatness, which makes it suitable as reference point for 3D profilometry. All inks could be printed, even ink H2-4 despite its printability value below 1. This indicates that some freedom in terms of printing can be allowed when evaluating printability and that the jetting must be dependent on other factors that printability only. The prints were scanned 3 times after deposition and after calcination at 500°C to evaluate their dimensions in the *x*-, *y*- and *z*- direction, similarly to the measurements performed with the reactive inks. Figure 7.8 reports the calculated shrinkage in function of the ink solid loading. As a reference point, shrinkage measured in Chapter 6 (Figure 6.14) for the reactive ink is also reported.

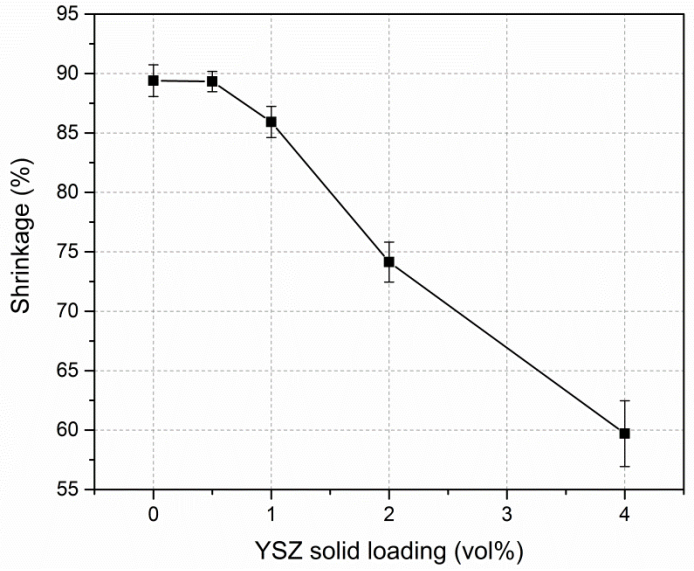

Figure 7.8: Film shrinkage evolution with solid loading.

Figure 7.8 shows that the shrinkage is not really affected with an addition of 0.5 vol% of YSZ particles. Similarly to the results obtained for reactive inks (Section 6.2.3, p.123), only vertical shrinkage (*z*-axis) was observed. From that loading value the shrinkage decrease significantly with a quasi linear behavior up to 4 vol%. The shrinkage after a loading of 4 vol% is however quite high

(60%). It is also noticeable that as the loading increases the measurements become less reproducible, as shown by the error bars. These measurements showed the potential of hybrid inks to substantially reduce the shrinkage of precursor based inks by adding crystalline particles to the solution. In chapter 5, an aqueous colloidal ink with loading of 3.7 vol% was deposited, meaning that the 96.3 vol % left are organics (solvents, dispersants, surfactants, etc). Shrinkage around this value is then to be expected in the *z*- direction, combined with a lateral shrinkage (around 20 vol %) due to particles sintering. Figure 7.8 shows that for similar solid loading (3.7 vol %), the hybrid shows a lower shrinkage combined with no lateral shrinkage, due to a lower amount of organics than in the colloidal ink. During the organics removal, colloids are still present in the layer together with the particles formed by sol-gel reaction, hence a lower shrinkage is observed.

To validate the efficiency of such films to obtain crack free films onto porous substrates hybrid inks were deposited onto a sintered NiO/YSZ porous substrate, similar to the one used in chapter 5 with the YSZ reactive inks. The microstructure of films deposited onto glass and porous NiO/YSZ substrate and calcined at 500°C for 1 h was investigated by SEM and surface pictures are reported on Figure 7.9.

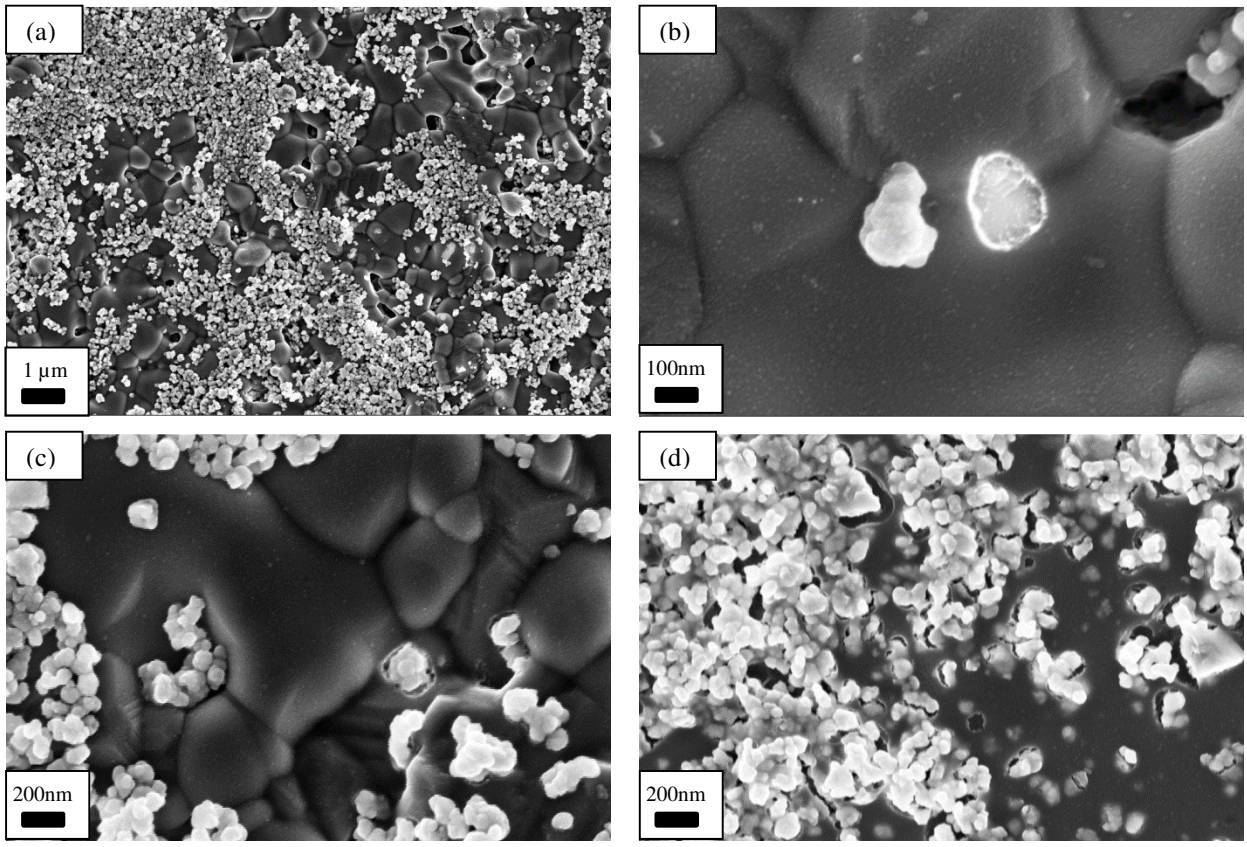

Figure 7.9: SEM images of the printed hybrid H2-1 (1 vol%) and calcined at 500°C for 1 h onto (a)-(c) NiO/YSZ substrate at different magnifications and (d) onto glass.

Figure 7.9 (a) - (c) shows the surface of the calcined hybrid film printed onto porous NiO/YSZ. As observed in Chapter 5, the printed film is difficult to distinguish from the substrate, due to its small thickness. Figure 7.9 (a) is a low magnification picture of the surface of the film. A strong agglomeration and inhomogeneous spreading of the particles is visible. Figure 7.9 (b) shows a part of the film where a particle delaminated from the surface, revealing the surface of the substrate, together with a pore from the substrate. The film is very thin, so thin that it is transparent to the SEM beam. However, due to the presence of this defect, Figure 7.9 (b) makes possible to verify that the film was deposited and that we are not looking at a non-covered part of the substrate. Figure 7.9 (b) shows also a pore covered by the film, and no crack is visible, unlike what was observed previously on the surface of calcined reactive inks. Similar features can be recognized in Figure 7.9 (c) and (b). Figure 7.9 (c) shows a pore filled with YSZ particles, without cracks surrounding it. Other pores are also visible without any damage on the film, confirming the positive effect of adding particles to the reactive in in terms of crack reduction above pores. However, a crack surrounding an agglomerate of YSZ particles is visible. This type of crack was not visible on previous observations and lead to questions about its origin. Further observation on films deposited

and calcined on glass gave some explanations. Figure 7.9 (d) shows the surface of hybrid ink H2-1 on glass and the same type of cracks are visible, and more abundant than on porous substrates. This crack formation is believed to originate from the particle size of the YSZ colloids. Measurements performed on Figure 7.6 showed that the particle size is between 100 and 200 nm. Profilometry measurements and SEM observation performed in chapter 5 on YSZ reactive ink showed that the film thickness in around 100 nm for both substrates, and is then smaller than the particle size. The crack formation around agglomerates is thus believed to originate from the size difference between the film and the particles. As the particles are larger and the film is only experiencing shrinkage is the *z*- direction, the film retracts around the particles, which are sticking out of the film and lead to crack around the particles. To solve this issue, smaller stabilized particles such as nanoparticles are required. However, as also discussed in Chapter 5, the stabilization of nanoparticles is challenging. Due to their small size, nanoparticles have a high surface area, which results in strong and fast agglomeration. To stabilize them, a high amount of dispersing agent is required to properly cover the surface. This high quantity of dispersing agent can significantly increase the viscosity of the ink, compromising the printability.

A possible solution is to use nanoparticles synthetized by continuous hydrothermal synthesis. This process is defined as a method of synthesis of crystalline nanoparticles in water under high pressure and temperature. In this process, metallic nitrates, mineralizer and supercritical water are mixed together in a reactor. Supercritical water has an increased ionic product Kw = $[OH^-].[H^+]$ and a lower dielectric constant, giving an appropriate reaction field for nanoparticle formation [2]. Fine and stable nanoparticles in aqueous suspension are obtained with this process, both at laboratory and production scale by continuous hydrothermal methods [3]. The suspension can then be added to chelated alkoxide using the preparation process previously described for the YSZ/YSZ hybrid inks.

When the preparation of these new hybrid inks based on continuous hydrothermal synthesis powder started, a second project at DTU Energy produced interesting results in synthesizing nanoparticles of gadolinium doped ceria (CGO) for inkjet printing of electrolyte for SOFC. CGO has better ionic conductivity than YSZ which makes it a good candidate to replace YSZ as electrolyte. However CGO as single material for electrolyte required low operating temperatures, due to the reduction of Ce^{4+} in Ce^{3+} that can occur in reducing conditions. When reduced, the material becomes a mixed ionic electronic conductor (MIEC) and expands, inducing a large strain, which at temperatures as high as 700-900°C is between 1-2 % [4]. On the other hand, a composite YSZ/CGO could be a

suitable combination to develop electrolyte for low temperatures. Moreover, due the low processing condition used for reactive inks, the direct reaction between ceria and zirconia which leads to the formation of resistive phases can be overcome [5]. As such, it seemed interesting to develop a second generation of hybrid inks, called "composite hybrid inks" in which two single materials are used, one as crystalline nanoparticle and one produced by sol-gel from a reactive ink.

7.2 **A second generation of hybrid inks: CGO/YSZ composite using hydrothermal synthesis**

7.2.1 Preparation of CGO nanoparticles

CGO nanoparticles were synthetized by dissolving $Ce(NO_3)_3 \bullet 6H_2O$ (99%, Sigma Aldrich) and $Gd(NO_3)_3 \bullet 6H_2O$ (99.9%, Sigma Aldrich) in deionized H_2O (DI H_2O) with concentrations of 0.04 mol L^{-1} for Ce(III) and 0.01 mol L^{-1} for Gd(III). KOH pellets (≥ 85%, Sigma Aldrich) were dissolved in DI H_2O to make solutions with concentrations of 0.1 $mol.l^{-1}$.

An in-house developed continuous flow-type apparatus was used to conduct the synthesis. The setup is reported somewhere else [6]. The Ce, Gd nitrates (reactant solution) and the KOH solutions were introduced separately at room temperature to the reactor, and were mixed at the first mixer. The outflow of the first mixer was fed subsequently to the second mixer and was mixed with deionized water at room temperature. Two thermocouples were inserted into the reactor, one to measure the temperature (T_1) of the feeding supercritical water flow and a one to measure the temperature (T_2) of the outflow of the second mixer. During synthesis, T_1, and T_2 were maintained at 396 °C and 290 °C respectively. The synthesized particles were collected as colloidal slurries at the reactor outlet. Figure 7.10 summarizes the nanoparticles preparation process.

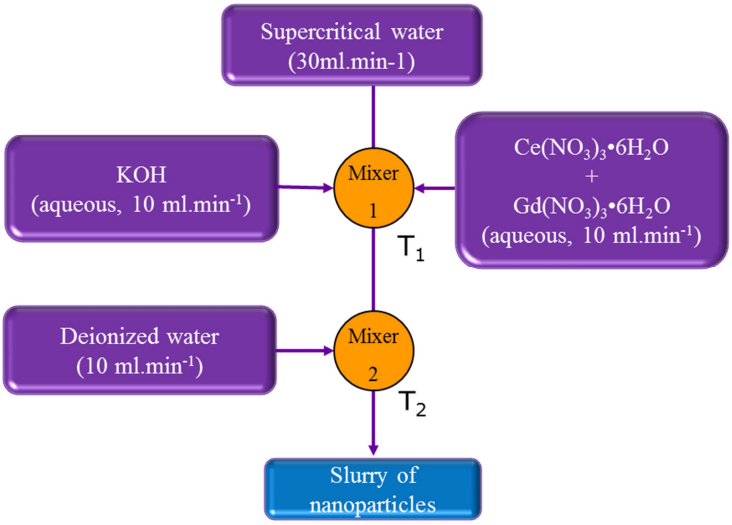

Figure 7.10: A schematic representation of nanoparticle preparation by hydrothermal synthesis.

The obtained slurry of nanoparticles may be added in the chelated alkoxide to make the hybrid composite ink. Prior to ink fabrication, the particles were separated from the slurry by centrifugation, washed with deionized H_2O and dried for subsequent characterization. The particle phase and size were characterized by microscopy and X-ray diffraction to evaluate the particle and crystallite size, as well as to verify that the material is indeed pure CGO. Figure 7.11 shows a XRD pattern (a) and transmission electron microscopy image (TEM) (b) of the obtained particles.

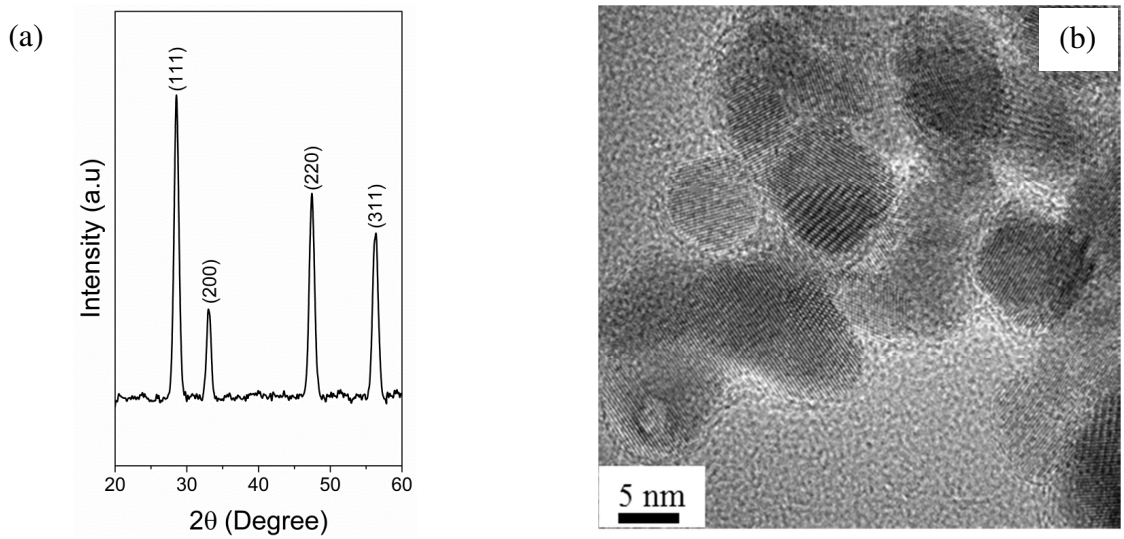

Figure 7.11: (a) XRD pattern of CGO nanoparticles synthesized by continuous hydrothermal synthesis and (b) TEM image of CGO nanoparticles obtained by hydrothermal synthesis (credit: Massimo Rosa).

Figure 7.11 (a) shows that the synthesized material is pure CGO and no secondary phases could be detected within the limit of the XRD technique. The crystallite size is evaluated at 9.8 nm *via* the Scherrer equation applied to peak (111). This value is validated by TEM observation (Figure 7.11 (b)) where an average crystallite size was measured at 9.3 ±0.8 nm (based on the measurements made over 10 particles).

The solid loading of the CGO suspension was measured by TG-DTA from room temperature to 300°C and the results are shown on Figure 7.12.

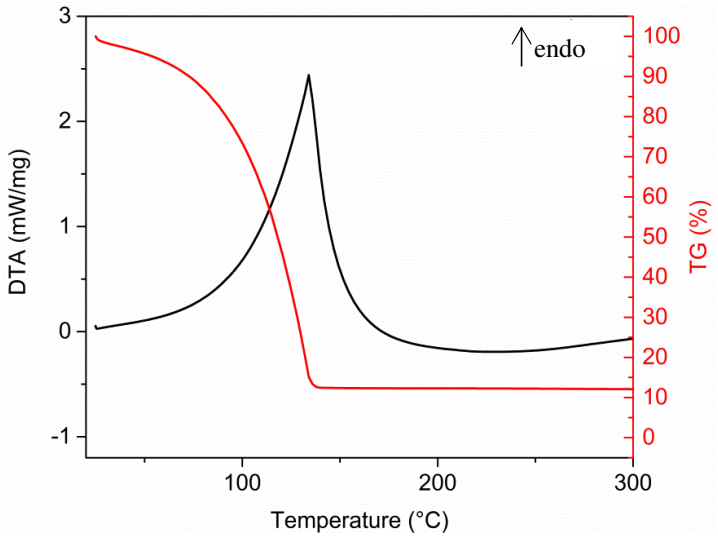

Figure 7.12: Thermal analysis (TG-DTA) of the CGO nanoparticle suspension

Figure 7.12 shows an endothermic peak in the interval 100-200°C, coupled with a mass loss in the same temperature interval, corresponding to the evaporation of water. The residual mass consists of only CGO nanoparticles. The solid loading of such ink is then estimated at 13 wt%, or 2.2 vol%.

7.2.2 Ink preparation

This suspension was then used to produce hybrid composite inks. The preparation protocol is similar to the preparation method used for the YSZ/YSZ hybrid ink described in the section 7.1.1 (p.138). Zirconium propoxide and MDEA were mixed under argon atmosphere to chelate the precursor. In a separate beaker under air yttrium nitrate is dissolved into ethanol and the mixture is added to the chelated precursor. The CGO suspension is then added and is both the source of water and nanoparticles. Figure 7.13 describes the preparation protocol of hybrid composite inks. The final concentration in zirconium is c= 0.1 $mg.l^{-1}$, the complexation ratio is r=4 and the water ethanol ratio is 60/40 vol %.

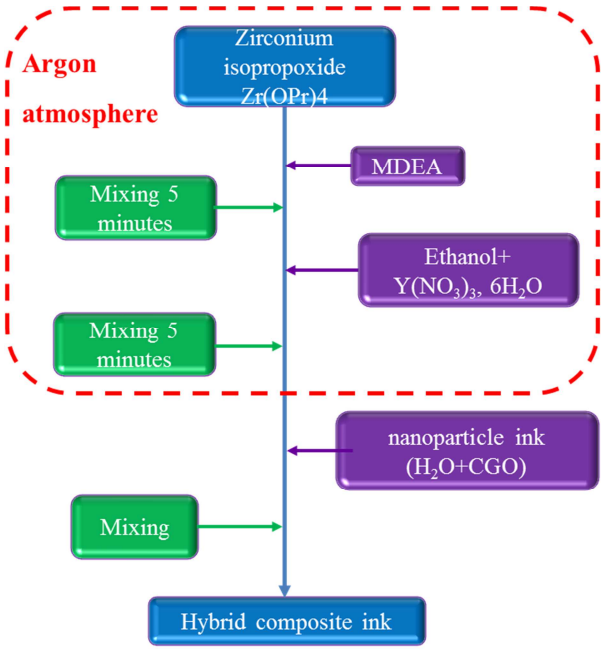

Figure 7.13: Preparation protocol for hybrid ink H1.

The solid loading of the final ink can be tuned by substituting part of the nanoparticle ink content with water. Similarly to the work described in section 7.1.1 (p.138) for the YSZ/YSZ hybrid inks, two inks with different solid loadings were produced. The first one consisted in using 100 vol% of the water needed in the reactive ink formulation by nanoparticle ink, while in the second one 50 vol % of the water was replaced by the nanoparticle ink. The final inks solid loading were 0.25 vol% and 0.5 vol %. The downside of this preparation technique is that, for a specific reactive ink formulation, the maximum solid loading is limited. To increase the solid loading, it is necessary to dilute the reactive ink in order to introduce more water. Another method could be to change the nanoparticle ink concentration by evaporating the solvent. However this method destabilizes nanoparticles and leads to agglomeration.

The normalized particle size distribution of both inks was measured after 3 days standing and is reported on Figure 7.14.

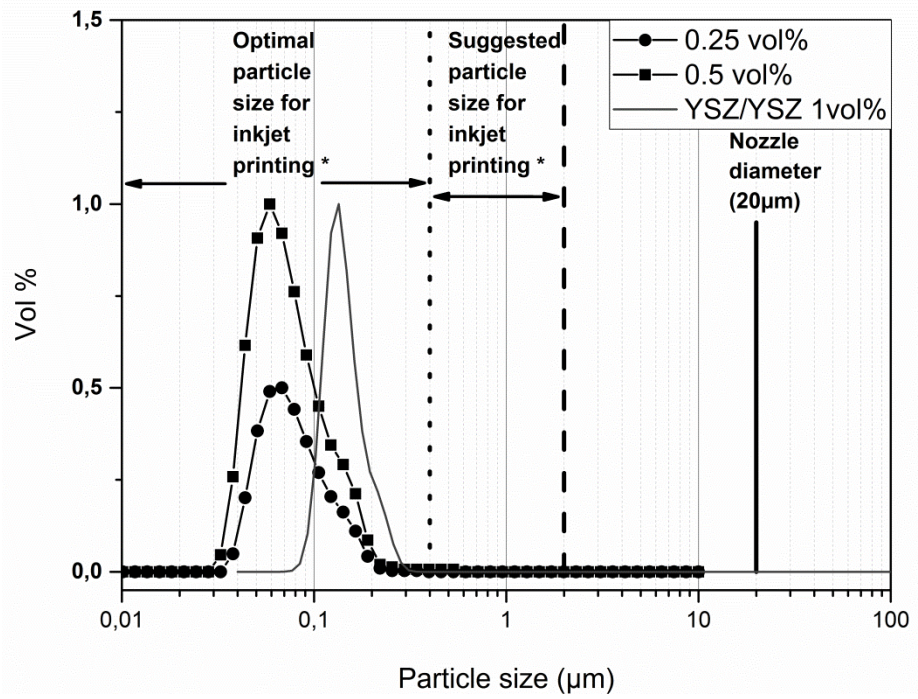

Figure 7.14: Particle size distribution of CGO particles in hybrid inks with different solid loading after 10 days of milling.

Figure 7.14 shows that the particle size of both inks is in the optimized particle size range for inkjet printing. More importantly, the particle size is lower than the one observed for the YSZ/YSZ hybrids (in grey in Figure 7.14). It was assumed in the previous study that the particle size of the YSZ colloids, being bigger than the final thickness after calcination, was the reason behind the cracks formation. The composite inks give then the chance to observe if this hypothesis is confirmed. Prior to deposition, the printability of both inks was evaluated by measuring viscosity, surface tension, and density.

Figure 7.15 shows the viscosity of the two inks after preparation.

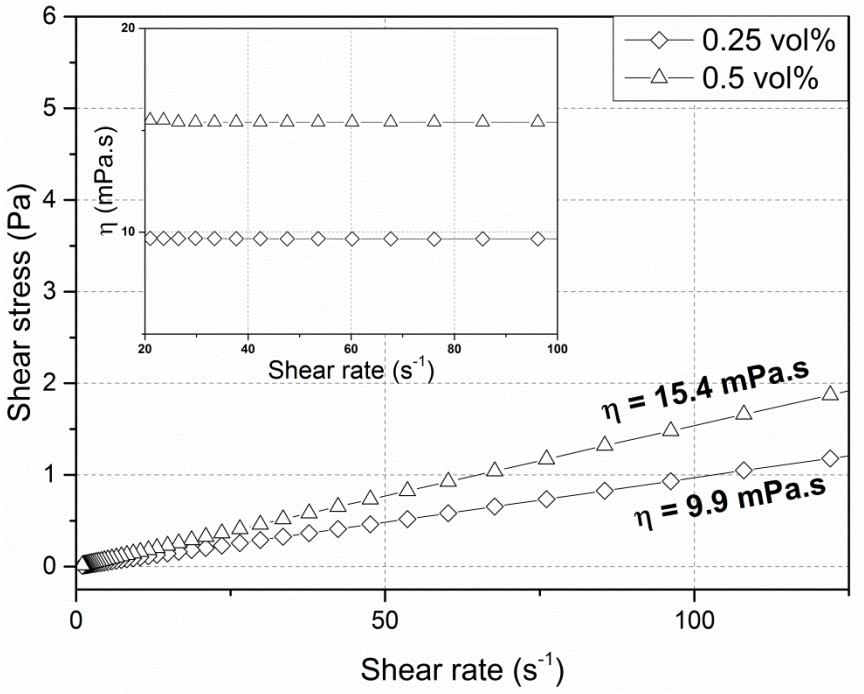

Figure 7.15: Flow curves and viscosity curves (inset) for the two hybrid composite inks developed.

Both the inks exhibit Newtonian behavior with a constant viscosity independent of the shear rate (inset). The viscosity values were calculated from the slope of the flow curves and the values obtained were 15.4 mPa.s for the 0.5 vol% ink and 9.9 mPa.s for the 0.25 vol % ink. Unlike the YSZ/YSZ hybrid inks, these inks do not show a non-Newtonian behavior, due to a better dispersion. Similarly to YSZ-YSZ inks surface tension and density depend mostly on the solvent system and the proportion of each solvent. As the solvent nature and proportions used are similar to the one used for the reactive ink and YSZ/YSZ hybrid (water/ethanol=60/40 vol%), similar values were measured. All measurements and resulting printability are reported Table 7.2.

Table 7.2: table viscosity and resulting printability values of composite hybrid inks.

	Solid loading	η ($\dot{\gamma}$=100 s^{-1})	σ	ρ	Z
	wt%	mPa·s	$mN.m^{-1}$	$g.cm^{-3}$	-
Ink_0.25	0.25	9.9	29.2	1.01	2,45
Ink 0.5	0.5	15.4	29.5	1.01	1,59

7.2.3 Phase characterization

The system YSZ/CGO is stable at room temperature and low calcination temperature. However, CGO and YSZ react at a high temperature to form an insulating phase that strongly affects the film conductivity and performance. The formation temperature of this phase depends on the microstructure of the material. In our case, the particles are nanometric, synonym of high surface area and increased reactivity so the formation will occur at a lower temperature than in the case of colloids (≈1200°C). To detect the formation temperature of the solid solution, ink 0.5 was analyzed by thermal XRD. The (220) peak evolution of both materials was followed to determine the formation temperature. Figure 7.16 shows the XRD patterns measured on powder synthesized by calcining the hybrid ink between room temperature and 1400°C .

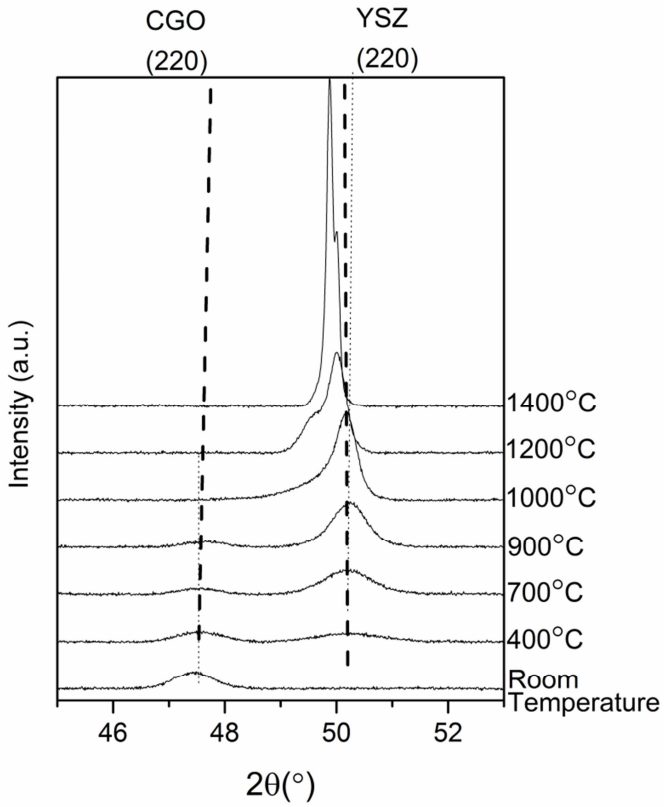

Figure 7.16: XRD patterns of peaks (220) of CGO/YSZ ink at different temperatures.

Figure 7.16 shows that only CGO is detected at room temperature, and the YSZ peak is detectable from 400°C. The YSZ crystallization temperature is lower than the one recorded for pure reactive ink (Figure 6.13), which means that CGO particles could be nucleation sites for YSZ formation. As the temperature increases the YSZ peak shows more intensity while the CGO peak's intensity

decreases, and both peak angles are shifting towards values in between both peaks. The CGO peak intensity is weak yet visible at 900 °C and is not visible at 1000 °C. From that temperature, a shoulder is visible on the left side of the YSZ peak, which intensifies at 1200°C and 1400°C. This peak corresponds to the formation of an intermediate solid solution, starting thus between 900 and 1000 °C [5]. Calcination and operating temperature should then be maintained below this critical temperature where an insulating phase is formed. In the rest of the study, a calcination temperature of 750°C has been chosen both to fit the material stability conditions and to achieve a reasonable densification of the film.

7.2.4 Microstructural characterization of the printed layer

A hybrid CGO/YSZ ink for inkjet printing has been optimized and a calcination range has been determined through thermal XRD measurement. Before depositing the ink, its printing ability is checked via observation of jetted droplet from the nozzle plate using drop view cameras installed on the piezoelectric printer. Figure 7.17 (a) shows the typical shape of the ink 0.5 ejected droplet, as observed using the camera mounted on the Ceradrop X-series. This ink has the highest solid loading of the two studied inks and is shown here as an illustration of the possibility to jet the composite hybrid inks. The droplet exhibits a sphere-like shape with diameter of ca. 30 µm at 500 µm from the nozzle plate. The droplet does not exhibit any presence of satellite droplets. From that point inks were ready to be deposited. The optimized inks were first printed on a sapphire substrate. This dense substrate will be further used for electrical conductivity measurement of the resulting films. Figure 7.17 (b)-(e) shows SEM images after calcination at 750°C.

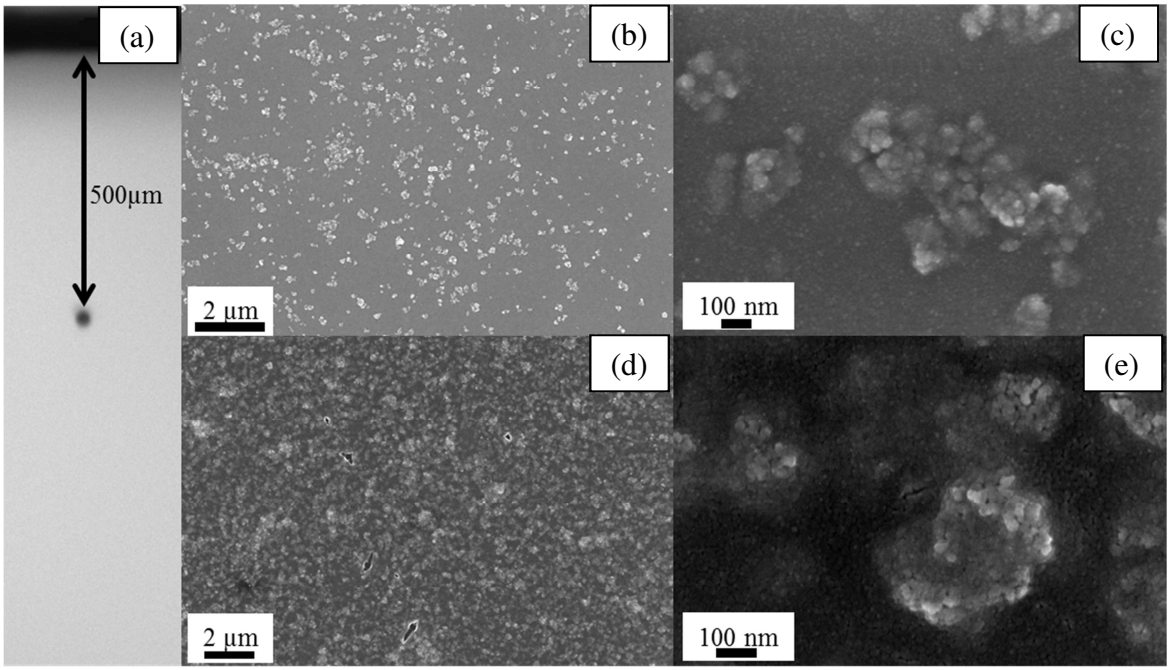

Figure 7.17: (a) Droplet of ink 0.5 ejected from Pixdro nozzle, and SEM images of the printed layer (ink 0.25) surface on sapphire at (b) low and (c) high magnification, followed by the SEM images of the printed layer (ink 0.5) surface on sapphire at (d) low and high (e) magnification.

Figure 7.17 (b) shows the surface view of the calcined ink 0.25 onto dense sapphire. The film is homogenous and continuous on the substrate. Microstructural features could be observed only in nanoscale at the CGO/YSZ interface at high magnification (Figure 7.17 (c)) showing a dense polycrystalline deposition. The large CGO particles are well dispersed into the YSZ network but isolated from each other due to the low solid loading, resulting in non-percolation of the particles. Figure 7.17 (d) shows the surface view of the calcined ink 0.5 onto dense sapphire and presents similar features in terms on continuity and homogeneity compared to the previous ink. A few defects are also noticeable onto the surface of the film. The CGO particles are also well dispersed into the YSZ matrix and much closer to each other due to the increased solid loading. A high magnification image (Figure 7.17 (e)) shows that, while the particles are indeed closer to each other, all particles are not percolating. Interestingly, film discontinuity around the particles observed in the case of larger particles (YSZ/YSZ) is not observed here for both inks, and confirms the hypothesis that the nominal particle size has a strong influence on the film quality. Moreover the particles (both YSZ and CGO) are very small and not fully sintered, which results in a large number of grain boundaries, which will affect the film conductivity. Inks were also deposited onto porous Ni/YSZ to verify the hypothesis that the particle loading will solve the cracking issues observed when using reactive inks. Figure 7.18 shows SEM images of both inks after calcination at 750°C.

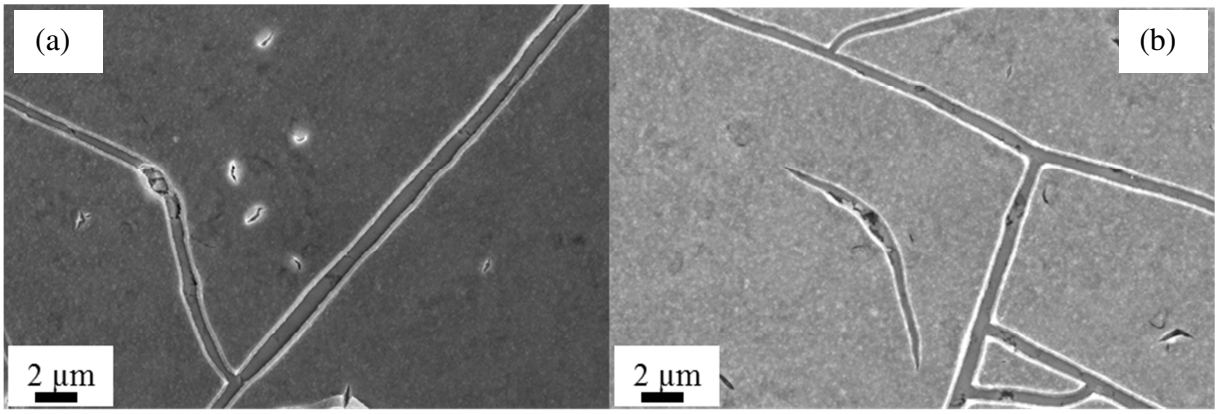

Figure 7.18: SEM images of the printed layer surface onto porous NiO/YSZ of (a) ink 0.25 and (b) ink 0.5.

Figure 7.18 (a) shows the surface view of the calcined ink 0.25 onto porous NiO/YSZ. The film is broken in large cracks that were not observed before. These large cracks could result from a not optimized calcination/sintering profile for this substrate. However the number of cracks due to substrate porosity is clearly reduced and a few defects are observable onto the surface of the film. The quality of the film could be improved by working in a dust-free environment such as a clean room. Similar observations were made on the film surface of calcined ink 0.5 (Figure 7.18 (b)), with large cracks and defects but still reduced compared to films made with reactive inks. The origin of these cracks was attributed to both the presence of pores in the substrate, the irregularity of the substrate and the high shrinkage of the reactive film. According to Figure 7.8 the shrinkage is not affected when the inks solid loading is below 0.5 vol%, which is the case with of the two hybrid inks. Yet, a significant improvement in terms of cracking was observed, demonstrating that the surface of the substrate is mainly responsible for the crack formation above pores. In summary observations on both types of substrates demonstrate that the hybrid ink concept shows interesting potential in yielding thin films onto dense and porous substrates, and that substrate surface quality plays a major role into a successful deposition. Higher nanoparticle concentration should be tried in future work to ensure full percolation of the nanoparticles.

7.2.5 Electrical characterization

The films printed onto sapphire showed in Figure 7.17 (b)-(e) were used for the electrical characterization. As for the reactive inks, the ionic conductivity of the calcined thin film was measured by electrochemical impedance spectroscopy (EIS) in air between 500-750 °C. The measurements were taken in the lateral configuration, i.e. in-plane electrodes deposited on the film surface (see drawings Figure 4.19). Total conductivity and activation energy (E_a) were then

calculated from the measured real impedance components (R_{el}) at different temperatures and normalized for the electrolyte/thin film geometry. Figure 7.19 shows the Arrhenius plot of the films on quartz and alumina calculated from the EIS data at different temperatures.

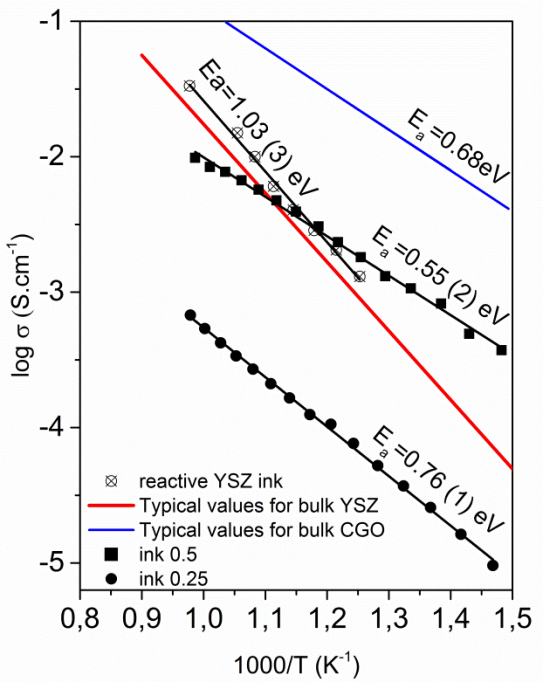

Figure 7.19: Arrhenius plot of the films on sapphire calculated from the EIS data at different temperatures along with typical conductivity values reported for YSZ thin film (red line,[7]**) and CGO bulk (blue line** [8] **)and values obtained for the reactive ink YSZ film (Chapter 6).**

For comparison typical YSZ [7] and CGO [8] bulk conductivities measured by EIS are shown as well as Arrhenius plots from previous studies of reactive ink in Chapter 6. The calculated activation energies are 0.76 eV (ink 0.25) and 0.55eV (ink 0.5). The conductivity of these films is much lower than the one observed for CGO. However, films made with ink 0.5 shows a higher conductivity than the reactive ink in the range 400-600 °C. The conductivity increases with increasing solid loading, which is explained by the increasing amount of CGO and the percolation. On the other hand, the activation energy decreases with increasing solid loading. An explanation is the increasing amount of grain boundaries due to the size of the nanoparticles, resulting in electronic conductivity instead of ionic conduction.

7.2.6 Summary for YSZ/YSZ and YSZ/CGO hybrid inks

In this study, hybrid inks consisting of nanoparticles suspended into a reactive ink were successfully developed and optimized for inkjet printing deposition. The addition method of nanoparticles, as well as their nominal size, has a strong influence on the film quality. Colloidal particles lead to film cracking due to the particle size, and non-stabilized particles quickly agglomerate and do not fulfill inkjet printing requirements. Particles have to be stabilized upon addition into the reactive ink and to be smaller than the final film thickness. Nanoparticles made by hydrothermal synthesis fulfill these requirements and hybrid inks made of different solid loading could be printed onto various substrates. Addition of particles strongly reduced the global shrinkage and the cracks due to porosity. Particularly, the study showed that the cracks observed in reactive ink printing onto porous substrates originate mainly from the substrate surface quality and not from the shrinkage.

The last part of the chapter deals with a different application of hybrid inks. In this part a solid state reaction is performed between particles and the reactive ink *in-situ* to synthetize a pure new phase at high temperature.

7.3 **Synthesis of bismuth titanate by *in-situ* solid state reaction using hybrid inks**

Some of the results described in this section were published published as proceeding paper for "the 230th International Academic Conference on Engineering, Technology and Innovations (IACETI), Bangkok, Thailand" 2017, (**Paper III**)and in "*Materials Letters"*,(**Paper IV**).

In the previous study, a composite hybrid ink i.e. based on one or two different materials (YSZ/YSZ and CGO/YSZ) was developed for the elaboration of electrolyte for fuel cell. Along the development of this ink, it was considered that this ink concept could be further explored. A proposed design consists in a synthetic method combining two different materials, one as colloid and one in the reactive ink, that react at a certain temperature to form a new phase as *in-situ* solid state reaction (SSR). The hybrid ink is prepared by suspending the colloids into the reactive inks, deposited and the new phase is formed after calcination. The global synthesis principle is summarized in Equation 7.1:

$$xA_{(s)} + yB_{(l)} \xrightarrow{Printing+T} A_xB_{y\,(s)} \qquad \textbf{Equation 7.1}$$

SSR synthesis is a widely spread technique to synthetize materials. However it is challenging with some materials to obtain a pure phase and avoid the formation of secondary phases that can alter the final properties. Furthermore, the SSR technique yields generally agglomerated and coarsened particles, with limitations on microstructural control and processing flexibility. It is particularly the case of bismuth and bismuth oxide compounds. These are generally highly diffusive and volatile. High temperature treatments in SSR can thus easily lead to bismuth evaporation, resulting in a poor control on composition, phases and properties [9]. Using hybrid inks, the final phase is formed during heat treatment of the suspension via solid state reaction, while the colloids powder is covered by nanoparticles coming from the sol-gel reaction and not directly exposed to air, as in SSR. To assess this hypothesis, the focus was set on the development of bismuth titanate $Bi_4Ti_3O_{12}$ (BiT).

BiT is considered one of the most promising high temperature lead-free piezoelectric materials [10,11]. It exhibits a high Curie temperature (T_c = 675°C) [12], very low fatigue and high dielectric constants [10], which makes it a potential candidate for applications in piezoelectric devices, memory storage (FERAM) in a wide range of high temperature environment, and electro optics devices [13,14].

BiT powder is usually prepared via solid state reaction (SSR) [15,16] by milling stoichiometric amount of bismuth oxide Bi_2O_3 and titania TiO_2 which can lead to the formation of secondary phases due to bismuth evaporation. Several wet-chemical techniques such as sol-gel [17], co-precipitation [18], hydrothermal [19] or polymeric precursor synthesis [20] can be alternatives to SSR to produce BiT powder. These techniques allow a better control of powder microstructure, stoichiometry and particle size and lead to enhanced properties. However, bismuth salts or alkoxides can be difficult to handle, while bismuth oxide powders are readily available, cheap and harmless. Here, bismuth titanate is prepared via a novel wet route by mixing bismuth oxide powder and the stable titanium reactive ink developed in chapter 5. The chemical reaction is described in Equation 7.2.

$$2Bi_2O_{3_{(s)}} + 3TiO_{2_{(l)}} \xrightarrow{Printing+T} Bi_4Ti_3O_{12_{(s)}} \qquad \textbf{Equation 7.2}$$

7.3.1 Bismuth titanate preparation and characterization

The first step is to verify if this process leads to the synthesis of pure bismuth titanate without secondary phases. As such an ink was prepared by directly adding the bismuth oxide particles into the TiO_2 reactive ink. The titania based reactive ink was prepared following the experimental protocol described in section 6.1.1 (p.101). Titanium (IV) isopropoxide ($Ti(OPr)_4$ (hereafter TiTTIP, Sigma-Aldrich)) and N-methyldiethanolamine (MDEA, Sigma-Aldrich) were mixed for 5 minutes under argon to avoid uncontrolled reactions (*i.e.* hydrolysis and condensation) between air humidity and the metal precursor. The molar complexation ratio was x = [MDEA]/[TiTTIP] = 4. Ethanol and water were separately slowly added to the TiTTIP/MDEA blend and mixed for 5 minutes. The ratio between ethanol and water was 40/60 vol %. Commercial β-bismuth oxide (Alfa Aesar) colloidal particles (particle size = 2µm) was added in the reactive ink in stoichiometric proportions to obtain $Bi_4Ti_3O_{12}$. Figure 7.20 summarizes the preparation protocol.

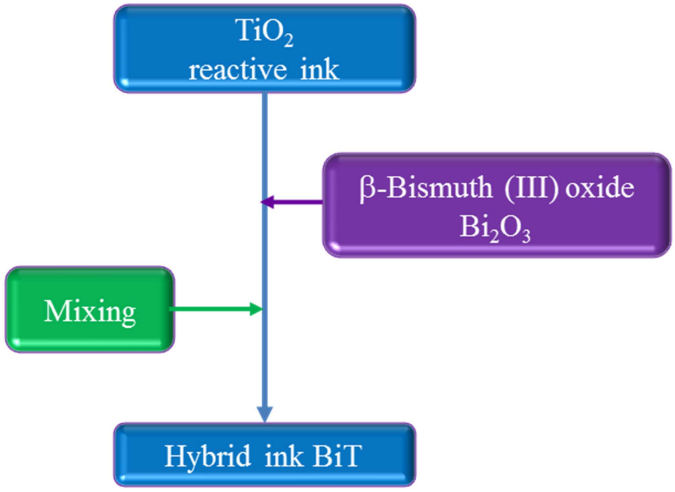

Figure 7.20: Preparation protocol of BiT ink

After mixing for 30 minutes the ink was dried at 120°C to remove the excess of water until a yellow paste was obtained. The paste was placed into several crucibles and calcined at different temperatures in air between 500°C and 800°C. The obtained powders were analyzed by X-ray diffraction to determine the crystallization temperature threshold and detect the potential presence of secondary phases. Figure 7.21 shows the XRD pattern of the powders calcined at different temperatures between 500 °C and 850 °C.

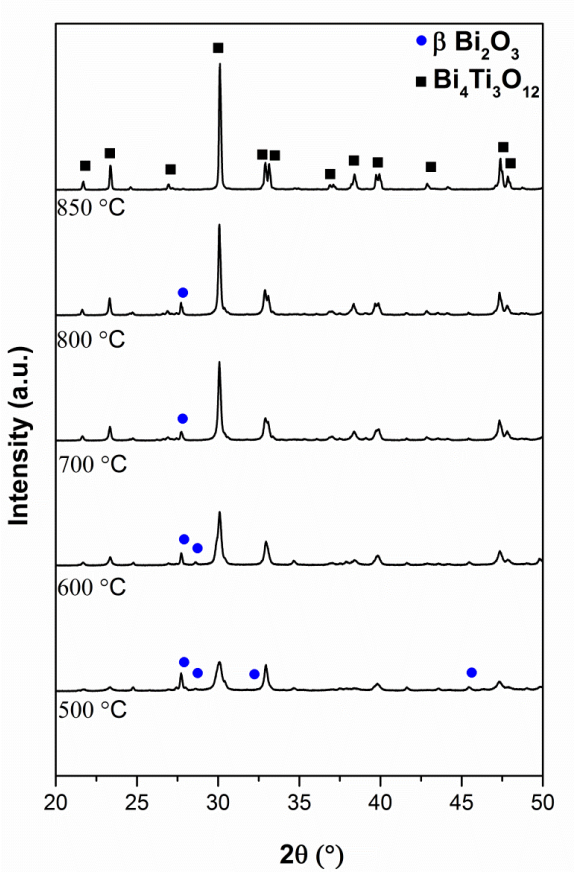

Figure 7.21: X-ray diffraction patterns of BiT powders after calcination at different temperatures.

The powder calcined at 500 °C exhibits a yellow color due to the presence of Bi_2O_3, which is confirmed by the XRD pattern. As the temperature increases the powders become whiter due to Bi_2O_3 loss and appearance of the BiT phase. The XRD patterns show the onset of the crystalline BiT in agreement with literature [21]. BiT has a Curie temperature (T_c) of 675 °C; hence the crystal belongs to a pseudo-tetragonal phase below T_c and pseudo-orthorhombic phase above. The splitting of the reflection at $2\theta \approx 33$ ° in the XRD patterns recorded at 700, 800 and 850 °C suggests indeed that these crystals have a pseudo-orthorhombic structure [21] at these temperatures. Finally the pattern recorded 850 °C exhibits a well-defined BiT crystalline structure. Moreover no signal from the Bi_2O_3 crystalline phase can be detected. As the temperature increases, the peak width decreases, corresponding to crystallite size increase. This suggests that the particles agglomerate and probably sinter during the heat treatment, leading to grain growth. The lattice parameters of the BiT phase in the sample calcined at 850 ˚C were a = 5.41 Å, b = 5.448 Å, and c = 32.84 Å, which are comparable with the values given in JCPDS 72-1019. Finally, within the limit of the XRD technique, no bismuth and/or titanium based secondary phases could be detected in the XRD patterns. To confirm that no secondary phases have been formed during the calcination, thermal analysis has been

performed on the paste obtained at room temperature. Moreover a dilatometry analysis has been performed on a pellet composed of the powder calcined at 500°C to evaluate the sintering temperature range. Figure 7.22 shows the thermogravimetric analysis (TGA) of the gelled ink coupled with the dilatometry plot of the pellet.

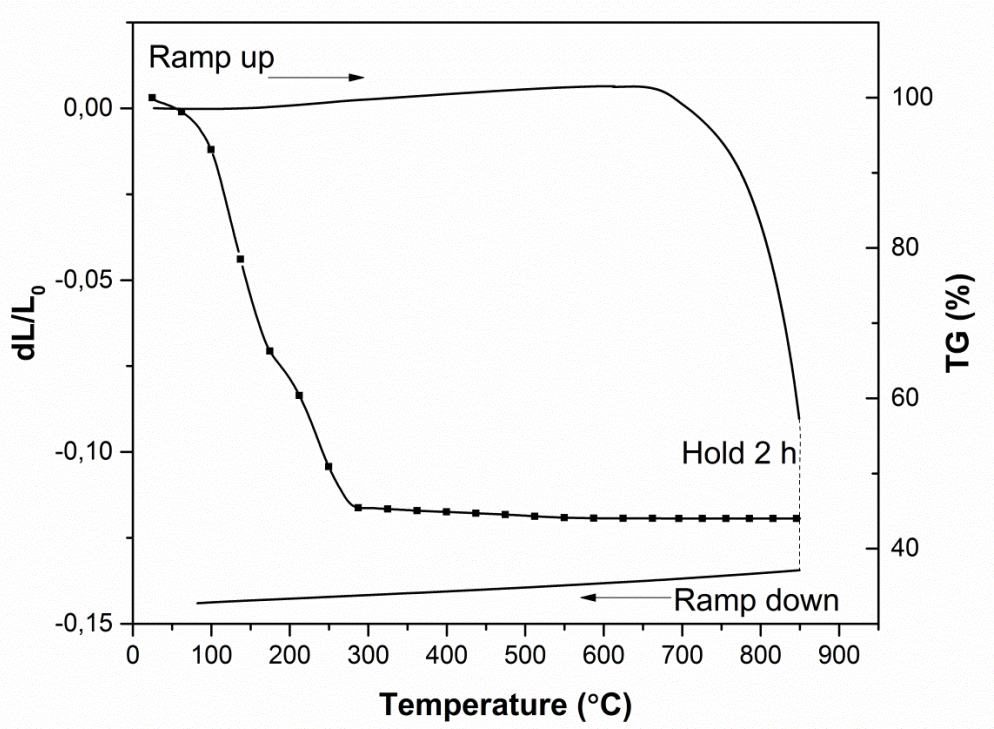

Figure 7.22: Thermogravimetric (symbols with line) and dilatometry (line) measurements of respectively a gelled ink and a BiT calcined at 500 °C from room temperature to 850 °C.

The TGA curve exhibits a strong mass loss between room temperature and 300°C due to organic burn off. From 300 to 850 °C no mass loss can be detected indicating that the bismuth oxide, trapped in the sol gel, does not evaporate even at high temperature, for which such phenomenon was observed [9]. A pure BiT phase can thus be obtained as the necessary stoichiometric ratio to obtain this phase is preserved. The sintering behavior of the pellet was studied by using a dilatometry measurement. No shrinkage is occurring between room temperature and 600 °C; a small expansion (0.1%) can however be noticed in that temperature range, due to chemical reactions and/or crystal lattice rearrangements. The shrinkage starts from 600°C and the highest size reduction is recorded between 700 and 800°C, leading to 14 % shrinkage. The measured density is 6.79 g/cm^3, which is in good agreement with literature [22].

Figure 7.23 shows SEM image of the powder calcined at 850°C for 1 h.

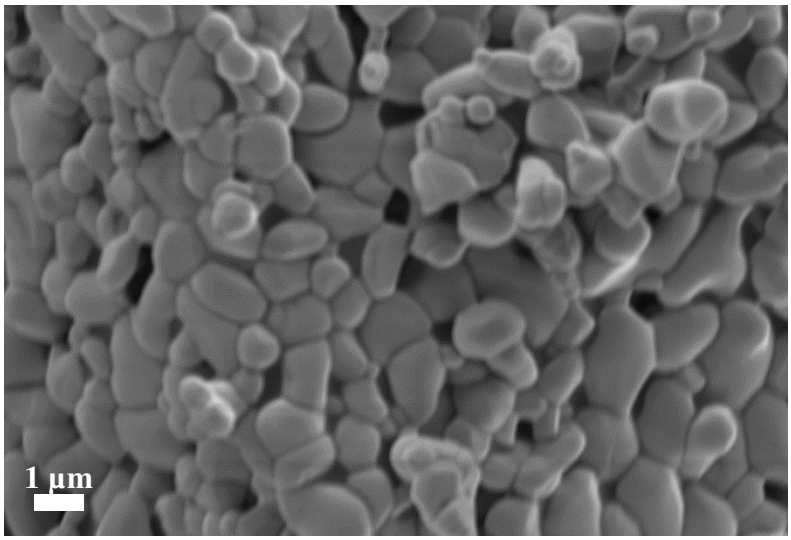

Figure 7.23: SEM image (secondary electrons) of BiT powder calcined at 850°C

Figure 7.23 shows that the grains are elongated and coarse (width > 1 µm). Despite a carbon coating prior to observation, the particles were difficult to observe due to the high dielectric constant of the material. Figure 7.24 shows the dielectric constant measurement of a BiT pellet calcined at 850°C together with measurements performed on powders synthetized by other processing routes [11,23,24].

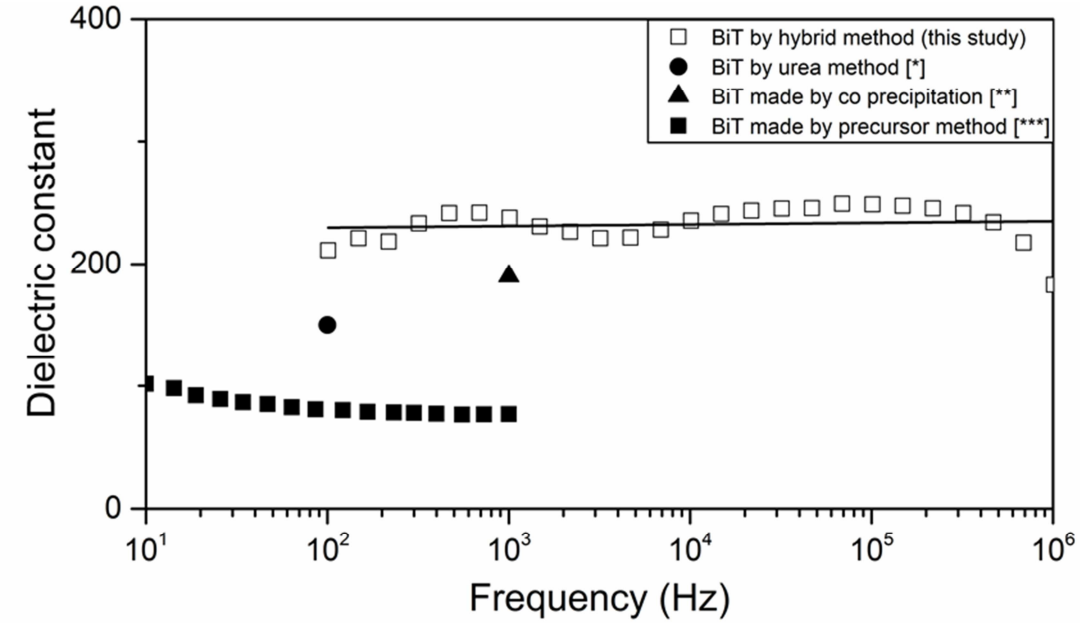

Figure 7.24: Dielectric measurement by impedance spectroscopy of BiT pellet calcined at 850 °C along with values reported for powder synthetized by urea method (*=[23], co precipitation (=[11]) and using polymeric precursors (***= [24]).**

Figure 7.24 shows that the average value of the dielectric constant at room temperature for this sample is 227 (value fitted linearly) which is approximatively 20% higher than those obtained on samples synthesized by other techniques. This result emphasizes the importance of the powder preparation method and demonstrates that using the hybrid concept leads to enhanced material properties.

These measurements showed the strong potential of this processing method to produce pure phases by *in-situ* SSR. The next step in the development is to fabricate a stable ink that can be deposited by inkjet printing *i.e.* that has suitable particle size and printability.

7.3.2 Ink preparation and characterization

A similar ink was produced and left to mill for 2 days to mill the particles. Figure 7.25 shows the aspect of the ink after 2 days of milling.

Figure 7.25: Aspect of the ink after 48 hours milling.

Figure 7.25 shows that the ink has fully gelled after 2 days of milling and cannot be processed by inkjet printing. As shown in section 6.1.1 (p.101), the reactive ink used here to suspend the bismuth oxide particle is stable for more 1200 hours, so it seems that the presence of bismuth oxide is destabilizing the reactive ink, probably by bonding either to the MDEA, which prevent it to shield the Ti cation to water attack, or to the Ti cation itself. To understand the mechanism of gel formation, inks at different stage of milling were characterized by FTIR spectroscopy. Figure 7.26 shows IR spectra for the ink in the entire range of frequencies explored.

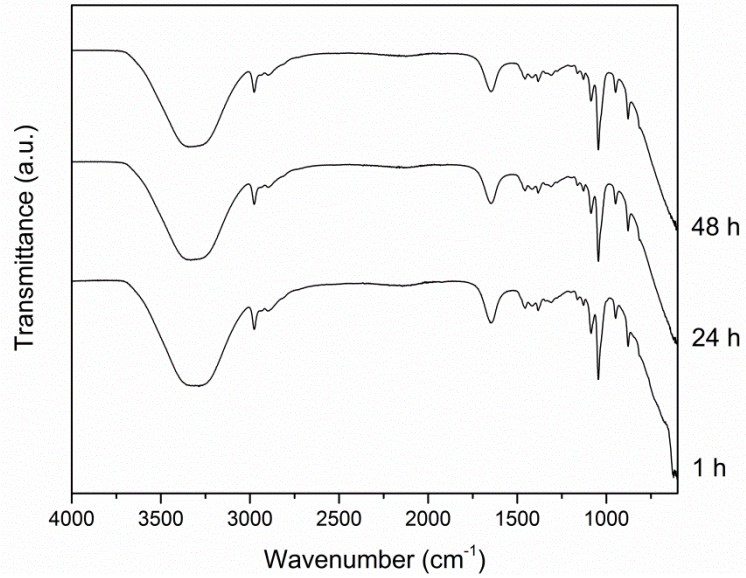

Figure 7.26: FTIR spectra for the ink after 1h, 24h and 48h milling

Figure 7.26 shows that the peaks positions and shape are similar for all milling time, indicating that no bonding involving organics is occurring during the gelation. Possible interactions are then to be found among metallic interactions. However, the wavenumbers for such elements are in a lower frequency range, and the equipment used for these measurements does not allow carrying out measurements in that frequency value area. Such measurements would be valuable to fully understand the destabilization mechanisms that lead to ink gelation. Raman spectroscopy is also an alternative method that could give valuable information to the bonding mechanisms.

In summary, the nominal particle size of bismuth oxide particle is too large to be printed, and the milling of the suspension leads to fast gelation of the hybrid ink, making it not usable for inkjet printing. For future research, several suggestions are presented. The identification of the gelation mechanism is a first crucial step to design the ink, and it can be performed by studying cation interaction using either FTIR or Raman spectroscopy at low frequencies. The preparation of the ink can also be improved by using smaller starting particles to limit the milling time; however smaller particles is synonym of larger surface area and increased reactivity, which can lead to a faster gelation.

While the ink could not be used for inkjet printing due to high viscosity and instability, its properties are suitable for other ceramic processes that require high viscosity such as screen printing, tape casting, extrusion or additive manufacturing techniques other than inkjet. 3D printing has been chosen as an alternative process

7.3.3 3D printing of bismuth titanate using hybrid inks

Three-dimensional printing, also well-known as the extrusion-based fuse deposition modeling (FDM) is one of the most attractive fabrication techniques for fabrication of three dimensional objects [25]. There are several advantages to this technique compared to traditional ceramic fabrication processes due to its ability to provides objects with complex geometries in short processing time, relatively low operating cost, user friendliness and the fact that it allows various types of printing materials [26]. As such, a three dimensional bismuth titanate (3D- BiT) by a two-step assembly method was fabricated, using the hybrid ink concept coupled with FDM technique, with the aim to develop 3D-BiT object with complex shape. For purposes of clarity, the hybrid ink will now be called hybrid gel.

Prior to printing the viscosity of the hybrid gel should be adjusted to match the requirements for FDM. A BiT gel was mixed with various amounts of PVP from 1.0 to 20% vol. The mixtures were then stirred at room temperature with constant stirring for 30 min until homogeneous thick pastes appeared. The resulting thick pastes were subjected to ultrasonic agitation at a frequency of about 24 kHz for 30 minutes.

The rheology characteristic of BiT thick paste with different % vol of PVP was evaluated before printing to find the suitable printing condition. The thick paste materials were characterized in rotational mode with controlled constant temperature of 21 °C. All the experiments were performed using a cone-parallel spindle of 25 mm in diameter and 4° angle (CP25-4). For non-Newtonian fluids, the relation between wall shear rate ($\dot{\gamma}_w$) and extrusion printing speed (v) can be obtained by the Rabinowitsch relation (Equation 7.3) [27]:

$$\dot{\gamma}_w = \frac{(3n+1)}{4n}\left(\frac{4Q}{\pi R^3}\right) \qquad \textbf{Equation 7.3}$$

where R is the capillary radius of nozzle (mm), Q is the volumetric flow rate through the capillary nozzle (mm^3/s), and *n* is a constant equal to the power-law index.

The extrusion printing speed (v) could be obtained by substituting $Q = \pi R^2 v$ in Equation 7.4:

$$\dot{\gamma}_w = \frac{(3n+1)}{4n}\left(\frac{8v}{D}\right) \qquad \textbf{Equation 7.4}$$

where v is the extrusion printing speed ($mm.s^{-1}$) and D is diameter of capillary nozzle (mm).

The rheological properties of the BiT thick paste materials with different content of PVP were investigated to optimize the printing condition. Figure 7.27 shows the rheological properties of the pastes with different amount of PVP.

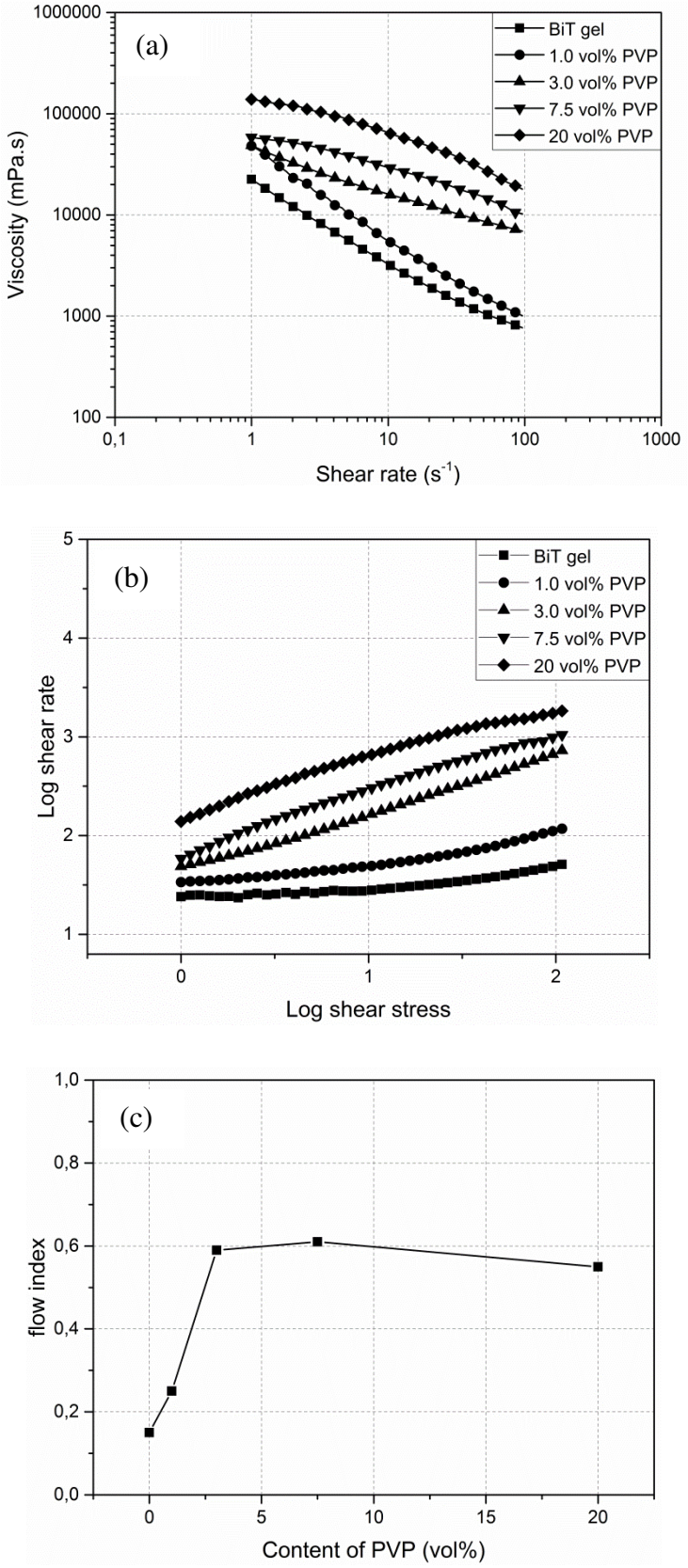

Figure 7.27: (a) Viscosity plot and the corresponding (b) double logarithmic power law plot for the complete series of BiT series showing the flow index (slope) and (c) flow index plot with different content of PVP.

Figure 7.27 (a) shows that at higher % vol of PVP the viscosity profiles are shifted to higher values of viscosity. This is due to the presence of high molecular weight PVP (Mw ≈ 1.300.000 $g.mol^{-1}$) which give resistance to the flowing behavior under applied shear stress [28,29].

Besides nozzle diameter and viscosity of the material, shear thinning behavior facilitates continuous flow through fine nozzles without clogging. Generally, this behavior is quantitatively estimated by evaluating the flow indexes (n). Figure 7.27 (b) shows the double logarithmic plot for the BiT composites; the slope of the straight line corresponds to the flow index (n) that can be used to identify the flowing mechanism of a system [30–33]. As shown in Figure 7.27 (c), all samples exhibit shear-thinning behavior (n < 1), lower n value indicating more-shear thinning activities. The increasing of the flow index (n) was observed when increasing the PVP content from 1.0% vol to 7.5% vol and whereas it slightly decreases when the PVP content is exceeding 7.5% vol.

Typically, the processing shear rate of extrusion process is in the range 1-100 s^{-1} [34]. Figure 7.28 shows the extrusion printing speed (v) (calculated from Equation 7.4).

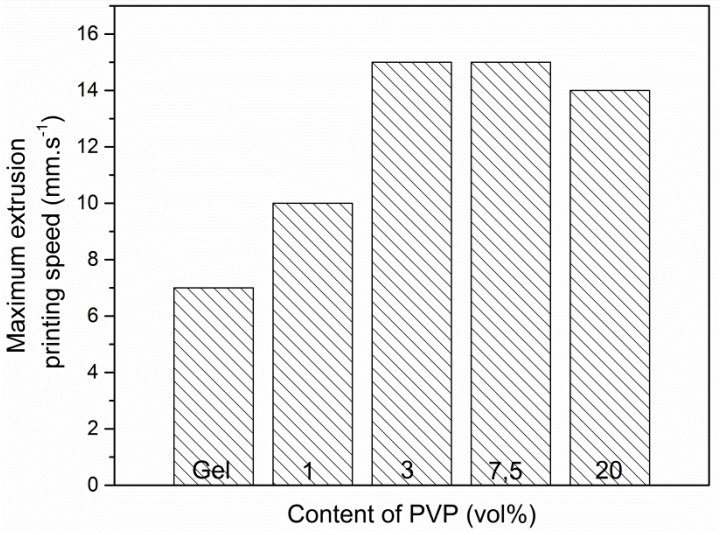

Figure 7.28: Processing window for BiT gel and its composite for 1.4 mm of extrusion nozzle.

Figure 7.28 shows that the extrusion printing speed could be expanded from 1 to 15 mm/s by increasing the PVP content at 3.0 vol% of PVP. Over this quantity of PVP, there is no significant effect of further PVP addition. By adjusting the PVP content the processing speed is expanded by 53%. The PVP molecules acts as processing aid which could reduced the wall shear rate ($\dot{\gamma}_w$) corresponding to the ability of printing at higher extrusion speed. Based on rheology results the BiT with 3.0% vol of PVP was selected for fabricating 3D objects by FDM technique.

The hybrid paste was transferred to an extrusion syringe with fixed nozzle of diameter 1.4 mm and then was printed by 3D printer (Zmorph 2.0S, ZMorph Sp. z o.o., Poland). Figure 7.29 shows the fabricated 3D-BiT object by extrusion-based FDM technique.

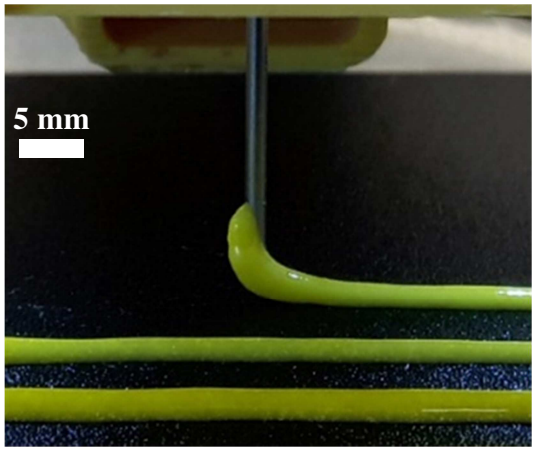

Figure 7.29: Extrusion based FDM technique for BiT at 3.0 vol% of PVP (3D-BiT).

Figure 7.29 shows that the optimized hybrid paste could be properly extruded by FDM and reproducible lines were deposited. By this technique, we could produce the printed object as complex shape with highly precise shape and dimension. However it was noticed that the paste drying was slow, limiting the possibility of building up objects for the time being. In future work, focus should be set on optimizing the drying behavior of such ink upon deposition without affecting the processing.

7.3.4 Summary for synthesis of bismuth titanate *via* reactive inks

In this study pure bismuth titanate $Bi_4Ti_3O_{12}$ was synthetized by using a novel hybrid ink concept consisting of bismuth oxide nanoparticles suspended into a titanium reactive ink and showed enhanced dielectric properties. However, uncontrolled gelification occurred in time making the ink unsuitable for inkjet printing deposition. The origin of such instability is believed to originate from an interaction between bismuth and titanium. The ink viscosity was adapted for 3D printing deposition by addition of a viscous component, i.e. PVP, and an optimal amount was determined for proper deposition. The ink could then be 3D printed as lines. However, the drying behavior needs to be optimized for deposition of complex objects.

7.4 **Conclusion**

In this chapter, hybrid inks consisting of crystalline particles in suspension in a reactive ink were successfully designed for inkjet printing. Optimal printing conditions (particle size, printability) were obtained by investigating different preparation methods and nominal particle sizes. They showed that particles should be stabilized prior to addition into the reactive ink to avoid agglomeration. Using commercial colloidal particles could solve the cracking issues observed on films printed using reactive inks on porous substrates, especially by reducing shrinkage and filling up pores. However, cracks at the particle/film interface were observed, due to a particle size larger than the film thickness. This issue was solved by using nanoparticles synthetized by continuous hydrothermal synthesis.

Hybrid inks can also be used to realize *in-situ* solid state reactions. As such pure bismuth titanate was synthetized by calcining at 750 °C a suspension of bismuth oxide particles in a titanium-based reactive ink. However, the suspension is unstable and gels at room temperature as a paste that cannot be used for inkjet printing. The paste was however optimized for 3D printing and lines could be deposited. Optimization of the paste is however necessary to fabricate 3D complex objects in the future.

Bibliography

[1] P. Carpio, E. Bannier, M.D. Salvador, A. Borrell, R. Moreno, E. Sánchez, Effect of particle size distribution of suspension feedstock on the microstructure and mechanical properties of suspension plasma spraying YSZ coatings, Surf. Coatings Technol. 268 (2015) 293–297. doi:10.1016/j.surfcoat.2014.08.063.

[2] Z. Fang, Supercritical Water, Rapid Prod. Micro- Nano-Particles Using Supercrítical Water. (2010) 92.

[3] E. Lester, M. Poliakoff, J. Li, B. Guy, N. Tinsley, P. Blood, Scale up production of nanoparticles using hydrothermal synthesis, NSTI-Nanotech 2007. 4 (2007) 316–319. http://www.nsti.org/publications/Nanotech/2007/pdf/1371.pdf%5Cnhttp://www.nsti.org/publications/Nanotech/2007/pdf/1371.pdf#page=1&zoom=auto,-99,798.

[4] D.W. Ni, J.A. Glasscock, A. Pons, W. Zhang, A. Prasad, S. Sanna, N. Pryds, V. Esposito, Densification of Highly Defective Ceria by High Temperature Controlled Re-Oxidation, J. Electrochem. Soc. 161 (2014) F3072–F3078. doi:10.1149/2.0121411jes.

[5] V. Esposito, D.W. Ni, D. Marani, F. Teocoli, K.T. Sune Thydén, D.Z. De Florio, F.C. Fonseca, Accelerated ceria–zirconia solubilization by cationic diffusion inversion at low oxygen activity, J. Mater. Chem. A. 4 (2016) 16871–16878. doi:10.1039/C6TA06308J.

[6] Y. Xu, Continuous Hydrothermal Flow Synthesis of Functional Oxide Nanomaterials Used in Energy Conversion Devices, (2017).

[7] J. Jiang, J.L. Hertz, On the variability of reported ionic conductivity in nanoscale YSZ thin films, J. Electroceramics. 32 (2014) 37–46. doi:10.1007/s10832-013-9857-1.

[8] M. Shirpour, G. Gregori, R. Merkle, J. Maier, On the proton conductivity in pure and gadolinium doped nanocrystalline cerium oxide, Phys. Chem. Chem. Phys. 13 (2011) 937–940. doi:10.1039/C0CP01702G.

[9] V. Esposito, B.H. Luong, E. Di Bartolomeo, E.D. Wachsman, E. Traversa, Applicability of Bi[sub 2]Ru[sub 2]O[sub 7] Pyrochlore Electrodes for ESB and BIMEVOX Electrolytes, J. Electrochem. Soc. 153 (2006) A2232. doi:10.1149/1.2358088.

[10] Z. Lazarevic, B.D. Stojanovic, J. a. Varela, An approach to analyzing synthesis, structure and properties of bismuth titanate ceramics, Sci. Sinter. 37 (2005) 199–216. doi:10.2298/SOS0503199L.

[11] F. Zhang, T. Karaki, M. Adachi, Preparation and characterization of nanosized Bi4Ti3O12 powders, Jpn. J. Appl. Phys. 47 (2008) 640. doi:10.1143/JJAP.45.7385.

[12] T. Takenaka, T. Gotoh, S. Mutoh, T. Sasaki, A new series of bismuth layer-structured ferroelectrics, Jpn. J. Appl. Phys. 34 (1995) 5384–5388. doi:10.1143/JJAP.34.5384.

[13] E.. Subbarao, A family of ferroelectric bismuth compounds*, J. Phys. Chem. Solids. 23 (1962) 665–676.

[14] a. Q. Jiang, G.H. Li, L.D. Zhang, Dielectric study in nanocrystalline Bi[sub 4]Ti[sub 3]O[sub 12] prepared by chemical coprecipitation, J. Appl. Phys. 83 (1998) 4878. doi:10.1063/1.367287.

[15] H.S. Shulman, M. Testorf, D. Damjanovic, N. Setter, Microstructure, Electrical Conductivity, and Piezoelectric Properties of Bismuth Titanate, J. Am. Ceram. Soc. 79 (1996) 3124–3128. doi:10.1111/j.1151-2916.1996.tb08086.x.

[16] M. Villegas, C. Moure, J.F. Fernandez, P. Duran, Low-temperature sintering of submicronic randomly oriented Bi4Ti3O12 materials, Ceram. Int. 22 (1996) 15–22. doi:10.1016/0272-8842(95)00047-X.

[17] A. V Prasada Rao, A.I. Robin, S. Komarneni, Bismuth titanate from nanocomposite and sol-gel processes, Mater. Lett. 28 (1996) 469–473. doi:10.1016/0167-577X(96)00107-3.

[18] P.H. Xiang, Y. Kinemuchi, T. Nagaoka, K. Watari, Sintering behaviors of bismuth titanate synthesized by a coprecipitation method, Mater. Lett. 59 (2005) 3590–3594. doi:10.1016/j.matlet.2005.07.002.

[19] Q. Yang, Y. Li, Q. Yin, P. Wang, Y.B. Cheng, Bi4Ti3O12 nanoparticles prepared by hydrothermal synthesis, J. Eur. Ceram. Soc. 23 (2003) 161–166. doi:10.1016/S0955-2219(02)00087-0.

[20] M.. Pechini, Method of Preparing Lead and Alkaline Earth Titanates and Niobate$ and Coating Method Using the Same To Form a Capacitor, 3,330,697, 1967.

[21] P. Pookmanee, S. Phanichphant, Characterization of Bismuth Titanate Powders, Adv. Mater. Res. 26–28 (2007) 247–250. doi:10.4028/www.scientific.net/AMR.26-28.247.

[22] S. Naz, S.K. Durrani, A.H. Qureshi, M.A. Hussain, N. Hussain, Nanosized bismuth titanate (Bi4Ti3O12) system drive through auto-combustion process by using suspension titania (TiO2), J. Therm. Anal. Calorim. 114 (2013) 719–723. doi:10.1007/s10973-013-3029-z.

[23] M. Anilkumar, S.R. Dhage, V. Ravi, Synthesis of bismuth titanate by the urea method, Mater. Lett. 59 (2005) 514. doi:10.1016/j.matlet.2004.10.038.

[24] A.Z. Simões, R.F. Pianno, C.S. Riccardi, L.S. Cavalcante, E. Longo, J.A. Varela, Dielectric properties of pure and lanthanum modified bismuth titanate thin films, J. Alloys Compd. 454 (2008) 66. doi:10.1016/j.jallcom.2006.12.066.

[25] H.P. Zhao, C.S. Ye, Z.T. Fan, 3D Printing of Calcia-Based Ceramic Core Composites, Adv. Sci. Technol. 88 (2014) 65–69. doi:10.4028/www.scientific.net/AST.88.65.

[26] K. Kim, W. Zhu, X. Qu, C. Aaronson, W.R. McCall, S. Chen, D.J. Sirbuly, 3D optical printing of piezoelectric nanoparticle-polymer composite materials, ACS Nano. 8 (2014) 9799–9806. doi:10.1021/nn503268f.

[27] A.. Collyer, D.. Clegg, Rheological measurement, Chapman & Hall, 1993.

[28] D. Wu, J. Wang, M. Zhang, W. Zhou, Rheology of carbon nanotubes-filled poly(vinylidene fluoride) composites, Ind. Eng. Chem. Res. 51 (2012) 6705–6713. doi:10.1021/ie2024454.

[29] S. Vidhate, A. Shaito, N.A. D'Souza, Crystallization, mechanical, and rheological behavior of polyvinylidene fluoride/carbon nanofiber composites, Polym. Polym. Compos. 112 (2008) 254–260. doi:10.1002/app.

[30] D. Marani, J. Hjelm, M. Wandel, Rheological analysis of stabilized cerium-gadolinium oxide (CGO) dispersions, J. Eur. Ceram. Soc. 34 (2014) 695–702. doi:10.1016/j.jeurceramsoc.2013.09.022.

[31] D. Marani, B.R. Sudireddy, J.J. Bentzen, P.S. Jørgensen, R. Kiebach, Colloidal stabilization of cerium-gadolinium oxide (CGO) suspensions via rheology, J. Eur. Ceram. Soc. 35 (2015) 2823–2832. doi:10.1016/j.jeurceramsoc.2015.03.043.

[32] D. Marani, B.R. Sudireddy, L. Nielsen, S. Ndoni, R. Kiebach, Poly(vinylpyrrolidone) as dispersing agent for cerium-gadolinium oxide (CGO) suspensions, J. Mater. Sci. 51 (2016) 1098–1106. doi:10.1007/s10853-015-9439-5.

[33] D. Marani, V. Esposito, B.R. Sudireddy, J.J. Bentzen, P.S. Jørgensen, D.W. Ni, F. Teocoli, R. Kiebach, Enhanced densification of thin tape cast Ceria-Gadolinium Oxide (CGO) layers by rheological optimization of slurries, Ceram. Int. 43 (2017) 5647–5653. doi:10.1016/j.ceramint.2017.01.098.

[34] Global Sabic, High & Low Shear Rate Rheology, (2013) 1–4. http://www.pod-sabic-ip.com/KBAM/Reflection/Assets/Thumbnail/10606_4.pdf.

Chapter 8 : Conclusions and outlook

8.1 **Conclusions**

In this thesis, inkjet printing has been used as a deposition technique for functional metal oxides thin films for energy production and storage devices. The technique has been described in terms of different droplet ejection mechanisms, ink/substrate interaction and ink requirements for the fabrication of functional thin films. Particularly, the ink requirements for ejection, especially particle size, viscosity and surface tension were thoroughly investigated and documented. Based on these requirements, the aim of the thesis was to develop suitable inks for inkjet printing of functional metal oxides thin films. The focus was particularly set on the particle size, ink printability, depending mainly on the viscosity, and the ink long term stability. Three different ink designs were investigated and their advantages/limitations were investigated. Drop-on-demand printers, i.e. thermal and piezoelectric based units were used to show the versatility of the inks with regards to the droplet ejection mechanism.

The first design consisted in colloidal particles suspended in aqueous medium using a low cost thermal inkjet printer (customized HP deskjet 1000). Suitable preparation methods yielded suitable inks in terms of particle size and printability for inks with different solid loadings. In the frame of SOFC development, a 1.2 µm YSZ electrolyte was successfully deposited with such inks on a porous NiO/YSZ anode. A sintering study showed that densification is reached at 1300°C. The study revealed that colloidal particle based inks are suitable for inkjet printing but not without some limitations such as a restrictive particle size, long processing time and high sintering temperature to reach full densification. Moreover the study put in evidence some limitations in using a low cost inkjet printer for this development of thin film. Missing droplets and imprecise deposition were observed in the deposition of single droplets of colloidal inks, and 5 printing passes were necessary to obtain a dense and tight electrolyte, making the process as it is not adapted as an industrial one. Finally an SOFC was tested with the electrolyte printed on a NiO/YSZ anode using an LSM/YSZ cathode, and produced an OCV above 1.15 V and a power peak density of 1.5 $W.cm^{-2}$ at 800°C.

The second ink design, which is called reactive ink, consisted of an aqueous alkoxide precursor based solution stabilized with a chelating agent to prevent premature alkoxide/water reaction (sol-

gel). The chelation mechanism was described using the case study of titanium ispropoxide, and was then successfully applied to the development of an ink based on a second alkoxide (zirconium propoxide). Printable and long-term stable inks were designed for the deposition of titania and YSZ thin films using a complexation ratio [MDEA]/[Alkoxide] of 4 for titanium and 12 for zirconium, allowing to quantify alkoxides reactivity. The study put in evidence the importance of different controlling parameters, when designing such inks for inkjet printing, such as the amount of chelating agent, the water/ethanol ratio and the alkoxide concentration, and their influence on the printability. Thin (100 nm), dense and defect-free thin films were deposited on dense and flat substrates with both printing technologies for both materials. However, cracked YSZ thin films were obtained on porous and irregular surfaces (NiO/YSZ anode) with cracks located above the pores, showing the importance of the substrate morphology. Finally, ionic conductivity measurements performed on YSZ films deposited on a dense substrate agree with data reported in literature.

The last design consisted in combining the colloidal and reactive ink concepts, *i.e.* suspending particles in the sol-gel based ink. Study on YSZ (particle)/YSZ (sol-gel) systems put in evidence the importance of particle addition method on the particle size distribution. Printable inks with different solids were successfully fabricated. Ink with solid loading as low as 4 vol% showed a significant decrease in shrinkage compared to reactive inks (ca. 30%) and a reduced presence of crack after calcination compared to reactive inks. Experiments also showed that using colloidal particles leads to broken films due to a particle size bigger than the film thickness. CGO nanoparticles made by continuous hydrothermal synthesis were used to replace colloidal particles at different solid loadings into the YSZ reactive ink and showed significant improvement in terms of cracking. However, crack free films were not obtained and further optimization is necessary on the ink (fabrication, calcination) and substrate surface. Electrical characterization on CGO/YSZ films showed lower conductivity than reported results, thought to be due to a lack of percolation of the CGO phase. Finally the ink concept was used for *in-situ* solid state reaction to obtain a pure phase at high temperature. This novel concept was tested through the synthesis of bismuth titanate $Bi_4Ti_3O_{12}$ (BiT) starting from bismuth oxide (particles) and stabilized (TiO_2). A pure BiT phase with enhanced dielectric properties could be obtained after ink calcination at 850°C, demonstrating the potential of such ink concept for the formation of a pure phase *in-situ*. However, uncontrolled ink gelation after 48 h aging time made the ink unsuitable for inkjet printing. The ink was then optimized for 3D printing by addition of PVP for viscosity adjustment and a solid object could be

deposited. The hybrid concept opened the path to a new way of designing composites and material synthesis *in-situ*. Moreover, it was shown that this ink concept is not limited to inkjet printing, which gives the freedom to use these inks with other processing methods.

8.2 **Outlook**

In this work, the development of the three ink designs for inkjet printing was performed and showed interesting results in all cases but also put in evidence the main issues for all inks. Nevertheless, these cases showed the high potential of inkjet printing in the development of functional thin films. Here further work for each ink design is suggested to overcome the issues observed and improve the process.

In Chapter 5, Issues observed with colloidal inks were due to the lack of precision of the printer, resulting in poor covering and the necessity to use multi deposition. As a suggestion, similar studies should be performed on a more stable printer to verify if the printer alone is at the origin of the non-tightness of the layer. Additionally, it would be of interest to determine the highest solid loading that can be used without affecting printability in order to reduce the amount of deposition to reach electrolyte tightness.

In Chapter 6, several issues with reactive inks were observed and unresolved, especially regarding crack formation on porous substrates. Further work should be focused on the resolution of the formation of cracks on porous substrates. Several solutions were suggested and tried such as the use of a sacrificial polymeric film, or the use of hybrid inks. While both solutions gave interesting preliminary results, they did not lead to crack-free films that can be used in applications. Hence focus should be set on these two methods and their optimization, particularly in terms of heat treatment. Another approach can also be considered, which consists in immersing the substrates in a polymeric solution that will fill up the pores and close the porosity. Upon calcination the polymeric filling with burn off and the dense film remain theoretically above the pores. Finally, the gelation triggered by the water/ethanol ratio in the case of titanium isopropoxide was not explained. Some interrogations still remain on the mechanism of the triggering, and particularly why this phenomenon occurs in the case of titanium isopropoxide and not for zirconium propoxide. Some additional tests, and particularly FTIR measurements on both inks (titanium and zirconium based) at different water/ethanol ratios could give some answers.

Finally in Chapter 7, issues related to the fast gelation of bismuth oxide/titanium reactive ink were identified. Preliminary results lead to think that the origin of the gelation is due to an interaction between bismuth and titanium but could not be proved. Future studies should be about understanding such mechanisms to find a methodology for preventing them. This interaction could be determined by performing FTIR or Raman spectroscopy at low frequency to see how the cations are interacting. Future activities should also be focused on the development of other systems with two or more materials, and not only limited to inkjet printing. Many material combinations can be designed, with imagination as the limit.

Inkjet printing is a very versatile process offering many possibilities, and despite its drawbacks is a promising deposition technique for devices in the future, both in research and in industry.

Appendices

Paper I:

Nucleophilic stabilization of water-based reactive ink for titania-based thin film inkjet printing

Journal of Physics and Chemistry of Solids 101 (2017) 10–17

Contents lists available at ScienceDirect

Journal of Physics and Chemistry of Solids

journal homepage: www.elsevier.com/locate/jpcs

Nucleophilic stabilization of water-based reactive ink for titania-based thin film inkjet printing

C. Gadea*, D. Marani, V. Esposito

DTU Energy, Technical University of Denmark, Risø Campus, Frederiksborgvej 399, DK 4000 Roskilde, Denmark

ARTICLE INFO

Keywords:
Inkjet
Thin film
Sol-gel
Rheology
Titania

ABSTRACT

Drop on demand deposition (DoD) of titanium oxide thin films (< 500 nm) is performed *via* a novel titanium-alkoxide-based solution that is tailored as a reactive ink for inkjet printing. The ink is developed as water-based solution by a combined use of titanium isopropoxide and n-methyldiethanolamine (MDEA) used as nucleophilic ligand. The function of the ligand is to control the fast hydrolysis/condensation reactions in water for the metal alkoxide before deposition, leading to formation of the TiO_2 only after the jet process. The evolution of the titanium-ligand interactions at increasing amount of MDEA is here elucidated in terms of long term stability. The ink printability parameter (Z) is optimized, resulting in a reactive solution with printability, Z, > 1, and chemical stability up to 600 h. Thin titanium oxide films (< 500 nm) are proved on different substrates. Pure anatase phase is obtained after annealing at low temperature (*ca.* 400 °C).

1. Introduction

Inkjet printing of inorganic materials has been spreading over the past years in several key technologies such as energy devices, sensors, electronics, biomedical applications and flexible electronics [1–8]. Research on inkjet printing of metal nanoparticles [9] and carbonaceous materials [10] have also been conducted. Such a rapid development is mainly due to its unique advantage of enabling a precise and selective deposition of materials into different architectures (thin films, 2D and 3D structures) with a very high resolution and minimal waste of materials [11–14]. The inkjet printing owns the further merits of being a low cost technique based on inks that can be easily formulated to be environmentally friendly. This fully meets the increasing demand on industry and academy to develop water-based systems for a more sustainable processing of materials [15–17].

Inkjet printing for inorganic materials is typically based on colloidal suspensions, *i.e.* a system containing oxide particles as solid loading. After deposition the printing is consolidated into a dense body either by the curing of special binders or *via* sintering process at high temperatures [12]. However, such a high temperature step might be incompatible with other components and substrates. In addition the formulation of a colloidal ink for inkjet printing requires very restrictive conditions in terms of particle size distribution and maximum solid loading, making colloidal inks challenging to design, stabilize and process [12,18].

Among alternatives particle-free systems to the colloidal approach, such as UV curable dielectric inkjet inks [19], an interesting one is using a reactive ink based on sol gel solutions. While reactive inkjet exists in diverse forms [20–23], sol-gel chemistry is a well-consolidated and versatile process which is used to synthesize metal oxide thin films and nano-structured materials at low temperature. By a combination of sequential reactions at room temperature, hydrolysis of metal alkoxide to form intermediate oxo-polymers and metal oxide polymeric condensation (by either dehydration or de-alcoholation), widely interconnected, extended and highly homogeneous 3D oxo-precursor structure is obtained [24]. Compared to the conventional colloidal approach, a lower consolidation temperature of such a precursor material is then expected, making reactive ink an attractive alternative. However, the alkoxide precursor can be extremely reactive towards the hydrolysis/condensation and highly sensitive to the presence of water at the different step of the printing. Zirconium, titanium, and tungsten alkoxides are just few examples of such high reactive precursors which cannot be used directly in presence of water. Such a strong reactivity makes the development of sol-gel solutions for inkjet printing in aqueous medium challenging. Dry conditions or specific atmospheres are generally required to manipulate these compounds and avoid uncontrolled reactions. Moreover, if not properly controlled, the ink could early react at the nozzle or even at the reservoir, leading to severe clogging of the printer.

A fine control over the sol-gel process can be achieved by nucleophilic ligands. These stabilize the alkoxides by coordinating the metallic center and forming more stable molecular complexes pre-

* Corresponding author.
E-mail address: chga@dtu.dk (C. Gadea).

http://dx.doi.org/10.1016/j.jpcs.2016.10.004
Received 23 July 2016; Received in revised form 19 September 2016; Accepted 17 October 2016
Available online 17 October 2016

cursors [25]. The hydrolysis/condensation reactions are thus inhibited and tolerance towards water is then achieved. Among the most used ligands there are carboxylic acids (*e.g.* acetic acid) [25] and alkanol amines (*e.g.* triethanolamine and methyldiethanolamine) [26,27]. Acidic ligands promote the rutile phase *via* a linear condensation of the reactants, whereas the anatase phase with a branched-like morphology is generally obtained in basic conditions [18–20]. A fine control of the precursors' reactivity is thus critical for the final morphology. However, unreactive ink can lead to wet and not resolved printings, with difficulties in the post-printing steps (*i.e.* drying, calcination, curing *etc.*). On the other hand, since chelating agent introduce electrostatic attraction in the solution, an excess of ligands can change the rheological properties, modifying the printability properties of the reactive inks.

In this work, we design a water-based TiO_2 reactive ink both with suitable printability features and characterized by remarkable long term stability. Titania is selected as case study for its high relevance in a variety of strategic technologies and because its potential of inkjet printing (either as colloidal or sol-gel ink) has been long proven [28–33]. Moreover, while the influence of ligands on the final properties of water-based titania reactive ink has been reported in a few cases [33], at the best of our knowledge, no studies describe the formulation and use of water-based reactive TiO_2 inks considering inkjet printability criteria and the limitations in the long term stability [33,34]. Further, we use an environmental friendly amine methyl-diethanolamine (MDEA) as basic nucleophilic ligand for the first time in water-based solution. This is selected to promote branch-like anatase polymerization which potentially better suit inkjet printing drop-by-drop processing.

2. Experimental

2.1. Ink preparation

Titanium (IV) isopropoxide ($Ti(OPr)_4$, hereafter TiTIP) (Sigma-Aldrich) was the titanium alkoxide precursor used in this study while n-methyldiethanolamine (MDEA, Sigma-Aldrich) was added as nucleophilic ligand to inhibit the reaction hydrolysis/condensation process. Mixing was carried out under argon to avoid uncontrolled reactions (*i.e.* hydrolysis and condensation) between air moisture and the metal precursor. TiTIP and MDEA were mixed and stirred for 5 min. Ethanol-water solution at 40–60 vol% ratio was separately prepared and slowly added to the TiTIP/MDEA blend and mixed for 5 min. To study the effect of MDEA on the final ink properties, inks at different molar ratio of complexation (*i.e.* x=[MDEA]/[TiTIP]=2, 4, 6, 8 and 10) have been prepared. Titanium concentration in the ink was kept at c=0.1 mg/l. The inks at different x are hereafter indicated as Ink$x$, where x refers to the molar ratio complexation and thus varies from 2 to 10.

2.2. Ink characterization

Rheological properties of the inks were explored using an Anton Paar rheometer (MCR 302), in rotational mode and at a constant temperature of 21 °C. A plate-plate measuring system was used with a diameter of 50 mm (PP50) and at gap distance of 0.5 mm under a solvent trap. The experiments were performed using three steps of pre-treatment: the first one at 0.1 s^{-1} for 1 min followed by 1 min at rest (0 s^{-1} shear rate), and the third one at 10 s^{-1} for 1 min. Flow curve measurements were conducted in step mode using 60 steps with a waiting time of 10 s. The shear rates investigated range from 1 s^{-1} up to 100 s^{-1}, in the up-ramp, and from 100 s^{-1} to 1 s^{-1} in the down-ramp. Viscosity was measured over time, from a few hours after preparation up to 1200 h (50 days) in order to estimate the long term stability. Ink surface tension was measured using a bubble pressure tensiometer (BP 50, Krüss), and density was evaluated by weighing 10 ml of ink. The printability of the inks was determined by calculation of their Z numbers defined as:

$$Z=\frac{\sqrt{\sigma\rho a}}{\eta} \quad (1)$$

where η is the ink viscosity (mPa s), σ is the surface tension (mN/m), ρ is the density (g/cm^3), and a is the characteristic length (μm) [35]. The parameter a is typically taken as the diameter of the printing nozzles [35].

Transmission FTIR spectra of the liquid inks were recorded in the 4000–400 cm^{-1} region, using a Perkin Elmer Spectrum Two spectrometer to clarify interactions between ligand and titanium central atom. The evolution of the crystallographic phase for material deriving from Ink4, was investigated using solid state detector, 0.01° step size, and 0.5 s step time (Bruker D8, Cu Kα radiation) and a hot chamber (MRI high temperature stage). A few droplets of ink aged for 600 h were dropped onto a platinum band inside the furnace chamber and diffraction patterns were recorded at different temperature between 100 °C and 750 °C using heating rate of 5 °C/s in a flow of air. Platinum XRD pattern was used as internal reference and crystallite size was determined using Scherrer Equation [36]. The value of the Cu-Kα radiation used for determination is 0.15406 nm and the k value is equal to 1.

Thermal analysis (DTA/TG) was performed on inks using a STA 409 PG (Netzsch) at a constant rate of 10 K min^{-1} under air.

2.3. Thin films deposition and characterization

Substrates used in this study are soda lime glass (Sigma Aldrich), indium tin oxide (ITO, Sigma Aldrich) and polycrystalline alumina (Keral 96, Kerafol). The surface free energy of the substrates has been measured using the methodology described in [37]. A commercially available thermal printer (HP Deskjet 1010) was used as a printing unit. The printer was modified to allow printing on flat and thick substrates (rigid or flexible) [12]. A compatible cartridge (HP 301 black) providing a 600×300 dpi resolution was cleaned to remove the original black ink and used to print the sol-gel inks. The cartridge contains 336 nozzles each having a diameter of 20 μm. To demonstrate the versatility of the inks a high resolution piezoelectric based printer (Pixdro LP 50) was also used. This printer is also equipped with a fiducial camera to observe droplet ejection. The print-heads are Spectra S class 128, equipped with 128 nozzles (nozzle diameter: 50 μm), using a firing frequency of 2.4 kHz. The waveform consisted in a 1 μs pulse to reach a voltage of 120 V, followed by a dwell of 1μs before going down to 0 V in 1 μs. The droplet velocity is 3 m/s. Printability numbers described earlier have been calculated based on the HP printer features. Each print made with both printers consists of a single layer. The printed layers were fired at 400 °C for one hour in air using a chamber furnace, with a heating ramp of 100 °C/h. Surface of the printed films was investigated by SEM (SUPRA 35, Zeiss) and with a numeric camera (NIKON D800).

3. Results and discussion

3.1. Inks properties

The printability of an inkjet ink is mainly controlled by its density, surface tension and viscosity [30,31,38,39]. For these physical properties, ranges of values ensuring the printability of the inks have been identified and associated with a dimensionless parameter indicated as Z number. Several authors attempted to define a reliable printability domain using the Z number. For instance, Jang et al. [40] proposed a range between 4 and 14, whereas Derby et al. [35] suggested values between 1 and 10. When Z number is outside this domains either no, poor or hardly stable and reproducible droplets can be can be ejected from the nozzle due to inadequate viscosity and/or surface tension

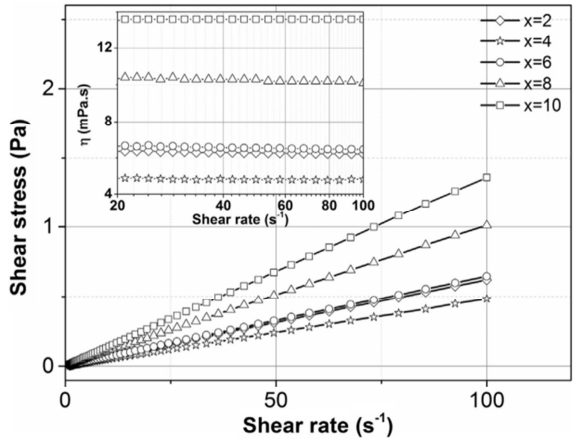

Fig. 1. Flow curves and viscosity curves (inset) for the five inks developed (4 h after preparation).

values [35]. The printability of the inks developed in this work was estimated with respect to both printability ranges.

In the case of reactive inks, the stability towards the hydrolysis/condensation process is a further crucial factor that affects printing behavior. In this regard, the selection of a suitable nucleophilic ligand and the identification of its optimal amount with respect to the alkoxide precursors is the main challenge.

In order to identify the optimal amount of MDEA, a series of inks having different molar complexation ratio x=2, 4, 6, 8, 10 were investigated for their viscosity, surface tension, and density and the corresponding Z number was then calculated. Fig. 1 shows the flow curves for the five prepared inks 4 h after the preparation, while the inset plot shows the corresponding viscosity curves. All the prepared inks exhibited a Newtonian behavior with constant viscosity independent on the shear conditions (inset). Accordingly, the viscosity values were simply determined from the slope of the flow curves. The obtained values together with measured values of the surface tension and the derived Z values for all the inks are reported in Table 1. A trend as function of the MDEA amount can be identified with the Ink4 possessing the lowest viscosity. The corresponding MDEA amount can be then recognized as the optimal amount that minimizes the interactions among the reactive components of the ink, thereby hindering the hydrolysis/condensation process. At lower amount of ligand (*e.g.* Ink2) a slightly higher viscosity value is obtained likely as a result of an inefficient "shielding" of the alkoxide towards water. Interestingly, when the amount of the ligand exceeds the optimal value (*e.g.* Ink6, 8, 10), even higher viscosity values are observed and likely associated with polycondensation of the alkoxide-ligand complexes [41]. However, the increments of MDEA content does not impact on the surface tension (see Table 1) as the observed values only vary in a range of few mN/m. For the printability, while all the inks (four hours after the preparation) possess a Z number within the printability

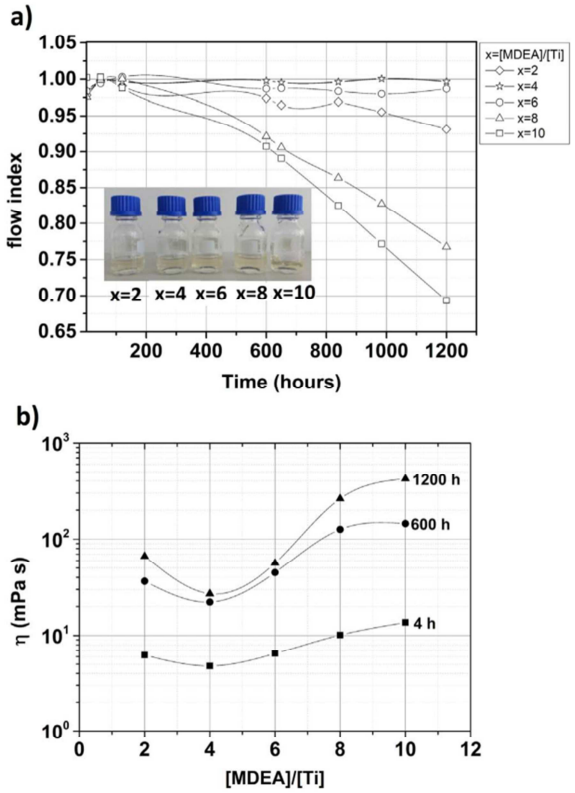

Fig. 2. Inks flow index measured over resting time (a) (inset: aspect of the inks after 1200 h of storage) and inks viscosity ($\dot{\gamma}$=100 s^{-1}) at 3 different resting time *versus* complexation ratio (b).

domain defined by Derby et al. [35] (1 < Z < 10), only ink4 is within the domain defined by Jang et al. (4 < Z < 14) [40].

The long-term stability of the prepared inks was then evaluated following the evolution of the rheology behavior over time. Except for the ink4 that maintained its Newtonian behavior on long-term, the other inks exhibited a transition to shear thinning flow, with a deviation from the Newtonian behavior that varies depending on the MDEA content. The shear thinning character of the inks was evaluated *via* the estimation of the flow index. This parameter can be mathematically determined *via* the analysis of rheological data using the logarithmic form of the power law [42]:

$$log(\tau)=log(K)+nlog(\dot{\gamma}) \quad (2)$$

where τ is the shear stress, $\dot{\gamma}$ the shear rate, K the consistency coefficient and n the flow index. This corresponds to a linear equation in which the flow index n is the slope identifying the character of the fluid: Newtonian when n=1, shear-thinning when n < 1 and shear-

Table 1
Inks printability after 4 h. 600 h and 1200 h of aging (ρ=0.95 cm^{-3}, a=20 μm for all measurements).

	t=4 h			t=600 h			t=1200 h		
	η (mPa s)	σ (mN/m)	Z	η (mPa s)	σ (mN/m)	Z	η (mPa s)	σ (mN/m)	Z
Ink2	6.22	27.01	3.64	36.50	27.43	0.63	66.5	27.3	0.34
Ink4	4.79	27.38	4.76	22.20	26.87	1.02	27.1	26.9	0.83
Ink6	6.47	28.77	3.61	44.91	28.13	0.51	56.4	28.3	0.41
Ink8	10.13	29.79	2.35	126.00	30.09	0.19	262	29.9	0.09
Ink10	1.64	30.48	1.76	145.00	30.94	0.17	421	30.9	0.06

thickening when n is > 1. Fig. 2(a) shows the obtained values as function of the ageing time for all the developed inks. A slight and slow decrease of the flow index from the unit to around 0.93 and 0.98 was observed for the Ink2 and Ink6 respectively, whereas a rapid and marked variation down to 0.76 and 0.67 was obtained for the Ink8 and Ink10, respectively. An increment over time of the viscosity was also observed for all the inks as indicated in Fig. 2(b), where the viscosity at 100 s^{-1} for each inks is plotted as function of the MDEA concentration for three selected ageing times: 4 h, 600 h, and 1200 h (see also Table 1). Ink4 is characterized by a slight variation of the viscosity values (less than 30 mPa s), whereas larger increments are detected for the other inks. Specifically, after 1200 h the viscosity values of Ink2 and Ink6, with a similar trend, increases of around 50–60 mPa s, while for Ink8 and Ink10 variation within a range of hundreds of mPa s is observed. Interestingly, all the inks after 1200 h are still transparent solution and no signals of TiO_2 precipitation could be depicted as indicated in the inset picture. This experimental finding is consistent with the formation of clear monolithic gels when a ligand is used with an alkoxide (titanium alkoxides) [41]. The rheological analysis clearly indicates a superior stability for the Ink4. The persistence of the Newtonian character over a long period indicates that the interactions among the components are efficiently and fully minimized and minimal alteration of this stable state occurs (*e.g.* small increasing of the viscosity). For Ink2 and Ink6 only slight differences from Ink4 are observed. By contrast, significant deviations are observed for Ink8 and ink10 [41]. The resulting increment of the viscosity can be explained as an effect of the increased internal interactions among the constituents that also cause the shear thinning flow behavior. Remarkably, no variations in the surface tension over time at fixed amount of MDEA are observed for all the inks (see Table 1). This designates the viscosity as the only physical properties changing and affecting the printability of the developed inks. After 600 h of ageing, Ink4 is the only ink still within the printability domain defined by Derby, whereas after an ageing of 1200 h none of the inks exhibits a Z number value within such a domain. Interestingly, none of the inks exhibit a printability number within Jang's domain even after 600 h.

To confirm the hypothesis of a polycondensation at the highest content of ligand and clarify the ligand interactions with the central atom (Ti), inks stored during 600 h were characterized by FTIR spectroscopy. Fig. 3(a) shows IR spectra for the two starting compounds (TiTIP and MDEA) and for the five developed inks in the entire range of frequencies explored. For the five inks and for the MDEA the broad bands attributed to the vibrational stretching of O–H bonds are observed in a wide range of frequency, centered at around 3350 cm^{-1}. These absorptions are significantly intense for the developed inks because of the presence of water, responsible also for the absorption at 1650 cm^{-1}, due to the H-O-H bending. The characteristics bands for the vibrational stretching (in the broad range of 2980–2780 cm^{-1}) and bending (in the broad range of 1450–1325 cm^{-1}) for C_{sp3}–H bonds can be identified for all the materials investigated. Eventually the stretching for the C-O, C-C, and Ti–O bonds are observed in the characteristic range of frequency (1110–600 cm^{-1}). The stabilization of the alkoxide in the aqueous solution is here identified by following the variation of the bands associated with stretching υ(C-O) and υ(C-N). Fig. 3(b) shows the same spectra in a narrower range of frequencies (1500–500 cm^{-1}). In the spectra of pure MDEA, the two bands are centered at 1076 (υ(C-O)) and 1028 (υ(C-N)) cm^{-1}, respectively. Since titanium is less electronegative than O and N, both the υ(C-O) and υ(C-N) bands are shifted to higher frequency (see positions of the peaks in Table 2). The largest shift is obtained for the Ink2. As the amount of MDEA increases, the band associated with υ(C-O) is only slightly shifted to lower frequencies without reaching again its original positions. This likely indicates that the alcoholic functions of MDEA, from low to high concentrations, are not free but coordinated with Ti atom of the alkoxide. As further support for this, the stretching of the (C_{sp3}–H) bonds next to the C-O functions coordinated with Ti, are also shifted to higher frequencies (2977 cm^{-1}) with respect to the same bonds in free MDEA (see also Fig. 3(c)). By contrast, the band associated with υ(C-N) modes exhibits a splitting into two distinct absorptions. The additional band, located at lower frequency, initially appears as a shoulder, visible

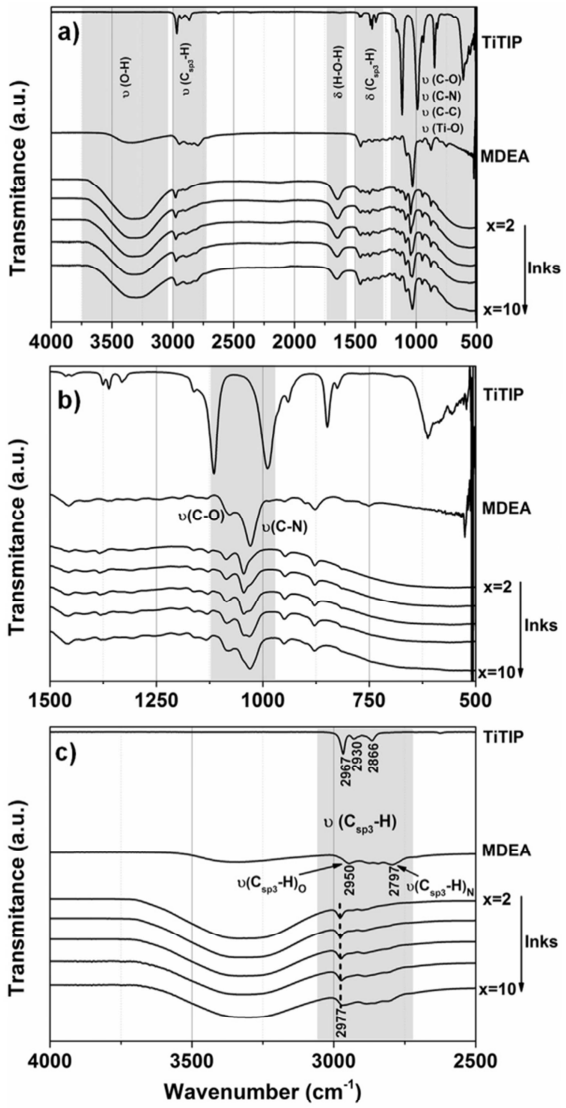

Fig. 3. FTIR spectra for the inks after 600 h resting (a), and detailed view of the pattern in the ranges 1500–1000 cm^{-1} (b) and 3200–2500 cm^{-1} (c).

Table 2
: υ(C-O) and υ(C-N) FTIR peaks position in MDEA and in the developed inks (600 h of ageing).

	υ (C-O) cm^{-1}	υ (C-N) cm^{-1}	
MDEA	1076	1028	
Ink2	1088	1044	
Ink4	1085	1044	Shoulder
Ink6	1085	1044	1029
Ink8	1084	1043	1029
Ink10	1083	Shoulder	1030

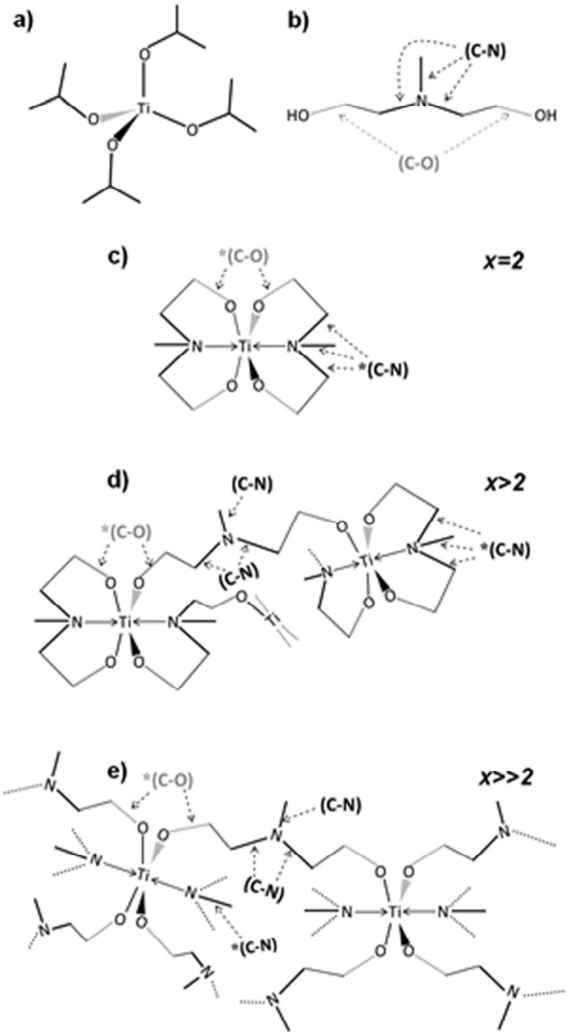

Fig. 4. Chemical structures of (a) Titanium isopropoxide (TiTIP), (b) MDEA, and (c), (d), (e) possible complexes formed at different [MDEA]/[Ti] molar ratio.

starting from Ink4. Its intensity and resolution increase with the content of MDEA until in Ink10 it is the main signals, centered at 1030 cm^{-1}, corresponding to the frequency υ(C-N) in pure MDEA (see Table 2). The υ(C-N) band centered at 1044 cm^{-1} in Ink2 is observed to follow an opposite evolution with its intensity and resolution progressively weakening until it appears as a shoulder in Ink10. This likely indicates that, as the amount of MDEA increases, a growing fraction of amine functions are not involved in a coordination of the Titanium atom and thus they result free.

In summary, according to FTIR spectra, different complexes are generated in the water/ethanol solution depending on the MDEA content. Possible coordination complexes are also represented in Fig. 4. Specifically, when the [MDEA]/[Ti] molar ratio is equal to 2, both the amine and alcoholic functions are involved in the coordination of the Ti central atom. In these conditions MDEA acts as tridentate ligands favoring the coordinative saturation of the Titanium atoms [27] (Fig. 4(c)). Despite the high stability of the obtained species, over time the hydrolysis/condensation process is occurring (viscosity increases and the flow index deviates from the unit) as the solvent mostly

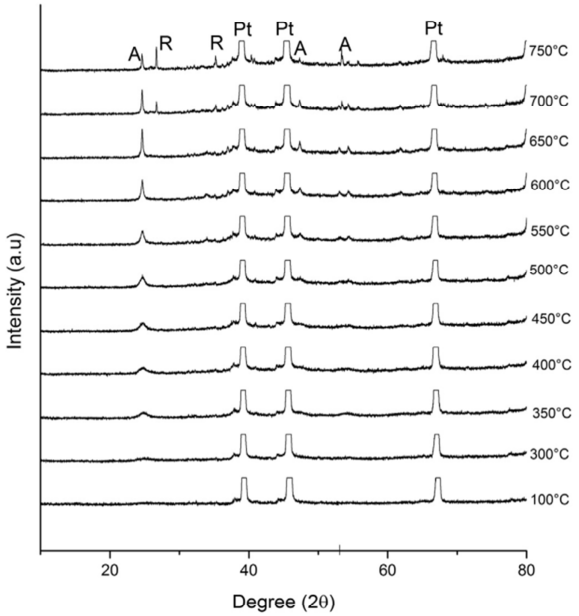

Fig. 5. XRD patterns of Ink4 (600 h of resting) at different temperature (A=anatase; R=rutile, Pt=Platinum).

consists of water. At higher complexation ratio (*e.g.* 6), an increasing fraction of amine functions are free, likely as consequence of a bridging coordination of MDEA *via* the alcoholic functions as indicated in Fig. 4(d) and (e). Accordingly, the absorption υ(C-N) due to free amine functions is dominant. Extended complexes are thus generated with a consequent increasing of the viscosity.

Based on the indications obtained on the long stability properties, only Ink4 was further explored and printed.

3.2. Phase and printing characterization

All characterization and printing have been performed on a 600 h aged ink and both fresh and aged inks were printable, with no observable influence of the aging time on the printing. Crystallization behavior for ink4 was explored by *in-situ* XRD experiments at different temperature. Fig. 5 shows XRD patterns at increasing temperature for Ink4 sample deposited as drops on the holder sample (Pt wire, used as reference). In all the patterns the signals deriving from Pt are identified. The anatase crystallographic phase is already detectable at temperature as low as 350 °C. At higher temperatures, the peaks associated with the anatase phase become sharper and more intense indicating an increasing in the crystallite size. As expected, at 700 °C transformation from anatase to rutile phase occurs. Thermal analysis (DTA/TG) performed on the ink show that mass loss relative to solvent evaporation and chelating agent is completed at 350 °C with an overall loss of *ca*. 80% of the starting weight (data not shown here). Based on these results, a crystallization temperature of 400 °C was then selected for the printings and crystallite size for the material treated at 400 °C was estimated *via* Scherrer equation to be around 7 nm.

The optimized Ink4 was deposited on three substrates with different surface energies, *i.e.*, ITO (36 mJ m^{-2}), polycrystalline alumina (65 mJ m^{-2}) and soda lime glass (70 mJ m^{-2}), by using two printers and print heads. To emphasize the effectiveness of the chemical strategy we have used two printers which use two different printing principles, *i.e.* thermal and piezoelectric inkjet. In thermal inkjet, the print head induces droplet formation by a fast bubble formation due to solvent evaporation at a heating element [43]. In the

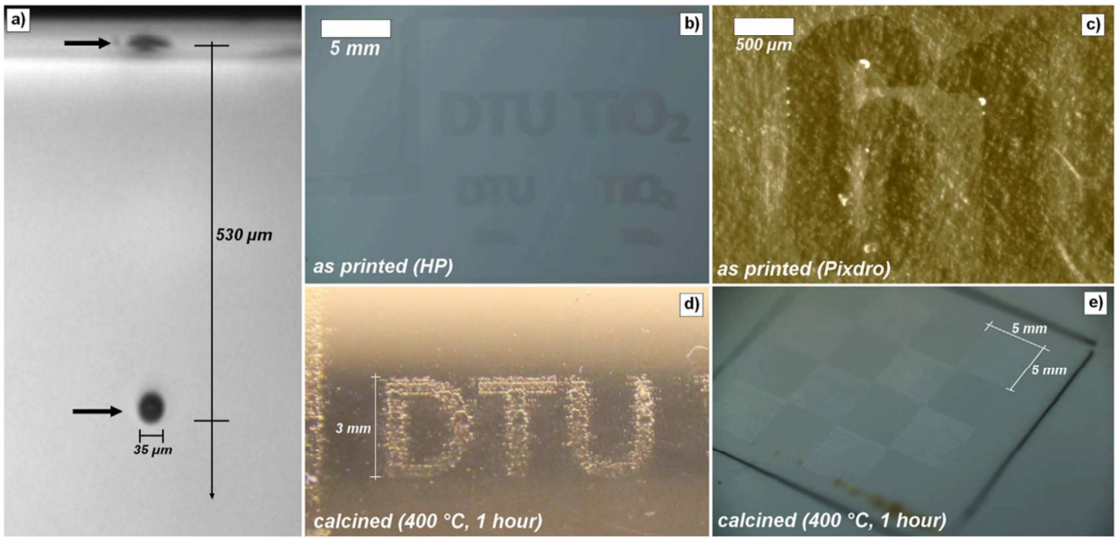

Fig. 6. (a) Droplet ejected from Pixdro nozzle, (b) as deposited "DTU" and "TiO_2" letters onto alumina (HP), (c) as deposited number "61" onto ITO (Pixdro), (d) letters printed (HP) onto alumina and calcined at 400 °C, (e) chessboard pattern printed (HP) onto ITO and calcined at 700 °C.

piezoelectric inkjet, the principle is based on electromechanical action of a piezoelectric element which squeezes a droplet out [43]. Since the ejection principle is quite different, the ink requirements for the inkjets are also different. Particularly, inks designed for thermal inkjet printing need to be heat resistant and this limits the choice of solvents that can be used. In piezoelectric systems, suitable viscosity and surface tension play a crucial role in the droplet formation. In general, there is a greater choice of inks for piezoelectric inkjet printing than for thermal inkjet printing. Fig. 6 shows a selection of features at the printing. Particularly, Fig. 6(a) shows the typical shape of the Ink4 ejected droplet, as observed using the fiducial camera mounted on the Pixdro printer. Remarkably the droplet exhibits a sphere-like shape with diameter of *ca.* 35 µm. The snapshot is taken at *ca.* 530 µm from the nozzle where the droplet does not exhibit any presence of satellite droplets. This result is consistent with the ability to print as indicated by the printability domain $1 < Z < 10$, which for Ink4, is Z=1.02. Fig. 6(b) and (c) show complex as deposited printings and defined shapes, such as letters and numbers on different substrates: Fig. 6(b) shows the printed "DTU" letters *(Danmarks Tekniske Universitet)* and "TiO_2" with different size on alumina substrate. This is done by using an inexpensive HP printer which indeed has a limited resolution and quality of the printing (see other examples of printing flaws by that printer in [12]). However, while letter and numbers appear rather clear in millimeter scale (first raw at the top) the precision is lost at the micron scale (last raw at the bottom). Angles and lines in the print resulted rather homogeneous and continuous in large size printings. On the other hand, Fig. 6(c) shows a rather small printing, *i.e.* the number "61", on ITO using the Pixdro printer. The higher quality of this printing with respect of the HP lays on the size of the characters with typical size between 100 and 400 µm as well as on complexity of the shape, *e.g.* sharp corners and smooth bending in the numbers. Similar results were observed on the soda-lime glass substrates, indicating a good coverage of the ink on substrates with surface tension in the range 36–70 mJ m^{-2}. Ink4 was thus successfully deposited using both printing techniques (thermal and piezoelectric) despite the different requirements for the techniques.

Fig. 6(d) and (e) show the effect of calcination at 400 °C for 1 h after printing. In Fig. 6(d), the "DTU" letters deposited are still perfectly visible and recognizable. However the prints definition is not as sharp as in the as printed material (compare Fig. 6(b) and (d)). Possibly, this is due to shrinkage of the ink as well as to possible wetting issue developed during the calcination. Similar features were also measured on a chessboard pattern in Fig. 6(e). In this case, the printing resulted stable and exhibited continuous squares connected at each corner. The continuity at the printing, *e.g.* at the letters (d) and the squares corners (e), indicates that a relatively low shrinkage in the plane directions occurred after calcination. This is a remarkable result for the reactive ink, especially considering that large mass loss (~80%), measured at the TG. Considering the TiO_2 theoretical density (4.23 g ml^{-1}) and the other organic components of the solutions, such a loss corresponds to a large change of volume in the printing after calcination, *i.e.* > 120 vol %. Such a large shrinkage is indeed critical and these results confirm the importance of controlling printability parameters. For the micro-structural features of the printing, Fig. 7 shows SEM images after calcination. Particularly, Fig. 7(a) shows the top view of an Ink4 layer deposited on ITO coated glass by inkjet printing and calcined at 400 °C for 1 h. The film resulted continuous and homogeneous on the substrate and microstructural feature could be observed only in nanoscale at high magnification (inset Fig. 7(a)), showing a dense polycrystalline deposition. Average particle size is estimated by picture analysis at 11 nm ± 1 nm (based on 30 measurements from 2 different locations along the sample). Fig. 7(b) and (c) show the printed layer at a cold fracture: in Fig. 7(a), a typical thickness of a single deposition by the HP was estimated to be around 480 nm, while, in Fig. 7(c), high resolution at the cross section reveals a dense and polycrystalline morphology of the film. This is kept throughout the deposition without any detectable flaws.

4. Conclusions

A stable aqueous sol gel based ink for inkjet printing using a nucleophilic ligand to delay hydrolysis and condensation reactions was successfully designed by rheology. Printability and stability were optimized by variating the amount of MDEA as nucleophilic ligand and measuring ink viscosity over time. The use of the MDEA to achieve the proper printability is a balance between an effective coordination of the metal center in the metal alkoxide, at low concentration, $x < 2$, and an early organic-inorganic polymerization of TiTIP and MDEA at high concentrations, $x \gg 2$. An optimized ink at x=4 was thus proven by printing small complex shapes (*e.g.* letters) and thin dense layer of *ca*

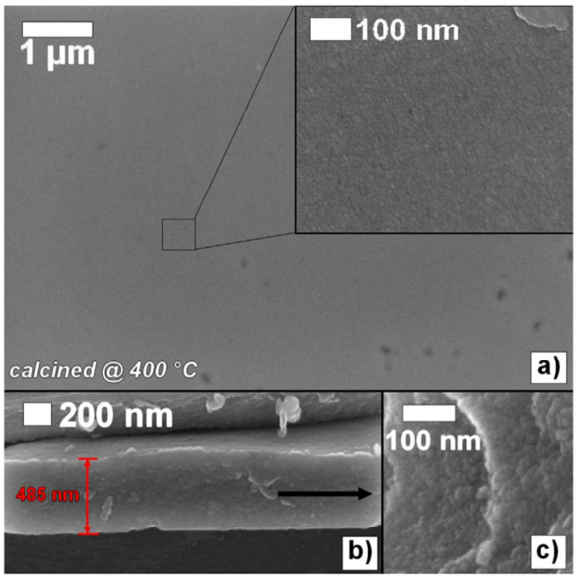

Fig. 7. SEM images of the printed layer surface at low (a) and high ((a) inset) magnification, followed by the layer cross section (b) together with a broken piece of thin film (c).

500 nm in thickness, on various substrates with surface tension in the 36–170 mJ m^{-2} range. The ink is purified from the organics at *ca.* 400 °C while phase transitions from amorphous Titania to anatase, and from anatase to rutile, occur at 400 °C and at 700 °C, respectively.

Prime novelty statement

We show how to design inks for inkjet printing of metal oxides by balancing of alkoxides and nucleophilic ligands, to avoid uncontrolled inorganic polymerization and achieve rheological properties for printability.

Acknowledgment

The authors would like to thank Séverine Ramousse, Kurt Engelbrecht, Quentin Hanniet and Gaëtan Guellec for their precious assistance.

References

[1] H. Sirringhaus, High-resolution inkjet printing of all-polymer transistor circuits, Science 290 (80) (2000) 2123–2126. http://dx.doi.org/10.1126/science.290.5499.2123.
[2] M. Singh, H.M. Haverinen, P. Dhagat, G.E. Jabbour, Inkjet printing-process and its applications, Adv. Mater. 22 (2010) 673–685. http://dx.doi.org/10.1002/adma.200901141.
[3] D. Tobjörk, R. Österbacka, Paper electronics, Adv. Mater. 23 (2011) 1935–1961. http://dx.doi.org/10.1002/adma.201004692.
[4] A.D. Taylor, E.Y. Kim, V.P. Humes, J. Kizuka, L.T. Thompson, Inkjet printing of carbon supported platinum 3-D catalyst layers for use in fuel cells, J. Power Sources 171 (2007) 101–106. http://dx.doi.org/10.1016/j.jpowsour.2007.01.024.
[5] T. Wang, B. Derby, Ink-jet printing and sintering of PZT, J. Am. Ceram. Soc. 88 (2005) 2053–2058. http://dx.doi.org/10.1111/j.1551-2916.2005.00406.x.
[6] H. Minemawari, T. Yamada, H. Matsui, J. Tsutsumi, S. Haas, R. Chiba, R. Kumai, T. Hasegawa, Inkjet printing of single-crystal films, Nature 475 (2011) 364–367. http://dx.doi.org/10.1038/nature10313.
[7] J. Ebert, E. Ozkol, A. Zeichner, K. Uibel, O. Weiss, U. Koops, R. Telle, H. Fischer, Direct inkjet printing of dental prostheses made of zirconia, J. Dent. Res. 88 (2009) 673–676. http://dx.doi.org/10.1177/0022034509339988.
[8] D. Kim, S. Jeong, J. Moon, K. Kang, Ink-jet printing of silver conductive tracks on flexible substrates, Mol. Cryst. Liq. Cryst. 459 (2006). http://dx.doi.org/10.1080/15421400600930458.
[9] J. Cheon, J. Lee, J. Kim, Inkjet printing using copper nanoparticles synthesized by electrolysis, Thin Solid Films 520 (2012) 2639–2643. http://dx.doi.org/10.1016/j.tsf.2011.11.021.
[10] T. Kawase, T. Shimoda, C. Newsome, H. Sirringhaus, Inkjet printing of polymer thin film transistors, Thin Solid Films 438-439 (2003) 279–287. http://dx.doi.org/10.1016/S0040-6090(03)00801-0.
[11] G. Deok, K. Chean, K. Bae, H. Jong, S. Won, J. Son, J. Hyung, Fabrication of lanthanum strontium cobalt ferrite (LSCF) cathodes for high performance solid oxide fuel cells using a low price commercial inkjet printer, J. Power Sources 306 (2016) 503–509. http://dx.doi.org/10.1016/j.jpowsour.2015.12.067.
[12] V. Esposito, C. Gadea, J. Hjelm, D. Marani, Q. Hu, K. Agersted, S. Ramousse, S.H. Jensen, Fabrication of thin yttria-stabilized-zirconia dense electrolyte layers by inkjet printing for high performing solid oxide fuel cells, J. Power Sources 273 (2015) 89–95. http://dx.doi.org/10.1016/j.jpowsour.2014.09.085.
[13] R. Cobas, S. Muñoz-pérez, S. Cadogan, M.C. Ridgway, X. Obradors, Surface charge reversal method for high-resolution inkjet printing of functional water-based inks, Adv. Funct. Mater. 25 (2015) 768–775. http://dx.doi.org/10.1002/adfm.201401638.
[14] T. Jungst, W. Smolan, K. Schacht, T. Scheibel, J. Groll, Strategies and molecular design criteria for 3D printable hydrogels, Chem. Rev. 116 (2016) 1496–1539. http://dx.doi.org/10.1021/acs.chemrev.5b00303.
[15] M. Michálek, G. Blugan, T. Graule, J. Kuebler, Comparison of aqueous and non-aqueous tape casting of fully stabilized ZrO2 suspensions, Powder Technol. 274 (2015) 276–283. http://dx.doi.org/10.1016/j.powtec.2015.01.036.
[16] A. Akbari-fakhrabadi, R.V. Mangalaraja, F.A. Sanhueza, R.E. Avila, S. Ananthakumar, S.H. Chan, Nanostructured GdeCeO2 electrolyte for solid oxide fuel cell by aqueous tape casting, J. Power Sources 218 (2012) 307–312. http://dx.doi.org/10.1016/j.jpowsour.2012.07.005.
[17] J.M. Lebeau, Y. Boonyongmaneerat, Comparison study of aqueous binder systems for slurry-based processing, Mater. Sci. Eng. A 458 (2007) 17–24. http://dx.doi.org/10.1016/j.msea.2007.01.112.
[18] I.M. Hutchings, Inkjet Technology for Digital Fabrication, Wiley, Chichester, UK, 2013.
[19] E.M. Hamad, S.E.R. Bilatto, N.Y. Adly, D.S. Correa, B. Wolfrum, M.J. Schöning, A. Offenhäusser, A. Yakushenko, Lab on a chip dielectric inks for microfluidic devices, Lab Chip 16 (2016) 70–74. http://dx.doi.org/10.1039/C5LC01195G.
[20] D.A. Gregory, Y. Zhang, P.J. Smith, X. Zhao, S.J. Ebbens, Reactive inkjet printing of biocompatible enzyme powered silk micro-rockets, Mater. Views (2016) 4048–4055. http://dx.doi.org/10.1002/smll.201600921.
[21] K. Black, J. Singh, D. Mehta, S. Sung, C.J. Sutcliffe, P.R. Chalker, Silver ink formulations for sinter- free printing of conductive films, Nat. Publ. Gr. (2016) 1–7. http://dx.doi.org/10.1038/srep20814.
[22] J.M. Chem, Z. Kao, Y. Hung, Y. Liao, Formation of conductive silver films via inkjet reaction system, J. Mater. Chem. (2011) 18799–18803. http://dx.doi.org/10.1039/c1jm13506f.
[23] B.S. Cook, Y. Fang, S. Kim, T. Le, W.B. Goodwin, K.H. Sandhage, M.M. Tentzeris, Inkjet Catalyst Printing and Electroless Copper Deposition for Low-Cost Patterned Microwave Passive Devices on Paper, 9, 2013, pp. 669–676. doi: http://dx.doi.org/10.1007/s13391-013-3027-0
[24] L.L. Hench, J.K. West, The sol-gel process, Chem. Rev. 90 (1990) 33–72. http://dx.doi.org/10.1021/cr00099a003.
[25] C. Sanchez, J. Livage, M. Henry, F. Babonneau, Chemical modification of alkoxide precursors, J. Non Cryst. Solids 100 (1988) 65–76.
[26] T. Kemmit, N.I. Al-Salim, G.J. Gainsford, Chemistry N-methyldiethanolamine-modified titanium isopropoxide, Aus. J. Chem. 55 (2002) 513–517. http://dx.doi.org/10.1071/CH02087.
[27] N. Martín-Arbella, I. Bretos, R. Jiménez, M.L. Calzada, R. Sirera, Metal complexes with N-methyldiethanolamine as new photosensitive precursors for the low-temperature preparation of ferroelectric thin films, J. Mater. Chem. 21 (2011) 9051–9059. http://dx.doi.org/10.1039/c1jm10846h.
[28] T. Nguyen, Y. Chen, J. He, Preparation of inkjet-printed titanium monoxide as p-type absorber layer for photovoltaic purposes, Thin Solid Films 572 (2014) 8–14. http://dx.doi.org/10.1016/j.tsf.2014.09.054.
[29] M. Arin, J. Watté, G. Pollefeyt, K. De Buysser, Low temperature deposition of TiO2 layers from nanoparticle containing suspensions synthesized by microwave hydrothermal treatment, J. Sol.-Gel Sci. Technol. 66 (2013) 100–111. http://dx.doi.org/10.1007/s10971-013-2972-2.
[30] M. Černá, M. Veselý, P. Dzik, C. Guillard, E. Puzenat, M. Lepičová, Fabrication, characterization and photocatalytic activity of TiO2 layers prepared by inkjet printing of stabilized nanocrystalline suspensions, Appl. Catal. B: Environ. 138–139 (2013) 84–94. http://dx.doi.org/10.1016/j.apcatb.2013.02.035.
[31] I. Fasaki, K. Siamos, M. Arin, P. Lommens, I. Van Driessche, S.C. Hopkins, B.A. Glowacki, I. Arabatzis, Applied catalysis A: general ultrasound assisted preparation of stable water-based nanocrystalline TiO2 suspensions for photo-catalytic applications of inkjet-printed films, Appl. Catal. A: Gen. 411–412 (2012) 60–69. http://dx.doi.org/10.1016/j.apcata.2011.10.020.
[32] M. Morozova, P. Kluson, J. Krysa, P. Dzik, M. Vesely, O. Solcova, Thin TiO2 films prepared by inkjet printing of the reverse micelles sol–gel composition, Sens. Actuators B Chem. 160 (2011) 371–378. http://dx.doi.org/10.1016/j.snb.2011.07.063.
[33] M. Arin, P. Lommens, N. Avci, S.C. Hopkins, K. De Buysser, I.M. Arabatzis, I. Fasaki, D. Poelman, I. Van Driessche, Inkjet printing of photocatalytically active TiO2 thin films from water based precursor solutions, J. Eur. Ceram. Soc. 31 (2011) 1067–1074. http://dx.doi.org/10.1016/j.jeurceramsoc.2010.12.033.
[34] P. Dzik, M. Veselý, J. Chomoucka, Thin layers of photocatalytic TiO2 prepared by inkjet printing of a solgel precursor, J. Adv. Oxid. Technol. 13 (2010) 172–183.
[35] B. Derby, Inkjet printing of functional and structural materials: fluid property

requirements, feature stability, and resolution, Annu. Rev. Mater. Res. 40 (2010) 395–414. http://dx.doi.org/10.1146/annurev-matsci-070909-104502.
[36] A. Monshi, Modified scherrer equation to estimate more accurately nano-crystallite size using XRD, World J. Nano Sci. Eng. 02 (2012) 154–160. http://dx.doi.org/10.4236/wjnse.2012.23020.
[37] R.A.S. Ferreira, Simple measurement of surface free energy using a web cam, Rev. Bras. Ensino Fis. 3312 (2012).
[38] G.D. Martin, S.D. Hoath, I.M. Hutchings, Inkjet printing – the physics of manipulating liquid jets and drops, J. Phys. Conf. Ser. 105 (2008) 012001. http://dx.doi.org/10.1088/1742-6596/105/1/012001.
[39] Helmut Kipphan, Handbook of Print Media, 2001
[40] D. Jang, D. Kim, J. Moon, Influence of fluid physical properties on ink-jet printability, Langmuir 25 (2009) 2629–2635. http://dx.doi.org/10.1021/la900059m.
[41] S. Doeuff, M. Henry, C. Sanchez, J. Livage, Hydrolysis of titanium alkoxides: modification of the molecular precursor by acetic acid, J. Non Cryst. Solids 89 (1987) 206–216. http://dx.doi.org/10.1016/S0022-3093(87)80333-2.
[42] D. Marani, J. Hjelm, M. Wandel, Rheological analysis of stabilized cerium-gadolinium oxide (CGO) dispersions, J. Eur. Ceram. Soc. 34 (2014) 695–702. http://dx.doi.org/10.1016/j.jeurceramsoc.2013.09.022.
[43] A. Lesch, F. Cortés-Salazar, V.C. Bassetto, V. Amstutz, H.H. Girault, Inkjet printing meets electrochemical energy conversion, CHIMIA Int. J. Chem. 69 (2015) 284–289. http://dx.doi.org/10.2533/chimia.2015.284.

Paper II:

Aqueous metal-organic solutions for YSZ thin film inkjet deposition

Journal of
Materials Chemistry C

PAPER

View Article Online
View Journal

Cite this: DOI: 10.1039/c7tc01879g

Aqueous metal–organic solutions for YSZ thin film inkjet deposition

C. Gadea, *[a] Q. Hanniet,[a] A. Lesch,[b] D. Marani,[a] S. H. Jensen[a] and V. Esposito[a]

Received 1st May 2017,
Accepted 17th May 2017

DOI: 10.1039/c7tc01879g

rsc.li/materials-c

Inkjet printing of 8% Y_2O_3-stabilized ZrO_2 (YSZ) thin films is achieved by designing a novel water-based reactive ink for Drop-on-Demand (DoD) inkjet printing. The ink formulation is based on a novel chemical strategy that consists of a combination of metal oxide precursors (zirconium alkoxide and yttrium salt), water and a nucleophilic agent, *i.e.* *n*-methyldiethanolamine (MDEA). This chemistry leads to metal–organic complexes with long term ink stability and high precision printability. Ink rheology and chemical reactivity are analyzed and controlled in terms of metal–organic interactions in the solutions. Thin dense nanocrystalline YSZ films below 150 nm are obtained by low temperature calcination treatments (400–500 °C), making the deposition suitable for a large variety of substrates, including silicon, glass and metals. Thin films and printed patterns achieve full densification with no lateral shrinkage and high ionic conductivity.

1. Introduction

Solid oxide fuel cells (SOFCs) are a mature technology where materials' processing is the key to improve performances and to boost commercial viability. In the past few decades, research has been focused on lowering the operating temperatures to make SOFCs more durable and financially competitive.[1–5] One promising approach is the reduction of the electrolyte layer thickness[6] to lower ohmic losses.[7] Several processes have been considered for the fabrication of thin-film electrolytes for SOFCs. While the deposition of films <10 μm using spray coating,[8] tape casting,[9] electrophoretic deposition (EPD)[10] and screen printing[11] is technically challenging, more advanced techniques, such as pulsed laser deposition (PLD),[12] chemical vapor deposition (CVD)[13] or spray pyrolysis,[14] can produce thin films with fine microstructures and compositions. However, the more advanced techniques are generally difficult to scale up and are not cost effective. Additive manufacturing such as Drop-on-Demand (DoD) inkjet printing represents a relatively new deposition technology with unique advantages including customizable patterns and shapes. This is of growing interest for SOFCs since it is ideal for controlled thin film deposition and shapes in multicomponent layer systems such as SOFCs.[15–18] The implementation of printheads with several hundred individually addressable nozzles, ejecting highly reproducible picoliter droplets (10^{-12} liter) of well-defined ink compositions, enables a comfortable route for up-scaling from the prototype development to the industrial fabrication level.

In a previous study, we deposited a 1.2 μm thick YSZ electrolyte layer by inkjet printing a colloid based solution (*i.e.* a stabilized oxide particle suspension in an aqueous medium) on a 9×9 cm^2 porous nickel oxide/yttria-stabilized zirconia (NiO/YSZ) anode.[15] YSZ printing showed high potential in terms of both processing flexibility and electrochemical performance of the cell.[15] However, inkjet printing of colloids shows some limitations and it does not suit thin film deposition $\ll 1$ μm. Indeed, the minimum layer thickness depends on the particle size of the colloid as the total thickness is the result of the particle packing and the number of layers needed to achieve a full coverage of the substrate.[15] The drying behavior of such an ink is also critical to avoid "coffee ring effects" leading to non-continuous films.[19] Moreover, stabilizing nanoparticles below 100 nm to achieve thinner films is challenging due to the large amount of stabilizers and additives needed to cover the particles' high surface area.[20] Finally, the consolidation of ceramic-powder based layers occurs at high temperatures (*e.g.* 1300 °C for *ca.* 100–500 nm YSZ powders[21]). This step imposes limitations on the substrates to be used, excluding silicon, metals, and nanostructured substrates, that are usually selected for thin-film based SOFCs made by PVD and CVD techniques.[14] Alternative to colloidal suspensions, particle-free, chemically reactive solutions contain only dissolved precursor salts or molecules. After printing, the precursors are converted into solid particles based on thermal, chemical or photochemical post-processing steps. Reactive inks for the deposition of metal oxide films usually contain dissolved precursors, such as metal alkoxide molecules in

[a] DTU Energy, Technical University of Denmark, Risø Campus, Frederiksborgvej 399, DK-4000 Roskilde, Denmark. E-mail: chga@dtu.dk
[b] Laboratoire d'Electrochimie Physique et Analytique, EPFL Valais Wallis, Rue de l'Industrie 17, CH-1950 Sion, Switzerland

alcoholic solution.[22–24] Reactive inks can be found in various forms.[25–28] The sol–gel process consists of a combination of reactions (hydrolysis and condensation) of the metal alkoxide which leads to the formation of a homogeneous oxo/hydroxo-polymeric matrix at room temperature.[29] Due to the presence of such a structure, sol gels do not need mass diffusion steps such as sintering at high temperatures to become dense; the precursor only requires a calcination step to remove by-products and additives and to crystallize the phase from the polymeric form. Alkoxide precursors are generally highly reactive, *e.g.* towards water, leading to an unavoidable premature gel formation. Therefore, full control of the sol gel precursor reactivity is crucial, especially for inkjet, where inorganic polymerization can lead to irreversible clogging of the nozzle or the reservoir. Inkjet printing of sol–gel based TiO_2 films was stabilized by adding a nucleophilic ligand (or chelating agent), *N*-methyldiethanolamine (MDEA).[30] MDEA stabilizes the alkoxide precursors by coordinating the metallic cation from water and thus inhibiting the hydrolysis/condensation reactions.[31] While several studies describing the deposition of sol–gel based YSZ electrolytes for SOFCs are reported in the literature using other processing methodologies such as spin coating[32,33] or dip coating,[34] to the best of our knowledge, no research on inkjet printing of YSZ sol–gel based ink with nanometric features has been reported so far. The use of reactive inks for SOFC electrolytes was solely done by Wang *et al.*[21] for the deposition of Gadolinium-doped Ceria (CGO) thick layers (10 μm and thicker) on porous NiO/YSZ and YSZ/CGO substrates and no analysis of the rheology and stability of YSZ reactive inks is available in the literature. In this work, we fill this gap for an environmentally-friendly water-based reactive YSZ ink, demonstrating its long term stability, suitable printability and versatility in depositing on several substrates by using both thermal and piezoelectric DoD inkjet printers.[35]

2. Experimental

2.1. Ink preparation

The YSZ ink formulae were elaborated to produce 8 mol% YSZ (*i.e.* $0.08Y_2O_3$–$0.92ZrO_2$) starting from zirconium(IV) propoxide ($Zr(OPr)_4$, 70 wt% in propanol, Sigma Aldrich) as the zirconium precursor and yttrium(III) nitrate hexahydrate ($Y(NO_3)_3{\cdot}6H_2O$, 99.8% trace metals basis, Sigma Aldrich) as the dopant. *N*-Methyldiethanolamine (MDEA, Sigma-Aldrich) was used as the nucleophilic agent. Ink preparation was carried out under an argon atmosphere to avoid any undesired reactions between zirconium alkoxide and ambient water. MDEA and $Zr(OPr)_4$ were mixed to chelate alkoxide molecules, followed by the addition of ethanol. In a separate reactor, yttrium nitrate salt was dissolved in water and kept under stirring until complete salt dissolution. The aqueous yttrium salt solution was then slowly added dropwise to the solution containing the chelated propoxide and mixed for 5 min. To screen the ink properties and identify an optimized formulation for printing, several parameters were varied: the water/ethanol volume ratio from 100/0 to 0/100, molar ratio r = [MDEA]/[$Zr(OPr)_4$] and the concentration c of zirconium from 0.1 to 0.2 g ml^{-1}. The hydrolysis ratio h = [H_2O]/[$Zr(OPr)_4$] was kept constant for all inks (h = 8). Herein, inks are labeled as Ink *r*-*c*-*X*, where *r* refers to the molar ratio of complexation, *c* to the zirconium concentration, and *X* to the water volume percentage.

2.2. Ink characterization

The rheological properties of the inks were explored using an Anton Paar Rheometer (MCR 302), in rotational mode and at a constant temperature of 21 °C. A plate–plate measuring system was used with a diameter of 50 mm (PP50) and at a gap distance of 0.5 mm. A solvent trap was used to avoid ethanol evaporation. The experiments were performed using three steps of pre-treatment: the first one at a shear rate of 1 s^{-1} for 1 min followed by 1 min at rest (shear rate = 0 s^{-1}), and the third one at 1 s^{-1} for 1 min. The pre-treatment steps were adopted to remove any effects due to the sampling and loading of the inks. Flow curve measurements were conducted in the step mode using 60 steps with a waiting time of 10 s. This procedure allows the samples to reach equilibrium and avoid possible transient effects. The shear rates investigated range from 1 s^{-1} up to 100 s^{-1}. The viscosity was measured over time, from a few hours after preparation up to 360 h (15 days) in order to estimate the long term ink stability. Ink surface tension was measured using a bubble pressure tensiometer (BP 50, Krüss), and the density was evaluated by weighing 10 ml of ink.

The printability of the inks was determined by calculation of their Z numbers defined as:

$$Z = \frac{\sqrt{\sigma \rho a}}{\eta} \quad (1)$$

where η is the ink viscosity (mPa s), σ is the surface tension (mN m^{-1}), ρ is the density (g cm^{-3}), and a is the characteristic length (μm).[36] The parameter a is typically taken as the nozzle diameter.[36] The specifications of the printers are given in Section 2.3.

2.3. Thin film deposition and characterization

The substrates used in this work were Si(100), quartz (Crystal GmbH), polycrystalline alumina (Keral96, Kerafol), and sintered nickel oxide/yttria stabilized zirconia (NiO/YSZ) made in-house. For the latter, the layers were produced by tape-casting, co-laminated as green materials at *ca.* 150 °C,[37] and sintered at 1300 °C for 6 h in air. The substrates had a 10–15 μm thick anode of NiO/YSZ cermet laminated to a ~300 μm thick NiO/YSZ support layer. The ratio of Ni to YSZ was 40/60 vol% both for the support layer and the active electrode layer. ZrO_2 stabilized with 8 mol% Y_2O_3 was used for the anode layer while ZrO_2 stabilized with 3 mol% Y_2O_3 was used for the support layer.

A commercially available thermal printer (HP Deskjet 1010) was used as a representative thermal inkjet printing unit. The printer was modified to allow printing on flat and thick substrates (rigid or flexible).[15] A compatible cartridge (HP 301 black) providing a 600 × 300 dpi resolution was cleaned to remove the original black ink and used to print the sol–gel inks. The cartridge contains 336 nozzles each having a diameter of 20 μm. A high resolution piezoelectric based X-Serie CeraPrinter

(Ceradrop) was used as a representative piezoelectric printing unit. Both working principles and main differences in terms of required ink properties are listed elsewhere.[30,35] This printer is equipped with a fiducial camera to observe droplet ejection and calculate droplet velocity. Disposable DMP cartridges DMC-11610 (Fujifilm Dimatix) containing 16 individually addressable nozzles (nozzle diameter = 21.5 μm) were used with a custom-made jetting waveform. In brief, the waveform consisted of a baseline at 5 V, a 5 μs segment at −10 V to fill the nozzle with ink from the reservoir and a droplet ejection segment at 40 V for 5 μs with well-defined slopes between each segment. The jetting frequency was varied between 1 and 10 kHz. The obtained droplet velocity was 5 m s^{-1}. Each print made with both printers consisted of a single layer.

The evolution of the crystallographic phase for each material was investigated by X-ray diffraction (XRD) using a solid state detector, 0.01° step size, and 0.5 s step time (Bruker D8, Cu Kα radiation). Diffraction patterns of powder resulting from the ink calcination at various temperatures were recorded. The crystallite size was determined using the Scherrer equation[38] with an internal reference. The value of the Cu Kα radiation used for determination is 0.15406 nm and the k value is equal to 1.

Thermal analysis (DTA/TG) was performed on inks using an STA 409 PG (Netzsch) at a constant rate of 10 K min^{-1} under air between 25 and 700 °C.

As result of XRD and TG-DTA characterization, the calcination of the printed patterns on different substrates was carried out at 500 °C for 1 h in air using a chamber furnace, with a heating ramp of 100 °C h^{-1} after 2 intermediate steps at 90 °C and 120 °C of 1 h each. Morphological characterization of the printed films was investigated by using scanning electron microscopy (SEM, SUPRA 35, Zeiss). Film surface and thickness characterization was carried out by using a high resolution 3D profilometer (Cyberscan, Vantage, using an LT9010 detector, a non-contact laser based method to analyze surfaces). The measured film dimensions were 5 × 5 mm^2 and the measurement step size was 50 μm for both x- and y-axis.

Electrochemical impedance spectroscopy (EIS) was performed in a symmetric 2-electrode configuration by using a Solartron 1260 frequency response analyzer over the frequency range of 1 Hz–86 kHz. As also reported in previous papers, such a configuration can be used to characterize the in-plane ionic conduction at the thin film samples on dielectric substrates.[39,40] Due to the high impedance of the thin films in the lateral direction, 200 mV AC voltages were used for the acquisition. Symmetric silver electrodes were painted on the surface to measure the lateral conductivity of the calcined samples. The electrode dimensions were measured to be *ca.* 1 mm in distance and 2 mm in width. EIS measurements were performed in the temperature range of 525–750 °C in synthetic air flow (10 sccm).

3. Results and discussion

3.1. Ink properties

The ability of an ink to be jetted is controlled by several intrinsic properties such as density, viscosity and surface tension of the fluid.[41–44] The printability number Z (eqn (1)), based on these physical properties, has been proposed and printability intervals are well-defined in the literature. For instance, Derby has suggested an interval between 1 and 10 based on simulations,[36] whereas Jang *et al.*[45] defined an interval between 4 and 14, using experimental observations on jetting of solvent mixtures. In our previous study, we showed that TiO_2 reactive sol–gel inks can be reproducibly printed with a printability number close to 1, where stability and control towards hydrolysis/condensation reactions in a reactive ink is the crucial factor.[30] Adding MDEA as the nucleophilic ligand to the solution the high stability of the ink for printing can be achieved. The ligand, however, is the most viscous component in the ink and reduces the printability number. As a result, the optimal amount of ligand to inhibit the hydrolysis/condensation reactions, while keeping a suitable printability number, has to be determined in relation to the metal–organic system and the media in use.

To identify the optimal MDEA content required for stability, the physical properties that define the printability number were investigated for a series of ink samples having different molar complexation ratios r = [MDEA]/[$Zr(OPr)_4$] from 9 to 15. Preliminary tests with $r < 9$ (results not shown) exhibited extremely quick gelation of the inks, and were not investigated further. Too high concentration of MDEA, *e.g.* $r > 15$, was not considered to avoid excessive shrinkage of the final printed pattern and polymerization of the ligand.[30] Moreover, inks having only water as the solvent system were investigated, *i.e.* ink r-0.1-100, to understand the water–precursor interaction, avoiding any effects of the co-solvents on the ink stability. Fig. 1 shows the flow curves of four such water-based inks, 1 h after their preparation.

The corresponding viscosity curves are presented in the inset. All prepared inks showed a Newtonian behavior, *i.e.* a constant viscosity value for the considered shear rate range.[30] Table 1 lists the viscosity values calculated from the slope of the flow curves in Fig. 1, along with the measured surface

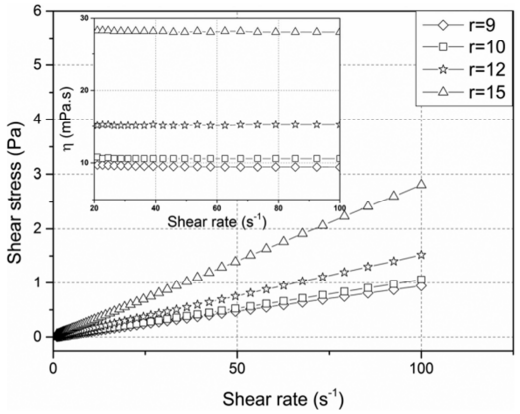

Fig. 1 Flow curve and viscosity curves (inset) of the four developed inks measured 1 h after preparation.

Table 1 Table viscosity and printability values

	t = 1 h			t = 48 h			t = 192 h			t = 360 h		
	η (mPa s)	σ (mN m^{-1})	Z (—)	η (mPa s)	σ (mN m^{-1})	Z (—)	η (mPa s)	σ (mN m^{-1})	Z (—)	η (mPa s)	σ (mN m^{-1})	Z (—)
Ink 9-0.1-100	9.4	33.4	2.83	11.5	33.6	2.32	37	33.5	0.72	148	33.3	0.18
Ink 10-0.1-100	10.6	33.1	2.50	13.1	32.9	2.02	18.3	33.4	1.45	25.9	33.2	1.02
Ink 12-0.1-100	15.2	31.4	1.70	16.7	31.1	1.54	16.7	31.7	1.55	18	31.2	1.43
Ink 15-0.1-100	28.1	31.3	0.92	29	31.5	0.89	26.5	31.2	0.97	28.9	31.6	0.90

tensions and printability. This analysis clearly indicates that the viscosity values increased with the amount of MDEA in the ink as a possible effect of polycondensation of the alkoxide–ligand complexes.[30,46] However, increasing the amount of MDEA did not affect the surface tension of the inks, which fluctuated by a few mN m^{-1}. The calculated printability numbers of inks aged for 1 h from Table 1 indicate that all inks except ink 15-0.1-100 exhibited a printability number within the $1 < Z < 10$ range.[36]

The long-term stability of the inks at different concentrations was evaluated following the evolution of printability over time. Fig. 2 shows the stability tests carried out with the ink samples and reported as printability as a function of r at different ageing times, from 1 to 360 h.

A green area in the plot represents the printable zone, which corresponds in this study to the viscosity range of inks having a printability number equal or lesser than 1, while a red area represents the viscosity range where inks are theoretically not printable ($Z < 1$). In this long-term stability study, the decrease in the Z value is strongly linked to a viscosity increase caused by a less effective hydrolysis/polymerization inhibition over time. The frontier viscosity value between the 2 zones ($Z = 1$) is based on typically observed values for surface tension (31 mN m^{-1}) and density (1 g cm^{-3}) for this type of ink (see also Table 1). As the hydrolysis ratio h was kept constant for all the inks, different complexation ratio intervals were studied for each concentration. For the inks with $c = 0.2$ g ml^{-1} (blue dots in Fig. 2),

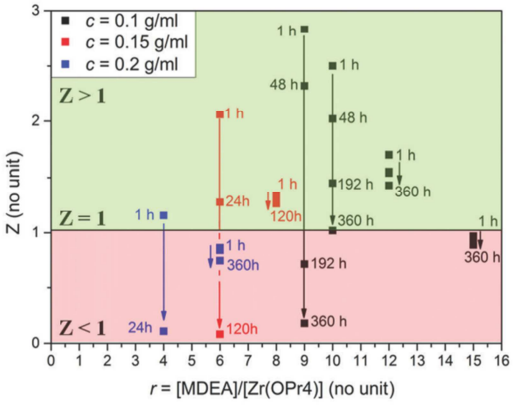

Fig. 2 Ink printability at different concentrations and aging time *versus* complexation ratio.

ink 4-0.2-100 was in the printability range for *ca.* 1 h, before going out of it with a too low Z after 24 h of aging. Despite being all the time outside of the printability range, the ink 6-0.2-100 gave a very stable Z value. For inks with $c = 0.15$ g ml^{-1} (red dots in Fig. 2), ink 6-0.15-100 was printable for approximately 24 h before its printability number dropped below 1. On the other hand, ink 8-0.15-100 exhibited a stable printability number >1 over 120 h. For $c = 0.1$ g ml^{-1} (black dot in Fig. 2), data showed that inks made with low MDEA content (r = 9 and 10) exhibited a rapid decrease of printability number after a few days of aging. Finally, at higher MDEA content (r = 12 and 15), ink viscosities showed a remarkable long-term stability but only ink 12-0.1-100 remains printable after 360 h.

In summary, these observations indicate clearly that long term-stability was more difficult to achieve at high concentrations of zirconium in the solution. As the complexation ratio is reduced due to concentration increase, the alkoxide is less and less "protected" towards water, leading to YSZ polymerization which increases viscosity over time.[30] However, improved stability might be reached by increasing the complexation ratio r and decreasing the hydrolysis ratio h. At low concentration ($c = 0.1$ g ml^{-1}), the same effect is observed for low complexation ratios (r = 9 and 10), which resulted in unstable inks. On the other hand, high MDEA content in ink 15-0.1-100 had the undesirable effect to decrease the printability. As also observed and demonstrated for Ti-based inks, the increase of viscosity for high MDEA concentrations can be the consequence of alkoxide–ligand complex polycondensation.[30,46] As a result of this detailed analysis, we defined a proper long-term stabilization for the complexation ratio with an optimal r of 12. As a consequence ink 12-0.1-100 achieved a suitable chelate effect on the alkoxide and preserved the printability in the long term.

It is worth noticing from Table 1 that ink surface tension σ was very slightly affected by MDEA content over time, making viscosity the main physical property controlling the printability. Another important feature of such inks is that the printability can be further refined and improved by diluting the solvent with a less viscous compound. We proposed ethanol, which not only reduces viscosity but also can improve the ink drying rate and reduce the surface tension. Such a use of alcohols in general is crucial in surface chemistry, especially when depositing water based inks. For example, the inks developed in this study contain propanol from the alkoxide, which reduces the high surface tension of water (72.8 mN m^{-1} at 20 °C) to much lower values (*ca.* 31 mN m^{-1}, see Table 1). Such a decrease improves the substrate wettability to maximize the substrate

Table 2 Viscosity/printability of ethanol diluted inks for ink 12-01-*X*

	t = 1 h				t = 360 h			
X water/ethanol (vol%)	η (mPa s)	σ (mN m^{-1})	ρ (g cm^{-3})	Z (—)	η (mPa s)	σ (mN m^{-1})	ρ (g cm^{-3})	Z (—)
100/0	15.2	31.4	1.06	1.70	18	31.7	1.06	1.43
80/20	15.1	30.3	1.03	1.65	17	30.1	1.03	1.47
60/40	14.9	29.5	1.01	1.64	16.7	29.1	1.01	1.46
40/60	12.8	27.3	0.99	1.82	14.8	27.8	0.99	1.57
20/80	12.5	26.1	0.96	1.79	11.3	26.4	0.96	1.98
0/100	7	24.5	0.94	3.07	8.01	24.8	0.94	2.68

coverage, leading to homogenously printed continuous thin films.[47] The key point in tailoring the solvent composition is then not only in the ink jetting process, but also in depositing the ink on substrates with different surface free energies and in improving the drying rate.

As a result of such an analysis, a series of optimized inks with r = 12 and c = 0.1 g ml^{-1}, with different water/ethanol ratios (from X = 0 to 100) were synthesized to evaluate the most promising ink for inkjet printing. The measured physical properties of the inks at different aging times are reported in Table 2. Such values indicate that all the inks were within the defined printable range in the considered aging time frame. As expected, both viscosity and surface tension were significantly decreased as the ethanol content increases, rising up the ink printability after 360 h of aging from 1.4 for X = 100 to 2.7 for X = 0. Moreover, the surface tension of the ink spans from 31 to 24 mN m^{-1}, when X is reduced. Such a decrease in surface tension results in better coverage of substrates, and opens the possibility of using a larger choice of substrates. However, while increasing the volume of ethanol can be beneficial for droplet formation and wettability the water/ethanol ratio can also have a strong influence on drying, where too fast drying can lead to clogging at the nozzle. In particular for the presented YSZ inks, clogging for $X < 40$ vol% inks (*i.e.* inks with more than 60 vol% ethanol) was observed. On the basis of these observations we conclude that from the presented matrix of inks, the ink with formula ink 12-0.1-60 is the most suitable for printing.

3.2. Ink jettability

The jettability of ink 12-0.1-60 was studied first by using a piezoelectric printer.

Fig. 3(a) shows a droplet of fresh ink 12-0.1-60 after ejection at a firing frequency of 1 kHz at different distances from the nozzle, observed with a camera mounted on a printer.

At a distance of 100 μm, a filament with a round head is formed, due to the ejection process and the surface tension difference between the ink and the nozzle plate. The droplet was not completely spherical at this stage. However, in the range 200–1000 μm, the ejected droplet exhibited a remarkable stable spherical shape in the considered nozzle–droplet distance range. Moreover, no satellite droplets could be observed in the whole distance range, indicating high quality printability. Such a result is in accordance with the ability to print when the printability (here, Z = 1.7) is in the range $1 < Z < 10$. Fig. 3(b) shows the result of the same analysis carried out with ink 12-0.1-60 aged

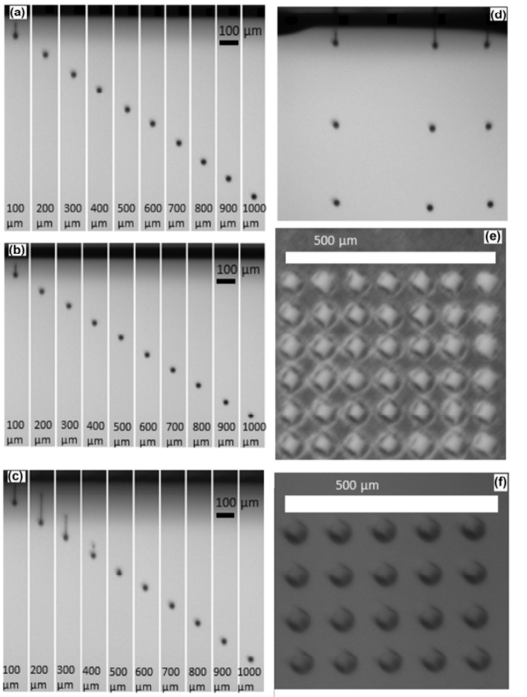

Fig. 3 Droplet at different nozzle distances (frequency = 1 kHz) of ink 12-0.1-60 as prepared (a), aged for 48 h (b), and aged for 1200 h (c), followed by droplets of fresh ink 12-0.1-60 (frequency = 10 kHz) (d) and optical pictures of an array of fresh ink 12-0.1-60 printed on NiO/YSZ (e) and alumina (f).

for 48 h on the shelf (Z = 1.5) with similar results to that for the fresh ink, verifying the reliability of the 48 h-term stability and printability at the jetting. With the conditions of jetting used in the experiment, the fully formed droplets showed a stable diameter in the range of 30–32 μm up to 48 h. Finally, Fig. 3(c) shows the jettability of ink 12-0.1-60 aged for 1200 h (50 days). The latter ink required a minor adjustment of the waveform, where just the nozzle filling voltage was slightly modified from −10 to −7 V while keeping the general waveform shape and the firing voltage the same. A long tail, which was not observed for fresher inks, could be noticed above the droplet in the distance range

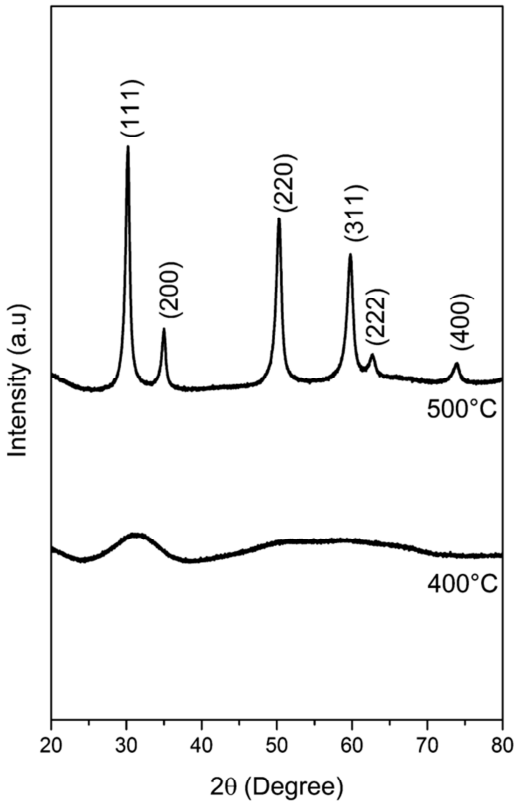

Fig. 4 XRD pattern of fresh ink 12-0.1-60 calcined at different temperatures.

100–300 μm, followed by breaking of the tail at 400 μm, resulting in the formation of a main droplet and satellite droplets. However, satellites merged at 500 μm to form again a spherical and stable droplet in the range 500–1000 μm. Such a change in jetting was attributed to a slight viscosity increase in the long term (18.1 mPa s, $Z = 1.3$ at 1200 h). Despite the presence of a long tail and satellite droplet in the first hundreds of micrometers from the nozzle, this observation demonstrates the outstanding stability of the ink after a long term aging of 50 days. Yet, the jetted droplet diameter was comparable to that measured for fresh inks and similar droplet shape stability was also observed in the 48 h aged ink at increased firing frequency, from 1 kHz to 10 kHz (Fig. 3(d)).

A series of droplets was deposited on two different substrates with different microstructures, *i.e.* dense alumina and the porous NiO/YSZ anode, using a lateral droplet spacing (*i.e.*, distance between the center of two adjacent droplets) of 100 μm. Fig. 3(e and f) shows the resulting patterns after deposition. For both substrates, the deposited droplets appear as circular dots and exhibited a reproducible diameter of *ca.* 52 ± 2 μm. This further illustrates the versatility to deposit this ink on very different surfaces at the micrometric scale.

3.3. Phase and microstructure characterization

The deposition of reactive ink based on sol–gel leads to the formation of an amorphous polymeric matrix. This material results from the hydrolysis and condensation reactions of the zirconium alkoxide, the yttrium based dopant, as well as solvents and agents such as MDEA. Therefore, a calcination step is necessary to remove the organics and crystallize the deposited layer. Previous thermal analysis (TG/DTA) performed on the sol–gel system using MDEA[30] showed that the mass loss relative to solvent evaporation and the chelating agent was completed at 350 °C. Based on those results, the crystallization behavior of ink 12-0.1-60 was studied using thermal XRD at temperatures above 350 °C. Fig. 4 shows the XRD patterns

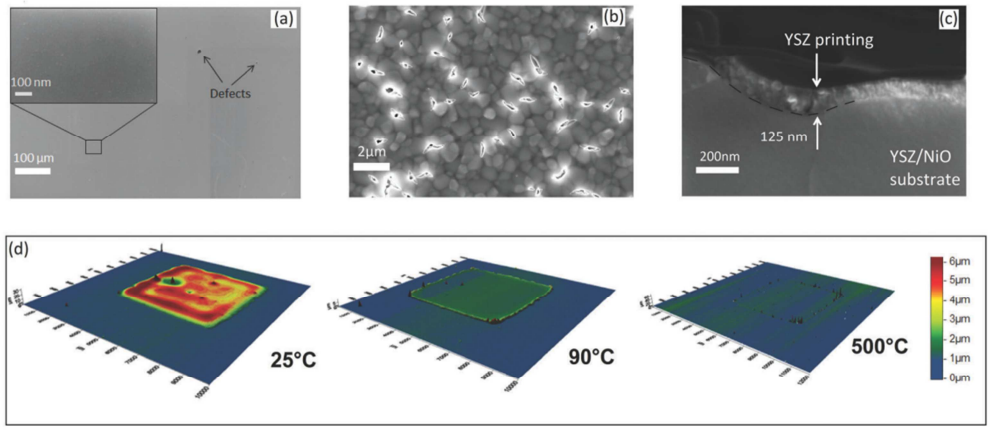

Fig. 5 SEM images of the printed fresh ink 12-0.1-60 on glass calcined at 500 °C for 1 h at low (a) and high (inset) magnification, printed and calcined on NiO/YSZ from the surface (b) and cross-sectional view (c), and 3D reconstruction of profilometry data at different temperatures (d).

performed on powder synthesized by calcining the ink at 400 °C and 500 °C for 1 h.

Diffraction patterns show that no clear crystalline formation could be observed for the powder calcined at 400 °C, while a well-defined pattern was observed at 500 °C. The pattern observed at 500 °C indicates that the formed material is indeed 8YSZ,[48] with a crystallite size evaluated at 15 nm *via* the Scherrer equation. In the light of such results, the calcination temperature of 500 °C was chosen for the firing of the printing.

Fig. 5 shows the microstructures of the film deposited with a thermal HP printer after calcination at 500 °C.

In particular, Fig. 5(a) shows the surface of calcined ink 12-0.1-60 on a dense glass substrate at low magnification after calcination. The resulting film is homogeneous and continuous, with a few defects probably due to the inaccuracy of the used HP printer.[15] Microstructural features could only be observed at very high magnification (inset Fig. 5(a)) and exhibits a very dense microstructure with very small grains of *ca.* 15 nm. The crystallite size estimation by SEM pictures was consistent with the crystallite size obtained from XRD measurements. The film thickness was estimated by SEM of sample cross sections while the evolution of the thickness with the calcination was measured by using 3D profilometry. The printing thickness was found to be slightly dependent on the substrate porosity with average values below 150 nm for one-layer printing, also confirmed by laser profilometry. Fig. 5(b) shows the typical microstructure of the printed electrolyte layer on a porous NiO/YSZ SOFC anode. Some notable differences with the deposition on glass (Fig. 5(a)) are readily noticed. Due to the porosity of the NiO/YSZ surface, the resulting film after calcination shows a relatively high number of cracks, all located above pores. The presence of such cracks can possibly be attributed to the following two effects:

– First, the combination of large pores and very low film thickness, (measured on a cross section (Fig. 5(c)) at around 100 nm) might induce film cracks due to capillary forces.

– Secondly, the film shrinkage during calcination could also induce these cracks. Sol gel based solutions contain a high amount of solvent and volatile elements and it results in very high volume shrinkage during heat treatment.[49] Note, however, that the cracks were not observed with the flat, pore-free soda-lime glass substrate (Fig. 5(a)).

The shrinkage of this ink has been estimated using 3D profilometry on a 5 × 5 mm^2 print of fresh ink 12-0.1-60 by measuring the print dimensions (length x, width y, and thickness z) at different stages of heat treatment. 3D images were then reconstructed and are shown in Fig. 5(d). No shrinkage was measured in the lateral (*i.e.* x- and y-) directions, even after calcination at 500 °C. However, a remarkable shrinkage of 90 vol% volume reduction after calcination was measured in the vertical (z-) direction. Such high shrinkage, along with the capillary pressure effect, will strongly participate in the collapse of the film through the pores of the substrate.

3.4. Electrical characterization

For electrical characterization, optimized ink 12-0.1-60 was printed onto quartz and alumina substrates using a thermal inkjet printer. The ionic conductivity of the calcined thin film was measured by electrochemical impedance spectroscopy (EIS) in air between 500 and 750 °C. The measurements were taken in the lateral configuration, *i.e.* in-plane electrodes deposited on the film surface (see drawings Fig. 6a). This is an optimal electrode/electrolyte configuration for nanometric thin films due both to the maximization of electrolyte impedance with respect to the geometrical features (thickness is below 150 nm) and to the minimization of the electrode contribution to the total impedance.[39,40] Fig. 6 shows typical Nyquist and Bode plots of the film on quartz taken at 750 °C in air (Fig. 6a) and the Arrhenius plot of the films on quartz and alumina calculated from the EIS data at different temperatures (Fig. 6b). Recorded Nyquist plots on quartz exhibited a single semi-arc due to a dominant

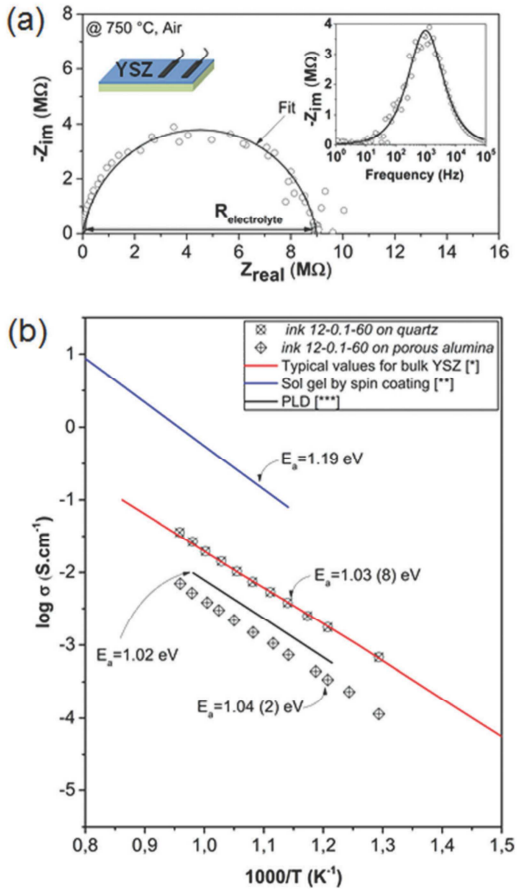

Fig. 6 (a) Typical Nyquist and Bode plots of the film on quartz taken at 750 °C in air and (b) Arrhenius plot of the films on quartz and alumina calculated from the EIS data at different temperatures along with typical conductivity values reported for YSZ thin film (red line, * = ref. 50), and values reported for 8YSZ thin film deposited by sol gel spin coating (blue line, ** = ref. 51) and PLD (black line, *** = ref. 52).

grain boundary contribution, *i.e.* a single R//C Voight element. This is modeled by a typical RQ circuit (solid line in Fig. 6a) while the inset of Fig. 6a shows a Bode plot of the same data. The RQ circuit resistance was 9.00 MΩ and the summit frequency was 972 Hz. The *n*-value for the constant phase element Q was 0.892. The calcined films on quartz resulted to be crack-free and homogeneous. The results are consistent with the average grain size of 15 nm measured by XRD and SEM. This electrical behavior is typical of nanocrystalline thin films[39,40] and the electrolyte ohmic resistance ($R_{eletrolyte}$ in Fig. 6a) is calculated at the relaxation of the equivalent RQ circuit. Total conductivity and activation energy (E_a) were then calculated from the measured real impedance components (R_{el}) at different temperatures and normalized for the electrolyte/thin film geometry (Fig. 6b).

For comparison typical YSZ thin film conductivity measured by EIS[50] is shown in Fig. 6b (red line) as well as Arrhenius plots from previous studies of 8YSZ thin films deposited by sol–gel (spin coating) (blue line),[51] and PLD (black line).[52] The calculated conductivity and activation energy (1.03 ± 0.08 eV) of our inkjet printed thin film are consistent with typical values reported for 8YSZ thin films. The conductivity at 750 °C (3.1×10^{-2} S cm^{-1}) is as expected for bulk YSZ[50] and the inkjet printed thin film shows performances comparable with other films deposited by PLD.[52] Fig. 6b also shows the results collected for the alumina substrate. In that case the film was partially cracked, due to the roughness and asperities of the alumina substrates. Despite the lower conductance, the inkjet layer showed comparable conductivity with PLD films, indicating an overall reliability of the deposited layers by inkjet on rough substrates.

4. Conclusion

Stable aqueous-based metal–organic solutions for inkjet printing were designed and demonstrated for printing of 8YSZ thin films and micrometric patterns. Ink printability and long term stability were optimized by the adjustment of the nucleophilic agent, metal oxide concentration and solvent composition. An optimized ink with c = 0.1 g ml^{-1}, [MDEA]/[Zr(OPr)$_4$] = 12 and water/ethanol = 60/40 vol% shows a remarkable long term stability of 360 h, with a printability Z number around 1, and an exceptional jettability after 1200 h of storage. Nanocrystalline 8YSZ thin films of 100–150 nm were obtained after calcination at 500 °C on different substrates including Si, quartz, polycrystalline Al_2O_3 and the tape cast NiO/YSZ SOFC anode substrate. The measured ionic conductivity agrees well with previously reported 8YSZ thin-film conductivity data. The formation of cracks in the printed films mainly depends on the quality of the substrate.

Acknowledgements

The authors would like to thank Mads Gudik-Sørensen (DTU) and Victor Costa Bassetto (EPFL) for their technical assistance. This project has received funding from the Fuel Cells and Hydrogen 2 Joint Undertaking under grant agreement No 700266. This Joint Undertaking receives support from the European Union's Horizon 2020 research and innovation program and Hydrogen Europe and N.ERGHY. Andreas Lesch thanks the Swiss National Science Foundation (SNSF) grant no. 154297.

References

1 T. Tsai, E. Perry and S. Barnett, *J. Electrochem. Soc.*, 1997, **144**, 1996–1998.
2 E. P. Murray, T. Tsai and S. Barnett, *Nature*, 1999, **400**, 649–651.
3 S. De Souza, S. J. Visco and L. C. De Jonghe, *Solid State Ionics*, 1997, **144**, 35–37.
4 B. Zhu, *J. Power Sources*, 1999, **84**, 39–44.
5 Q. X. Fu, S. W. Zha, W. Zhang, D. K. Peng, G. Y. Meng and B. Zhu, *J. Power Sources*, 2002, **104**, 73–78.
6 S. De Souza, S. J. Visco and L. C. De Jonghe, *Solid State Ionics*, 1997, **98**, 57–61.
7 R. O'Hayre, S.-W. Cha, W. Colella and F. B. Prinz, *Fuel Cell Fundamentals*, John Wiley and Sons Ltd, Chichester, United Kingdom, 2006.
8 J. Ding and J. Liu, *Solid State Ionics*, 2008, **179**, 1246–1249.
9 F. G. E. Jones and J. T. S. Irvine, *Ionics*, 2002, **8**, 339–343.
10 L. Jia, Z. Lü, X. Huang, Z. Liu, K. Chen, X. Sha, G. Li and W. Su, *J. Alloys Compd.*, 2006, **424**, 299–303.
11 Y. Zhang, X. Huang, Z. Lu, Z. Liu, X. Ge, J. Xu, X. Xin, X. Sha and W. Su, *J. Power Sources*, 2006, **160**, 1065–1073.
12 K. Rodrigo, J. Knudsen, N. Pryds, J. Schou and S. Linderoth, *Appl. Surf. Sci.*, 2007, **254**, 1338–1342.
13 G. Cao, H. W. Brinkman, J. Meijerink, K. J. Vries and A. J. Burggraaf, *J. Am. Ceram. Soc.*, 1993, **76**, 2201–2208.
14 V. Esposito, I. Garbayo, S. Linderoth and N. Pryds, *Epitaxial Growth of Complex Metal Oxides*, Elsevier Ltd, Cambridge, United Kingdom, 2015, pp. 443–478.
15 V. Esposito, C. Gadea, J. Hjelm, D. Marani, Q. Hu, K. Agersted, S. Ramousse and S. H. Jensen, *J. Power Sources*, 2015, **273**, 89–95.
16 C. Li, H. Shi, R. Ran, C. Su and Z. Shao, *Int. J. Hydrogen Energy*, 2013, **38**, 9310–9319.
17 R. I. Tomov, M. Krauz, J. Jewulski, S. C. Hopkins, J. R. Kluczowski, D. M. Glowacka and B. A. Glowacki, *J. Power Sources*, 2010, **195**, 7160–7167.
18 G. Deok, K. Chean, K. Bae, H. Jong, S. Won, J. Son and J. Hyung, *J. Power Sources*, 2016, **306**, 503–509.
19 R. Dou, T. Wang, Y. Guo and B. Derby, *J. Am. Ceram. Soc.*, 2011, **94**, 3787–3792.
20 A. D. Pomogailo and V. N. Kestelman, *Metallopolymer Nanocomposites*, 2005.
21 C. Wang, R. I. Tomov, R. Vasant Kumar and B. A. Glowacki, *J. Mater. Sci.*, 2011, **46**, 6889–6896.
22 B. Yoldas, *J. Sol–Gel Sci. Technol.*, 1998, **13**, 147–152.
23 H. S. Chen, R. V. Kumar and B. A. Glowacki, *J. Sol–Gel Sci. Technol.*, 2009, **51**, 102–111.
24 M. Chouiki and R. Schoeftner, *J. Sol–Gel Sci. Technol.*, 2010, **58**, 91–95.

25 D. A. Gregory, Y. Zhang, P. J. Smith, X. Zhao and S. J. Ebbens, *Mater. Rev.*, 2016, 4048–4055.
26 K. Black, J. Singh, D. Mehta, S. Sung, C. J. Sutcliffe and P. R. Chalker, *Nat. Publ. Gr.*, 2016, 1–7.
27 J. M. Chem, Z. Kao, Y. Hung and Y. Liao, *J. Mater. Chem.*, 2011, 18799–18803.
28 B. S. Cook, Y. Fang, S. Kim, T. Le, W. B. Goodwin, K. H. Sandhage and M. M. Tentzeris, *Electron. Mater. Lett.*, 2013, **9**, 669–676.
29 L. L. Hench and J. K. West, *Chem. Rev.*, 1990, **90**, 33–72.
30 C. Gadea, D. Marani and V. Esposito, *J. Phys. Chem. Solids*, 2017, **101**, 10–17.
31 C. Sanchez, J. Livage, M. Henry and F. Babonneau, *J. Non-Cryst. Solids*, 1988, **100**, 65–76.
32 L. Rose, O. Kesler, Z. Tang and A. Burgess, *J. Power Sources*, 2007, **167**, 340–348.
33 S. Kim, S. Pil and S. Woo, *J. Power Sources*, 2002, **110**, 222–228.
34 M. Gaudon, C. Laberty-robert, F. Ansart and P. Stevens, *Solid State Sci.*, 2006, **26**, 3153–3160.
35 A. Lesch, F. Cortés-Salazar, V. C. Bassetto, V. Amstutz and H. H. Girault, *Chim. Int. J. Chem.*, 2015, **69**, 284–289.
36 B. Derby, *Annu. Rev. Mater. Res.*, 2010, **40**, 395–414.
37 A. Hauch and M. Mogensen, *Solid State Ionics*, 2010, **181**, 745–753.
38 A. Monshi, *World J. Nano Sci. Eng.*, 2012, **2**, 154–160.
39 K. Mohan Kant, V. Esposito and N. Pryds, *Appl. Phys. Lett.*, 2012, **100**, 16–20.
40 S. Sanna, V. Esposito, J. W. Andreasen, J. Hjelm, W. Zhang, T. Kasama, S. B. Simonsen, M. Christensen, S. Linderoth and N. Pryds, *Nat. Mater.*, 2015, **14**, 1–5.
41 M. Černá, M. Veselý, P. Dzik, C. Guillard, E. Puzenat and M. Lepičová, *Appl. Catal., B*, 2013, **138–139**, 84–94.
42 I. Fasaki, K. Siamos, M. Arin, P. Lommens, I. Van Driessche, S. C. Hopkins, B. A. Glowacki and I. Arabatzis, *Appl. Catal., A*, 2012, **411–412**, 60–69.
43 G. D. Martin, S. D. Hoath and I. M. Hutchings, *J. Phys.: Conf. Ser.*, 2008, **105**, 12001.
44 H. Kipphan, *Handbook of Print Media*, 2001, vol. 13.
45 D. Jang, D. Kim and J. Moon, *Langmuir*, 2009, **25**, 2629–2635.
46 S. Doeuff, M. Henry, C. Sanchez and J. Livage, *J. Non-Cryst. Solids*, 1987, **89**, 206–216.
47 Y. Yuan and T. R. Lee, *Springer Ser. Surf. Sci.*, Springer Berlin Heidelberg, Berlin, Germany, 2013, p. 3.
48 D. S. Patil, K. Prabhakaran, C. Durgaprasad, N. M. Gokhale, A. B. Samui and S. C. Sharma, *Ceramics*, 2009, **35**, 515–519.
49 C. B. Carter and M. G. Norton, *Ceramic Materials: Science and Engineering*, 2007.
50 J. Jiang and J. L. Hertz, *J. Electroceram.*, 2014, **32**, 37–46.
51 Y. W. Zhang, S. Jin, Y. Yang, G. B. Li, S. J. Tian, J. T. Jia, C. S. Liao and C. H. Yan, *Appl. Phys. Lett.*, 2000, **77**, 3409–3411.
52 X. Guo, E. Vasco, S. Mi, K. Szot, E. Wachsman and R. Waser, *Acta Mater.*, 2005, **53**, 5161–5166.

Paper III:

Assembly three dimensional bismuth titanate (3D-bit) by extrusion-based fuse deposition modeling technique

ASSEMBLY THREE DIMENSIONAL BISMUTH TITANATE (3D-BiT) BY EXTRUSION-BASED FUSE DEPOSITION MODELING TECHNIQUE

[1,2]NUNTANID PHATHARAPEETRANUN, [1]CHRISTOPHE GADEA, [2]BUSSARIN KSAPABUTR AND [1]VINCENZO ESPOSITO

[1]Department of Energy Conversion and Storage, DTU Energy, Technical University of Denmark

[2]Department of Materials Science and Engineering, Faculty of Engineering and Industrial Technology, Silpakorn University, Thailand

Email: [1]nuntanid.ph@gmail.com and [2]vies@dtu.dk

Abstract: Bismuth Titanate ($Bi_4Ti_3O_{12}$, BiT) are synthesized via sol-gel technique and combined with polyvinylpyrolidone (PVP) to obtain a thick paste composite for three dimensional shaping by extrusion-based fuse deposition modeling (FDM) technique. The phase compositions were investigated by X-ray diffractometry (XRD). Dilatometry measurement was performed to find out the suitable sintering temperature. Single phase with orthorhombic structure of BiT was obtained after calcination at 850˚C for 1 h. The thick paste with different % vol. of PVP (1.0, 3.0, 7.5, 20% vol.) before printing was evaluated by rheology to optimize the extrusion condition. At 3.0% vol. of PVP, the printing speed of thick paste material was enlarged over 50% of BiT gel.

Keywords: 3D printing, $Bi_4Ti_3O_{12}$, Rheology, Sintering

1. INTRODUCTION

Three-dimensional printing, also well-known as the extrusion-based fuse deposition modeling (FDM) is one of the most attractive fabrication techniques for fabrication three dimensional objects [1]. There are several advantages to this technique compared to traditional ceramic fabrication process due to its ability to provides objects with complex geometries in short time processing, relatively low operating cost, user friendly and allow various types of printing materials [2]. Sun K. et al. prepared lithium ion micro-battery by FDM technique [3]. The obtained micro-battery exhibited high energy and power density, suggesting that it could be applied in autonomously powered micro devices. Recently, Castles et al. fabricated 3D dielectric material using barium titanate ($BaTiO_3$) powder as filler and ABS polymer as matrix using FDM technique [4]. The dielectric constant of composite with 20% vol. of $BaTiO_3$ was 6.24, which matched those of bulk unprinted materials, indicating that the FDM technique can be applied for manufacturing process for ferroelectric and dielectric composites materials.

Bismuth titanate ($Bi_4Ti_3O_{12}$, BiT) is one of bismuth based ferroelectric compounds and belongs to the Aurivillius compounds family that can be represented by the general formula: $(Bi_2O_2)^{2-}(A_{m-1}B_mO_{3m+1})^{2+}$. Its crystalline structure consists of $(Bi_2Ti_3O_{10})^{2+}$ layers alternating with $(Bi_2O_2)^{2-}$ layers perpendicular to the c-axis [5]. It has high Curie temperature (675˚C), a good mechanical properties, environmental friendly (lead-free), low dielectric dissipation and a relatively high dielectric constant $\varepsilon \approx 200$ [6]. Recently, lead-free piezoelectric ceramics have attracted considerable attention due to environmental concerns, and BiT is considerable to be a good material for high temperature piezoelectric applications, memory storage and optical display devices [7-10].

In this work, we fabricate 3D-shaped BiT by a two-step assembly method, using hybrid-sol-gel chemistry and FDM technique, with the aim to develop 3D-BiT object with complex shape.

2. DETAILS EXPERIMENTAL

2.1. Materials and Procedures

The starting precursors used in this work included titanium isopropoxide (Sigma-Aldrich, $Ti(OCH(CH_3)_2)_4$), N-methyl-diethanolamine (Sigma-Aldrich, $CH_3N(C_2H_4OH)_2$), ethanol (Sigma-Aldrich, C_2H_5OH), distillated water (H_2O), bismuth (III) oxide powders (Sigma-Aldrich, Bi_2O_3) and polyvinylpyrrolidone (Sigma-Aldrich, PVP, Mw ≈ 1,300,000). All chemicals were analytical reagent grade and used without further purification

2.2. Preparation of bismuth titanate ($Bi_4Ti_3O_{12}$) via sol-gel technique

For BiT synthesis (schematic diagram 1), 7.66 mL of $Ti(OCH(CH_3)_2)_4$ was stabilized by 5.93 mL of $CH_3N(C_2H_4OH)_2$ under argon flow. The mixture was stirred for 10 min, then 0.51 mL of C_2H_5OH and 0.91 mL of distillated water were added drop wise into the solution under magnetic stirring, respectively. The prepared solution was stirred vigorously for 10 min to achieve complete dissolution and mixing. Then, 8.86 g of Bi_2O_3 was added with corresponding to 10% wt. excess to the solution and stirred continuously for 30 min at room temperature until a BiT yellow gel was obtained.

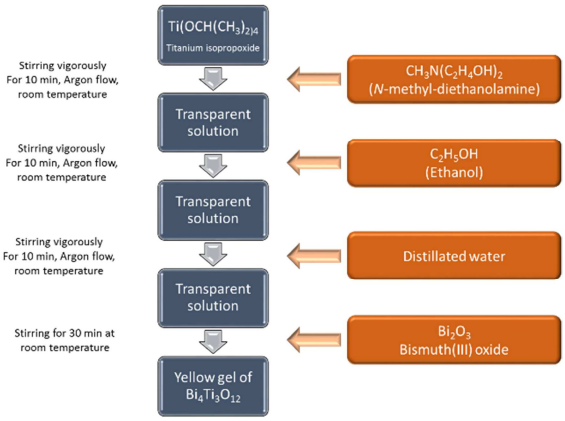

Schematic diagram 1. Flow of synthesize bismuth titanate ($Bi_4Ti_3O_{12}$) via sol-gel technique

The phase identification performed at room temperature using a monochromatic Cu-Kα radiation X-ray diffractometer (XRD: Bruker D8 Robot Tools X-ray diffraction, Bruker, Germany). The XRD analysis was carried out ex-situ with a scan speed of 0.6° 2θ/min at a 2θ range of 20° to 60° of several calcined samples at 500, 600, 800, 850 °C for 1 hour. The calcined powders ($Bi_4Ti_3O_{12}$) at 500 °C were used for pellet fabrication by uniaxial hydraulic press. A horizontal assembly dilatometer (NETZSCH DIL 402C) was applied to determine the shrinkage behavior. The BiT pellet was heated in chamber furnace in static air environment with temperature program; ramp up heating rate 1°C/min from 25°C to 850°C and holding at 850°C for 2 h and ramp down with cooling rate 5°C/min from 850°C to 25°C.

2.3 Fabrication of 3-dimensional of bismuth titanate ($Bi_4Ti_3O_{12}$) by FDM technique

3D-bismuth titanate (3D-BiT) was fabricated by a FDM technique (schematic diagram 2). First, 20 mL of BiT gel was mixed with various % vol. of PVP from 1.0 to 20% vol. The mixture was then stirred at

room temperature with constant stirring for 30 min until homogeneous thick paste appeared. The resulting thick paste was subjected to ultrasonic agitation at a frequency of about 24 kHz for 30 minutes. The whole mass was transferred to an extrusion syringe with fixed nozzle of diameter 1.4 mm and then was printed by 3D printer (Zmorph 2.0S, ZMorph Sp. z o.o., Poland).

The rheology characteristic of bismuth titanate ($Bi_4Ti_3O_{12}$) thick paste with different % vol. of PVP were evaluated before printing by a rotational rheometer (MCR viscometer 302, Anton Paar, Austria) in order to find the suitable printing condition.

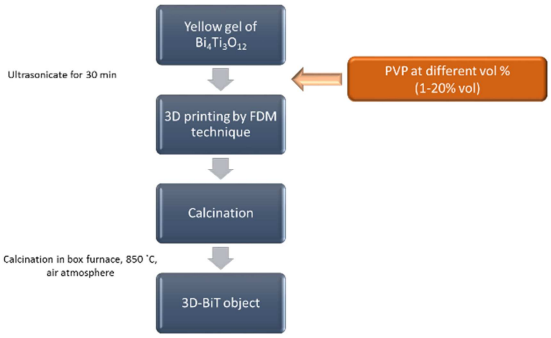

Schematic diagram 2. Flow of assembly 3D-BiT by FDM technique

The thick paste materials were characterized in rotational mode with controlled constant temperature of 21 °C. All the experiments were performed using a cone-parallel spindle of 25 mm in diameter and 4° angle (CP25-4).

For non-Newtonian fluids, the relation between wall shear rate ($\dot{\gamma}_w$) and extrusion printing speed (v) can be obtained by the Rabinowitsch relation [11]:

$$\dot{\gamma}_w = \frac{(3n+1)}{4n}\left(\frac{4Q}{\pi R^3}\right) \quad (1)$$

where R is capillary radius of nozzle (mm), Q is the volumetric flow rate through the capillary nozzle (mm^3/s), and n is a constant equal to the power-law index.

The extrusion printing speed (v) could be obtained by substitute $Q = \pi R^2 v$ in equation (1);

$$\dot{\gamma}_w = \frac{(3n+1)}{4n}\left(\frac{8v}{D}\right) \quad (2)$$

where v is the extrusion printing speed (mm/s) and D is diameter of capillary nozzle (mm).

3. RESULTS AND DISCUSSION

3.1. Phase composition of $Bi_4Ti_3O_{12}$ (BiT)

To understand the crystallization behavior of $Bi_4Ti_3O_{12}$, the milled gel powders were calcined in air at temperature ranging from 500-900˚C for 1 h. Fig. 1 shows the XRD pattern of the calcination powders at different temperatures. The calcined powder at 500˚C exhibits in yellow color of the residual Bi_2O_3 corresponding to the presence of Bi_2O_3 phase in XRD pattern. The powders calcined at 600˚C becomes more white while XRD pattern shows the onset crystalline nature of BiT in agreement with literature [12, 13]. It is known that BiT has a ferroelectric Curie temperature of 675°C; below this temperature, the crystal belongs to a pseudo-tetragonal phase, and above this temperature, it is transformed into a pseudo-orthorhombic phase. This could be confirmed by the splitting profile peaks around 2θ of 33˚ of the powders calcined at 800˚C and 850˚C suggests that at this calcination temperature, these crystals have a pseudo-orthorhombic phase [12, 13]. The XRD pattern of calcined sample at 850˚C shows well-defined BiT crystalline structure and there is no signal of Bi_2O_3 crystalline phase. The line width is decreased and intensity of diffraction line is increased, suggesting the particles were agglomerated, fused together and some grain growth occurred. The structural parameters of the BiT calcined sample at 850 ˚C were a = 5.41 Å, b = 5.45 Å, and c = 32.84 Å which these parameters are comparable with the values given in the JCPDS 72-1019 [14].

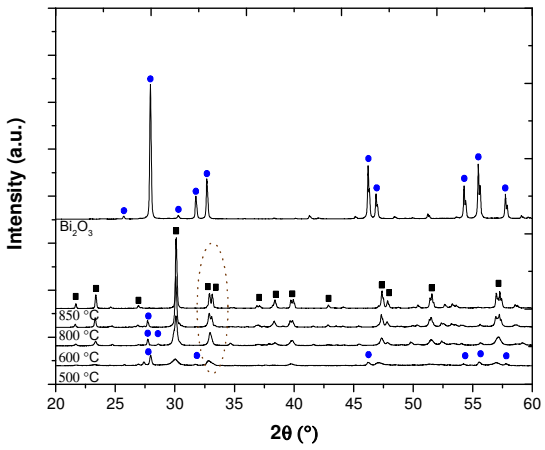

Fig. 1: XRD patterns of $Bi_4Ti_3O_{12}$ powders prepared from the sol-gel method after calcination at different temperature

Fig. 2 shows the dilatometry plot of the 500˚C calcination of BiT pellet. The curve predicts that there is no shrinkage on heating up to a temperature of 600˚C. However, between 25˚C and 600˚C, there is some small expansion of 0.1% in the BiT pellet, probably due to the reaction of some intermediate chemical and/or the arrangement within the crystal lattice. The shrinkage started from 600°C while a great shrinkage can be observed after heating between 700°C and 800˚C. The overall dimension change is around 14% reduction from the original length. These results are in good agreement with literature [15]. Based on dilatometry results, the suitable sintering temperature of BiT is selected at 850°C.

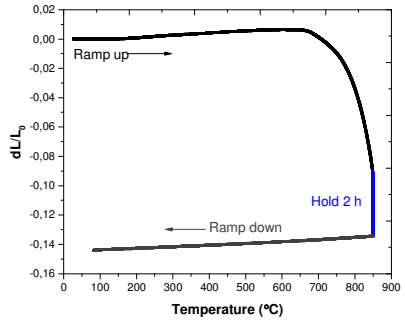

Fig. 2: Linear shrinkage curve of calcined BiT from room temperature to 850˚C

3.2 Rheology of BiT compounds

The rheological properties of the BiT thick paste materials with different content of PVP were then investigated to optimize the printing condition. As presented in Fig. 3*a*, at higher % vol of PVP, the viscosity profiles are shifted to higher values of viscosity. This is due to the presence of high molecular weight of PVP ($M_w \approx 1{,}300{,}000$) which give resistance to the flowing behavior under applied shear stress [16, 17].

Besides nozzle diameter and viscosity of material, shear thinning behavior facilitates continuous flow through fine nozzles without clogging. Generally, this behavior is quantitatively estimated by evaluating the flow indexes (n). Fig. 3*b* shows the double logarithmic plot for the BiT composites; the slope of the straight line corresponds to the flow index (n) that can be used to identify the flowing mechanism of a system [18-21]. As shown in Fig. 3*c*, all samples exhibit shear-thinning behavior (n<1), lower n value indicating more-shear thinning activities. The increasing of flow index (n) was observed when increasing content of PVP from 1.0% vol to 7.5% vol and then slightly decrease when the PVP content is exceeded 7.5% vol.

Typically, the processing shear rate of extrusion process is in the range 1-100 s^{-1} [22]. The extrusion printing speed (v) is calculated from equation (2), at 3.0% vol of PVP, the extrusion printing speed could be expanded from 1 to 15 mm/s (Fig. 4)

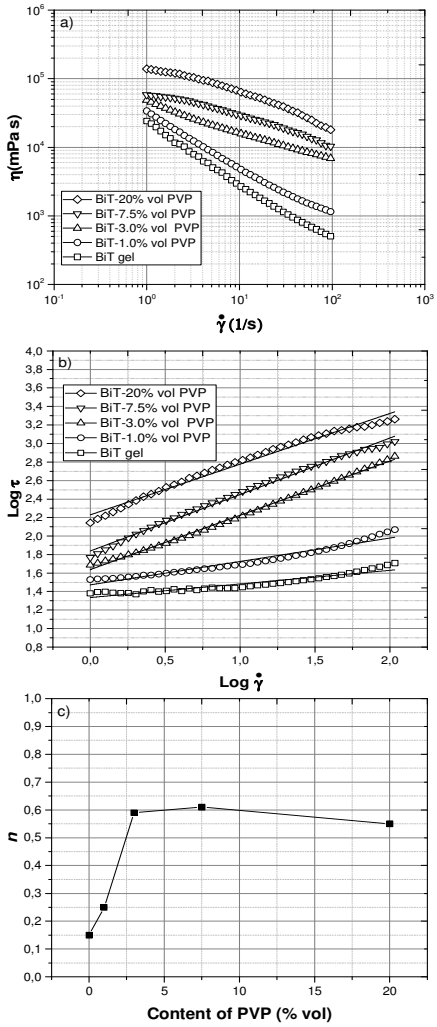

Fig. 3: (a) Viscosity plot and the corresponding (b) double logarithmic power law plot for the complete series of BiT series showing the flow index (slope) and (c) flow index plot with different content of PVP

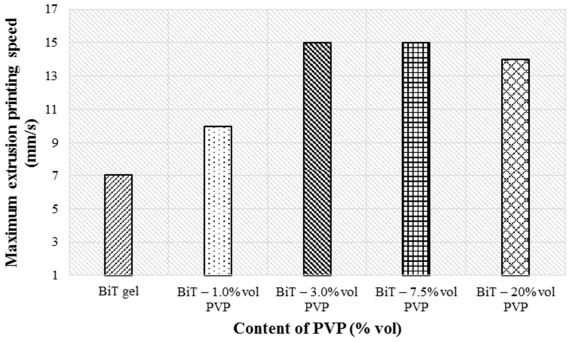

Fig. 4: Processing window for BiT gel and its composite for 1.4 mm of extrusion nozzle

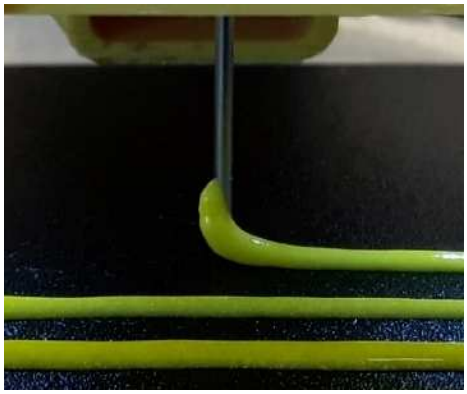

Fig. 5: Extrusion based FDM technique for BiT at 3.0% vol of PVP (3D-BiT)

Over 3.0% vol of PVP, there is no significant effect of further adding PVP. Upon the addition of PVP, the processing speed is expanded by 53%. PVP molecule acts as processing aid which could be reduced the wall shear rate ($\dot{\gamma}_w$) corresponding to the ability of printing at higher extrusion speed. Based on rheology results the BiT with 3.0% vol of PVP was selected for fabricating 3D object by FDM technique.

Figure 5 shows fabricated 3D-BiT object by extrusion-based FDM technique. By this technique, we could produce the printed object as complex shape with highly precise in shape and dimension.

CONCLUSIONS

In conclusion, the 3D bismuth titanate (3D-BiT) is successfully fabricated by two step assembly method, sol-gel followed by extrusion-based fuse deposition modeling (FDM) technique. BiT phase compositions, densification behavior and rheology of printing materials are investigated. Upon the adding 3.0% vol of PVP, corresponding to the ability to enlarge the extrusion printing speed of the thick paste materials over 50% compare to pure gel BiT.

ACKNOWLEDGEMENTS

The authors would like to thank Department of Materials Science and Engineering, Faculty of Engineering and Industrial Technology, Silpakorn University, the Royal Golden Jubilee Ph.D program (RGJ), Thailand for financial supporting and Department of Energy Conversion and Storage, DTU Energy, Technical University of Denmark for supporting the research.

.

REFERENCES

1. Zhao, H., C. Ye, and Z. Fan "3D printing of calcia-based ceramic core composites", Advances in Science and Technology, vol.88, no.88, 2014.
2. Kim, K., et al. "3D optical printing of piezoelectric nanoparticle–polymer composite materials", ACS nano, vol.8, no.10, pp. 9799-9806, 2014.
3. Sun, K., et al. "3D printing of microbatteries", American Ceramic Society Bulletin, vol. 92, no.6, pp. 11-11, 2013.
4. Castles, F., et al. "Microwave dielectric characterisation of 3D-printed $BaTiO_3$/ABS polymer composites", Scientific reports, vol.6, 2016.
5. Aurivillius, B. "Mixed bismuth oxides with layer lattices. 2. Structure of $Bi_4Ti_3O_{12}$", Arkiv for kemi, vol.1, no.6, pp. 499-512. 1950.
6. Macedo, Z.S., C.R. Ferrari, and A.C. Hernandes. "Impedance spectroscopy of $Bi_4Ti_3O_{12}$ ceramic produced by self-propagating high-temperature synthesis technique", Journal of the European Ceramic Society, vol.24, no.9, pp. 2567-2574, 2004.
7. Takenaka, T. and K. Sakata. "Grain orientation and electrical properties of hot-forged $Bi_4Ti_3O_{12}$ ceramics", Japanese Journal of Applied Physics, vol.19, no.1, pp. 31, 1980.
8. Yang, Q.B., et al. "$Bi_4Ti_3O_{12}$ nanoparticles prepared by hydrothermal synthesis", Journal of the European Ceramic Society, vol.23, no.1, pp. 161-166, 2003.
9. Yao, Y.Y., et al. "Doping effect on the dielectric property in bismuth titanate", Journal of Applied Physics, vol.95, no.6, pp. 3126-3130, 2004.
10. Yuji, N., et al. "Defect Control for Large Remanent Polarization in Bismuth Titanate Ferroelectrics –Doping Effect of Higher-Valent Cations–", Japanese Journal of Applied Physics, vol.39, no.12B, pp. L1259, 2000.
11. Collyer, A.A. and D.W. Clegg. "Rheological measurement", Chapman & Hall, 1993.
12. Zhang, F., T. Karaki, and M. Adachi. "Coprecipitation synthesis of nanosized $Bi_4Ti_3O_{12}$ particles", Japanese Journal of Applied Physics Part 1-regular Papers Brief Communications and Review Papers, vol.45, no.9B, pp. 7385-7388, 2006.
13. Pookmanee, P. and S. Phanichphant. "Characterization of bismuth titanate powders". Advanced Materials Research, vol.24-25,pp. 247-250, 2007.
14. Phases, P.D.F.-I., JCPDS International Centre for Diffraction Data. Swarthmore, PA, pp. 8-50, 1988.
15. Naz, S., et al. "Nanosized bismuth titanate ($Bi_4Ti_3O_{12}$) system drive through auto-combustion process by using suspension titania (TiO_2)", Journal of Thermal Analysis and Calorimetry, vol.114, no.2, pp. 719-723, 2013.
16. Wu, D., et al. "Rheology of carbon nanotubes–filled poly (vinylidene fluoride) composites", Industrial & Engineering Chemistry Research, vol.51, no.19, pp. 6705-6713, 2012.
17. Vidhate, S., et al. "Crystallization, mechanical, and rheological behavior of polyvinylidene fluoride/carbon nanofiber composites", Journal of applied polymer science, vol.112, no.1, pp. 254-260, 2009.
18. Marani, D., J. Hjelm, and M. Wandel. "Rheological analysis of stabilized cerium-gadolinium oxide (CGO) dispersions", European Ceramic Society. Journal, vol.34, no.3, pp. 695-702, 2014.
19. Marani, D., et al. "Colloidal stabilization of cerium-gadolinium oxide (CGO) suspensions via rheology", Journal of the European Ceramic Society, vol.35, no.10, pp. 2823-2832, 2015.
20. Marani, D., et al., "Poly (vinylpyrrolidone) as dispersing agent for cerium-gadolinium oxide (CGO) suspensions", Journal of materials science, vol.51, no.2, 2016.
21. Marani, D., et al. "Enhanced densification of thin tape cast Ceria-Gadolinium Oxide (CGO) layers by rheological optimization of slurries" Ceramics International, vol.43, no.7, pp. 5647-5653, 2017.
22. Sabic Global. "Innovative Plastics High & Low Shear Rate Rheology", Accessed on July 11, 2017. Available from: http://www.pod-sabic ip.com/KBAM/Reflection/Assets/Thumbnail/10606_4.pdf, 2013.

Paper IV:

Stoichiometric control in $Bi_4Ti_3O_{12}$ synthesis by novel hybrid solid state reaction

Stoichiometric control in $Bi_4Ti_3O_{12}$ synthesis by novel hybrid solid state reaction

C. Gadea*[a], N. Phatharapeetranun [b], B. Ksapabutr[b] J.-C. Grivel [a], V. Esposito [a]

a: DTU Energy, Technical University of Denmark, Risø Campus, Frederiksborgvej 399, DK - 4000 Roskilde, Denmark

b: Department of Materials Science and Engineering, Faculty of Engineering and Industrial Technology, Silpakorn University, Thailand
email: [a] chga@dtu.dk and [b]nuntanid.ph@gmail.com

Key words: Bismuth titanate, synthesis, sol-gel, colloids, dielectric

Abstract

The synthesis of bismuth titanate $Bi_4Ti_3O_{12}$ (BiT) is performed via a novel solid state reaction. The reaction is designed to control the stoichiometric content of the highly volatile element, *i.e.* Bi. The chemical route consists in trapping bismuth oxide colloids in a stabilized titanium based sol gel solution. The resulting colloidal-solution hybrid ink can be processed via various ceramic processes. After gelation of TiO_2 in the sol-gel component the mixture reacts at high temperature (850 °C) to yield the BiT phase. The obtained material is *c*-axis oriented, and its lattice parameters, shrinkage and density matches the pure $Bi_4Ti_3O_{12}$ phase. The sintered material exhibits enhanced higher dielectric constant (232) than usually reported for this phase.

1. Introduction

Bismuth titanate $Bi_4Ti_3O_{12}$ (BiT) is considered one of the most promising high temperature lead-free piezoelectric materials [1,2]. BiT is a member of the Aurivilius family and its structure consists of a triple perovskite unit $[Bi_2Ti_3O_{10}]^{2-}$ sandwiched between $(BiO_2O_2)^{2+}$ layers [3,4]. It exhibits a high Curie temperature (T_c = 675°C) [5], very low fatigue and high dielectric constants [1], which makes it a potential candidate for applications in piezoelectric devices, memory storage (FERAM) in a wide range of high temperature environment, and electro optics devices [3,6].

BiT powder is usually prepared via solid state reaction (SSR) [7,8] by milling stoichiometric amount of bismuth oxide Bi_2O_3 and titania TiO_2. Bismuth is, however, a highly volatile element and high temperature treatments in SSR can easily lead to bismuth evaporation, resulting in a poor control on composition, phases and properties [9]. Furthermore, the SSR technique yields generally agglomerated and coarsened particles, with limitations on microstructural control and processing flexibility [10]. Several wet-chemical techniques such as sol-gel [11], co-precipitation [12], hydrothermal [13] or polymeric precursor synthesis [14] can be alternatives to SSR to produce BiT powder. These techniques allow a better control of powder microstructure, stoichiometry and particle size and lead to enhanced properties. However, bismuth salts or alkoxides can be difficult to handle, while bismuth oxide powders are readily available, cheap and harmless. In this work, bismuth titanate is prepared via a novel wet route by mixing bismuth oxide powder and a stable titanium based sol gel solution, called reactive ink, previously developed for inkjet printing [15]. The resulting suspension, here called "hybrid ink", can potentially be deposited by various ceramic processes such as tape casting, inkjet or 3D printing after viscosity and particle size adjustments. By this method, BiT is formed during heat treatment of the suspension via solid state reaction, while the bismuth powder is covered by TiO_2 and not directly exposed to air, as in SSR. In this communication, we describe the experimental protocol used to produce pure BiT, and characterize the material obtained at high temperature as well as a measurement of its dielectric properties.

2. Experimental

The titania based reactive ink was prepared following the protocol described in [15]. Titanium (IV) isopropoxide (Ti(OPr)4 (hereafter TiTTIP, Sigma-Aldrich)) and N-methyldiethanolamine (MDEA, Sigma-Aldrich) were mixed for 5 minutes under argon to avoid uncontrolled reactions (*i.e.* hydrolysis and condensation) between air humidity and the metal precursor. The molar complexation ratio was x = [MDEA]/[TiTTIP] = 4. Ethanol and water were separately slowly added to the TiTTIP/MDEA blend and mixed for 5 minutes. The ratio between ethanol and water was 40/60 vol%. β-bismuth oxide (Alfa Aesar) was added in the reactive ink in stoichiometric proportions to obtain $Bi_4Ti_3O_{12}$ and the mixture was stirred for 48 hours to form a gel. The gel is calcined at different temperatures between 500 °C and 850 °C for 1 hour (ramp: 3 °C/min).

Thermogravimetry analysis was performed on a gelled ink using a STA409 PG (Netzsch) at a constant rate of 10 K/min under air.

The phase identification was performed at room temperature using a monochromatic Cu-Kα radiation X-ray diffractometer (XRD: Bruker D8 Robot Tools X-ray diffraction, Bruker, Germany). The XRD analysis was carried out *ex-situ* with a scan speed of 0.6° /min over a range of 20° to 50° on several samples calcined between 500 and 850 °C for 1 hour. Lattice parameters were calculated by using the indexing method. The elemental analysis was carried out using Bruker QUANTAX 70 Energy Dispersive X-Ray Spectrometer coupled to a TM 3000 scanning electron microscope.

Shrinkage evolution measurement was performed by dilatometry. Pellets were fabricated by pressing the powder calcined at 500 °C with a uniaxial hydraulic press. A horizontal assembly dilatometer (NETZSCH DIL 402C) was used to determine the shrinkage behavior. The BiT pellet was heated a in box furnace in static air environment with temperature program; ramp up heating rate 1 °C/min from 25 °C to 850 °C and holding at 850 °C for 2 hours and ramp down with cooling rate of 5 °C/min from 850 °C to 25 °C.

The dielectric constant of the pellet sample was measured with an Impedance/Gain-Phase Analyzer (Solartron 1260A, Solartron Analytical, UK). All measurements were carried out in air at room temperature, in the frequency range of 100 Hz to 1 MHz and applied biasing voltage of 0.5 V.

3. Results and Discussion

The crystallization behavior of BiT was studied by X-ray diffraction on the milled gel powders calcined in air at different temperatures. Figure 1 shows the XRD pattern of the powders calcined at different temperatures between 500 °C and 850 °C. The powder calcined at 500 °C exhibits a yellow color due to the presence of Bi_2O_3, which is confirmed by the XRD pattern. As the temperature increases the powders become whiter due to Bi_2O_3 loss and appearance of the BiT phase. The XRD patterns show the onset of the crystalline BiT in agreement with literature [16]. BiT has a Curie temperature (T_c) of 675 °C; hence the crystal belongs to a pseudo-tetragonal phase below T_c and pseudo-orthorhombic phase above. The splitting of the reflection at $2\theta \approx 33$ ° in the XRD patterns recorded at 700, 800 and 850 °C suggests indeed that these crystals have a pseudo-orthorhombic structure [16] at these temperatures. Finally the pattern recorded 850 °C exhibits a

well-defined BiT crystalline structure. Moreover no signal from the Bi_2O_3 crystalline phase can be detected. As the temperature increases, the peak width decreases, corresponding to crystallite size increase. This suggests that the particles agglomerate and probably sinter during the heat treatment, leading to grain growth. The lattice parameters of the BiT phase in the sample calcined at 850 ˚C were a = 5.41 Å, b = 5.448 Å, and c = 32.84 Å, which are comparable with the values given in JCPDS 72-1019. Finally, within the limit of the XRD technique, no bismuth and/or titanium based secondary phases could be detected in the XRD patterns. EDS analysis was performed on the powder calcined at 850 °C (not shown here), indicating that elemental balance of the starting chemicals was kept while neither segregation nor presence of second phases could be detected.

Figure 2 shows the thermogravimetric analysis (TGA) of the gelled ink coupled with the dilatometry plot of a pellet composed of powder calcined at 500˚C for 1 hour. The TGA curve exhibits a strong mass loss between room temperature and 300˚C due to organic burn off. From 300 to 850 °C no mass loss can be detected indicating that the bismuth oxide, trapped in the sol gel, does not evaporate even at high temperature, for which such phenomenon was observed [9]. A pure BiT phase can thus be obtained as the necessary stoichiometric ratio to obtain this phase is preserved. The sintering behavior of the pellet was studied by using a dilatometry measurement. No shrinkage is occurring between room temperature and 600 °C; a small expansion (0.1%) can however be noticed in that temperature range, due to chemical reactions and/or crystal lattice rearrangements. The shrinkage starts from 600°C and the highest size reduction is recorded between 700 and 800°C, leading to 14% shrinkage. Measured density is 6.79 g/cm^3, which is in good agreement with literature [17].

Figure 3 shows the dielectric constant measurement of a BiT pellet calcined at 850°C together with measurements performed on powders synthetized by other processing routes [2,18,19]. The average value of the dielectric constant at room temperature for this sample is 227 (value fitted linearly) which is approximatively 20% higher than those obtained on samples synthesized by other techniques and reported in Figure 3. This result emphasizes the importance of the powder preparation method and demonstrates that using the hybrid concept “sol-gel + colloids” leads to enhanced material properties.

Conclusion

In this study bismuth titanate $Bi_4Ti_3O_{12}$ powder was synthetized for the first time by suspending bismuth oxide particles in a stable titanium based sol-gel solution, followed by a heat treatment. Pure *c*-axis oriented bismuth titanate was obtained after calcination at 850 °C. With this technique bismuth is trapped into a sol gel a matrix and cannot evaporate allowing the synthesis of pure BiT without secondary phases in a one step process. The dielectric constant was determined using impedance measurements and was evaluated as 20% higher than previously observed values.

Acknowledgement

The authors would like to thank the Department of Materials Science and Engineering, Faculty of Engineering and Industrial Technology, Silpakorn University, the Royal Golden Jubilee Ph.D program (RGJ), Thailand for financial support.

Bibliography

[1] Z. Lazarevic, B.D. Stojanovic, J. Varela, Sci. Sinter. 37 (2005) 199–216. doi:10.2298/SOS0503199L.

[2] F. Zhang, T. Karaki, M. Adachi, Jpn. J. Appl. Phys. 47 (2008) 640. doi:10.1143/JJAP.45.7385.

[3] E.. Subbarao, J. Phys. Chem. Solids. 23 (1962) 665–676.

[4] T. Kikuchi, A. Watanabe, K. Uchida, Mat. Res. Bull. 12 (1977) 299–304.

[5] T. Takenaka, T. Gotoh, S. Mutoh, T. Sasaki, Jpn. J. Appl. Phys. 34 (1995) 5384–5388. doi:10.1143/JJAP.34.5384.

[6] a. Q. Jiang, G.H. Li, L.D. Zhang, J. Appl. Phys. 83 (1998) 4878. doi:10.1063/1.367287.

[7] H.S. Shulman, M. Testorf, D. Damjanovic, N. Setter, J. Am. Ceram. Soc. 79 (1996) 3124–3128. doi:10.1111/j.1151-2916.1996.tb08086.x.

[8] M. Villegas, C. Moure, J.F. Fernandez, P. Duran, Ceram. Int. 22 (1996) 15–22. doi:10.1016/0272-8842(95)00047-X.

[9] V. Esposito, B.H. Luong, E. Di Bartolomeo, E.D. Wachsman, E. Traversa, J. Electrochem. Soc. 153 (2006) A2232. doi:10.1149/1.2358088.

[10] J. Ng, S. H., Xue, J., & Wang, J. Am. Ceram. Soc. 65 (2002) 2660–2665. doi:10.1111/j.1151-2916.2002.tb00512.x.

[11] A. V Prasada Rao, A.I. Robin, S. Komarneni, Mater. Lett. 28 (1996) 469–473. doi:10.1016/0167-577X(96)00107-3.

[12] P.H. Xiang, Y. Kinemuchi, T. Nagaoka, K. Watari, Mater. Lett. 59 (2005) 3590–3594. doi:10.1016/j.matlet.2005.07.002.

[13] Q. Yang, Y. Li, Q. Yin, P. Wang, Y.B. Cheng, J. Eur. Ceram. Soc. 23 (2003) 161–166. doi:10.1016/S0955-2219(02)00087-0.

[14] M.. Pechini, 3,330,697, 1967.

[15] C. Gadea, D. Marani, V. Esposito, J. Phys. Chem. Solids. 101 (2017) 10–17. doi:10.1016/j.jpcs.2016.10.004.

[16] P. Pookmanee, S. Phanichphant, Adv. Mater. Res. 26–28 (2007) 247–250. doi:10.4028/www.scientific.net/AMR.26-28.247.

[17] S. Naz, S.K. Durrani, A.H. Qureshi, M.A. Hussain, N. Hussain, J. Therm. Anal. Calorim. 114 (2013) 719–723. doi:10.1007/s10973-013-3029-z.

[18] M. Anilkumar, S.R. Dhage, V. Ravi, Mater. Lett. 59 (2005) 514. doi:10.1016/j.matlet.2004.10.038.

[19] A.Z. Simões, R.F. Pianno, C.S. Riccardi, L.S. Cavalcante, E. Longo, J.A. Varela, J. Alloys Compd. 454 (2008) 66. doi:10.1016/j.jallcom.2006.12.066.

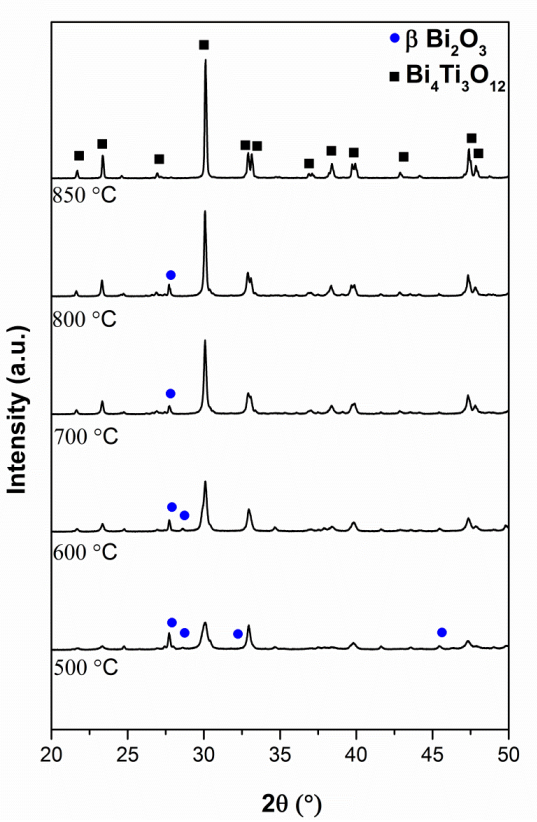

Figure 1: X-ray diffraction patterns of BiT powders after calcination at different temperatures.

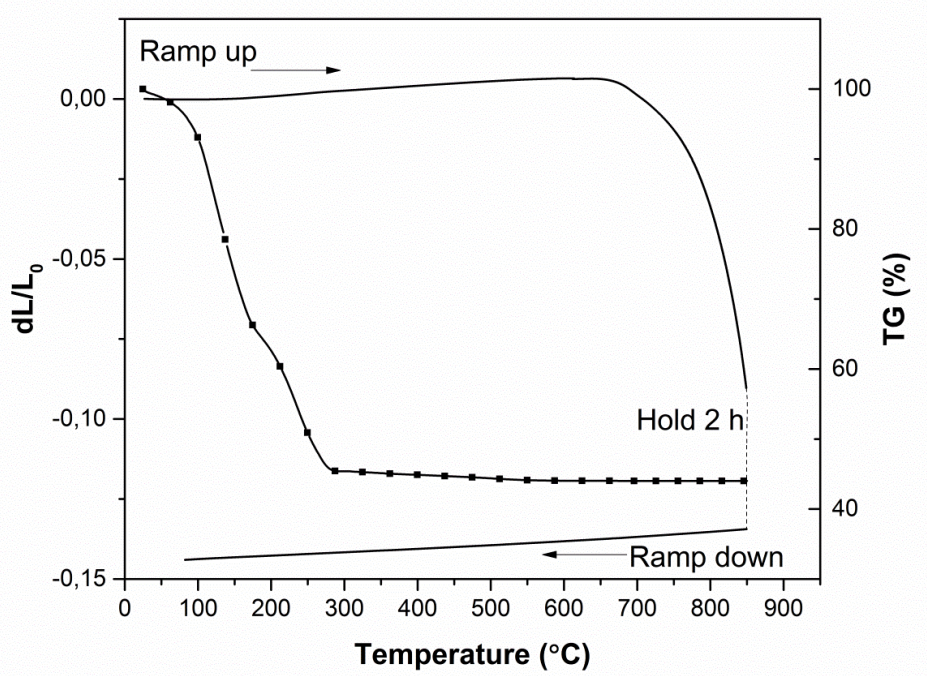

Figure 2: Thermogravimetric (symbols with line) and dilatometry (line) measurements of respectively a gelled ink and a BiT calcined at 500 °C from room temperature to 850 °C.

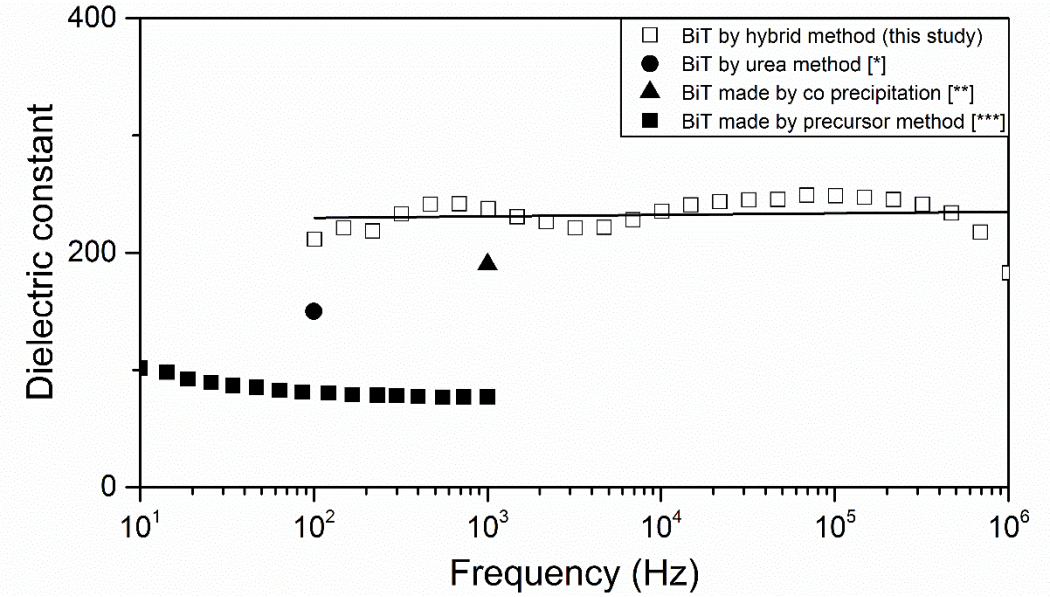

Figure 3: Dielectric measurement by impedance spectroscopy of BiT pellet calcined at 850 °C along with values reported for powder synthetized by urea method (*=[18]), co precipitation (**=[2]) and using polymeric precursors (***=[19])

Fabrication of thin yttria-stabilized-zirconia dense electrolyte layers by inkjet printing for high performing solid oxide fuel cells

Journal of Power Sources 273 (2015) 89–95

Contents lists available at ScienceDirect

Journal of Power Sources

journal homepage: www.elsevier.com/locate/jpowsour

Fabrication of thin yttria-stabilized-zirconia dense electrolyte layers by inkjet printing for high performing solid oxide fuel cells

Vincenzo Esposito*, Christophe Gadea, Johan Hjelm, Debora Marani, Qiang Hu, Karsten Agersted, Severine Ramousse, Søren Højgaard Jensen

DTU Energy Conversion and Storage, Technical University of Denmark, Risø Campus, Frederiksborgvej 399, DK-4000 Roskilde, Denmark

HIGHLIGHTS

- A gas-tight electrolyte of 1.2 μm for SOFC is made by a low-cost inkjet printer.
- Thin layers are deposited by colloidal inks with nanometric powders.
- Multiple printing on a flexible substrate achieves the continuity in the printing.

ARTICLE INFO

Article history:
Received 24 July 2014
Received in revised form
5 September 2014
Accepted 11 September 2014
Available online 19 September 2014

Keywords:
SOFC
Inkjet printing
YSZ
Colloidal suspension

ABSTRACT

In this work, we present how a low-cost HP Deskjet 1000 inkjet printer was used to fabricate a 1.2 μm thin, dense and gas tight 16 cm^2 solid oxide fuel cells (SOFC) electrolyte. The electrolyte was printed using an ink made of highly diluted (<4 vol.%) nanometric yttria stabilized zirconia (YSZ) powders (50 nm in size) in an aqueous medium. The ink was designed to be a highly dispersed, long term stable colloidal suspension, with optimal printability characteristics. The electrolyte was made by a multiple printing procedure, which ensures coverage of the several flaws occurring in a single printing pass. Together with an optimized sintering procedure this resulted in good adhesion and densification of the electrolyte. The SOFC exhibited a close-to-theoretical open circuit voltage and a remarkable peak power density above 1.5 W cm^{-2} at 800 °C.

1. Introduction

Additive manufacturing methods are of great importance in modern industry and inkjet printing of inorganic materials by use of colloidal suspensions as inks, has recently been spreading in several key technologies such as electronics [1], sensors [2], energy devices [3–6] and biomedical applications [7,8]. Despite that inkjet printing is usually considered a relatively low throughput fabrication method compared to other printing methods, it presents unique advantages in terms of customizable shapes and for printing of functional layers. Moreover, it is ideal for the fabrication of multi-component 2D and 3D architectures, which are formed additively drop by drop and layer by layer [9]. A technological domain in which these features are highly desirable is the solid oxide fuel cell (SOFC). This is especially relevant for the planar SOFC design, where the multi-material multilayers used in the components are well-interconnected and have different microstructural features [10–12]. Moreover, inkjet printing is ideal for the deposition of layers of about 1 μm in thickness [13] and this thickness range is valuable for the fabrication of SOFC electrolytes [14]. Among the different inkjet printing methods, Drop on Demand (DoD) printing by piezoelectric- or thermal-inkjet printing, has been used to fabricate SOFCs and SOFC components [10,15,16]. This is of great commercial interest due to the low-cost and high availability of such equipment on the market. Moreover, the different materials are prepared by simple chemistry and conventional powder technology methods, where the inks are stabilized in water-/alcohol-based suspensions [13].

In a typical planar SOFC, the electrolyte is made of 8 mol.% yttria-stabilized zirconia (8YSZ) [17–19]deposited on a tape casted NiO/8YSZ electrode layer on top of a NiO/3YSZ support layer [20]. Upon printing the electrolyte, the electrode and the support layer can be either a green material (i.e. the ceramic electrode shaped by the organic binder before the firing) or a consolidated pre-sintered

* Corresponding author. Tel.: +45 46 77 56 37; fax: +45 46 77 58 00.
E-mail address: vies@dtu.dk (V. Esposito).

http://dx.doi.org/10.1016/j.jpowsour.2014.09.085
0378-7753/

NiO/YSZ substrate. After the printing, a sintering step at high temperatures, usually above 1200 °C [21], is required to obtain a dense and consolidated YSZ electrolyte layer.

High density of the electrolyte is a critical factor for the SOFC operation. The presence of flaws, pinholes or other defects can drastically reduce performance of the SOFC due to leaking of the fuel/oxidant gases through the electrolyte to the electrodes or by increasing resistance to oxygen ion diffusion in the electrolyte.

Several studies described the deposition of thin YSZ layers for SOFC anode layers using laboratory or commercial DoD printers [10–12]. Although these studies show that electrolytes and other components can be manufactured by inkjet printing, only a few studies report SOFCs with functional electrolytes with thicknesses of about 1 μm. Early promising results were obtained by Sukeshini and Cummins, who printed a YSZ electrolyte of about 10 μm by multiple printing (up to 12 layer-over-layer depositions) in a fully inkjet-printed SOFC [12]. In this and in other cases, multiple printings were necessary to seal the electrolyte to achieve acceptable performance and leak tightness of the cells. The importance of multiple printing was also recognized by Tomov et al. who deposited a 6 μm thick electrolyte by multiple printing (up to 10 printed layers) [10]. Recently, Li et al. successfully demonstrated that a 1.5 μm YSZ electrolyte layer for a SOFC could be printed by a single-layer deposition of ink containing nanoparticles in large agglomerates (between 0.2 and 5.5 μm) using a low-cost printer [16]. However, the resulting SOFC exhibited low power density and a low open circuit voltage indicating a leaky electrolyte.

In this work, we describe the manufacturing process of a printed and densified thin 8YSZ electrolyte of about 1 micron thickness and the subsequent electrochemical test results of a full anode-supported cell with this electrolyte. The electrolyte was printed onto a 9 × 9 cm^2 green layer of NiO/8YSZ anode using a modified low-cost DoD thermal printer, starting by diluted inks of nano-sized 8YSZ particles in water based suspension. To the best of our knowledge, this is the cells with the largest area inkjet-printed electrolyte reported so far.

2. Experimental

2.1. Ink preparation

Commercially available 8YSZ (8 mol.% yttria, TOSOH) nanometric powder was used for the fabrication of the electrolyte by inkjet printing. A water based ink was formulated by suspending the powders in a mix of 80 wt.% water and 20 wt.% ethanol. The powders were added to the liquid medium at two concentrations: 3.7 vol.% (concentrated ink) and 0.9 vol.% (dilute ink) of YSZ. Polyvinylpyrrolidone (PVP), dissolved in 53% weight ratio in pure ethanol, was used as dispersant and added into the YSZ suspension at ca. 8 mg m^{-2} of solid surface area. All constituents were then milled in a rotational mill in a PET flask at 100 rpm using zirconia milling balls for 10 days. The particle size distribution after mixing was measured using a laser particle size analyzer (Beckman Coulter, LS 13320).

2.2. Ink characterization

Rheological measurements were carried out with an Anton Paar rheometer (MCR 302), in rotational mode and at a constant temperature of 21 °C. A plate–plate measuring system was used with a diameter of 50 mm (PP50) and a gap distance of 0.6 mm. The experiments were performed using three steps of pre-treatment: the first one at 0.1 s^{-1} for 1 min followed by 1 min at rest (0 s^{-1} shear rate), and the third one at 10 s^{-1} for 1 min. Flow curve measurements were conducted in step mode using 60 steps with a waiting time of 10 s. The shear rates investigated range from 10 s^{-1} up to 1000 s^{-1}, in the up ramp, and from 1000 s^{-1} to 10 s^{-1} in the down ramp.

Ink surface tension was measured using a bubble pressure tensiometer (BP 50, Krüss).

The printability of the inks was assessed by determining their *Z*, Weber (*We*), and Reynolds (*Re*) numbers, graphically combined as report by Derby [28,31], and defined as:

$$We = \frac{v^2 \rho a}{\sigma} \quad (1)$$

$$Re = \frac{v \rho a}{\eta} \quad (2)$$

$$Z = \frac{1}{Oh} = \frac{\sqrt{\sigma . \rho . a}}{\eta} \quad (3)$$

where v is the drop velocity, η is the ink viscosity, σ is the surface tension, ρ is the density, and a is the characteristic length [28]. The parameter a is typically taken as the diameter of the printing nozzles (20 μm). The *We* and *Re* numbers were calculated within the typical reported range of values for the drop velocity (1–30 m s^{-1}) [22].

2.3. SOFC fabrication

2.3.1. NiO/YSZ substrates

The substrates used for the tested SOFC consisted in thin NiO/YSZ functional anode layer deposited onto a thicker NiO/YSZ anode support. The ratio between Ni and YSZ was 40/60 vol.% both for the support layer and the active electrode layer [23]. ZrO_2 stabilized with 8 mol.% Y_2O_3 was used for the anode layer while ZrO_2 stabilized with 3 mol.% Y_2O_3 was used for the support layer. The layer produced by tape-casting and co-laminated as green materials at ca. 150 °C [23]. The substrates had a 10–15 μm thick anode of Ni/YSZ cermet laminated to a~300 μm thick Ni/YSZ support layer.

2.3.2. Electrolyte layer deposition by inkjet printing

A commercially available printer (HP Deskjet 1000) was used as a printing unit. The printer was modified to allow a range of different print head/substrate distances and to print on thick and stiff substrates. A compatible cartridge (HP 301 black) providing a 600 × 300 dpi resolution was cleaned to remove the original black ink and used to print the ceramic ink. The YSZ inks were inserted into the cartridge manually using syringes. Two printing procedures were used for the printing:

- “Single Droplets” printing (SD), consisting in printing isolated droplets using a square-chess-like pattern, it was aimed to control the quality of the single droplet or presence of flaws in the DoD printing;
- “Continuous Printing” (CP), consisting in printing droplets one after the other sequentially in lines, it was used to print a continuous layer. Additive depositions were carried out on the CP pattern, depositing a layer on top of the other, up to 5 times.

Waiting time of around 15 s between each print was necessary to allow the solvent in the ink to evaporate and the print to dry.

2.3.3. Firing of half-cell

The half-cell consisting of the support, anode and electrolyte layers was subsequently fired in air. The firing consisted in a multistep debinding procedure below 700 °C for 48 h in total, to

remove the organic materials for the anode and anode support substrate [24]. The simultaneous sintering of the anode and the printed electrolyte was carried out in several different conditions in single-step sintering procedures, with sintering temperature between 1000 and 1300 °C. The holding times at the sintering temperatures were 0.1, 2, and 6 h. Different holding times were used to characterize the sintering and the densification of the electrolyte.

2.3.4. Deposition of the cathode layer

Cathode ink was deposited by screen printing onto the electrolyte side of the sintered half cell (anode support/anode/electrolyte). The cathode ink was a mix of $La_{0.75}Sr_{0.25}MnO_{3-\delta}$ (LSM) and YSZ (LSM/YSZ = 50/50 vol.%). The printing speed used was 60 mm s^{-1}, the printing gap was 1 mm and the squeegee pressure was 7 bar. The printed cathode layers were then sintered at 1050 °C for 2 h. An LSM cathode contact layer was then screen printed on top of the cathode layer using the same printing described above and sintered at 1000 °C for 5 h. Further detail about the printing and the cathode specifications is described in the another paper [25].

2.4. Cell tests

2.4.1. Gas leak testing

The leak testing system used in this study works by sealing a cell of 5.3 × 5.3 cm^2 in area. The half-cells, including the sintered ink-jet printed YSZ electrolyte, were tested before cathode deposition over a manifold connected to a vacuum system. In the test, the space beneath the cell was evacuated and the pump closed off. The flow of gas into the system was measured from the rate of pressure increase, measured by a barometric gauge. The test returns a measured vacuum leak as a pressure drop slope, which was compared with a fully dense reference. Leak measurements were also carried out by monitoring the cell voltage during electrochemical single cell testing as a function of the fuel flow rate, and are described below.

2.4.2. Test fixture

The electrochemical tests were carried out using an alumina test fixture with 0.8 mm and 2.1 mm recessions on the anode and cathode side, respectively. The recessions were 40 mm wide and 40 mm long. The cathode side was contacted using a custom alumina flow-field with 19 gas channels (1 mm wide) and 20 contact ribs (1 mm wide, except the outermost ribs which were 1.5 mm wide) clad with gold strip current collectors and fine gold meshes. The anode compartment seal was made using a thin (0.08 or 0.1 mm) Au foil cut into a frame and two alumina frames were placed on top of the cells (on the cathode side) to press the cell down onto the gold seal. The anode contact component was a flat Ni-mesh resting on a Ni flow field of the same design as the cathode alumina flow-field.

2.4.3. Electrochemical measurements

The electrochemical test was performed in a FuelCon test rig. The impedance was recorded using a Solartron 1255B unit with amplitude of 60 mA (rms). The impedance data was collected from 96.9 kHz to 96.8 mHz with 12 points per decade. The cell voltage and voltage across the current shunt resistor (reference channel) were compensated (set to zero) with custom-built electronic circuitry in order to maintain maximum resolution of the Solartron unit. *I–V* curve measurements were carried out using current steps with variable step lengths and step duration of 10 s.

3. Results and discussion

Previous results on the inkjet printing of SOFC electrolytes starting from colloidal inks have shown that the probability of obtaining dense and gas-tight layers is greater when using multiple printings as compared with single-pass printings [10,15,16]. The total thickness of the printed layer depends on several factors, such as the concentration of the solid load, the particle size distribution, as well as the number of printing passes. Ink printability and wetting properties of the ink on the substrate are important to obtain a high green density of the deposited layer on the substrate [26]. Finally the sintering is crucial in the formation of the final dense layer.

3.1. YSZ-ink properties

Colloidal inks suitable for inkjet printing have to meet several key requirements [9,13]. Some important parameters associated to the solid phase in the ink are the concentration (volume fraction) of the solid, the use of a small particle size, a narrow particle size distribution, and good dispersion of the particles. Other parameters related to the ink are suitable rheological behavior, drying properties and surface tension of the liquid media. These are especially crucial to form suitable droplets upon ejection as well as to obtain stable printing with suitable wetting at the substrate [27].

For the deposition of a thin layer, nanometric powders are desirable since, when the droplet is deposited, and the ink is dried, the powders form a thin coating of packed particles, where the thickness is a result of particle size and solid concentration in the media. These two parameters are also fundamental to prevent clogging in the nozzle. Typical solid loading concentrations in colloidal inks for inkjet applications are below 10 vol.% [13]. The YSZ inks developed for this work had solid loadings of 3.7 vol.% (20 wt.%) and 0.9 vol.% (6 wt.%). The dilution in these inks was kept high with the aim to produce thin layers. Small particles are ideal for such diluted inks and small particles are usually easily dispersed in the liquid media. Nanometric YSZ powders with average particle size of ca. 50 nm were used. However, nanoparticles tend to agglomerate and to prevent this PVP was used to obtain well dispersed and stable inks [28]. A slight excess of PVP was used because an excess of a polymeric dispersant may cause some flocculation in the suspension, which tends to stabilize the ink rather than being detrimental due to the low solid loading of the ink. The resulting inks were found to exhibit excellent stability and a narrow particle size distribution. The particle size distribution for the YSZ-inks was measured immediately after preparation, after 10 days of milling and, in order to estimate the long term stability, after 100 days of storage without agitation. Fig. 1 shows the typical particle size distribution within the range of 0.06 and 0.34 μm with

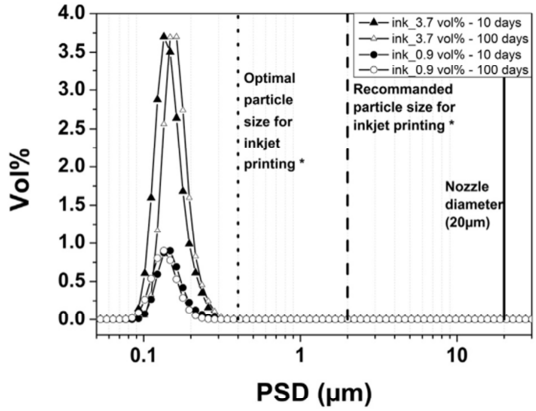

Fig. 1. Particle size distribution for the YSZ ink at low (3.7 vol.%) and high dilution (0.9 vol.%) after milling for 10 days and after 100 days of storage (* = [29]).

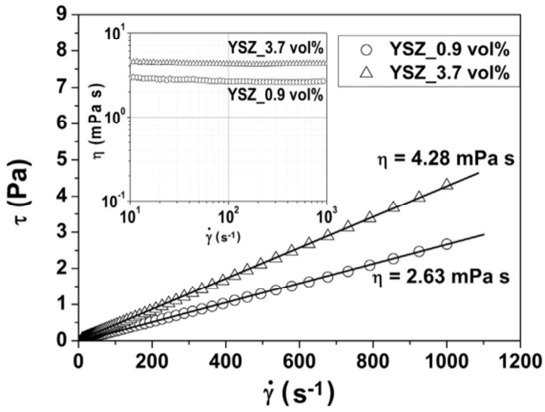

Fig. 2. Flow curves and viscosity curves (inset) for the two YSZ inks developed.

a max at around 100 nm. Such nanometric powders exhibited high stability with no precipitation and preserving the same distribution even after 100 days of storage. Moreover, to avoid clogging of the print head nozzle the particle size should preferably be less than 10% of the nozzle diameter, while the optimal value has been estimated to be around 2% [29]. The HP-Deskjet 1000 has a nozzle diameter of around 20 μm diameter which for a maximum particle size of 0.34 μm corresponds to (0.34 μm/20 μm) = 1.7%.

The rheology of the inks was characterized using dynamic conditions. Fig. 2 shows the flow curves for the two inks with the correspondent viscosity curves (the inset). Both inks exhibit Newtonian behavior with a constant viscosity independent of the shear rate (inset). The viscosity values were calculated from the slope of the flow curves. The values obtained were 4.28 mPa s for the 3.7 vol.% ink and 2.63 mPa s for the 0.9 vol.% ink.

These values are usually considered suitable for a thermal DoD inkjet system [13]. The surface tension of the ink was measured using a bubble pressure tensiometer and yielded a value of 36 mN m^{-1}.

A range of the parameters, *Z*, *We*, and *Re* numbers (defined in Experimental section) yielding optimal printability of inks has been identified in literature. For *Z*, Jang et al. [30] proposed a range between 4 and 14, whereas Derby et al. [31] suggested a value for *Z* between 1 and 10. Moreover, Derby proposed the *We*–*Re* numbers diagram to illustrate the regime of printability for the ink properties. Such a diagram is displayed in Fig. 3 and shows that the *We* and *Re* values calculated for the two developed inks are within the identified printability region. The properties of the developed inks are summarized in Table 1.

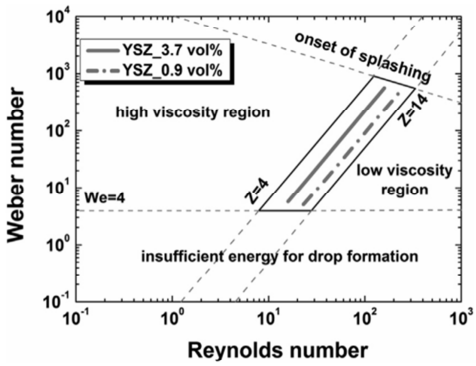

Fig. 3. Weber–Reynolds numbers diagram defining the regime for ink properties which ensure good printing characteristics. This diagram has been proposed by Derby [27].

Table 1
Ink properties.

Ink	Vol.%	η (mPa s)	σ (mN m^{-1})	ρ (g cm^{-3})	*Z*
20 wt.%	3.7	4.28	36.4	1.14	6.73
6 wt.%	0.9	2.63	36.2	1.01	10.28

3.2. Inkjet printing and sintering of the YSZ electrolyte

The use of a low-cost inkjet process for the fabrication of a continuous layer leads to formation of some critical flaws.

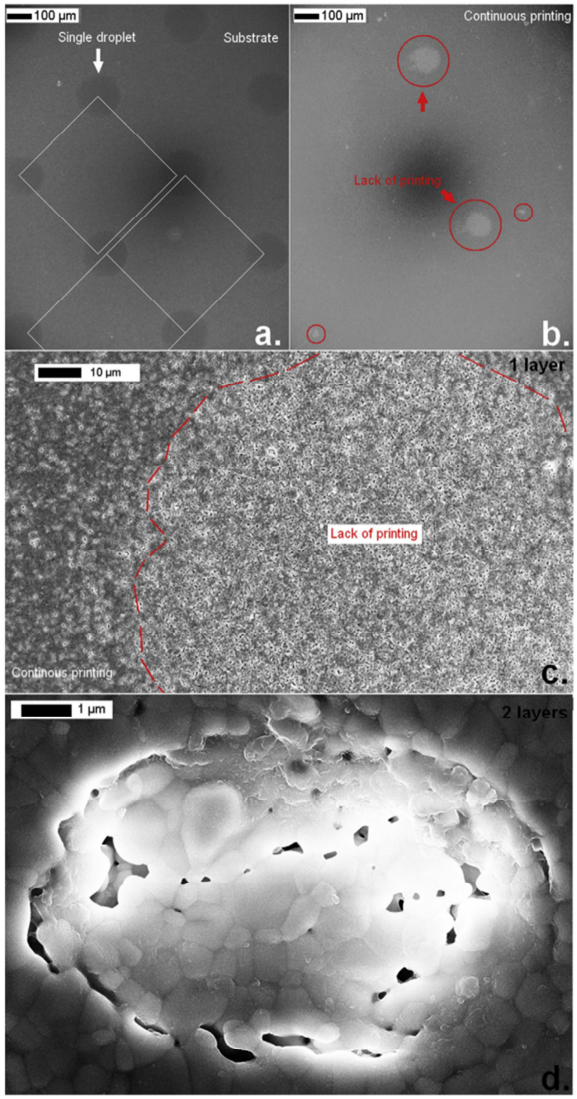

Fig. 4. SEM observations of the YSZ printings, after sintering at 1300 °C for 5 min. (a) 0.9 vol.% ink printed as single droplets, (b) continuous print using the 3.7 vol.% ink, (c) high magnification of printing flaw shown in (b), (d) typical defect on a two layer deposition.

Particularly, since each single layer is formed drop by drop, any alignment errors and/or lack of deposition (missing drops) during the printing create discontinuity in the layer. Moreover, extremely dilute inks can lead to poor packing of the particles, leaving residual porosity and presence of pinholes in the sintered layer. Fig. 4a–d shows the typical flaws observed by SEM after printing of the diluted YSZ inks; Fig. 4a shows the typical alignment of the droplets obtained by inkjet of the highly diluted ink (0.9 vol.% of YSZ loading) after sintering at 1300 °C for 6 h. The alignment is crucial for the formation of a continuous single layer, where all the droplets forming the continuous layer have to be placed in the desired positions. The SEM observations on the layers produced using single droplet printing (SD) indicated that, although the droplets were designed in an ordered pattern, a certain misalignment in the range of few micrometers occurred for some of the droplets (see white squares superimposed in Fig. 4a). This effect is possibly associated with the lack of precision in the mechanical movement system. Fig. 4b shows the results of continuous printing (CP) of a single layer of the concentrated (low dilution) ink. This showed evidence of missing droplets in several areas of various sizes and shapes. Particularly, several large circular regions of around 100 μm in diameter were observed. In these cases, the size was similar to the droplets formed by SD and the lack of printing is probably caused by an imprecise impact of the droplets on the substrate or a defective droplet formation at the nozzle. Other small defects with irregular shapes were also observed in the CP (see red (in the web version) circles in Fig. 4b) and are attributed to the presence of imperfections at the substrate surface, which may impair the settling of the particles after printing. A closer look at the circular flaw after sintering at 1300 °C for 6 h is shown in Fig. 4c. In this figure the bright area corresponds to the slightly porous surface of the substrate and red (in the web version) lines are superimposed to highlight the edges of the defect. Presence of porosity around the edge could be observed, suggesting an excessive dilution of the ink at the boundary between the drops. On the other hand, all the covered areas showed homogeneity and a high degree of packing of the particles which led to densification of the layer after sintering at 1300 °C. It is also worth noticing that no coffee-stain rings or other particle agglomeration effects were detected in the samples. This observation confirms the suitable printing characteristics of the developed inks. However, the presence of the several defects detected at the CP single layer highlights the need for using a multiple-printing approach to fabricate a gas-tight electrolyte with the present printing technology. Fig. 4d shows a typical SEM image of the 2-layer deposition by the 3.7 vol.% ink after sintering at 1300 °C for 6 h. Particularly, the picture shows the filling-in of a small defect in the first layer by the second print-pass. The particles in the flaws exhibited sintering with presence of residual porosity. This effect can possibly be attributed to an excessive dilution on the solid, where the low concentrations of the material can only partially cover the defect. This effect generated porosity and resulted in a discontinuous layer. Increasing the number of print-passes (depositions) should minimize this issue.

Fig. 5a–e shows SEM images of the printed electrolyte using the 3.7 vol.% ink exposed to various sintering profiles. Fig. 5a–c shows the particles sintered at 1000 °C, 1150 °C and 1300 °C for 6 min. The short dwelling time used made it possible to follow the evolution of the microstructure primarily as function of the temperature. Fig. 5a shows that, at 1000 °C, the YSZ particles in the deposit are of a round shape and with a homogenous size of ca. 100 nm. The packing is rather high with no agglomeration. However, large voids among the particles, probably formed during the ink drying process, were observed. Fig. 5b shows that at 1150 °C the YSZ particles are connected by the typical necking, indicating an incipient sintering at the layer with formation of small and larger porosity (below 1 μm), where the latter probably was due to the voids as shown in Fig. 5a. The result after sintering at 1300 °C is shown in Fig. 5c. The figure clearly shows that the treatment led to a full densification and grain growth. The original particle grew to the micrometer range and the resulting layer was rather dense with annihilation of all the porosity, including the voids in Fig. 5b.

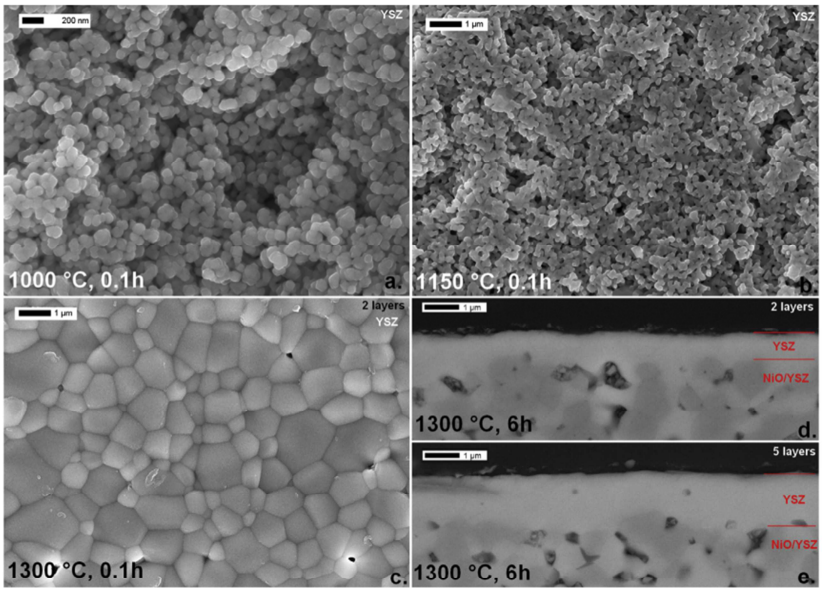

Fig. 5. SEM observations of the YSZ printings by the 3.7 vol.% ink. (a) continuous printing sintered at 1000 °C for 6 min, (b) 1150 °C for 6 min, (c) 1300 °C for 6 min, and the cross-section pictures of the half cells made by of (d) 2-layer and (e) 5-layer depositions after sintering at 1300 °C for 6 h.

Table 2
Leak test results and thickness measurements of 2-layer and 5-layer electrolyte half cells.

Sample	Number of printed layers	Sintering conditions	Reference pressure slope (mbar s^{-1})	Measured pressure slope (mbar s^{-1})	Electrolyte thickness (μm)
2-Layer	2	1300 °C/6 h	0.46	0.46	0.6
5-Layer	5	1300 °C/6 h	0.46	0.08	1.2

In conclusion the 3.7 vol.% ink is proven to be suitable for the formation of continuous YSZ layers and a sintering temperature around 1300 °C can be used for the densification. However, as discussed above, printing defects suggest that multiple printing with more than 2-layers should be used to avoid pinholes in large-area cells. Fig. 5d and e shows the cross-section at the half cells, after sintering at 1300 °C for 6 h, for 2-layer and 5-layer depositions using the 3.7 vol.% ink. Both the layers resulted dense and homogenous and typical thickness of *app.* 0.6 μm and 1.2 μm were estimated for the 2-layer and the 5-layer samples, respectively. The relation between the thickness and number of depositions/print-passes was found to be non-linear and this was attributed to heterogeneous roughness of the substrate surface and to the lack of deposition of the continuous printing.

To further characterize the tightness of the printed layers leak tests were carried out with the sintered 5 × 5 cm^2 half cells. Table 2 shows that leak test performed on the 2-layer electrolyte exhibits a measured pressure slope value similar to the reference pressure slope, indicating insufficient electrolyte gas tightness. The pressure slope measured with the 5-layer electrolyte was very low compared to the reference (sheet of steel), indicating a high tightness of the electrolyte.

3.3. Cell performance

Two SOFCs with a 2-layer and a 5-layer electrolyte, respectively, were manufactured with a 4 × 4 cm^2 active area (defined by the cathode) as described in the Experimental section. The cell produced with the 2-layer electrolyte was not leak tight and open circuit voltages of less than 0.7 V were observed in dilute (9%) hydrogen. Moreover, the electrolyte gas tightness decreased rapidly during the test, most likely due to re-oxidation of the Ni-cermet anode. This is in agreement with the ex-situ leak testing that was carried out and reported in the previous section. The cell with the 5-layer electrolyte was significantly more leak tight. Open circuit cell voltages in the range 1.07–1.15 V were observed in dry hydrogen fuel at flow rates in the range 6.7–31.7 ml min^{-1} cm^{-2}, as can be seen in Fig. 6. The leak was quantified by calculation of a total leak current, a measure of the total leak, both external (e.g. through seals and anode support) and internal (electrolyte pinholes, cracks), using the relations derived by Rasmussen et al. [32]. No systematic variation of the leak current with the fuel flow was observed, indicating the absence of large cracks or holes in the cell or the sealing gasket used on the anode side.

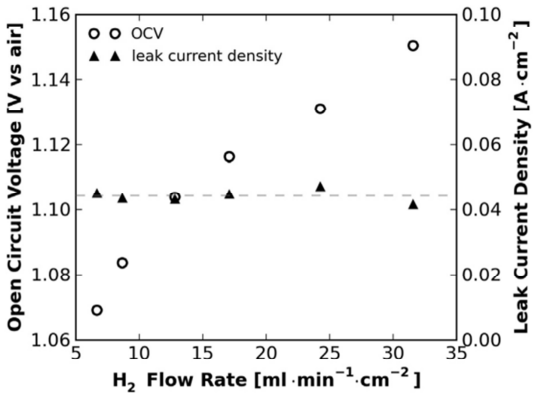

Fig. 6. Observed open circuit cell voltage (open circles) and calculated total leak current density (according to Rasmussen et al., filled triangles) of 5-layer electrolyte SOFC operates with dry hydrogen supplied as the fuel at the indicated flow rates and air as the oxidant. The dotted horizontal line represents the average leak current density (0.044 A cm^{-2}), calculated using the active area of the cell (=16 cm^2).

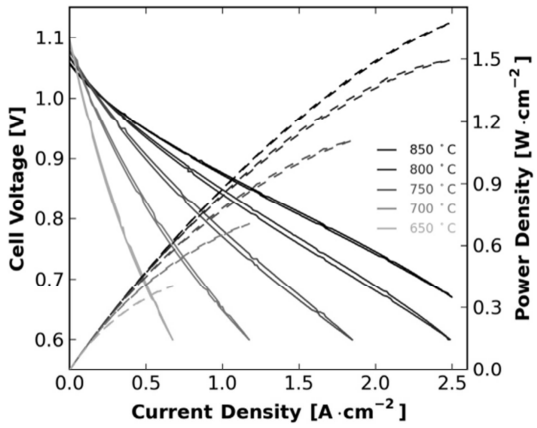

Fig. 7. Polarization curves recorded for the 5-layer electrolyte SOFC (active area = 16 cm^2) which was tested with a composite LSM–YSZ cathode and an LSM current collection layer. The fuel was 96% H_2 and 4% H_2O supplied at a total flow rate of 26 ml min^{-1} cm^{-2}. The lower voltage limit was set to 0.6 V and the maximum current limit to 2.5 A cm^{-2} (40 A).

Polarization curves were recorded at operating temperatures in the range from 850 °C down to 650 °C with 50 °C increments. Fig. 7 shows polarization and power curves for the 5-layer electrolyte SOFC. At 750 °C the area specific secant resistance was 0.26 Ω cm^2 (0.21 Ω cm^2 after correction for fuel utilization) and the observed power density at 0.6 V was 1.2 W cm^{-2} [33].

The theoretical area specific resistance contribution from a 1.2 μm thick 8YSZ layer is 0.004 Ω cm^2 at 750 °C based on bulk conductivity data for 8YSZ [34]. An ohmic resistance of approximately 0.05–0.06 Ω cm^2 was observed at 750 °C (see Fig. 8). This is more than ten times greater than the theoretical resistance expected from the electrolyte layer in the tested cell, but on the other

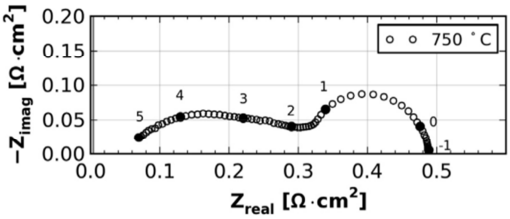

Fig. 8. Nyquist plot of the electrochemical impedance spectrum recorded with the 5-layer electrolyte SOFC at 750 °C and with 96% H_2 + 4% H_2O as the fuel and air as the oxidant. The impedance data was collected with 12 points per decade, indicated in the figure by filled symbols (also marked with the logarithm of the frequency), starting at 96.9 kHz (at low Z_{real} values). The dashed gray line indicates the theoretical resistance of the 1.2 μm thick 8YSZ electrolyte based on bulk conduction properties. The data in the plot was corrected for lead inductance.

hand a quite similar offset of 50–60 mΩ cm^2 is often seen and has previously been reported with a 10 μm thick ink-jet printed YSZ electrolyte [35]. Additionally, the cathode deposition method was reported to affect the series resistance [35]. Explanations to the observed high series resistance could be limited measurement range (the maximum frequency was 96.5 kHz). Other contributions to the observed ohmic resistance could be imperfect contacting of the electrolyte by the cathode layer, current constriction, or secondary phases formed at the interface [36]. Significant current collection losses are deemed unlikely as a sufficiently conducting current collection layer was used.

The ohmic resistance observed in electrochemical impedance spectroscopy can be assigned to the electrolyte, if it is measured to sufficiently high frequency, and assuming that there are no additional contributions to the ohmic resistance from current collection and the porous composite electrodes. Sufficient conductivity in the cathode current collection layer was confirmed by in-plane van der Pauw conductivity measurements [37]. Even though the observed ohmic resistance was much higher than the theoretical value, most of the impedance of this cell is related to the electrodes, and by improving the electrodes and ensuring a better contact to the electrolyte, a significant reduction in both ohmic and polarization resistance can be expected. This highlights the potential performance gain of cells with thin electrolyte, and further supports the feasibility of ink-jet based printing techniques for production of solid oxide cell components.

4. Conclusions

A 1.2 μm SOFC YSZ electrolyte was successfully fabricated by inkjet printing using a low-cost HP Deskjet 1000 DoD inkjet printer and an optimized 3.7 vol.% YSZ colloidal water-based ink. Missing droplets and imprecise impact on the anode substrate was observed to produce areas with lack of deposition when printing single layers. Inks with high dilution and nanometric particles improve printability and stability, however printing of multiple layers seems necessary to cover the defects formed during single layer printing. 2 layers were insufficient, but 5 layers resulted in a gas tight electrolyte. Although the electrolyte resistance was higher than expected from calculations using known bulk-electrolyte resistance, an SOFC tested with the electrolyte, an LSM/YSZ cathode and a Ni/YSZ anode produced an OCV above 1.15 V and a power peak density of 1.5 W cm^{-2} at 800 °C.

Acknowledgments

The authors gratefully acknowledge support from Energinet.dk through the ForskEL programme (project # 2012-1-10747).

References

[1] H. Minemawari, T. Yamada, H. Matsui, J. Tsutsumi, S. Haas, R. Chiba, R. Kumai, T. Hasegawa, Nature 475 (2011) 364–367.
[2] T. Wang, B. Derby, J. Am. Ceram. Soc. 88 (2005) 2053–2058.
[3] H. Sirringhaus, T. Kawase, R.H. Friend, T. Shimoda, M. Inbasekaran, W. Wu, E.P. Woo, Science 290 (2000) 2123–2126.
[4] M. Singh, H.M. Haverinen, P. Dhagat, G.E. Jabbour, Adv. Mater. 22 (2010) 673–685.
[5] D. Tobjörk, R. Österbacka, Adv. Mater. 23 (2011) 1935–1961.
[6] A.D. Taylor, E.Y. Kim, V.P. Humes, J. Kizuka, L.T. Thompson, J. Power Sources 171 (2007) 101–106.
[7] J. Ebert, E. Ozkol, A. Zeichner, K. Uibel, O. Weiss, U. Koops, R. Telle, H. Fischer, J. Dent. Res. 88 (2009) 673–676.
[8] R.L. Kenion, W.Y. Lee, in: 2011 IEEE 37th Annu. Northeast Bioeng. Conf, 2011, pp. 1–2.
[9] G.D. Martin, S.D. Hoath, I.M. Hutchings, J. Phys. Conf. Ser. 105 (2008) 012001, 1–14.
[10] R.I. Tomov, M. Krauz, J. Jewulski, S.C. Hopkins, J.R. Kluczowski, D.M. Glowacka, B.A. Glowacki, J. Power Sources 195 (2010) 7160–7167.
[11] I. Van Driessche, S. Hopkins, P. Lommens, X. Granados, D. Andreouli, B. Glowacki, I.M. Arabatzis, M. Arin, S. Ricart, I. Fasaki, E. Georgiopoulos, R. Tomov, Nanosci. Nanotechnol. Lett. 5 (2013) 466–474.
[12] D. Young, A.M. Sukeshini, R. Cummins, H. Xiao, M. Rottmayer, T. Reitz, J. Power Sources 184 (2008) 191–196.
[13] H. Kipphan, in: H. Kipphan (Ed.), Handbook of Print Media, Springer-Verlag, Berlin, Heidelberg, New York, 2001, pp. 711–730.
[14] J. Will, A. Mitterdorfer, C. Kleinlogel, D. Perednis, L.J. Gauckler, Solid State Ionics 131 (2000) 79–96.
[15] C. Wang, R.I. Tomov, R. Vasant Kumar, B.A. Glowacki, J. Mater. Sci. 46 (2011) 6889–6896.
[16] C. Li, H. Shi, R. Ran, C. Su, Z. Shao, Int. J. Hydrogen Energy 38 (2013) 9310–9319.
[17] A. Weber, E. Ivers-Tiffée, J. Power Sources 127 (2004) 273–283.
[18] X. Xin. Z. Lü. X. Huang. X. Sha. Y. Zhang. W. Su. Mater. Res. Bull. 41 (2006) 1319–1329.
[19] X. Chen, K. Khor, S. Chan, L. Yu, Mater. Sci. Eng. A 335 (2002) 246–252.
[20] S.P. Jiang, S.H. Chan, J. Mater. Sci. 39 (2004) 4405–4439.
[21] F. Teocoli, D.W. Ni, K. Brodersen, S.P.V. Foghmoes, S. Ramousse, V. Esposito, J. Mater. Sci. 49 (2014) 5324–5333.
[22] A.L. Yarin, Annu. Rev. Fluid Mech. 38 (2006) 159–192.
[23] A. Hauch, M. Mogensen, Solid State Ionics 181 (2010) 745–753.
[24] J. Glasscock, V. Esposito, S.P.V. Foghmoes, T. Stegk, D. Matuschek, M.W.H. Ley, S. Ramousse, J. Eur. Ceram. Soc. 33 (2013) 1289–1296.
[25] M.J. Jørgensen, M. Mogensen, J. Electrochem. Soc. 148 (2001) A433–A442.
[26] J. Wang, J. Evans, Phys. Rev. E 73 (2006) 021501, 1–8.
[27] B. Derby, Annu. Rev. Mater. Res. 40 (2010) 395–414.
[28] D. Marani, J. Hjelm, M. Wandel, J. Eur. Ceram. Soc. 34 (2014) 695–702.
[29] I.M. Hutchings, in: I.M. Hutchings, G.D. Martin (Eds.), Inkjet Technology for Digital Fabrication, Wiley, 2013, pp. 1991–1994.
[30] D. Jang, D. Kim, J. Moon, Langmuir 25 (2009) 2629–2635.
[31] B. Derby, N. Reis, MRS Bull. (2003) 815–818.
[32] J.F.B. Rasmussen, P.V. Hendriksen, A. Hagen, Fuel Cells 8 (2008) 385–393.
[33] M. Mogensen, P.V. Hendriksen, in: S. Singhal, K. Kendals (Eds.), High Temp. Solid Oxide Fuel Cells, Elsevier Science, 2003, pp. 261–289.
[34] C.C. Appel, N. Bonanos, A. Horsewell, S. Linderoth, D. Roskilde, J. Mater. Sci. 6 (2001) 4493–4501.
[35] M. Sukeshini, R. Cummins, T.L. Reitz, R.M. Miller, J. Am. Ceram. Soc. 92 (2009) 2913–2919.
[36] D.Z. de Florio, R. Muccillo, V. Esposito, E. Di Bartolomeo, E. Traversa, J. Electrochem. Soc. 152 (2005) A88–A92.
[37] M. Van der Pauw, Philips Res. Reports 13 (1958) 1–9.

Bonus : Music list

As a bonus, I would like to share a very short list of some artist that inspired me during these three years, and even before. Maybe this list will inspire you as much as it inspired me.

The author

Band	Album
Angus & Julia Stone	Angus & Julia Stone
Camera Obscura	Biggest Bluest Hi-Fi
Coconut records	Nighttiming
Cocoon	Welcome home
Daft Punk	Discovery
Exsonvaldes	Aranda
Frank Sinatra	Come fly with me
God help the girl	God help the girl
Indochine	Black city parade
John Williams	Star Wars: a new hope
Marilyn Manson	Mechanical animals
Moby	Play
Nephew	USA DSB
Nobuo Uematsu	Distant Worlds
Ok Go	Of The Blue Color of the Sky
Papa Roach	Infest
Placebo	Black Market Music
Radio Elvis	Les Conquêtes
Sparklehorse	Good Morning Spider
Tarmac	L'Atelier
The National	Boxer
The Smashing Pumpkins	Adore
Walk The Moon	Walk The Moon